Contemporary, decadal, and millennial-scale permafrost- and vegetation dynamics and carbon release in an alpine region of Jotunheimen, Norway

Helen Hallang

Submitted to Swansea University in fulfilment of the requirements for the Degree of Doctor of Philosophy

Swansea University

2021

Summary

Climatic warming in northern alpine regions facilitates the thawing of permafrost, the associated release of soil carbon into the atmosphere, and the altitudinal shifts in vegetation patterns. Here, a multi-disciplinary approach is adopted to investigate the response of an alpine permafrost landscape (Jotunheimen, Norway, with focus on Galdhøpiggen) to climatic changes over long- to medium timescales. First, a gas analyser is used to explore how ecosystem respiration is affected by ecosystem (soil and vegetation) and geomorphological (cryogenic disturbance) factors during the peak growing season. A palaeoecological record is then analysed to infer the past dynamics of the alpine tree lines and the lower limit of permafrost on Galdhøpiggen over the millennial- and centennial scales. Finally, remotely sensed satellite imagery is combined with observed air temperatures to create a model that provides an estimation of land surface temperatures over the past six decades. The model is then used to predict surface 'greenness' over the same period.

Palynological evidence from Galdhøpiggen indicates that the altitudinal limits of alpine tree lines have shifted by hundreds of metres in response to climatic changes over the millennial scale. Since 1957, the model predictions indicate substantial increases in land surface temperatures and growing season surface 'greenness' (i.e., vegetation abundance) in Jotunheimen, but the change has not been spatially uniform. The highest increases were recorded over the low- and mid-alpine heaths above the tree line (1050-1500 m a.s.l.), which was attributed to increased shrub cover. This trend could facilitate carbon release from the ground, as peak growing season ecosystem respiration was found to be most strongly controlled by soil microclimate and plant growth forms. The likely future scenario in response to warming in Jotunheimen will be continued permafrost degradation, with higher altitudes (≥1500 m a.s.l.) experiencing decreased cryoturbation, increased shrub encroachment and higher surface CO_2 emissions.

Declarations and statements

Declaration

This work has not previously been accepted in substance for any degree and is not being concurrently submitted in candidature for any degree.

Signed: ..... 

Date: 09.09.2021

Statement 1

This thesis is the result of my own investigations, except where otherwise stated. Where correction services have been used, the extent and nature of the correction is clearly marked in a footnote(s). Other sources are acknowledged by footnotes giving explicit references. A bibliography is appended.

Signed ..... 

Date: 09.09.2021

Statement 2

I hereby give consent for my thesis, if accepted, to be available for photocopying and for inter-library loan, and for the title and summary to be made available to outside organisations.

Signed: ..... 

Date: 09.09.2021

Authorship declarations

Paper 1: *Carbon dioxide emissions from periglacial patterned ground under changing permafrost conditions and shrub encroachment in an alpine landscape, Jotunheimen, Norway*

Located in: Chapter 3

Candidate contributed: The candidate's contributions to the publication include leading the design of the work, the acquisition and analysis of the data, interpretation of the results, solely drafting the manuscript and corresponding with the reviewer. Percentage contribution: 75%

Co-authors contributed:

Dr John Hiemstra: Contributed to the design of the project, the acquisition and interpretation of the data, and revised the manuscript.

Dr Sietse Los: Contributed to the design of the project and the interpretation of the data and revised the manuscript.

Prof John Matthews: Contributed to the acquisition and interpretation of the data and revised the manuscript.

Dr Cynthia Froyd: Contributed to the design of the project and interpretation of the data and revised the manuscript.

All authors approved the final manuscript before publication.

We the undersigned agree with the above stated 'proportion of work undertaken' for the published manuscript presented in Chapter 3 of this thesis:

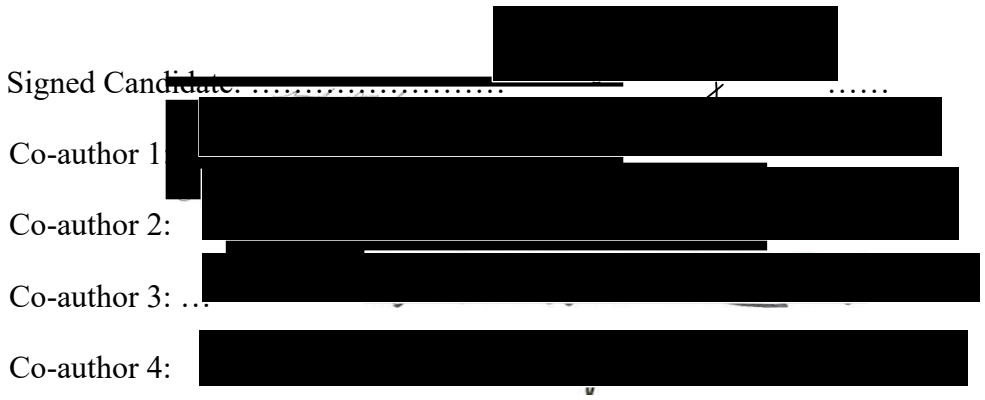

Paper 2: *Tree line shifts, changing vegetation assemblages and permafrost dynamics on the slope of Galdhøpiggen (Norway) over the past ~4400 years*

Located in: Chapter 4

Candidate contributed: The candidate's contributions to the publication include leading the design of the work, the acquisition and analysis of the data, interpretation of the results and solely drafting the manuscript. Percentage contribution: 80%

Co-authors contributed:

Dr Cynthia Froyd: Contributed to the design of the project, the acquisition and interpretation of the data and revised the manuscript.

Dr John Hiemstra: Contributed to the design of the project and interpretation of the data and revised the manuscript.

Dr Sietse Los: Contributed to the design of the project and interpretation of the data and revised the manuscript.

All authors approved the final manuscript before publication.

We the undersigned agree with the above stated 'proportion of work undertaken' for the manuscript presented in Chapter 4 of this thesis:

Signed Candidate: ……

Co-author 1: ……

Co-author 2:

Co-author 3: …

Paper 3: *Permafrost, thermal conditions, and vegetation patterns since the mid-20th century: a remote sensing approach applied to Jotunheimen, Norway*

Located in: Chapter 5

Candidate contributed: The candidate's contributions to the publication include leading the design of the work, the acquisition and analysis of the data, interpretation of the results and solely drafting the manuscript. Percentage contribution: 70%

Co-authors contributed:

Dr Sietse Los: Contributed to the design of the project, the acquisition and interpretation of the data and revised the manuscript.

Dr John Hiemstra: Contributed to the design of the project and interpretation of the data and revised the manuscript.

All authors approved the final manuscript before publication.

We the undersigned agree with the above stated 'proportion of work undertaken' for the manuscript presented in Chapter 5 of this thesis:

Signed Candidate: [redacted]

Co-author 1: ..... [redacted]

Co-author 2: ..... [redacted]

Contents

Acknowledgements

I wish to express my deepest gratitude to my supervisors, Dr John Hiemstra, Dr Sietse Los and Dr Cynthia Froyd, whose individual expertise helped to put together this multi-disciplinary project. Your advice, support, and encouragement through each stage of the process has been invaluable. I would also like to thank Professor John Matthews for providing his expert knowledge on the field and during the preparation of manuscripts throughout this project. I whole-heartedly appreciate the guidance that all of you provided during my study.

I am grateful to the Luxembourgish Ministry of Higher Education and Research for providing the funding that made it possible for me to undertake this project, and to the Quaternary Research Association for funding the peat core analysis. I would further like to thank Swansea University and the College of Science for the opportunity to develop my career in research, and for providing the financial support that allowed me to participate in the Swansea University Jotunheimen Research Expedition in 2018.

I would like to thank everyone involved with the project presented in Chapter 3, especially Dr Emilia Urbanek for providing the advice and equipment that made the field work possible, Mats Hiemstra and Geraint Owen for assistance in the field, Professor Neil Loader and Dr Kath Ficken for their help with laboratory analyses and Grahame Walters for arranging the equipment. I would also like to recognise the wonderful postgraduate community, whose assistance not only contributed towards the success of this project but made it a pleasant experience.

Finally, I am indebted to my family and close friends for their continued support, and to my partner Ashleigh for inspiring and challenging me every step of the way.

I would also like to thank the examiners, Prof Peter North and Prof Robert Whittaker, for their time and contribution to improving this thesis.

List of tables

List of figures

Abbreviations

AMS: Accelerator mass spectrometry

ANOVA: Analysis of variance

CONISS: Constrained cluster analysis

EOS: Earth Observing System

ER: Ecosystem respiration

FPA: Focal Plane Assembly

GPA: Gross primary production

HF: Hydrofluoric acid

LARS: Least angle regression

LIA: Little Ice Age

LOI: Loss on ignition

LST: Land surface temperature

LST_{gs}: Growing season land surface temperature

LWIR: Long-wave infrared

MAAT: Mean annual air temperature

MODIS: Moderate Resolution Imaging Spectrometer

MWIR: Mid-wave infrared

NASA: National Aeronautics and Space Administration

NDVI: Normalised Difference Vegetation Index

$NDVI_{gs}$: Growing season Normalised Difference Vegetation Index

NE: North-east

NEE: Net ecosystem exchange

NHZ1: Northern hemisphere zone 1

NIR: Near infrared

PAR: Pollen accumulation rate

PVC: Polyvinyl chloride

R_e : Ecosystem respiration

RH: Relative humidity

RMSE: Root mean squared error

R_s: Soil respiration

SOC: Soil organic carbon

SOM: Soil organic matter

SVP: Saturated vapour pressure

SWIR: Short-wave infrared

TBA: Tertiary butyl alcohol

T_{day}: Mean daily air temperature

TLP: Total land pollen

T_{max}: Maximum daily air temperature

T_{min}: Minimum daily air temperature

VIS: Visible light

VPD: Vapour pressure deficit

XRF: X-Ray Fluorescence

Chapter 1

Introduction

1.1. Introduction: Rationale, study site and thesis structure

High-latitude and high-altitude regions are among the most vulnerable to climatic changes on a global scale (Biskaborn et al., 2019). With rates of warming twice as high as the global mean (Stocker et al., 2013), sub-surface permafrost is warming and thawing (Romanovsky et al., 2010; Serreze et al., 2000; Streletskiy et al., 2017). Permafrost degradation can result in the release of previously frozen carbon from the soil into the atmosphere (Turetsky et al., 2019). Warming surface temperatures can further provide more favourable growing conditions for tundra plants, facilitating the shift – both latitudinal and altitudinal – of previously uninhabitable surfaces to shrubs and grasses (Myers-Smith et al., 2011). Both mechanisms have the potential to affect local and regional carbon- and nutrient cycling, and energy balance (Serreze and Barry, 2011; Schuur et al., 2015). However, the consequences of climatic warming vary, and depend on the specific conditions (i.e., topography, ice content of permafrost, composition of substrate, nutrient availability, etc.) of the area of interest.

The present thesis investigates the response of an alpine permafrost landscape to climatic changes over different timescales. The area of interest is a mountainous region in north-east Jotunheimen (Norway), with specific focus on the mountain of Galdhøpiggen. The region provides an excellent field laboratory to study shifts in permafrost occurrence and vegetation patterns in response to changing air temperatures over time. This is achieved by using complementary methods to examine the processes across abiotic and biotic components of the landscape.

The approach adopted in this study is multi-disciplinary, as well as multi-scale, both spatially and temporally (see sub-Section 1.1.3). Combining multiple disciplines and spatiotemporal scales could be considered novel, as there is generally little interaction between communities of periglacial geomorphologists, palaeoecologists and remote sensing specialists.

Chapter 3 investigates how ecosystem respiration (R_e) is affected or controlled by ecosystem (soil and vegetation) and geomorphological (cryogenic disturbance) factors by exploring the rates of R_e across an altitudinal transect on Galdhøpiggen. Chapter 4 extends the temporal scale, investigating the dynamics of the alpine tree line and the lower limit of permafrost on Galdhøpiggen over the millennial scale. Chapter 5

extends the spatial scale by examining changes in air- and surface temperatures and vegetation cover in Jotunheimen over the past six decades, and tests whether there are spatial differences in the rate of change. The specific aims of each study are outlined in more detail in the introductions of the corresponding chapters.

Simultaneously, the applicability of the methods used for studying the response of this alpine area to past and present climatic warming is tested in all parts of the research project. Whilst Jotunheimen is a well-studied region (see sub-Section 1.1.2), some of the methods presented here have not previously been used in this area and complement the existing knowledge. For example, Chapter 3 will discuss the use of a portable infrared gas analyser to measure surface CO_2 emissions and test the novel idea that disturbance by cryogenic processes in the soil might create 'preferential pathways' for CO_2 release. Chapter 4 combines four different methods used in palynological assessments to improve the accuracy of the past environmental reconstruction and the identification of past local vegetation assemblages. Chapter 5 combines satellite remote sensing and meteorological data to model land surface temperatures and surface 'greenness' values for the past 60 years; the results are used to estimate the past positions of the alpine tree lines and the possible past distributions of sub-surface permafrost, which has not been done at a similar resolution in this area before.

1.1.1. Study site selection

The area of interest in this study is the mountainous north-eastern section of Jotunheimen in southern Norway. The topographic, climatic and vegetational properties of this area are described in detail in Chapter 5. Two chapters (3 and 4) will focus specifically on Galdhøpiggen, the highest peak in Scandinavia and northern Europe. The sub-surface thermal- and permafrost conditions, and the methods used to measure and monitor them on Galdhøpiggen are outlined in more detail in sub-Section 1.2.4 and Chapters 3 and 5. Present and past vegetation distribution and dynamics are discussed in Chapters 3 and 4.

Galdhøpiggen was selected as a study site based on a combination of factors. First, it is a high-latitude (north of 60° N) mountain underlain by high-altitude sub-surface permafrost, making this area one of the most vulnerable to climatic warming (Biskaborn et al., 2019). Second, Galdhøpiggen is easily accessible, with a (13 km

long) paved road leading from the valley up to the altitude of ~1900 m a.s.l. on the north-facing slope. This allows for repeated field measurements in the space of a single day (as outlined in Chapter 3), and the transport of heavy equipment between sites. Third, Galdhøpiggen provides a setting where sub-surface permafrost ranges from sporadic to continuous, with periglacial landforms (sorted circles) present at various altitudes. Vegetation assemblages (belts) on the north-facing slope include the sub-alpine dense woodland (~850-1025 m a.s.l.), low-alpine dwarf-shrub heath (~1025-1350 m a.s.l.), mid-alpine grass-dominated heath (~1375-1600 m a.s.l.) and the sparsely vegetated lichen and grass-dominated high-alpine vegetation belt (~1600-2200 m a.s.l.) (Matthews et al., 2018). Such drastic vegetational and thermal differences occur over relatively small distances, further facilitating research activities. Moreover, this landscape provides a setting where different vegetation assemblages grow above varying extents of sub-surface permafrost. Finally, Galdhøpiggen has been the focal point of numerous studies over the past decades. Both geomorphological (Farbrot et al. 2011; Haugland et al., 2004; Lilleøren et al., 2012; Matthews et al., 1998; Ødegård et al., 1988; Ødegård et al., 1992; Winkler et al., 2016) and ecological (e.g., Matthews 1992, 1999; Matthews et al., 2018; Robbins and Matthews, 2010, 2014) properties of the north-facing slope have been investigated in detail. This provides an excellent baseline for a multi-disciplinary study that aims to combine different methods to explore the response of the area to climatic warming.

1.1.2. Structure of the thesis

The present Introduction is followed by the Methodology Chapter (Chapter 2), which provides additional detail about the background, the technical aspects of the equipment and full laboratory procedures to complement the Methodology sections in Chapters 3-5. The main body of the thesis consists of three Chapters (3-5), each outlining the research done on a specific spatiotemporal scale (Table 1.1). Chapter 3 examines the soil CO_2 emissions over a small spatial and temporal scale: across a transect on the north-facing slope of Galdhøpiggen during a single peak growing season. Chapter 4 is a palynological study that investigates the long-term dynamics of the tree line and tundra vegetation belts on the north-facing slope of Galdhøpiggen over the past c. 4000 years.

Chapter 5 extends the spatial scale and uses satellite-derived land surface temperatures and NDVI to model and describe the thermal and vegetational conditions and trends in north-east Jotunheimen over the period 1957-2019.

Table 1.1. The primary research questions by chapter, and the spatial and temporal scales of the main methods used in each study.

Main research questions	*Method*	*Chapter*	*Spatial scale*	*Temporal scale*
What are the main biotic and abiotic controls on peak growing season ecosystem respiration (R_e)?	Field-based measurements	3	Local (Galdhøpiggen)	*Short:* July 2018
How have the alpine tree line and lower limit of permafrost fluctuated over millennial and centennial scales?	Palynological analysis	4	Landscape (Galdhøpiggen)	*Long:* 4350 cal. yr BP-present
How have the temperature and vegetation cover changed over the past six decades, and are there spatial differences in the rate of change?	Satellite remote sensing	5	Regional (NE Jotunheimen)	*Medium:* 1957-2019

The final section (Chapter 6) is a synthesis of the three preceding chapters, providing a coherent summary of the observed changes, comparing the methods used in the three research chapters and discussing future implications. Chapters 3-5 have appendices that provide additional detail to the results associated with the relevant project.

1.2. Introduction: background and concepts

1.2.1. Impacts of climatic changes on high-latitude and alpine ecosystems

In the face of changing climate, high-latitude and high-altitude ecosystems are among the most vulnerable on the globe. Today, regions north of 60° N are experiencing rising surface air temperatures at more than double the rate of the global mean, a process known as Arctic amplification (Overland et al., 2019; Stocker et al., 2013).

The drivers behind the amplified temperature increase are manifold, likely involving various climate feedbacks and processes operating on a range of spatial and temporal scales (Cho et al., 2018; Serreze and Barry, 2011). One of the proposed main causes is the decline of snow and ice cover, which reduces surface albedo and allows the surface to absorb more heat, creating a positive feedback that leads to further warming (Chapin, 2005; Graversen et al., 2008). Other contributing factors are alterations in cloud cover, water vapour and oceanic circulation, changes in atmospheric heat transport, soot-covered snow, and increased concentrations of black carbon aerosols in the atmosphere (Francis and Hunter, 2006; Graversen et al., 2008; Hansen and Nazarenko, 2004; Serreze and Barry, 2011; Shindell and Faluvegi, 2009).

Due to the amplification effect, high-latitude ecosystems are predicted to experience the consequences of climate warming more intensely compared to the rest of the globe (Hinzman et al., 2013). Permafrost thaw driven by warming has already become a pressing problem, reshaping the landscape, transforming ecosystems, and disrupting livelihoods in the north. Permafrost degradation is considered one of the most potentially destructive consequences of climate change due to its capacity to release large quantities of buried carbon into the atmosphere. The resulting positive feedback loop could have devastating impacts for the planet. Arctic amplification is predicted to intensify in the future, and it will continue to impact biological, hydrological, and geophysical systems across the circumpolar north (Hinzman et al., 2013; Serreze and Barry, 2011).

High-altitude ecosystems are similarly vulnerable to warming air temperatures and changing precipitation regimes. Mountain permafrost is particularly sensitive to climate variation (Hipp et al., 2012) and has globally warmed by 0.19 ± 0.05 °C between 2007-2016 (Biskaborn et al., 2019).

Permafrost warming and degradation in alpine regions is accompanied by the upslope shifts of trees and shrubs, as the conditions for vegetation growth become more favourable at higher altitudes (Dial et al., 2007; Hallinger et al., 2010; Myers-Smith et al., 2011).

The following sub-sections (1.2.2-1.4.1) will highlight the observed and predicted consequences of warming on high-latitude alpine permafrost ecosystems and their components based on contemporary literature and introduce a range of methods to examine environmental change in these environments.

1.2.2. Permafrost and cryogenic processes in periglacial soils

Permafrost, the subsurface ground that remains below 0 °C for a minimum of two consecutive years (Ballantyne, 2018), underlies an estimated 22% of the exposed land surface of the northern hemisphere (Zhang et al., 1999). As the permafrost zone is not uniform and ranges from continuous to sporadic (Figure 1.1), the actual land area occupied by permafrost is approximately 12.8 – 18% (Gruber, 2012). Permafrost occurrence and thickness are largely controlled by the surface energy balance, and to some extent by local and regional conditions such as topography, hydrology, vegetation, subsurface materials, and snow cover thickness (Schuur et al., 2008). Permafrost occurrence therefore varies across latitudes, but around 70% is located between 45°N and 67°N (Zhang et al., 1999).

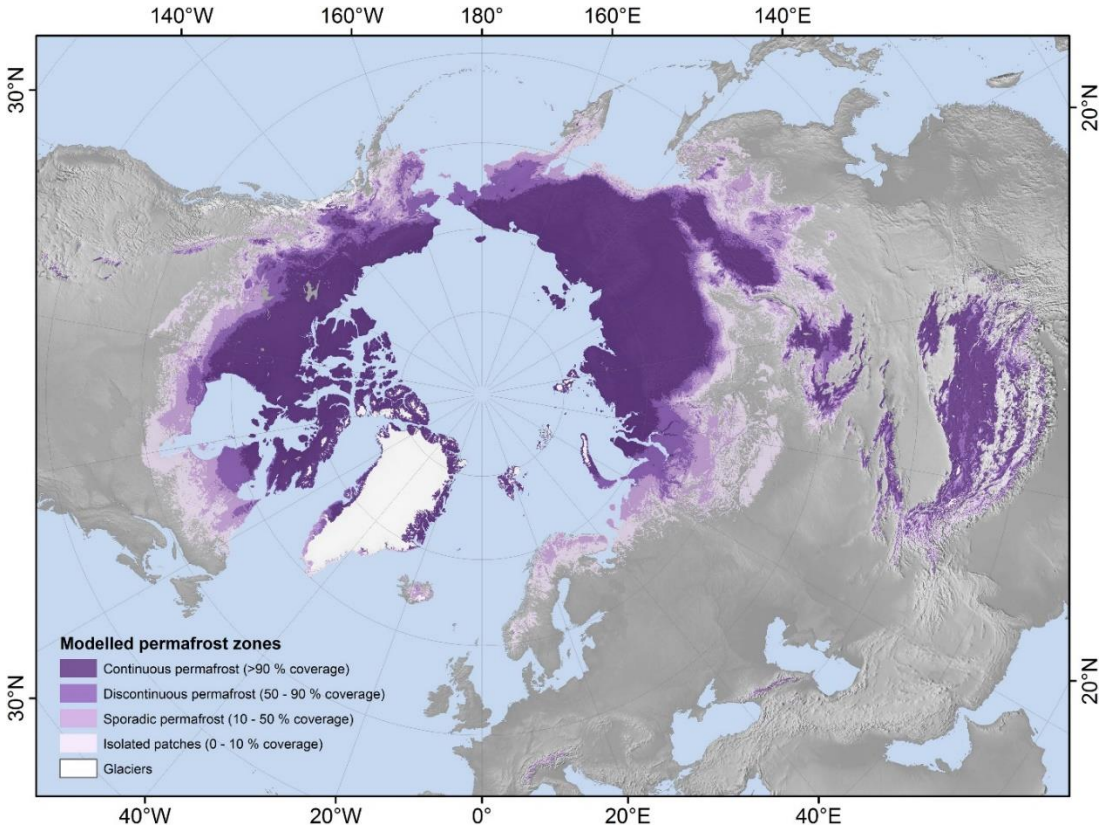

Figure 1.1. Northern hemisphere permafrost distribution at 1 km^2 resolution. Map taken from Obu et al. (2019).

The thermal dynamics of permafrost soils in a given location are often presented in a thermal regime graph (Figure 1.2). Such graphs illustrate the maximum and minimum ground temperatures measured throughout the year at given depths, and the mean annual ground temperatures (MAGT). As the depth increases, the amplitude of measured temperatures decreases, eventually reaching the depth of zero annual amplitude, where the MAGT fluctuates by less than <0.01°C.

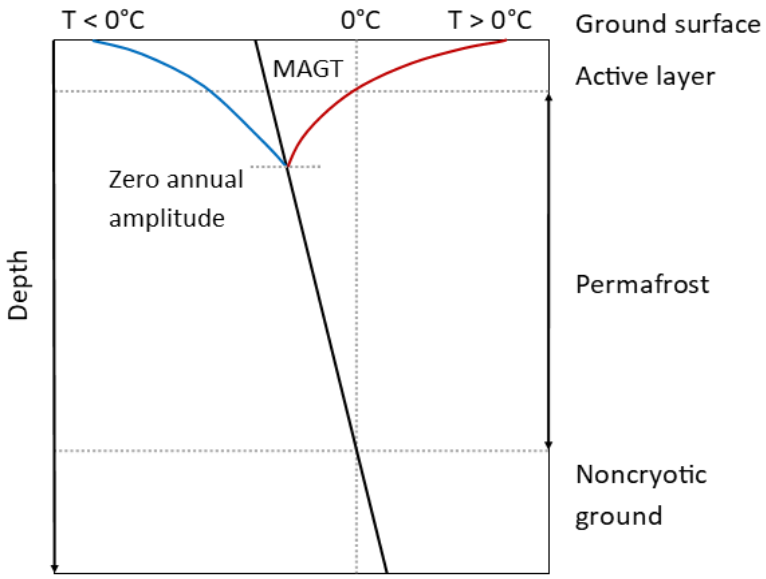

Figure 1.2. A simplified representation of the ground thermal regime in a permafrost region, illustrating the temperature change with increasing depth. The blue line represents the temperatures below mean annual ground temperatures (MAGT), and the red line indicates the values above MAGT. Zero annual amplitude is the depth at which the MAGT remains constant (fluctuating by less than <0.01°C). Figure modified from Ballantyne (2018).

Above the subsurface permafrost zone lies the active layer: a near-surface ground layer which remains frozen in the winter and thaws in the summer (Figure 1.2). The depth of the active layer can vary from tens of centimetres to several metres, depending on local conditions and climate (Schuur et al., 2008). The thickness of the active layer shapes the ecosystem by influencing local hydrology, plant rooting depth and the quantity of soil organic matter that thaws in the summer (Schuur et al., 2008).

Cryogenic processes in the active layer shape the landscape in periglacial environments. Cryoturbation, the movement of soil due to repeated freezing and thawing, can create distinct patterns reflected in distribution of sediment and vegetation on the ground surface (Ballantyne, 2018; Bockheim, 2007; Schuur et al., 2008). These patterns can take the form of circles, stripes, polygons or nets, and can be described as sorted or non-sorted depending on their morphology (Walker et al., 2004). The size and shape of the feature are determined by the local environmental conditions (Vonlanthen et al., 2008). Cryoturbation is most intense in soils with poor drainage (Bockheim, 2007) and areas where ground freezes upward from the permafrost table and downward from the surface (Schuur et al., 2008).

Several processes have been proposed to explain the genesis of patterned ground, but the two main processes likely to be responsible in most cases are differential frost Heave and buoyancy-driven soil circulation (Ballantyne, 2018). Due to the mixing of the soil, patterned ground features affect several ecosystem properties and processes such as vegetation patterns, active layer depth, soil pH, carbon sequestration and energy fluxes (Walker et al., 2004).

Sorted circles are a form of patterned ground. They usually develop on surfaces with little vegetation and fine soil, and form circles with bare centres and borders consisting of larger clasts and boulders (Ballantyne, 2018; Figure 1.3). The diameters of these features range from 10 cm to 4 m, with wider circles usually surrounded by larger boulders (Ballantyne, 2018). In permafrost landscapes, the thickness of the active layer can control the width of the circles, as smaller circles are often found on ground with thinner active layers (Uxa et al., 2017).

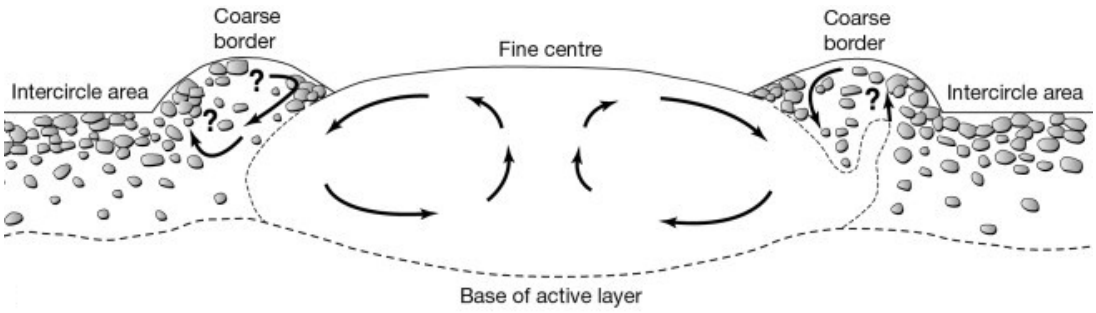

Figure 1.3. An illustration of the sub-surface circular movement of non-frozen sediment and clasts within sorted circles proposed by Hallet and Prestrud (1986) and reproduced by Ballantyne (2018).

Depending on the intensity of frost activity, sorted patterned ground can be considered active or relict. Active sorted circles experience continuing uplift and sorting of clasts through freeze-thaw processes, whilst relict circles have been inactive for a period of time (Ballantyne, 2018). Due to regular disturbance, active sorted circles have little or no vegetation cover (Haugland, 2006; Matthews et al., 1998). Relict circles can be vegetated, but their centres can remain bare if some frost disturbance still occurs (Haugland, 2006; Winkler et al., 2016).

Seasonal freeze-thaw cycles and the depth of the active layer in permafrost soils are being altered by warming air temperatures. Widespread thawing of permafrost has been documented across the circumpolar north and in high alpine environments over the past decades, causing concern over the stability of carbon stores in frozen soils (Natali et al., 2015; Vonk et al., 2015).

1.2.3. Carbon storage capacity of permafrost soils

Permafrost soils across the globe, including Arctic, Antarctic but also alpine areas, contain vast quantities of carbon as cold-climate ecosystems provide favourable conditions for long-term carbon storage (Schuur et al., 2008). Short growing seasons, low solar energy input and long, harsh winters combined with poorly drained soils lead to slow rates of primary production, respiration, and decomposition (Virkkala et al., 2018). Albeit slow, the primary production rates in cold environments exceed the decomposition rates, facilitating the accumulation, burial, and storage of organic carbon (Belshe et al., 2013).

The total estimated terrestrial permafrost carbon content in the northern circumpolar permafrost zone is ~ 1,330 – 1,580 Pg (Hugelius et al., 2014; Schuur et al., 2015). This is equivalent to almost half of global soil organic carbon (SOC) stores, and close to double the amount present in the atmosphere today (Virkkala et al., 2018; Schuur et al., 2008). Out of all the soil carbon within the top 0-3 m of the planet's soils, around 44% is found in the northern hemisphere permafrost region (Tarnocai et al., 2009).

1.2.4. Permafrost environments – sinks or sources of carbon?

The exchange of carbon between terrestrial ecosystems and the atmosphere is dominated by two fluxes. Ecosystems sequester carbon via photosynthesis (gross primary production: GPP), whilst the combination of plant- and microbial respiration (ecosystem respiration: ER) release carbon dioxide (CO_2) back into the atmosphere (Virkkala et al., 2018). A delicate balance exists between these fluxes. Whether high-latitude and alpine ecosystems will act as a sink or a source of carbon in the future is uncertain because warming can affect the carbon cycle in contrasting ways (Belshe et al., 2013; Lundin et al., 2016; McGuire et al., 2012).

Increased atmospheric greenhouse gas concentrations lead to higher air temperatures, creating suitable conditions for permafrost degradation. As permafrost thaws, previously frozen SOC becomes available for microbial decomposition by heterotrophs, resulting in increased ecosystem respiration and carbon emissions from soils into the atmosphere (Belshe et al., 2013; McGuire et al., 2009; Schuur et al., 2008). The extent of carbon emissions is regulated by both the size of the newly exposed SOC pool and the rate of microbial decomposition (Doetterl et al., 2015; Schuur et al., 2008). Furthermore, higher temperatures can stimulate soil microbial activity and accelerate carbon and nitrogen cycling in cold alpine soils (Donhauser and Frey, 2018). However, soil microbial communities are also influenced by the moisture content of the soil, and excess moisture hinders microbial activity (Kim et al., 2014). Therefore, the effects of increased air and soil temperature on soil microbial activity will in part depend on the precipitation patterns throughout the seasons. Whilst precipitation is predicted to increase significantly in the Arctic due to climate change, alpine areas are not expected to experience drastic changes in precipitation in the future (Donhauser and Frey, 2018). Nevertheless, it is predicted that both alpine and Arctic regions will experience decreased snowfall that will be replaced by rain, which will have further implications for the soil temperature due to the loss of thermal insulation in the winter in the form of snow cover (Phillips and Schweizer, 2007).

It is evident that the effect of warming on carbon emissions from cold-climate ecosystems is not straightforward, as it can lead to both positive and negative feedback loops. In addition to the possible carbon losses from the soil via respiration, higher temperatures and atmospheric carbon concentrations also have the potential to stimulate primary production. Longer growing seasons and increased availability of soil nutrients released by decomposition of previously frozen organic material could lead to higher rates of photosynthesis in tundra plants (Belshe et al., 2013; Natali et al., 2011). If the resulting carbon sequestration rates exceed ecosystem respiration, the feedback could in turn be negative, resulting in increased uptake of carbon from the atmosphere. The encroachment of vegetation to previously uninhabitable higher latitudes and altitudes, discussed in further detail below, also has the potential to sequester carbon and offset emissions from heterotrophic respiration.

The carbon cycle in permafrost environments is further influenced by cryogenic disturbances in the soil (Figure 1.4). Surface disturbance can negatively affect plant

roots (Kade and Walker, 2008), reducing vegetation cover and thus carbon inputs from photosynthesis, which in turn affects the thickness of the organic layer. Sparse plant cover offers insufficient insulation to the soil, which further exacerbates frost activity (Kade and Walker, 2008) and reduces the capacity of cryoturbated landscapes to sequester carbon. Organic matter mixed with mineral soil via cryoturbation has been documented to increase rates of short-term microbial respiration by 40% (Klaminder et al., 2013). Moreover, alpine tundra sites experiencing freeze-thaw disturbance have been found to be sources of CO_2 (Becher et al., 2015; Lundin et al., 2016) whilst non-disturbed, vegetated areas were weak sinks (Fox et al., 2008).

Conversely, cryoturbation can transport SOC from the carbon-rich near-surface layer to deeper, colder soil horizons with limited microbial activity, where it can potentially become stored in permafrost, contributing to carbon storage (Schuur et al., 2008). Whilst SOC content is expected to be highest near the ground surface due to inputs from photosynthesizing vegetation, cryoturbation can redistribute significant amounts of carbon (Schuur et al., 2008). A study in northern Alaska revealed that over half (55%) of active-layer and near-surface permafrost SOC has been relocated by cryoturbation (Bockheim, 2007). Cryoturbation is expected to become more widespread across high latitudes as temperatures rise, and there is evidence that this process may in fact increase carbon storage in some areas (Bockheim, 2007; Kaiser et al., 2007).

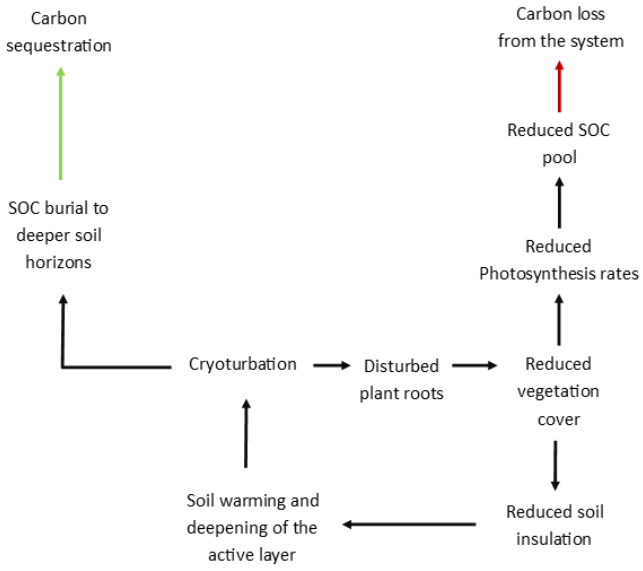

Figure 1.4. A simplified illustration of the influence of cryoturbation on the carbon cycle in a periglacial environment.

The effect of permafrost degradation on soil carbon emissions and future climate feedbacks is also controlled by the ice content of permafrost. Areas underlain by ice-rich permafrost are facing substantial changes in topography and local ecosystem dynamics as permafrost thaws (Schuur et al., 2008). The breakdown of ice-rich permafrost can transform the landscape by bringing about saturated soils, wetlands and thermokarst lakes (Vonk et al., 2015). Waterlogged soils and ponds provide anaerobic conditions for decomposition, facilitating the release of another potent greenhouse gas, methane (CH_4), into the atmosphere (Vonk et al., 2015; Wik et al., 2013). This creates an additional pathway for carbon exchange between the biosphere and the atmosphere, influencing the carbon cycle and potentially contributing to future warming.

Based on the synthesis of relevant research, high-latitude tundra ecosystems have been carbon sinks throughout the Holocene (Belshe et al., 2013; Hicks Pries et al., 2012). However, this process has reversed since the mid-1980s, and a meta-analysis of 54 studies reveals that tundra environments are now acting as a source of CO_2 (Belshe et al., 2013). The effects of climate change will not be uniform across permafrost regions, and whilst the occurring changes are rapid and dramatic, the consequences are not fully understood, and these ecosystems are currently poorly monitored (Grosse et al., 2016). Moreover, high-latitude and alpine treeless tundra ecosystems are highly heterogeneous, encompassing various plant communities and environmental conditions that can vary significantly within only a metre (Aalto et al., 2013; Fox et al., 2008). Landscape heterogeneity has the potential to offset some of the effects of climate change, but this topic has received little attention so far (Post et al., 2009; Ylänne et al., 2015).

1.3. Tundra greening and its regional and global effects

For terrestrial high-latitude ecosystems, a major consequence of rising temperatures has been the increase in vegetation cover, accompanied by the northward movement of vegetation belts (Frost et al., 2019), with similar upslope shifts noted in alpine areas (Grytnes et al., 2014; Klanderud and Birks, 2003; Post et al., 2009; Tape et al., 2006). In the literature, this is referred to as ‘the greening of the Arctic’. In addition to increased biomass and altered distribution, there have been observed changes in the composition and density of tundra vegetation over the past decades (Myers-Smith et

al., 2011; Pearson et al., 2013). Climatic warming is considered to be one of the main drivers of these trends because tundra plant growth is, to an extent, limited by temperature. In addition to altering physiological processes, higher temperatures can increase the availability of nutrients for plant uptake by boosting soil microbial activity (Chapin, 1983).

Especially notable is the increasing expansion of trees and shrubs at the expense of other tundra plants (i.e., graminoids, herbaceous plants). Shrubs are woody perennial plants that are often the tallest forms of vegetation in the treeless tundra. The tallest tundra shrubs (e.g., *Betula nana*) can reach up to 4 m in height, whilst dwarf shrubs (e.g., *Vaccinium uliginosum*) generally remain between 0.1-0.4 m and prostrate shrubs (e.g., *Salix herbacea*), which extend their stems laterally over the ground, remain below 0.1 m in height (Myers-Smith et al., 2011). The encroachment of shrubs, or 'shrubification,' is widespread, as surges in woody shrub abundance and biomass have been detected throughout the Arctic tundra (Myers-Smith et al., 2011; Tape et al., 2006). In alpine ecosystems, the upslope advancement of shrubs and various other alpine plants has also been observed across continents (Anthelme et al., 2007, Cannone et al., 2007, Dullinger et al., 2003; Walther et al., 2005). For example, the altitudinal progression of juniper in Sweden (Hallinger et al., 2010) and the shifts in willow and alder cover in Alaska (Dial et al., 2007) are well documented. However, these trends are not uniform and tundra 'greenness' as well as tundra productivity vary spatially and temporally.

At lower elevations in the sub-alpine vegetation belt, tree lines are also advancing (e.g., Cazzolla Gatti et al., 2019; Grace et al., 2002; Holtmeier and Boll 2005; Kullmann, 2001). A large-scale study in southern Swedish Scandes by Kullman and Öberg (2009) found that tree lines of *Betula pubescens, Picea abies* and *Pinus sylvestris* have advanced upslope on average by 70-90 m in 95% of the monitored sites over the past century. Maximum upshifts of 200 m were recorded and the ascent is unprecedented, although the authors stress that tree line advancement is highly site-dependent and is less likely to occur on wind-exposed slopes, highlighting again the heterogeneity of such trends.

Satellite imagery is widely used to assess the tundra vegetation dynamics over the recent decades. Indices such as the NDVI (Normalised Difference Vegetation Index, discussed in further detail below) can be used to detect positive and negative trends in

the ‘greenness’ of the observed area. Therefore, the ‘greening’ of the tundra can refer to both an increase in the satellite-derived index and to vegetation changes observed in the field (Myers-Smith et al., 2020). Negative trends in NDVI, termed ‘browning’, have also been observed across high-latitude tundra environments (Myers-Smith et al., 2020).

Tundra greening, as viewed from space, is largely a result of vegetation moving onto previously bare surfaces, increased shrubification or changing plant traits and/or phenology (Boelman et al., 2011; Martin et al., 2017; Pattison et al., 2015). Such transformations are brought about by more favourable growing conditions. Climatic warming in high-latitude and high-altitude environments positively affects NDVI, as warming can result in longer growing seasons due to earlier snowmelt as well as enhanced microbial activity, which in turn increases the nutrient availability of the soils (Myers-Smith et al., 2011). Precipitation (Cui and Shi, 2010; Wang et al., 2003) and increased atmospheric CO_2 concentrations (i.e., ‘CO_2 fertilisation’) (Los, 2013) are additional drivers of NDVI around the globe; for some regions, they can be similarly important as temperature.

Conversely, browning, which is essentially the loss of photosynthetically active plant material, can be caused by deteriorating growing conditions and extreme events (Myers-Smith et al., 2020). Shorter growing seasons due to climatic anomalies and reduced water and/or nutrient availability can have adverse effects on the temperature– and nutrient limited tundra vegetation (Martin et al., 2017). Tundra vegetation is vulnerable to various hazards, such as extreme climatic events (e.g., winter warming, extreme weather events), permafrost degradation resulting in the transformation of the landscape and its hydrology, pest outbreaks and fire (Bjerke et al., 2014; Bokhorst et al., 2008; Lara et al., 2018; Lund et al., 2017; Rocha et al., 2012; Treharne et al., 2019). However, overall long-term observations point to tundra greening as the dominant trend across the high latitudes (Myers-Smith et al., 2020).

Such local- and regional-scale changes in tundra vegetation cover have a range of wider ecological consequences as they influence several biosphere-atmosphere feedbacks (Figure 1.5; Pearson et al., 2013; Post et al., 2009). Increased vegetation height and cover can intensify land surface- and atmospheric warming through reduced surface albedo and increased evapotranspiration (Euskirchen et al., 2007; Keenan and Riley, 2018; Sturm et al., 2001). Further, it can alter greenhouse gas balances (Post et

al., 2009), soil moisture (Hinzman et al., 2013), carbon and nutrient cycles (Frost et al., 2019) and global-scale soil carbon storage (Myers-Smith et al., 2020). Whilst tundra plants can reduce the CO_2 concentration of the atmosphere by sequestering carbon, shrubification is likely to create an overall positive feedback to climate warming (Cahoon et al., 2012; Chapin et al., 2005; Pearson et al., 2013).

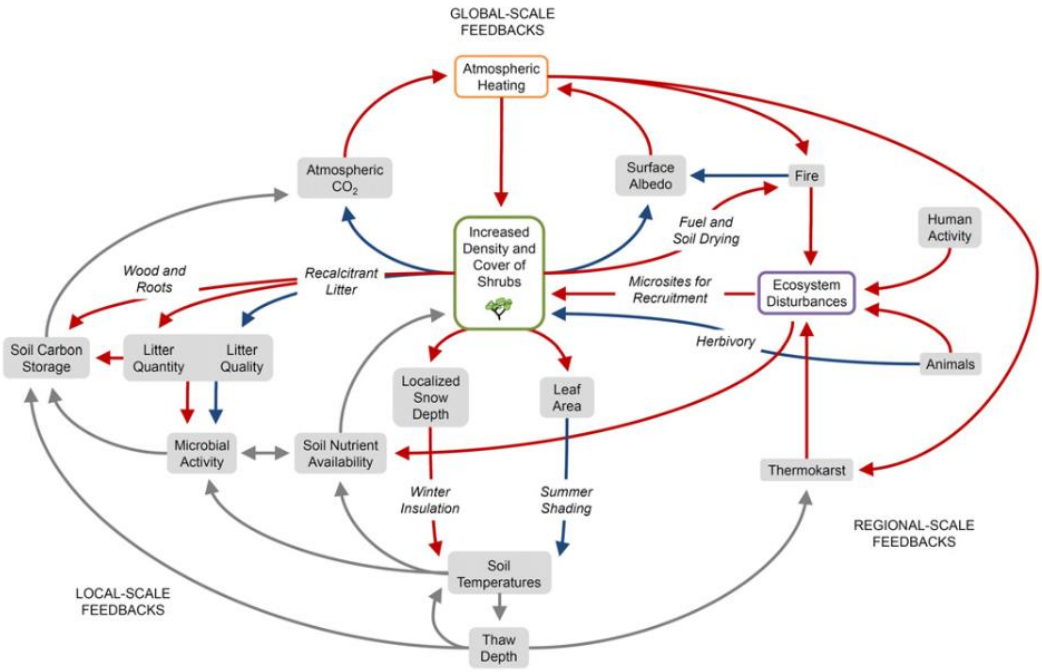

Figure 1.5. The potential influence of increased shrub cover and density on ecosystem processes. Feedbacks are indicated by red (positive), blue (negative) and grey (undetermined) arrows. Figure taken from Myers-Smith et al. (2011).

1.3.1. Permafrost-vegetation interactions in tundra environments

Vegetation cover in tundra environments affects the exchange of energy between the permafrost soils and atmosphere. Vegetation cover generally tends to be darker compared to bare soil or snow cover, lowering the surface albedo of the tundra and leading to increased shortwave absorption by the vegetation. The vegetation-driven lower albedo is especially notable in the spring and summer months (Blok et al., 2011; Loranty et al., 2011; Pomeroy et al., 2006; Wilcox et al., 2019). During the growing season, increased canopy height and cover act as a shade and reduce the soil temperatures. Cooler soils in the summer reduce the active layer depths and constrain permafrost thaw (Blok et al., 2011). Shrub removal experiments have indeed shown the deepening of the active layer in the summer, regardless of the increased albedo of

the surface after the removal (Blok et al., 2010; Nauta et al., 2014). In the winter, taller shrubs trap snow, increasing the thickness of the snow cover over the shrub-covered landscape. Snow accumulation insulates the soil, and this can lead to higher soil temperatures compared to sites with no shrub cover (Sturm et al., 2001). An experiment in Scandinavia reported higher mean wintertime soil temperatures, increased active layer depths and changes in vegetation composition after artificially increasing the snow cover on a sub-arctic peat plateau for several years (Johansson et al., 2013). Warmer soils facilitate decomposition in the winter, releasing nutrients and creating favorable conditions for increased shrub growth, forming a positive feedback loop (Sturm et al., 2001). In spring, shrubs protruding through the snowpack can bring forward the timing of snowmelt due to their lower albedo, which in turn exposes the ground earlier in the season, amplifying permafrost thaw (Wilcox et al., 2019). Conversely, it has also been recorded that shrubs can provide shade, thus delaying the snowmelt around them and creating longer duration snow patches (Marsh et al., 2010; Myers-Smith et al., 2011). The contrasting ways in which shrub cover affects the active layer depth in permafrost tundra environments highlights the complex interactions between the two. The effect is likely site-specific, and dependent on the height, thickness and extent of the shrub cover. Therefore, it has been suggested that in order to determine the overall effect of shrubification on permafrost stability, the summer cooling effect and the winter warming effect both need to be considered (Myers-Smith et al., 2011).

1.3.2. The influence of surface disturbances on shrubification

Whilst warming air temperatures are widely considered to be one of the key drivers of enhanced vegetation growth and spread in high latitude- and alpine tundra (Martin et al., 2017; Tape et al., 2006), there is evidence that other factors may also facilitate the expansion of shrubs in cold environments. Surface disturbance caused by cryogenic action, permafrost thaw, animal trampling, human activity or fire can create microsites for shrub seedlings to develop and dominate (Figure 1.5), contributing to increased shrub cover (Myers-Smith et al., 2011). Frost et al. (2013) find that cryogenic surface disturbances in the form of patterned ground facilitated the establishment and spread of *Alnus* in northwest Siberia. The authors recorded that all newly established shrubs were growing on bare microsites created by frost heave in the soil, and concluded that

the rapid expansion of shrubs in the area despite the lack of recent summer warming is driven by cryogenic disturbances. However, surface disturbances do not always lead to increased shrub recruitment, especially in circumstances where the post-disturbance conditions are more favourable for other plants (e.g., graminoids) that outcompete the shrubs (Kumpula et al., 2011; Myers-Smith et al., 2011).

Moreover, on sites that experience low to intermediate cryogenic disturbances, soil temperature and pH are found to control the plant community distribution as opposed to the disturbance itself (Mod et al., 2014). Similarly, cryogenic disturbance in the form of frost heave was not the controlling factor of species distribution in a study in northern Sweden; rather, the observed changes in vegetation dynamics (including shrubs) depended on the composition of the initial, surrounding plant species (Becher et al., 2018).

Whilst climatic warming and disturbances have been identified as the key drivers of shrubification, it is important to stress that shrub establishment and growth is influenced by numerous factors and processes, such as soil moisture and temperature, available nutrients, CO_2 concentrations, solar radiation, active layer depth, snow cover depth and duration, growing season length and biotic interactions (Myers-Smith et al., 2011). Therefore, it remains a challenge to identify the main driver(s) of shrub growth on a given site, and it is best to simultaneously consider a variety of environmental factors to fully comprehend the influence of surface disturbances on plant communities.

1.3.3. The effect of surface shrub cover on soil respiration

Surface vegetation cover can affect soil respiration through determining the quantity and quality of litter input, by affecting soil microclimate and by contributing to CO_2 emissions through autotrophic root respiration (Raich and Tufekcioglu, 2000). Several studies have found a link between vegetation type and soil respiration in Arctic and alpine environments (e.g., Cahoon et al., 2012; Grand et al., 2016).

Shrub-covered ground has been observed to have lower soil organic carbon stocks, faster rates of respiration and a high carbon turnover compared to non-shrub (heath and tussock) tundra in both permafrost (Wilmking et al., 2006) and non-permafrost environments (Parker et al., 2015). The proposed explanations for this include greater

plant productivity (Ge et al., 2017), increased abundance of ectomycorrhizal fungi associated with shrub cover, the winter warming effect of snow trapped by shrubs, the change in the type of litter added to the system (Parker et al., 2015) and higher litter input rates (Phillips and Wurzburger, 2019).

Moreover, Cahoon et al. (2012) found that woody shrub-covered sites can be a net source of CO_2 in warm soil conditions (> 10 °C). Therefore, in permafrost environments where soils store large amounts of carbon, soil warming and shrub encroachment could potentially lead to increased carbon loss from the ecosystem (Cahoon et al., 2012; Parker et al., 2015; Wilmking et al., 2006).

1.4. Mountain permafrost

Mountain permafrost (also known as alpine permafrost) in Europe is generally lower in ice- and organic material content in comparison to permafrost in low-altitude Arctic ecosystems (Figure 1.6) (Etzelmüller et al., 2020). The active layer of mountain permafrost soils is usually thicker, and the soils have a higher temperature and a lower water content as a result of good drainage (Donhauser and Frey, 2018). As a result, mountain permafrost soils are found to have lower rates of cryoturbation and thus redistribution of organic matter compared to Arctic soils (Donhauser and Frey, 2018). However, this is not the case at the main study site in this thesis, Galdhøpiggen, where strong evidence of past cryoturbation has left a mark on the landscape in the form of sorted circles across altitudes (see Chapter 3).

The distribution of mountain permafrost is controlled by local surface microclimate. Mountain permafrost environments experience large spatial differences in surface conditions due to the highly heterogenous topography of mountains (Isaksen et al., 2003). These topographic effects (for example the slope, or depressions in the ground) influence the local microclimate through controlling the amount of incoming solar radiation and precipitation that reaches the surface, the air flow, and the transfer of heat between the surface and the atmosphere (Barry, 2008).

The temperatures below ground (i.e., ‘ground temperatures’), and by association the absence or presence of permafrost, are largely influenced by this exchange of energy between the surface and the atmosphere. High-altitude areas with sparse vegetation cover and/or limited snow cover can experience a high correlation between air-,

surface- and ground temperatures, as observed in Jotunheimen (Isaksen et al., 2003). However, this relationship is not always straightforward, as surface properties can act as a buffer between the atmosphere and the ground (Haeberli et al., 2010).

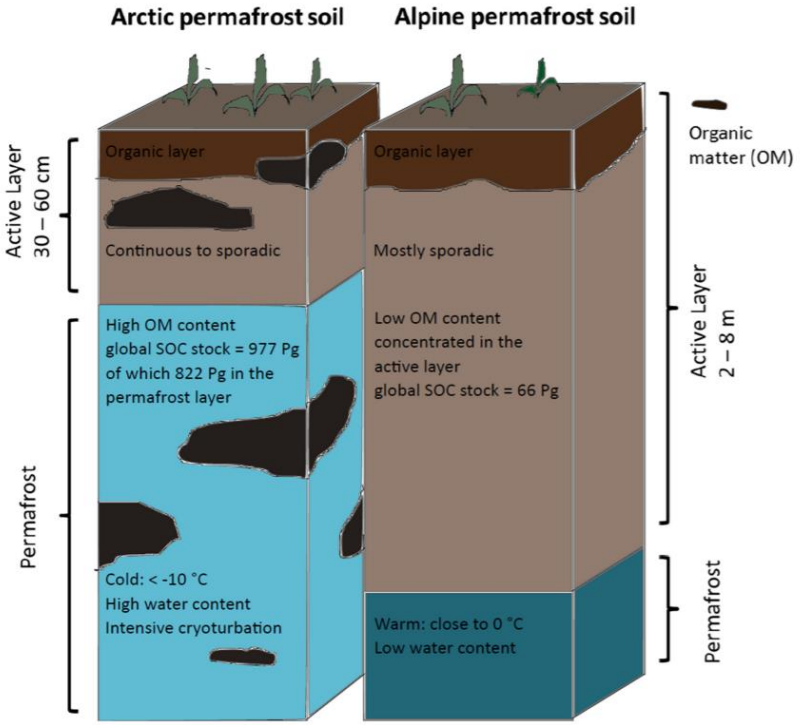

Figure 1.6. Comparison of typical properties and features of Arctic and alpine permafrost soils. SOC = Soil organic carbon, OM = organic matter. Figure reproduced from Donhauser and Frey (2018).

As alpine areas are experiencing rates of warming that significantly exceed the global average, the biogeochemical cycles in these regions could be altered more severely compared to lower altitudes (McGuire et al., 2009). Biogeochemical reactions are expected to accelerate in response to warming, resulting in increased photosynthesis and respiration (provided that other environmental factors, such as moisture- and nutrient availability are not limiting factors) (Donhauser and Frey, 2018). Despite the cold conditions, mountain permafrost soils host a highly diverse community of soil microbes, which govern the carbon- and nutrient cycling in harsh conditions with restricted plant growth (Donhauser and Frey, 2018). With ongoing warming and changes in soil moisture, shifts are predicted in the structure and function of microbial communities (Donhauser and Frey, 2018).

Research concerning mountain permafrost in cold regions is still relatively young, as systematic research did not begin until around 1970 (Haeberli, 2013). The most common research topics include the distribution patterns of mountain permafrost, its influence on near-surface properties and microclimate, and climate-related monitoring

(Haeberli et al., 2010). Due to the increased human activity in alpine environments, topics such as geophysical properties, slope stability and infrastructure are also receiving more attention (Haeberli et al., 2010).

Long-term monitoring projects have been set up in alpine areas to observe thermal changes in mountain permafrost (Etzelmüller et al., 2020). The PACE (Permafrost and Climate in Europe) project led the drilling of boreholes into mountain permafrost between 1998 and 2000 across several sites in Europe (including the main study site, Galdhøpiggen) (Isaksen et al., 2001). Twenty years of monitoring revealed that permafrost has warmed at all sites down to depths of 50 m or more, with increases in active layer thickness between c. 10% and 200%. On Galdhøpiggen, the thickness of the active layer was found to have Increased 5% per decade from the start of the study period in 1999 (Etzelmüller et al., 2020).

1.4.1. Estimating the distribution of mountain permafrost in Jotunheimen

During the past three decades, numerous studies have documented the present, past, and future state of mountain permafrost in Jotunheimen, several of which focus on Galdhøpiggen. In the 1990 and early 2000s, the methods used to create empirical permafrost distribution models were largely indirect (Etzelmüller et al., 2020). The methods included bottom temperature of snow measurements (Hauck et al., 2004; Isaksen et al., 2002), DC resistivity soundings (Ødegård et al., 1996), air temperature measurements (Etzelmüller et al., 1998) and electrical resistivity tomography (Isaksen et al., 2002).

Figure 1.7 is a comprehensive permafrost distribution map for Norway, which was produced by Gisnås et al. (2017) based on the combination of meteorological data (air temperatures, snow cover, freezing-degree days) with land cover- and sediment data.

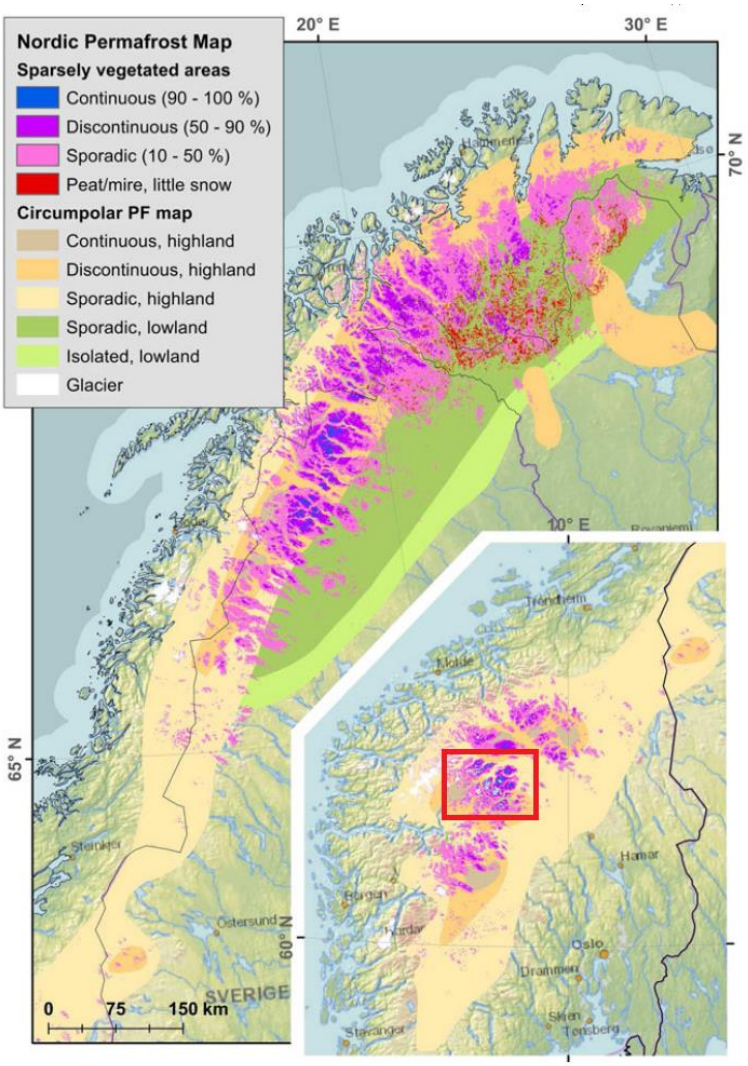

Figure 1.7. Permafrost distribution in Norway illustrated by two overlapping maps: the Nordic Permafrost Map by Gisnås et al. (2017) and Circumpolar PF Map by Brown et al. (1997). The left panel depicts northern Norway, southern Norway is shown in the lower right image. The red rectangle indicates Jotunheimen, the area of interest in this thesis. The map is modified from Gisnås et al. (2017).

With the inception of the PACE project and the borehole drilled 129 m deep into permafrost on the peak of Galdhøpiggen (Juvasshøe) in 1999, models could be developed by incorporating direct ground temperature measurements (Etzelmüller et al., 2020). Six additional boreholes were drilled on the north-facing slope of Galdhøpiggen in 2008 (Table 1.2.; Figure 1.8), further improving the monitoring capacity and the knowledge of mountain permafrost processes. Numerous studies have included ground temperatures from these seven boreholes to investigate the thermal dynamics of permafrost (Farbrot et al., 2011; Isaksen et al., 2003, 2011), to model the ground temperatures for the period 1860-2100 (Hipp et al., 2012) and the past permafrost limits throughout the Holocene (Lilleøren et al., 2012).

Table 1.2. The properties of Galdhøpiggen boreholes. Table modified from Lilleøren et al. (2012), with additional information from Farbrot et al. (2011) and Isaksen et al. (2001). Boreholes JuvBH1-JuvBH6 were drilled in 2008, PACE in 1999. Active layer depths were measured in the period Sept 2008 – Aug 2010.

Borehole ID	Elevation (m a.s.l.)	Borehole depth (m)	Surface conditions	Active layer depth (m)	Permafrost presence	Depth to bedrock (m)	Permafrost thickness (m)
PACE	1894	129	Blockfield	~2.2	Yes	3-4	~380
JuvBH1	1851	10	Blockfield	~1.5	Yes	4.5	-
JuvBH2	1771	10	Blockfield	<2	Yes	2	-
JuvBH3	1561	10	Till	~8	Yes	2	-
JuvBH4	1559	15	Bedrock	>8	Yes	0	-
JuvBH5	1458	10	Till	N/A	No	4.5	-
JuvBH6	1307	10	Till	N/A	No	>10.5	-

However, determining the exact position of the lower altitudinal limit of discontinuous permafrost on the north-facing slope of Galdhøpiggen remains a challenge due to its patchy distribution below ground. Based on abovementioned indirect measurements, various altitudes have been proposed as the present-day lower limit of permafrost: 1450-1500 m a.s.l. (Ødegård et al., 1996), 1450 m a.s.l. (Farbrot et al., 2011), 1460 m a.s.l. (Isaksen et al., 2002), 1470 m a.s.l. (Isaksen et al., 2011) and 1410-1470 m a.s.l. (Hauck et al., 2004). The lowest altitude on Galdhøpiggen where patches of sporadic permafrost have been recorded was 1350 m a.s.l. (Isaksen et al., 2002). Throughout this thesis, the lower limit of permafrost on Galdhøpiggen is assumed to be at 1450 m a.s.l., which is roughly the mid-point of this estimated range. However, the exact position of this limit will be subject to changes in time in response to warming, and, given that the most recent estimates are a decade old, it is possible that it is somewhere between 1450-1500 m a.s.l. today. The lower limit of permafrost is therefore considered to be a transitional zone rather than a set limit.

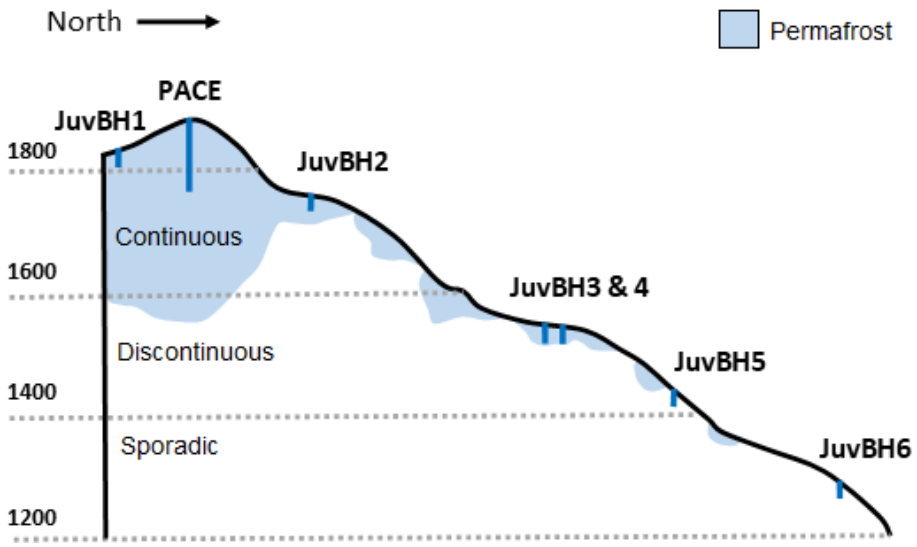

Figure 1.8. A sketch of the north-facing slope of Galdhøpiggen between the altitudes 1200-1800 m a.s.l. illustrating the rough distribution of permafrost and the position of boreholes. Figure modified from Lilleøren et al. (2012).

Chapter 2

Methodology

Due to the paper-based structure of this thesis, the original Chapters (3-5) were chosen to be presented in their submitted format, where methods and research design of individual studies are described in their respective chapters. The present chapter contains additional material on methods used in Chapters 3-5 that was not included in the publications due to restricted word counts. Here, comprehensive background information, the technical aspects of the equipment and the detailed laboratory procedures are provided, where appropriate. Section 2.1 introduces the concepts used in Chapter 3, Section 2.2 corresponds with Chapter 5 and Section 2.3 outlines the methods used in Chapter 4. Overview of full methods and study designs used in individual studies can be found in the respective chapters.

2.1. Measuring CO_2 efflux from the ground

2.1.1. Soil respiration and carbon fluxes

In the soil, CO_2 is mainly produced by plant roots and heterotrophic microbes through respiration and released to the atmosphere through air-filled pores present in the soil. In permafrost areas, soil respiration and the release of CO_2 into the atmosphere are influenced by soil conditions and microclimate. The two main controls, soil temperature and soil moisture, affect soil respiration by stimulating microbial activity and decomposition of organic material (Illeris et al., 2003; Larsen et al., 2007). Higher soil temperatures generally lead to increased microbial activity (Klaminder et al., 2013). Soil moisture, however, limits soil respiration at both extremes. Respiration in very dry soils is limited by water availability, whilst water-saturated soils in turn create an environment where respiration is limited by low oxygen concentration (Dagg and Lafleur, 2011). Other significant controls on respiration and CO_2 efflux include physical properties of the soil (texture, porosity, type, organic layer thickness), chemical properties (soil nutrients), surface vegetation cover and active layer depth (Figure 2.1). In a heterogeneous tundra, these conditions can vary within metres (Aalto et al., 2013).

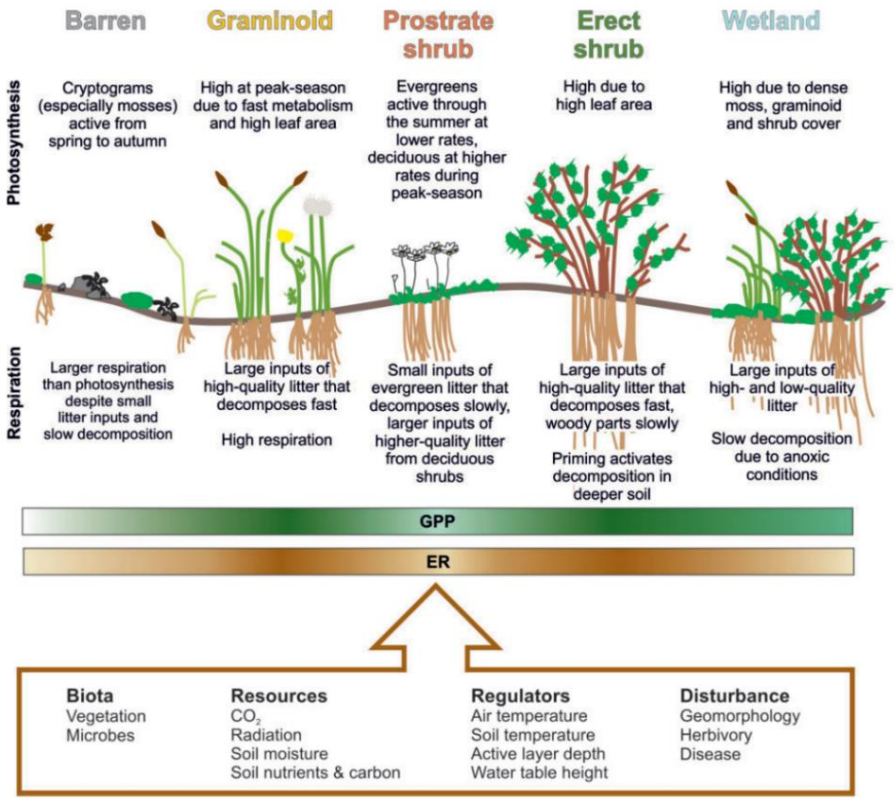

Figure 2.1. Controls on CO_2 fluxes from the ground in different tundra environments. GPP = gross primary production, ER = ecosystem respiration. Figure taken from Virkkala et al. (2018).

The exchange of CO_2 between ecosystems and the atmosphere is often expressed in terms of fluxes. The most frequently studied and reported flux is the net ecosystem exchange (NEE) (Virkkala et al., 2018). NEE is the difference between the carbon accumulated and stored in the ecosystem via photosynthesis (gross primary productivity, GPP) and carbon lost through plant and microbial respiration (ecosystem respiration, ER) (Figure 2.1). Ecosystem respiration combines heterotrophic respiration by soil microorganisms and autotrophic respiration by plants and plant roots (Hermle et al., 2010), and is here expressed in µmol C m^{-2} s^{-1}. A positive NEE indicates that the ecosystem is a source of CO_2, whilst negative NEE indicates that CO_2 is taken up from the atmosphere and stored.

As photosynthesis and respiration peak during the growing season, most CO_2 flux studies in tundra ecosystems have been conducted during summer, and data on wintertime emissions are presently scarce (Belshe et al., 2013; McGuire et al., 2012). In addition to seasonal variation, GPP and ER can vary inter-annually and diurnally,

with daytime GPP rates exceeding ER and ER rates prevailing at night (Virkkala et al., 2018).

Whilst NEE indicates whether the ecosystem is a sink or a source of CO_2, ER and soil respiration are the processes that control carbon emissions and future carbon balance (Virkkala et al., 2018). For this reason, Chapter 3 of this thesis will focus on investigating the rates of ecosystem respiration across different land cover types in an alpine tundra environment within three weeks during the peak growing season (July).

2.1.2. The chamber method

To advance our understanding of high-latitude and alpine carbon fluxes, a proportion of research has focused on monitoring the emissions and the uptake of greenhouse gases in the field. The two most commonly used methods of measuring CO_2 fluxes between land and atmosphere are the eddy covariance technique and the chamber measurement method (Marushchak et al., 2013). The eddy covariance technique is tower-based and allows constant, undisturbed measurements over a larger area and longer time span (McGuire et al., 2012).

In this study, the chamber method is used. This method involves an infrared gas analyser (Figure 2.2) that measures CO_2 emissions over a small area of ground, taking account of small-scale spatial variability in the heterogeneous tundra environments (McGuire et al., 2012). Whilst laborious, the chamber method is less costly and easier to operate than the tower-based methods (Virkkala et al., 2018). Using a chamber will also allow the researcher to focus on the separate components like plants, soil or moss, and their carbon exchange with the atmosphere (McGuire et al., 2012). CO_2 gas analyser survey chambers can be manual or automated, and come in different sizes, with diameters ranging from 10 to 100 cm (Virkkala et al., 2018).

The CO_2 flux chamber method has been used in Greenland, Canada, Russia and Svalbard, but the highest number of studies come from Alaska and Fennoscandia (Virkkala et al., 2018). In northern Sweden, the method has been applied on non-sorted circles, which were found to be net sources of CO_2 at present (Becher et al., 2015).

2.1.3. LI-COR (LI-8100A) infrared gas analyser

The portable infrared gas analyser LI-COR (LI-8100A) (Figure 2.2) was used in this study to measure CO_2 efflux from the ground in Jotunheimen during the peak growing season in July 2018 (see Chapter 3). The design, theory of operation and the CO_2 efflux measurement cycle are briefly summarised below; full detail can be found in the LI-COR (LI-8100A) User Manual (LI-COR Biosciences, 2015).

LI-COR (LI-8100A) consists of the analyser control unit (the yellow box in Figure 2.2) which is connected to a portable survey chamber. The control unit contains the infrared gas analyser, up to two rechargeable 12-volt lead acid batteries, memory card and the wireless card required to connect to the device (LI-COR Biosciences, 2015). The system was operated in the field using an iPhone 4s through the purpose-built application LI-8100APP.

Figure 2.2. Portable infrared gas analyser (LI-COR, LI-8100A) with a ⌀ 10 cm chamber. Plastic collars have been installed into the ground in preparation for the measurement. The chamber on the image is 'closed' whilst the measuring is taking place.

To ensure the portable survey chamber is sealed properly to the ground, the chamber is placed on top of plastic collars pre-inserted into the soil. Here, polyvinyl chloride (PVC) collars cut from a pipe (100 mm in diameter, 45 mm in height) were inserted ~20 mm deep into the ground for a minimum of 24 hours before the first measurement and were left in for the duration of the study period (three weeks). To calculate the total system volume used in the flux calculation, the volume of air inside the plastic collar needs to be determined (LI-COR Biosciences, 2015). This is done by estimating the offset through measuring the distance between the surface of the soil and the top of the collar. The measurement value is inserted into the LI-8100APP prior to the observation.

2.1.4. LI-COR (LI-8100A): Theory of operation

The survey chamber is connected to the analyser control unit through a cable and three tubes to allow air to move between the two units. There is a constant air flow pumped from the control unit to the survey chamber, where the shape of the chamber allows for mixing of gases (Figure 2.3). Air flowing from the survey chamber back to the control unit first passes through a filter, before entering the infrared gas analyser, where CO_2 and water vapour (H_2O) concentrations are measured. Atmospheric gas molecules absorb infrared radiation at certain wavelengths (around 4.3 and 2.6 μm for CO_2 and H_2O, respectively) (Auble and Meyers, 1992). Inside the gas analyser, infrared light is emitted through the air sample, and some of it will be absorbed by CO_2 and H_2O. Based on the amount of infrared absorption, concentrations and flux rates are calculated for each gas (Auble and Meyers, 1992).

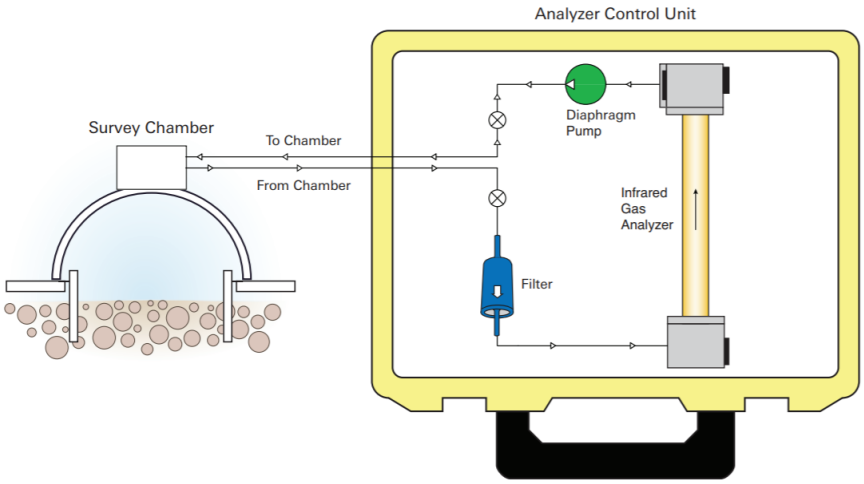

Figure 2.3. An illustration of the measurement flow path between the chamber and the Analyser Control Unit. Figure taken from the LI-COR (LI-8100A) User Manual (LI-COR Biosciences, 2015).

2.1.5. LI-COR (LI-8100A): The measurement cycle

The observation begins with the chamber closing and sealing over the PVC collar, after which the device begins recording data (Figure 2.4). At the start of each observation, there is a 10-30 second 'dead band' to ensure steady mixing of the gases inside the chamber. The data were logged during the 90-180 second observation, and the chamber opens again to allow gases to escape from the chamber in preparation for

the next observation (this is known as the purge). The cycle is then repeated. In this study, three consecutive observations were made. Each observation lasted for 120 seconds to ensure that the chamber CO_2 concentration changes were minimal. The duration of the dead band was 30 seconds, and the purge period was 30 seconds.

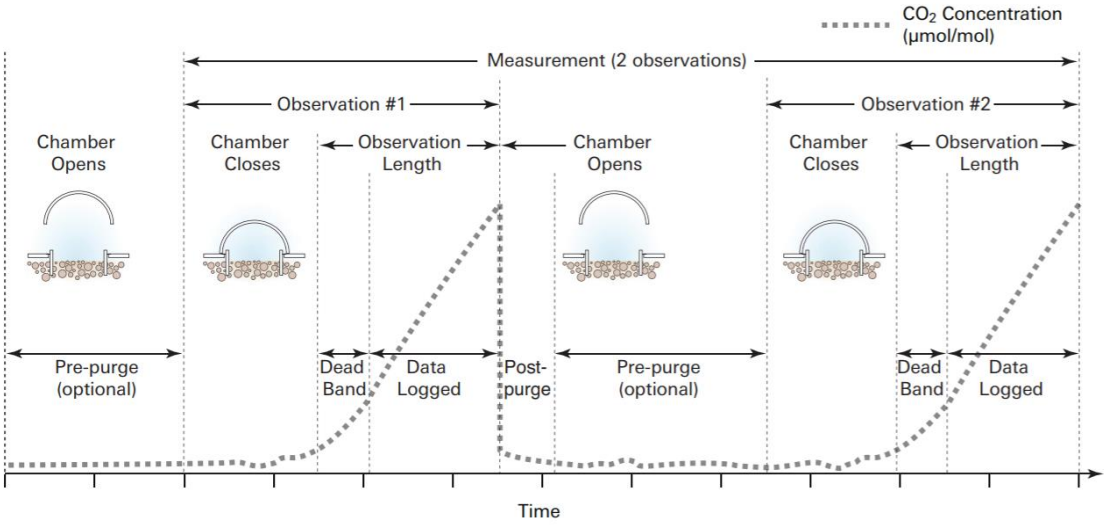

Figure 2.4. An illustration of a measurement cycle consisting of two measurements using a closed chamber. Figure taken from the LI-COR (LI-8100A) User Manual (LI-COR Biosciences, 2015).

2.1.6. Addressing the research gaps in CO_2 flux studies

A review by Virkkala et al. (2018) analysed 93 studies on the topic of CO_2 flux chamber measurements in tundra environments during the growing season, highlighted several weaknesses and research gaps, and made suggestions to improve future research. This sub-section outlines their findings and suggestions and summarises how these research gaps were addressed in this thesis.

One of the main weaknesses of reviewed CO_2 flux studies was the use of small data sets, which make it difficult to cover all environmental gradients, such as topography and hydrology. Moreover, data are lacking from various topographical conditions, higher elevations, and barren surfaces. Virkkala and co-workers also recommended including information on the local disturbance regimes to improve our understanding of biogeochemical cycles in the tundra. Here, these gaps are addressed by measuring CO_2 efflux repeatedly (n = 460 measurements) across different altitudes and topographical conditions from 1550 m a.s.l. up to high altitudes of 1950 m a.s.l. The

study sites include barren surfaces, and the study uses the (lack of) vegetation cover extent to identify locally disturbed surfaces.

Virkkala et al. (2018) also identified a need to include more information on soil chemistry. To date, most CO_2 flux studies conducted in tundra environments have included information on soil temperature and moisture, air temperature, photosynthetically active radiation, active layer depth and water table depth. However, relatively few studies have included descriptions of soil types, SOC and nitrogen content, litter biomass estimates and data on soil microbes. The authors further suggest including information on pH and soil nutrients (phosphorus). Here, soil samples were taken from each study site and analysed for SOC, nitrogen, phosphorus, and a range of other elements. The pH of each sample was also determined.

Virkkala and co-workers stress the importance of carefully designing the study, including the diameter of the chamber that will be used, and the manner and timing of inserting the collar into the soil. To ensure minimal soil disturbance that could result in erroneous readings, the collars in this field study were inserted a minimum of 24 hours before the first CO_2 efflux measurement.

2.1.7. Soil- and atmospheric conditions at the time of CO_2 efflux measurement

Soil moisture and temperature were recorded simultaneously using two ECH2O Model EC-5 soil probes by inserting the probes into the top 30 mm of soil so that they were parallel with the soil surface. Probes were inserted adjacent to the soil collar during the CO_2 efflux measurements. Care was taken not to affect either measurement.

Air temperature (T) (C°), relative humidity (RH) (%) and wind speed (m/s) were also recorded during each chamber measurement with a Kestrel 3000 Pocket Weather Meter at 1 m height above the ground surface. These data were used to calculate vapour pressure deficit (VPD) using the following equations:

$$Saturated\ vapour\ pressure\ (SVP)\ (kPa) = \frac{610.78 \times e^{(\mathrm{T}/(\mathrm{T}+238.3)\times 17.2694))}}{1000}$$

$$Vapour\ pressure\ deficit\ (kPa) = SVP \times \frac{1 - RH}{100}$$

2.1.8. Soil chemical – and elemental analysis

Soil samples were taken from each study site (i.e., each sorted circle, n = 15) for chemical analysis. Soil pH was measured by mixing 5 g of homogenised soil with 10 ml of deionised water and taking the reading with a standard pH probe.

An XRF (X-Ray Fluorescence) spectrometer (Rigaku NexCG ED-XRF) was used to determine the concentration of a range of elements in the soil, including phosphorus (P), the soil nutrient that is considered the most likely limiting factor of soil respiration.

Soil samples were placed in small plastic pots with a transparent clingfilm base and placed in the XRF analyser. The XRF determines the concentration of different elements in soil by emitting X-rays through the sample to 'excite' it, and measuring the secondary (fluorescent) X-rays emitted back from the sample (Thermo Fisher Scientific, 2021). As these fluorescent X-rays differ between elements, this technique allows the determination of the concentration of each element. Three trials were run with the XRF (n=45), and the mean of the three results was used to represent the soil P concentration at each study site.

2.1.9. Carbon, nitrogen, and the C:N ratio

Soil carbon and nitrogen content and the C: N ratio were determined by using a Sercon 20/20 isotope ratio mass spectrometer interfaced with an ANCA GSL elemental analyser at Swansea University. In preparation, a small amount of soil (0.40-0.41 mg) was measured out into individual tin capsules, which were folded and rounded with tweezers. A similar amount of the reference substance, acetanilide, was also measured into tin capsules (n=13). All tin capsules were placed into the mass spectrometer for analysis.

The samples pass through four stages in the mass spectrometer, described in detail by Mellon (2003). First, the molecules present in a sample are ionised. Second, the ions are accelerated through the mass spectrometer and separated based on their mass-to-charge ratio. Third, the abundances of separated ions are measured by a detector as an electrical signal, and finally, the signal passes a recording device that converts it into a format that is suitable for Interpretation.

Three soil samples were prepared per study site (n=45) and the mean of the three outputs was calculated to represent the fraction of C, N, and the C:N ratio of the soil at each site.

2.1.10. Determination of the soil organic matter content by loss on ignition

One soil sample from each study site was analysed for bulk density (g cm^{-3}) and loss-on-ignition (LOI), following the method outlined by Chambers et al. (2011). The samples were placed in pre-weighed ceramic crucibles, weighed again, and dried overnight at 105 °C. To determine the dry weight of each soil sample, individual crucibles containing samples were weighed after drying, and the weight of the crucible was deducted from the final weight. The crucibles containing dry samples were then ignited at 550 °C for four hours to combust all organic matter (also known as 'ashing'), cooled to room temperature in a desiccator and weighed again. The weight of the remaining sample was calculated by deducting the crucible weight from the post-ignition weight. The results were used to calculate the bulk density, organic matter content and organic matter density of each sample, using the following equations:

$$Bulk\ density\ (g/cm^{-3}) = \frac{dry\ weight\ (g)}{volume\ of\ fresh\ sample\ (cm^3)}$$

$$Organic\ matter\ content\ (\%) = \frac{dry\ weight\ (g) - weight\ of\ sample\ after\ ashing\ (g)}{dry\ weight\ (g)} \times 100$$

$$Organic\ matter\ density\ (g/cm^{-3}) = bulk\ density\ \ (g/cm^{-3}) \times organic\ matter\ content\ (\%)$$

2.2. Remote sensing of alpine- and tundra landscapes

Satellite remote sensing is a commonly used method to investigate spatial and temporal trends on the land surface, e.g., in surface temperature, albedo, and 'land-surface greenness' by using vegetation indices. Sensors attached to satellites measure electromagnetic radiation reflected or emitted by the Earth (Figure 2.5) (Tempfli et al., 2009).

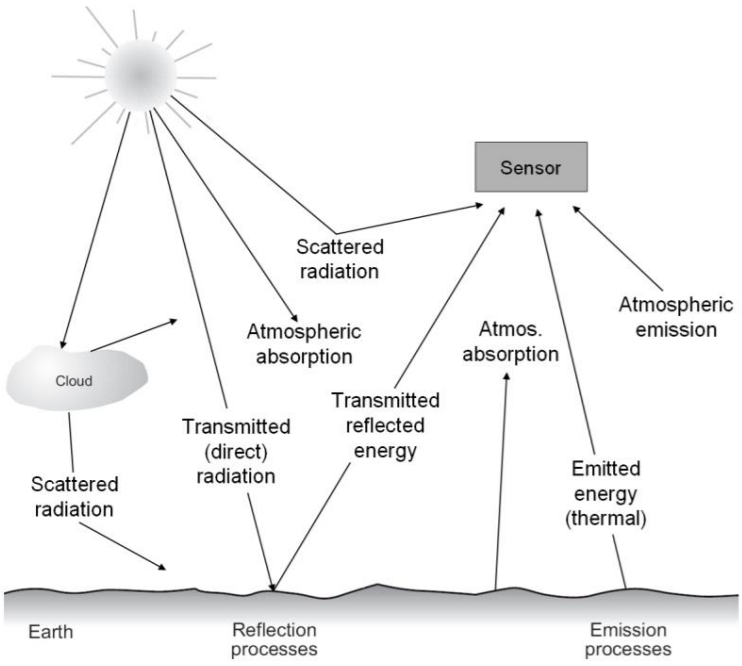

Figure 2.5. An illustration of the main energy interactions between the Earth's surface, atmosphere, and a remote sensor. Figure taken from Tempfli et al. (2009).

In the northern hemisphere, satellite imagery has been used to detect thermal and vegetational changes in the Arctic permafrost landscapes (e.g., Langer et al., 2010; Muster et al., 2015; Raynolds et al., 2008; Stow et al., 2004; Westermann et al., 2011), but also alpine permafrost regions (Haeberli, 2013; Olthof and Pouliot, 2010; Wilson and Nilsson, 2009; Zhang et al., 2009). Using satellite-derived data to examine thermal and vegetational dynamics in alpine tundra complements field-based, *in-situ* research projects. The ability to acquire information simultaneously over large spatial- and temporal scales and over remote, inaccessible areas is a great advantage of remote sensing techniques.

2.2.1. Moderate Resolution Imaging Spectroradiometer (MODIS)

Remotely sensed data analysed in this thesis are acquired from the Moderate Resolution Imaging Spectroradiometer (MODIS, Figure 2.6), an imaging sensor attached to the Terra and Aqua satellites. As a part of the NASA Earth Observing System (EOS) program, the satellites were launched into Earth's orbit to a height of 705 km on December 18, 1999, and May 4, 2002, respectively (additional information available from the NASA MODIS website: modis.gsfc.nasa.gov/). The satellites view the surface of the entire planet every 1 or 2 days. Terra passes the equator from north to south in the morning, whilst Aqua passes the equator from south to north in the afternoon. This provides a view of the same area at four different times of the day (once on the way up and once on the way down), keeping the time of observation consistent from year to year minimises erroneous readings due to optical effects. Combining multiple observations for a length of time (8 days, 16 days or a month) minimises the effects of cloud cover (Lindsey and Herring, 2020). MODIS has a viewing swath width of 2330 km; it collects data in 36 spectral bands (ranging from 0.405 to 14.385 μm) and at three resolutions (250 m, 500 m, 1000 m), each resolution using a different range of bands (Running et al., 1994). In Chapter 5, the bands used for NDVI (NIR and red) are available at 250 m resolution, whilst temperature is available at 1-km resolution. Each range of bands captures information about different features, such as surface reflectance, land surface- and atmospheric temperature, snow cover and several vegetation indices representing surface vegetation cover.

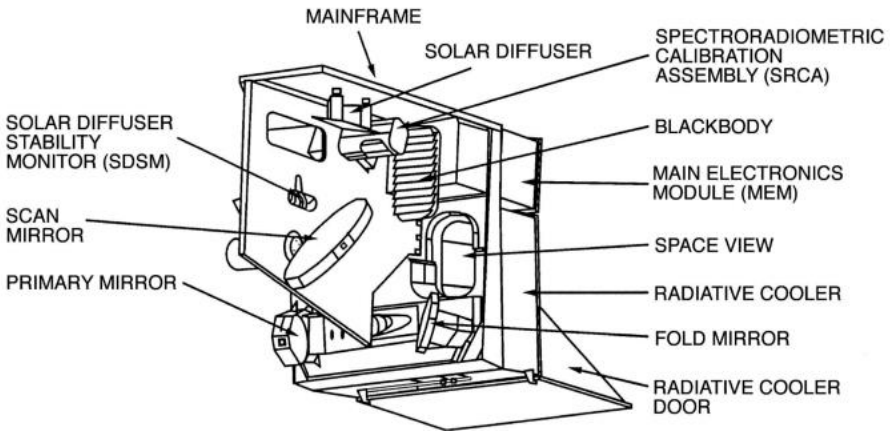

Figure 2.6. Main components of the MODIS imaging sensor. Figure taken from the NASA MODIS website: modis.gsfc.nasa.gov/about/components.php).

The components and the working principles of MODIS are briefly summarised below; full details can be found on the NASA MODIS website (modis.gsfc.nasa.gov/about/components.php). The scan mirror in MODIS (Figure 2.6) deflects visible- and infrared light travelling from the Earth's surface onto the four Focal Plane Assemblies (FPAs), which are cooled to 83K by the radiative cooler. The light is then split between the four FPAs, and the 36 spectral bands are separated into Visible (VIS), Near Infrared (NIR), Short- and Mid-Wave Infrared (SWIR/MWIR), and Long-Wave Infrared (LWIR). Each FPA then focuses light onto a distinct section of detector pixels, which in turn generates a specific signal, dependent upon the type of light it is sensitive to. These signals provide information about the observed surface. To ensure the accuracy of the observations, several components of the MODIS help to calibrate the system. MODIS has onboard calibration (e.g., the blackbody and the solar diffuser) to assure that the signals measured in solar and thermal bands are consistent.

Chapter 5 of this thesis explores the use of MODIS land surface temperatures (LSTs) and the normalised difference vegetation index (NDVI) over a mountainous area with patches of underlying permafrost in southern Norway. The Aqua MODIS Vegetation Indices (MYD13A3, version 6.0) data were used to derive NDVI (Didan et al., 2015). Land surface temperatures were derived from Aqua MODIS MYD21A1D (temperature around noon) and MYD21A1N (temperature around midnight), both products were version 6.0 (Hulley et al., 2016). The following sub-sections introduce these MODIS products and summarise their application in tundra environments.

2.2.2. Normalised difference vegetation index (NDVI)

NDVI is the normalised difference ratio between the red reflectance and near infrared (NIR) reflectance. As the red wavelength of the electromagnetic spectrum (0.620–0.670 μm) is absorbed by leaf pigments (e.g., chlorophyll) in live green leaves, near-infrared radiation (0.841–0.876 μm) is strongly reflected by leaf cells (Pettorelli, 2013; Choubin et al., 2019). Red reflectance is therefore low over vegetated land, and generally decreases with vegetation abundance. Concurrently, near-infrared reflectance is generally high over vegetated surfaces and increases as the canopy becomes denser (Beck et al., 2006). This differential response between red and near

infrared reflectance is unique to vegetation and allows monitoring of vegetation from space.

Using MODIS data, NDVI is calculated for every pixel using the following equation, where NIR is the near-infrared reflectance, and 'red' signifies the red reflectance:

$$NDVI = \frac{(NIR - red)}{(NIR + red)}$$

The theoretical range of NDVI is between -1.0 and +1.0; the observed range is from –0.1 (e.g., snow and ice), to 0.8 (or higher dependent on sensor characteristics and level of corrections applied to the data) for dense vegetation. NDVI is linked to the amount of vegetation cover; for example, NDVI values of 0.6 and above indicate the highest possible density of green leaves (i.e., tree cover), values between 0.4-0.6 correspond to areas with moderate vegetation; NDVI values of 0.2-0.4 indicate sparse vegetation cover and NDVI around 0.05 indicates bare soil (Al-doski et al., 2013; Groß et al., 2018).

NDVI has been applied in numerous fields of research covering different areas across the globe. In high-altitude and high-latitude tundra, remotely sensed NDVI time series have been used to monitor vegetation dynamics over a large areas (e.g., Beck et al., 2006). More specifically, it can be applied to study shrub expansion (Forbes et al, 2010; Macias-Fauria et al., 2012) and vegetation properties (Liu et al., 2017; Raynolds et al., 2012), but also disturbances and recovery after fires (Barrett et al, 2012; Boelman et al., 2011), winter warming (Phoenix and Bjerke, 2016), permafrost degradation (Cray and Pollard, 2015; Nitze et al., 2018), and herbivory (Newton et al., 2014).

Despite its versatility, optical remote sensing faces several challenges. Remotely sensed images can often become obscured by atmospheric conditions at the time of data collection. This includes cloud cover, airborne dust and aerosols, and atmospheric turbulence (Beck et al., 2006; Lagouarde et al., 2015). In high-latitude tundra, and also in mountainous regions, frequent and dense cloud cover is common, and poses a particularly difficult challenge for optical remote sensing (Beamish et al., 2020; Stow

et al., 2004; Westermann and Boike, 2011). Additionally, the analysis is further limited by short growing seasons as well as snow and ice cover in tundra landscapes (Hope and Stow, 1995; Stow et al., 2004). Due to the short growing season, vegetation growth, including the onset of leaves and other phenological changes, take place rapidly, which may not be captured fully if the temporal frequency of observations is low (Stow et al., 2004).

2.2.3. Predicting missing values in remotely sensed datasets

Numerous spatial and temporal approaches have been proposed to overcome the problem of missing values due to dense cloud cover obstructing the remote observation (e.g., Jönnson and Eklundh, 2004; Moreno et al., 2014; Neteler, 2010; Verger et al., 2013; Zhu et al., 2015). In Chapter 5, we employ the 'gapfill' package in R that was recently published by Gerber et al. (2018). This method aims to predict missing values in spatio-temporal satellite datasets. It is based on a subset-predict procedure and uses both spatial coherence and temporal seasonal regularity. More specifically, the method first iteratively selects spatio-temporal subsets of data that surround the missing values (i.e., the 'prediction set'). The individual images are then assigned a score that is based on comparing all images in this prediction set. The images are ranked within subsets according to their score. Finally, the missing values are predicted through quantile regression (Figure 2.7). The advantage of 'gapfill' is that it considers the seasonal dynamics through time, as well as spatial coherence. The method has been validated against previously established methods and has been found to significantly outperform the alternatives (Gerber et al., 2018). The open-source 'gapfill' package is free and available to use in the statistical software R (R Core Team 2020).

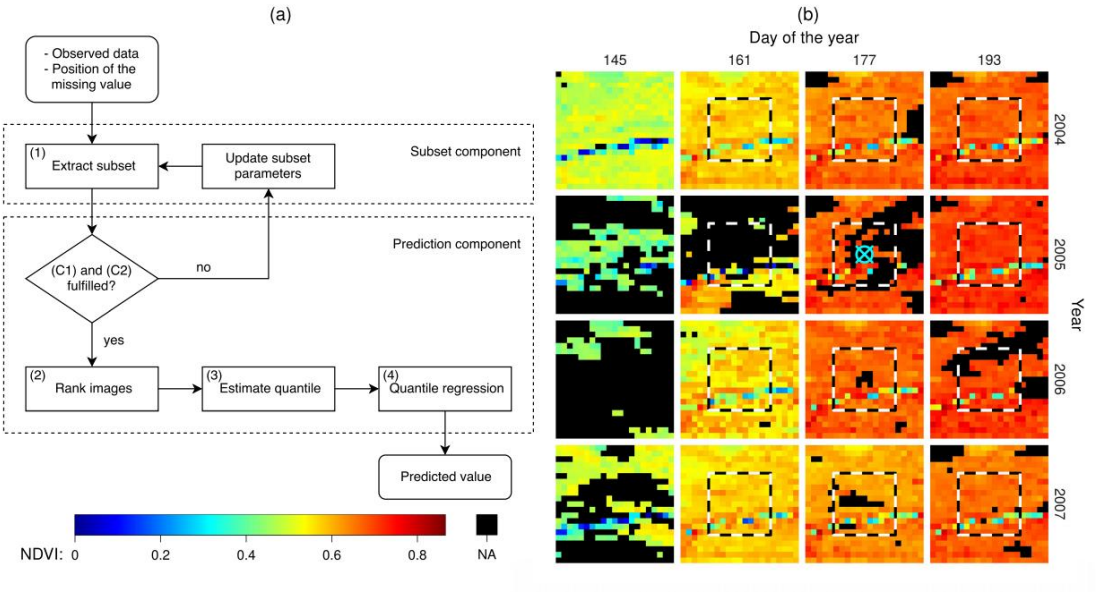

Figure 2.7. Visual representation of the main steps involved in the 'Gapfill' method. (a) Breakdown of the steps involved in predicting missing values presented in a flow chart. (b) Example MODIS NDVI data set, where satellite images are arranged in a matrix by years and days of the year. Black areas represent missing values. Figure taken from Gerber et al. (2018).

2.2.4. MODIS land surface temperatures

The rapid increase in land surface temperatures at high latitudes has been documented by using both field measurements and satellite data (Comiso 2003, 2006; Overland et al., 2019; Serreze and Barry 2011). As discussed in Chapter 1, tundra land surfaces, especially those underlain by permafrost, are sensitive to climatic changes. Woody shrub encroachment driven by atmospheric warming can transform the landscape and decrease its albedo, facilitating further warming of the surface. Such drastic changes in surface properties affect the surface energy balance and the distribution of incoming solar radiation into sensible heat flux and latent heat flux (Muster et al., 2015).

Satellite-derived radiometric land surface temperatures (LSTs) depend on the surface energy balance and have been frequently used over the last decade to analyse the thermal conditions of remote alpine- and Arctic permafrost landscapes (Tomlinson et al., 2011). LSTs reflect the combination of surface- and atmospheric conditions, as both control the energy transfer between the surface and the atmosphere (Jin and

Dickinson, 2010; Muster et al., 2015). Remotely observed LSTs are an invaluable tool for monitoring and detecting climatic warming in these vulnerable ecosystems.

The accuracy of satellite-derived thermal infrared MODIS LSTs has been tested in several studies (e.g., Wan et al., 2002), and it has been found that the accuracy is better than 1 °C in the range from −10 to 50 °C (Wan et al., 2004). In high-Arctic tundra, Westermann et al. (2011) found that under clear sky conditions, weekly averages of MODIS LSTs and temperature data recorded with field-based thermal imaging system agreed to within less than 2 K (or 2 °C). Similarly, Muster et al. (2015) tested the accuracy of MODIS LSTs over an Arctic permafrost landscape with variable patterns of vegetation cover by comparing MODIS data to in-situ radiometer measurements. The authors found a slight overall cold bias and reported that the accuracy of MODIS LSTs was -1.1 °C and concluded that their results strongly suggest that MODIS LSTs are a reliable method to measure surface temperatures in Arctic tundra.

Despite the high accuracy estimates, seasonal temperature bias of MODIS LST data has previously been reported. In Arctic environments, studies have recorded a slight warm bias (overestimation of temperature) in the summer, and a strong wintertime cold bias (underestimation of temperature) (Langer et al., 2010; Muster et al., 2015; Westermann et al., 2011; Westermann et al., 2012). This has been explained by the seasonal difference in measurements taken during clear-sky conditions. In summer, the surface warms more under clear skies compared to cloudy conditions due to higher incoming net solar radiation. In winter, however, clear skies allow the long-wave radiation emitted by the land surface to escape into the atmosphere, which cools the surface. Conversely, a thick cloud cover in the winter re-emits the long-wave radiation back towards the Earth and warms the land. A strong negative bias can also be created in cases where the MODIS cloud detection algorithm fails to detect cloud cover and leads to admixing of colder cloud top temperatures (Westermann et al., 2011). This can lead to MODIS LST measurements that are 10°C/10 K lower than *in situ* surface temperature measurements (Muster et al., 2015; Westermann et al., 2012). This problem needs to be acknowledged when using MODIS LSTs. In Chapter 5, an attempt was made to eliminate the influence of the wintertime cold bias by focusing exclusively on growing season surface temperatures in order to delineate permafrost distribution in the area.

2.2.5. MODIS LSTs as a proxy for permafrost presence

Unlike vegetation cover, which is visually detectable on aerial photographs, and which is possible to estimate from satellite-derived data by using proxies like the NDVI, permafrost distribution cannot be directly detected from airborne instruments. Whilst permafrost activity is linked to numerous above-ground features and landforms (i.e., patterned ground, thaw slumps, pingos, ice wedges), permafrost is still a sub-surface phenomenon defined by ground temperature and can extend below areas with none of the above surface features. Nevertheless, studies have attempted to use proxies such as certain vegetation types or changes in the size of lakes and ponds to determine permafrost distribution, but such methods are more appropriate for regional rather than large-scale studies (Stow et al., 2004; Westermann et al., 2011; Yoshikawa and Hinzman 2003).

To date, permafrost mapping has often been reliant on near-surface air temperatures derived from meteorological stations that can be far apart (Hachem et al., 2009, 2012). MODIS LSTs provide a temperature measure that is closer to ground temperatures than near-surface air temperature, and accounts for spatial differences across the landscape (Hachem et al., 2009). Whilst there is currently no universal remote-sensing method to accurately assess the presence of sub-surface permafrost or its thermal state (Obu et al., 2019), LSTs have increasingly been used in permafrost modelling (Langer et al., 2010; Westermann et al., 2011, 2012).

However, this method must be approached with caution because the relationship between surface and below-surface temperatures is not always straightforward. Moreover, satellite-bound instruments can only record the temperature of the top of the canopy in densely vegetated areas, failing to capture the temperature of the surface below the canopy (Westermann et al., 2011). Modelling schemes have been proposed to overcome these problems and to estimate subsurface conditions from measured LSTs (e.g., Marchenko et al., 2009; Sazonova and Romanovsky, 2003).

In Chapter 5, an attempt is made to infer sub-surface permafrost occurrence by using satellite-derived LSTs. Whilst acknowledging the limitations of this method, the attempt was made based on the findings of a previous study from the area that found a high correlation between air-, ground surface- and ground temperatures at higher elevations on Galdhøpiggen (Isaksen et al., 2003).

2.2.6. Relationship between MODIS LSTs and NDVI

MODIS LSTs have previously been successfully used in monitoring vegetation and land cover changes (Bhatt et al., 2013; Coops et al., 2009; Zhang et al., 2004). As may be expected, MODIS LSTs are negatively correlated with increasing elevation and slope, but the relationship between LSTs and aspect is found to be insignificant (Peng et al., 2020). However, several studies based in mid-latitude ecosystems have reported a negative relationship between satellite-derived LSTs and vegetation indices (i.e., NDVI) (Coops et al., 2009; Goward et al., 1985; Mildrexler et al., 2007; Nemani et al., 1996; Price, 1990; Wan et al., 2004). This negative relationship is explained by the differences in the reflectance and emittance properties of bare soil and vegetation, as the temperature of vegetated ground is lower than that of soil (Coops et al., 2009). Over densely vegetated (i.e., forested) surfaces with high levels of evapotranspiration, a larger proportion of incoming radiation is partitioned to latent heat flux, which cools the canopy, whereas bare, dry soils can heat up more considerably (Mildrexler et al., 2007). Therefore, as the vegetation density over a surface increases, the LST is expected to decrease.

In Arctic tundra ecosystems, however, this trend is reversed due to the cold permafrost soils providing an energy sink below ground, resulting in the bare surfaces being cooler than the aboveground vascular vegetation (Hope et al., 2005). Therefore, NDVI generally displays a positive relationship with increasing temperatures (particularly growing season temperatures) in tundra environments (Blok et al., 2011; Cui and Shi, 2010; May et al., 2020; Raynolds et al., 2008; Walker et al., 2003).

2.3. Palynological analysis for environmental reconstruction

2.3.1. Introduction and applications

Palaeoecology investigates long-term vegetation patterns through various techniques, including pollen analysis (Twiddle, 2012). Pollen analysis (palynology) uses fossil pollen preserved in sediment to reconstruct past vegetation composition. Palynology encompasses both pollen grains (produced by angiosperms and gymnosperms) and spores (produced by ferns and cryptogams). Pollen grains (between 10 μm and 100 μm in size) consist of the male nucleus for fertilisation, surrounded by an extremely resistant outer wall made of cellulose and sporopollenin (Bennett and Willis, 2001). Plants generally produce an abundance of pollen grains, which are dispersed by insects or wind. The majority of released airborne pollen will become mixed with pollen from other sources in the atmosphere and eventually land on the ground as pollen rain. However, as the sporopollenin in the grain wall is vulnerable to oxidation, pollen grains are only preserved indefinitely in anaerobic conditions, provided by environments such as bogs and water bodies (Bennett and Willis, 2001). The preserved pollen is then extracted from the peat (or lake sediment) sample through the use of strong chemicals (such as HCl and NaOH, and a mixture of sulphuric acid and acetic anhydride during acetolysis) that remove other components of peat, leaving pollen grains intact (Birks and Birks, 1980). Pollen grains are then identified according to their physical characteristics, which differ among taxa (Birks and Birks, 1980).

Following the identification, the data are collated into a pollen diagram that summarises all encountered taxa and their relative abundance as a percentage of the total sum. The age of individual samples from a peat core (or a lake core) can be determined using the radiocarbon dating method (Libby, 1972). Combining the age estimate with the relative pollen abundance of the same sample provides a description of the vegetation composition at the site at this point in time (Birks and Birks, 1980). Dating several samples throughout the peat core allows ages to be modelled for all samples, and peat accumulation rates to be estimated for different sections of the core (e.g., Reimer et al., 2020). Based on these estimates, a pollen profile can be used to reconstruct past vegetation communities through time. Pollen analysis can also be applied in climate reconstructions, as past vegetation, represented by fossil pollen, is shown to respond to past fluctuations in temperature and precipitation (Twiddle, 2012). In Scandinavia, this method has been used in pollen-based climate

reconstructions (Seppä and Birks, 2001), to investigate the dynamics of past spread of arboreal species (Giesecke and Bennett, 2004) and the response of past tree lines to climatic changes (Barnett et al., 2001), and to detect land use changes (Kuoppamaa et al., 2009). The following sub-sections present the methods used in Chapter 4 to extract pollen from a peat core, to count and identify the pollen, and to interpret the pollen profile.

2.3.2. Coring and sub-sampling

A 46-cm-long core was collected from the centre of a mire at 1000 m a.s.l. on Galdhøpiggen, Jotunheimen (Figure 2.8a). A Russian peat corer with a 5 cm diameter chamber was used for the extraction of the core. Whilst the peat layer of the mire extended deeper, only the top 46 cm (including the surface moss polster) was extracted and analysed for the purposes of this study. The core was wrapped in plastic film and placed in a plastic tube for transportation to Swansea University's cold store. The core was then stored in dark conditions at 5 °C prior to sub-sampling.

For laboratory analyses, the core was sub-sampled at 1 cm intervals to produce a total of 46 samples. A modified syringe was used to measure out a known volume (1 cm^3) of peat material (Figure 2.8b) which was then placed in a labelled plastic test tube. The 5 cm thick moss polster covering the top of the core (Figure 2.8a) was removed and cut into segments at 1 cm resolution from the top down. To assure enough pollen was extracted from each segment (i.e., 'depth'), 2 cm^3 of material was measured with the modified syringe and placed in a test tube. Prior to analysis, 2 tablets of known concentration of an exotic marker spore (*Lycopodium*) and 20 ml of water were added into the test tubes containing the peat- and the moss polster samples.

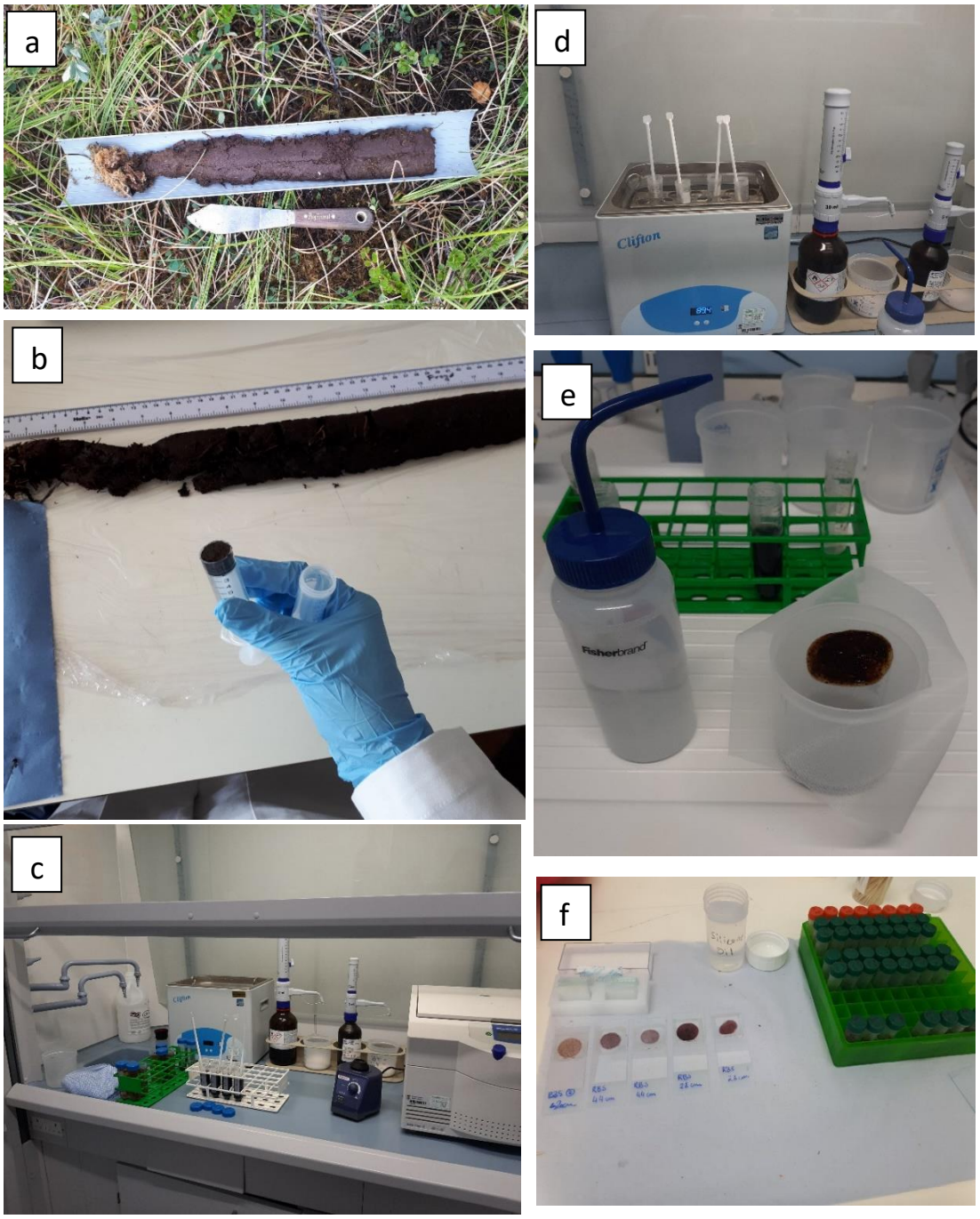

Figure 2.8. Various stages of pollen extraction from a peat core: (a) ~50 cm peat core collected from a mire, (b) sub-sampling of the core, (c) preparation for water bath, (d) acetolysis in a water bath, (e) preparation for fine-sieving and (f) preparation of slides for the microscope analysis.

2.3.3. Determining the organic matter content by loss on ignition

Sediment samples with a volume of 1 cm^3 were analysed at 2-centimetre intervals for bulk density (g cm^{-3}) and loss-on-ignition (LOI), following the method outlined by Chambers et al. (2011). Due to the scarcity of material in the top 15 cm, samples were taken only from depths between 16 and 44 cm. The results were used to calculate the bulk density, organic matter content and organic matter density of each sample. The protocol and calculations used are outlined in full in sub-Section 2.1.10.

2.3.4. Extraction of pollen from peat

The full extraction procedure is outlined by Bennett and Willis (2001). What follows here is the protocol that was used for the analysis of the peat core in Chapter 4, with some modifications from Bennett and Willis (the main steps are outlined below and in Figure 2.9). Whilst the use of hydrofluoric acid (HF) is common in the extraction process to remove silica and silicates, the mineral content of the peat core used in this study was minimal as it consisted largely of organic material. A number of samples were tested prior to analysis to determine whether HF was required to produce clear slides where pollen is easily distinguishable under the microscope. Four samples were treated with HF, whilst another four samples followed the rest of the procedure but skipped the HF step. Comparison of the output from both types of samples established that both approaches produced equally good results and it was decided to discontinue the use of the HF extraction. Images of some of the stages involved in pollen extraction are shown in Figure 2.8.

Step 1: To estimate the concentration of the pollen and spores, a known volume of exotic suspension was added to each sample (Stockmarr, 1971). Two tablets of *Lycopodium* (Batch no. 3862, concentration: 9666 spores per tablet) were added to each test tube containing 1 cm^3 of peat sample and 20 ml of water. The contents were mixed using a whirlimix and left overnight to allow the tablets to dissolve.

Step 2: To remove carbonates, 7% HCl was added to each test tube, and tubes were placed in a hot water bath at 90 °C for 30 minutes. This step was followed by a water wash, i.e., samples were centrifuged at 3000 rpm for 5 minutes, excess liquid was decanted and remaining sample whirlimixed, distilled H_2O was added, and samples

were centrifuged again. The water wash was repeated several times until the supernatant was clear.

Step 3: The removal of humic acids and the breakdown of sediment was achieved by adding 10% NaOH to the tubes and placing them in a water bath at 90 °C for 5 minutes.

Step 4: The mixture in each tube was then sieved through a fine sieve (180 μm mesh size) using distilled water to remove large particles. This step was followed by several consecutive water washes of the remaining fine material.

Step 5: Glacial acetic acid (CH_3COOH) was used as a deflocculant; samples were centrifuged and liquid decanted.

Step 6: The acetolysis step removes polysaccharides (e.g., cellulose), which are present on the surface of pollen grains and often in the sediment. Nine parts of acetic anhydride ($(CH_3CO)_2O$) were mixed with one part of sulphuric acid (H_2SO_4) and the mixture was added to the remaining material. The test tubes were then placed in a water bath at 90 °C for three minutes.

Step 7: Samples were washed with CH_3COOH and transferred into smaller tubes, followed by several water washes.

Step 8: To increase the contrast of pollen grains, three drops of aqueous safranin dye was added to each sample; samples were then washed with water.

Step 9: Tertiary butyl alcohol (TBA) was added to the samples to dehydrate the pollen grains and the remaining sample was transferred into small tubes. Silicone oil was added and thorougly mixed into the sample with a cocktail stick to avoid clumping of the material. The tubes were left open for 24 hours to let the TBA evaporate.

Step 10: Remaining residue from each sample was mounted on individual microscope slides, covered with a coverslip and sealed. Each slide thus obtained represents a given depth in the profile.

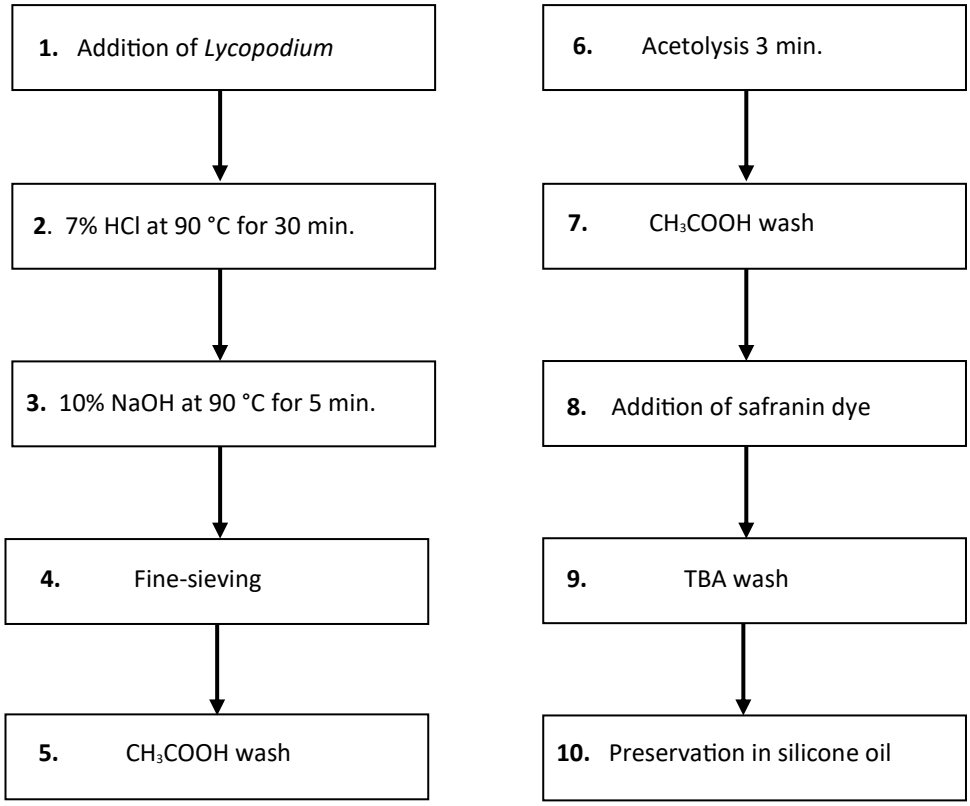

Figure 2.9. The chronological order of the stages involved in pollen extraction from peat samples.

2.3.5. Pollen identification and counting

Microscope slides with residue were placed under a Leica DM 2000 light microscope and examined in transverse sections, using magnifications of x400 and x1000. All encountered pollen grains were counted and identified according to their unique shape, size, and surface pattern (Bennet and Willis, 2001). Reference material was used to compare the unidentified grains with pollen grains of known taxa. These materials ranged from reference slides containing real pollen grains (Swansea University collection), to published guides containing photographs and keys (e.g., Moore, 1994; Reille 1992), to online databases with detailed descriptions (e.g., *paldat.org*). Examples of pollen grains of different taxa found in the Raubergstulen (Norway) core are illustrated in Figure 2.10. Following the protocol, a total of 500 land pollen (TLP) grains and spores were counted and identified per depth level, excluding the added exotic.

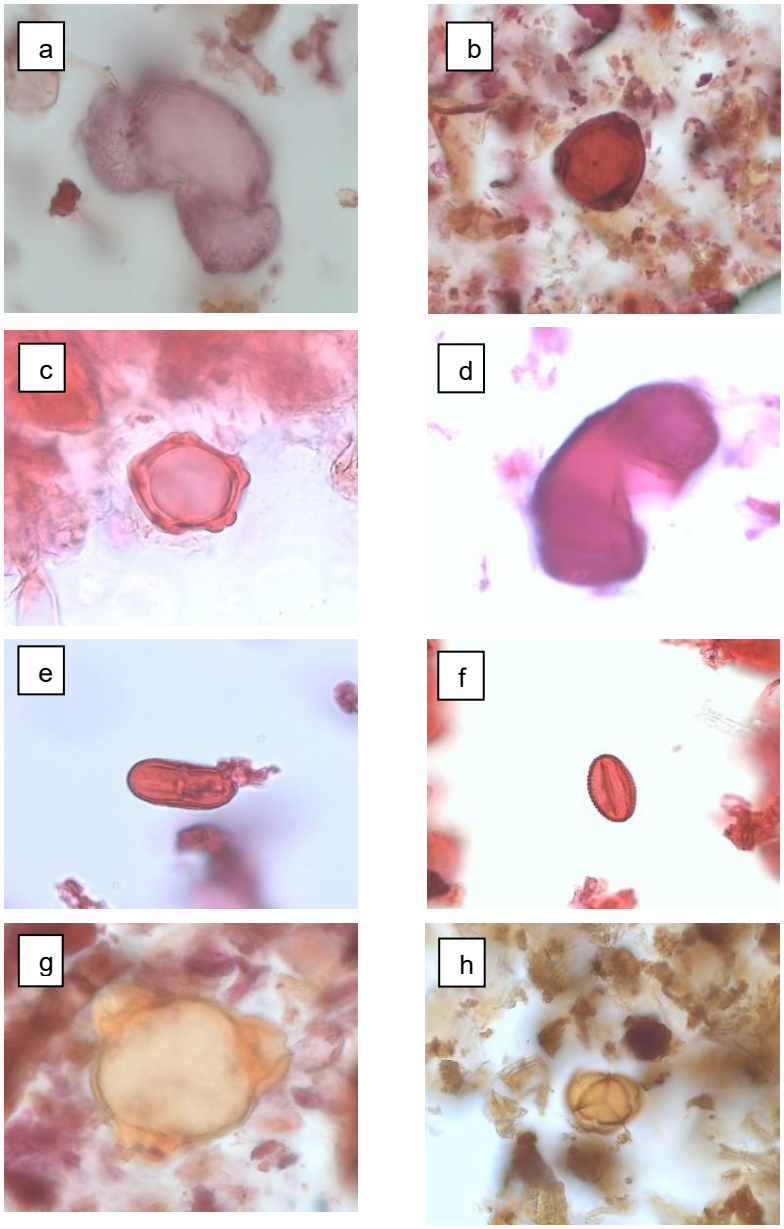

Figure 2.10. Individual pollen grains of different taxa found throughout the Raubergstulen peat core at various levels of magnification. (a) *Pinus sylvestris* (mean grain size: 50-70 µm), (b) *Betula pubescens* (20-30 µm), (c) *Alnus* (23-30 µm), (d) *Picea abies* (>100 µm), (e) Apiaceae (20-30 µm), (f) *Salix* (10-25 µm), (g) *Epilobium* (51-100 µm), (h) *Empetrum nigrum* (26-50 µm). Images were taken using a Leica DM 2000 light microscope with an attached camera.

2.3.6. Calculation of pollen relative abundance, concentration, and accumulation rates

Pollen relative abundance and concentration at each depth were calculated following Bennett and Willis (2001). The relative abundance of each taxon was calculated by dividing the pollen grain count of a taxon at a given depth with the sum of TLP counted at that depth:

$$Relative\ abundance\ (\%) = \frac{Counted\ pollen\ of\ a\ taxa}{Sum\ of total\ land\ pollen}$$

The known volume of added exotic (*Lycopodium*) was used to calculate the fossil pollen concentration (no. of grains per unit volume of peat, e.g., grains cm^{-3}) of each taxon by using the following equation:

$$Concentration = \frac{Counted\ pollen\ of\ a\ taxa}{Counted\ Lycopodium} \times \frac{Lycopodium\ spores\ per\ tablet\ \times\ no.\ of\ tablets}{Sediment\ volume\ (cc)}$$

If sediment accumulation rates are known, pollen concentration values can be used to calculate pollen accumulation rates, i.e., the number of pollen grains incorporated annually per unit area of substrate (grains cm^{-2} $year^{-1}$) :

$$Pollen\ accumulation\ rate\ (PAR) = \frac{pollen\ concentration\ (cm^3)}{sediment\ accumulation\ rate\ (cm\ yr^{-1})}$$

2.3.7. Radiocarbon dating and age calibrations

The humin fraction of three peat samples (taken at 10 cm, 24 cm and 46 cm depth) was dated using accelerator mass spectrometry (AMS) radiocarbon dating at Queen's University Belfast. The resulting ^{14}C dates for samples taken at depths of 24 cm and 46 cm were converted to calendar ages (cal. yr BP) using the calibration software CALIB (8.2) (Stuiver et al., 2021) and the IntCal20 radiocarbon age calibration curve

(Reimer et al., 2020; see Supplementary Figure 4.2) The dates were determined using a 2σ error (Stuiver and Reimer, 1993) meaning that there is a 95% probability that the reported median calibrated age falls within the estimated age range. The 'greater than modern' radiocarbon date ($F^{14}C$ = 1.0915 ± 0.0021) at 10 cm depth was calibrated using the post-bomb calibration dataset 'Northern hemisphere zone 1' (NHZ1) by Hua et al. (2013) and the online calibration resource CALIBomb (Available from: calib.org/CALIBomb/). This dataset was selected because it is appropriate for latitudes in the northern hemisphere above ~40°N, which is the closest match to the Galdhøpiggen study site.

The R package 'clam' (2.2) (Blaauw, 2010) was then used to create an age-depth model based on linear interpolation between the three dated levels of the core (10, 24 and 26 cm) and the surface. The input file contained both ^{14}C ages and the calibrated $F^{14}C$ date. By default, 'clam' uses the northern hemisphere terrestrial calibration curve (IntCal13) from Reimer et al. (2013), and the calibration assumes a Gaussian distribution. The post-bomb calibration curve is again provided by Hua et al. (2013). To include the negative (i.e., post-1950 AD) radiocarbon date, the 'NHZ1' calibration curve was selected (R command: *postbomb=1*), and the calendar scale was set to BC/AD (R command: *BCAD=TRUE*). In the input *.csv* file, the ^{14}C ages were included for depths 24 cm and 46 cm. The non-^{14}C dates (i.e., at 10 cm and at the surface) were assigned negative values to indicate their departure from 1950 AD towards modern times. Knowing that the calibrated date at 10 cm is c. 2000 AD, this depth was assigned the value '-50' in the input file. The surface of the consolidated peat core was set at 6 cm, excluding the modern moss polster. Assuming that the 5 cm thick moss polster represents 2-4 years of pollen accumulation (Lisitsyna and Hicks, 2014) and taking into account that the core was collected in 2018, the age of the surface was set to 2014 (represented by '-64' in the input file). An age-depth model was created in R (3.6.3). The calibrated output for ^{14}C dates was comparable to the age ranges produced by the CALIB (8.2) software (Stuiver et al., 2021).

2.3.8. Plotting diagrams

All pollen diagrams were created in psimpoll (4.27) (Bennett, 2000). The percentage diagram was plotted using input files with calculated relative abundance values for each taxon. Statistically significant pollen assemblage zones based on the relative pollen abundance diagram were determined using the constrained cluster analysis (CONISS) (Grimm, 1987).

Input files containing pre-calculated concentration values for nine dominant taxa (≥5%) were used to create pollen concentration and -influx diagrams. The concentration diagram summarises the concentration of pollen grains in one cubic centimetre of peat sample. The influx diagram was created by using the concentration values and an input file with calibrated ages for dated depths. The influx diagram illustrates pollen 'influx' (grains cm^{-2} $year^{-1}$), also known as pollen accumulation rate (PAR).

2.3.9. Interpretation of pollen profiles: estimating local community composition

The interpretation of pollen profiles can be complicated due the relationships between pollen deposition and vegetation. It is often assumed that the proportion of pollen in the profile depends on the local abundance of its source plants; however, the pollen production and dispersal methods of individual plant species show considerable variation. Plants that reproduce through wind-dispersed (anemophilous) pollen (e.g., *Pinus sylvestris*) generally produce more pollen than those with insect-dispersed (entomophilous) pollen (e.g., *Empetrum, Vaccinium*) (Bennett and Willis, 2001). Dispersal of airborne pollen is affected by atmospheric conditions, and the falling velocity of pollen grains further depends on their size and shape (Jackson and Lyford, 1999). For example, *Pinus* pollen grains are equipped with two air bladders, facilitating their dispersal (Twiddle, 2012). Moreover, wind can transport pollen for short as well as long distances, complicating the estimation of the distance to the source. Therefore, an accurate reconstruction of the past environment in terms of the abundance of past local species remains a challenge. However, when it comes to estimating past positions of tree lines and their dynamics, any meaningful interpretations depend on the accuracy of estimating the local presence of individual

species. Various methods have been used in palynological studies to improve this quantification, as will be discussed in the following sub-sections.

2.3.10. Relative pollen abundance

Relative pollen abundance (%) is the abundance of pollen of a species in relation to the sum of other species present in a sub-sample, or at a given depth. Relative abundance is presented in pollen percentage diagrams, which is a common method of representing pollen data. The value is often used in environmental reconstruction as an indicator of the local presence of individual taxa, which can be used to infer past vegetation community structures around the sampling area (Huntley and Birks, 1983; Lisitsyna et al., 2001). However, as the data for each species in a percentage diagram are represented as a percentage of the total pollen sum from the sample, the abundance of any one species is dependent on the presence of other species. This complicates any comparisons spatially (between individual sites) or temporally (different points in time) (Hicks, 2001; Prentice and Webb, 1986). Nevertheless, relative pollen abundance values have previously been used as indicators for local and regional presence of different tree species in Europe. Huntley and Birks (1983) set the threshold values for *Betula* (tree birch) as follows: 10% indicates local presence, 25% local dominance and 50% a birch-dominated woodland. For *Alnus*, a value of 8% is estimated to mark its local presence in Norway (Moe and Odland, 1992). The regional presence of major European trees was estimated by Lisitsyna et al. (2011). The authors report threshold values of 10%, 5% and 1% for pine, birch, and spruce, respectively. The minimum values indicating regional presence of *Alnus* and *Quercus* are reported as 2.5% and 1.5% respectively, and as low as 0.5% for low pollen producers *Ulmus*, *Juniperus*, *Fraxinus* and *Tilia*.

However, the method of using relative pollen abundance alone to reconstruct past assemblages in open alpine and Arctic environments must be approached with caution. Palynological records from sparsely vegetated tundra sites can still be dominated by long-distance derived arboreal pollen (up to 90%), and relative abundance values alone cannot distinguish between local and regional pollen (Pardoe, 2006, 2014). To improve the accuracy of estimating the local presence of taxa, relative abundance should be used in combination with other established methods, such as indicator species,

macrofossils, or pollen accumulation rates. This is the approach taken in Chapter 4 of this thesis.

2.3.11. Pollen accumulation rates

Pollen accumulation rates (PARs) are defined as the net number of grains accumulated per unit area of sediment surface per unit time (Davis, 1969). PARs have successfully been used to determine the local presence of birch, pine, and spruce at their limit in northern Fennoscandia (Hicks, 2001) and to detect land use changes in a sparsely settled boreal forest (Kuoppamaa et al., 2009). The advantage of this method is that PAR values are not affected by the presence or absence of other, more abundant, taxa, allowing each taxon to be analysed individually over space and through time. Using several pollen traps to estimate deposition rates, Hicks (2001) concluded that the long-term (18-year) average pollen deposition is a good indicator of the presence, absence, and abundance of arboreal species around the sample site. Hicks (2001) proposed PAR threshold values of <500, 300-500 and 25-50 to indicate the absence of birch, pine, and spruce (respectively) within a 1-km radius. At the other extreme, PAR values of >1500, >2000 and >300 were found to relate to a dense local cover of birch, pine and spruce, respectively.

2.3.12. Modern analogue technique

A number of pollen studies have used the modern analogue technique, which involves determining the modern pollen-vegetation relationships in a given area and applying them to pollen profiles constructed from sediment core analysis to quantify past vegetation assemblages. Examples of this include Jackson's (1991) work on altitudinal gradients in North America. More relevant to our study area, surface pollen studies using moss polsters and their application to Holocene pollen data have been studied in Jotunheimen since the late 1980s (e.g., Caseldine 1989; Caseldine and Pardoe, 1994; Pardoe 1996, 2006, 2014). A common method is to collect and analyse surface moss polsters for pollen, as the trapped pollen is expected to reflect the modern vegetation distribution in the surrounding area. Moss polsters are estimated to represent 2-5 years of pollen deposition and are considered a good analogue for a peat sample, but cannot be used to calculate PAR (Lisitsyna and Hicks, 2014; Pardoe, 2006). Moss polsters can be a useful tool in tundra environments that have a relatively small relevant source

area of pollen. Many tundra species, including shrubs and herbs, are insect-pollinated and of smaller stature compared to trees, which can result in pollen source areas that are 600-800 m in radius (Oswald et al., 2003). Moreover, Bunting (2003) states that for cores extracted from mires, the non-arboreal and spore component of the pollen spectra will be dominated by local species from within just a few metres from the sample site. These findings are supported by Caseldine (1989), who found that up to 60% of surface pollen on the dwarf-shrub heath on Storbreen glacial forelands could be locally derived, due to the ability of mosses to catch poorly distributed local pollen. Moreover, certain species (e.g., *Empetrum*, *Rumex*, Cyperaceae and *Salix*) exhibited a high correspondence between pollen and the vegetation on isopollen maps. Whilst the glacial forelands are treeless, long-distance arboreal pollen was still found on the moss polsters, but the relative amounts of arboreal pollen were lowest in heath communities dominated by local pollen. Although the modern analogue technique has had success in determining the local presence and abundance of species in tundra environments, Caseldine and Pardoe (1994) stress that distinguishing vegetation communities immediately above and below the tree line still remains a challenge.

2.3.13. Indicator species

Building on the modern analogue technique used on the glacial forelands in Jotunheimen, Pardoe (2006, 2014) highlights the value of using indicator species to distinguish between plant communities in a pollen profile and to assess the presence of certain communities. Pardoe (2014) finds a strong correlation between the presence of indicator taxa in the vegetation and their representation in the pollen spectrum. Local non-arboreal taxa that produce little pollen (e.g., *Empetrum* and *Salix*) are found to accurately indicate the vegetational composition of local assemblages. Moreover, even a small proportion of herbaceous species present in the profile might assist in determining past local tree cover. *Empetrum*, *Vaccinium* and Ranunculaceae were strong indicators of the past presence of a herb-rich understorey and local tree cover on a sampling site in Haugabreen in Jotunheimen (Pardoe 2006; 2014). The author suggests that the presence of indicator taxa combined with the magnitude of PARs will be more appropriate for distinguishing alpine vegetation than the overall pollen composition. A similar method was adopted by Kuoppamaa et al. (2009), who combined pollen accumulation rates with indicator taxa associated with disturbed

ground (e.g., *Epilobium*, *Plantago major*, *Ranunculus*) to successfully detect past land use changes. To date, indicator species have been successfully used in palynology to identify plant communities in other parts of the world (e.g., Oswald et al., 2003), and for assessing past disturbance (e.g., Kuoppamaa et al., 2009) and anthropogenic activity (e.g., Behre, 1981).

Chapter 4 will combine these four commonly used indicators of local presence (i.e., relative pollen abundance (%), pollen accumulation rates, indicator species and modern analogue technique) to reconstruct past vegetation assemblages on Galdhøpiggen over the past ~4000 years.

Chapter 3

Carbon dioxide emissions from periglacial patterned ground under changing permafrost conditions and shrub encroachment in an alpine landscape, Jotunheimen, Norway

Fieldwork for this project was carried out on the Swansea University Jotunheimen Research Expedition in 2018. This paper constitutes Jotunheimen Research Expeditions Contribution No. **215** (see: http://jotunheimenresearch.wixsite.com/home).

Co-authors: Hiemsta JF, Los SO, Matthews JA, Froyd CA

Published in: *Permafrost and Periglacial Processes* (2020) 31(4): 524-537. (DOI: https://doi.org/10.1002/ppp.2078).

Abstract

Whether Arctic and alpine ecosystems will act as a future net sink or source of carbon remains uncertain. The present study investigates ways in which ecosystem (soil and vegetation) and geomorphological (cryogenic disturbance) factors may control or affect the future release of carbon in an alpine permafrost landscape. Rates of ecosystem respiration (R_e) were examined using a portable gas analyzer across an altitudinal transect ranging from mid- to high-alpine vegetation zones underlain by discontinuous to continuous permafrost on Galdhøpiggen (Norway). Measurements were made of R_e during the peak growing season on active and relict sorted circles exhibiting varying levels of frost disturbance and shrub encroachment. Re was found to be controlled more strongly by soil microclimate and plant growth forms than by geomorphic indicators of cryoturbation in thawing permafrost or by atmospheric conditions. The results indicate that increasing shrub cover leads to elevated R_e, while an increase in surface disturbance has the potential to lower R_e. We conclude that vegetation is likely to colonize frost-disturbed surfaces at progressively higher altitudes as freeze–thaw processes slow down or cease, and this will result in increased R_e.

3.1. Introduction

In a warming world, changes in high-latitude and high-altitude environments are largest and arguably have the greatest impacts on regional climate change feedbacks (Turetsky et al., 2019). Arctic regions are currently experiencing air temperatures rising at a rate that is nearly twice as high as the global mean (Meredith et al., 2019; Graversen et al., 2008; Serreze and Barry, 2011). One of the potentially most destructive consequences of this warming has been the widespread thawing of permafrost across periglacial landscapes and the resulting release of greenhouse gases such as CO_2 and CH_4 from thawed soils (Vonk et al., 2015; Natali et al., 2015; Euskirchen et al., 2017). Permafrost underlies an estimated 22% of the exposed land surface of the northern hemisphere (Zhang et al., 1999) and permafrost soils contain vast quantities of carbon that can thus be mobilised (Schuur et al., 2008).

Whether Arctic and alpine tundra ecosystems will in the future act as a net sink or source of carbon is uncertain (McGuire et al., 2012; Belshe et al., 2013; Lundin et al., 2016; Celis et al., 2017; Euskirchen et al., 2017). As permafrost thaws, previously frozen Soil Organic Carbon (SOC) becomes available for microbial decomposition, resulting in increased ecosystem respiration and carbon emissions into the atmosphere (Schuur et al., 2008; Belshe et al., 2013; McGuire et al., 2009). However, net effects remain difficult to predict as longer growing seasons and increased availability of newly released soil nutrients may lead to higher rates of plant photosynthesis, stimulating primary production and carbon uptake (Natali et al., 2011; Belshe et al., 2013), which would counteract the increasing carbon release. It is still more complex since increased vegetation cover will lower albedo, and thereby increase the shortwave radiation absorbed by the land surface, which in turn can lead to higher temperatures (Pearson et al., 2013).

Changing environmental conditions combined with rising temperatures have already resulted in northward and upward altitudinal shifts of vegetation in Arctic and alpine tundra ecosystems over the past decades (Post et al. 2009; Grytnes et al. 2014); this includes a change in composition and density of tundra vegetation (Pearson et al., 2013). Especially notable is the encroachment of shrubs (′shrubification′) relative to other tundra plants throughout the Arctic (Myers-Smith et al., 2011; Tape et al., 2006). Changes in tundra vegetation can have a range of wider ecological consequences as

they influence several biosphere-atmosphere feedbacks, such as greenhouse gas balances (Pearson et al., 2013; Post et al., 2009).

Vegetation distribution and the carbon sequestration capacity of tundra landscapes are further influenced by geomorphological factors such as freeze-thaw processes in periglacial soils. Throughout high-latitude and high-altitude regions, cryoturbation – the mixing of soil due to seasonal freezing and thawing – can also affect the tundra carbon cycle in contrasting ways (Aalto et al. 2014; Ballantyne, 2018). Surface disturbance can negatively affect plant roots (Kade and Walker, 2008), reducing vegetation cover and decreasing photosynthesis-driven carbon inputs from the atmosphere to the terrestrial biosphere. Poorly insulated soil further exacerbates frost activity (Kade and Walker, 2008), and reduces the capacity of cryoturbated ground to sequester carbon. Conversely, mixing can transport soil organic carbon from the carbon-rich near-surface layer to deeper, colder soil horizons with limited microbial activity, where it can potentially become 'buried' in permafrost, and contribute to long-term carbon storage (Schuur et al., 2008). The efficacy of this process was illustrated by Bockheim (2007) who found that 55% of active-layer and near-surface permafrost SOC had been redistributed to lower depths via cryoturbation.

However, the process of cryoturbation is extremely susceptible to climatic changes due to its dependence on soil moisture and temperature (Kaiser et al., 2007; Aalto et al., 2014), which further complicates the estimation of its long-term effects. Some studies have suggested that cryoturbation is expected to increase as the Arctic warms (Bockheim, 2007), and evidence points to increased carbon storage through this process (Kaiser et al., 2007). Conversely, others have reported a complete cessation of cryogenic surface processes in response to increased air temperatures (Aalto et al., 2014).

Cryoturbation drives the formation of patterned ground, of which sorted circles, studied here, are ubiquitous in periglacial landscapes (Frost et al., 2013). Sorted circles are created by differential frost heave and buoyancy-driven soil circulation (Ballantyne, 2018); which is characterized by the circulatory movement of material upwards and outwards in the central part of the sorted circle, and downwards near the borders (Ballantyne, 2018; Kessler et al., 2001; Hallet, 2013). This may be expected to produce predominantly vertical structures in the subsurface, which provides the

intriguing possibility of creating preferential paths for carbon fluxes. This is another way in which carbon release from the deeper subsurface could be enhanced.

The present study investigates the possible ways in which ecosystem (soil and vegetation) and geomorphological (cryogenic disturbance) factors control or affect the release of carbon in permafrost landscapes. Galdhøpiggen, an alpine site in Jotunheimen, southern Norway was chosen because it provides an altitudinal transect that represents areas of discontinuous to continuous permafrost, and mid- to high-alpine vegetation belts (see Matthews et al., 2018). Numerous studies over the last several decades have investigated the vegetation succession (e.g., Matthews et al., 2018; Matthews 1992, 1999; Robbins and Matthews, 2010, 2014; Matthews and Vater, 2015), the patterned ground landforms (Ødegård et al., 1988; Matthews et al., 1998; Haugland et al., 2004; Winkler et al., 2016), and the distribution of permafrost in Jotunheimen (Ødegård et al., 1992; Farbrot et al. 2011; Hipp et al., 2012; Lilleøren et al., 2012). Thus, we have excellent background information and understanding of the geomorphology and ecology of the study area.

Sample sites were located on active and relict sorted circles with varying degrees of vegetation cover and visibly disturbed ground surface. Ecosystem respiration (R_e) was recorded with a portable infrared gas analyser on sites representative of different permafrost conditions. This setup allows space-for-time substitution following the ergodic principle (Clifford et al. 2009) and is assumed to provide an indication of how R_e may change over time with changing permafrost conditions and/or vegetation encroachment.

The specific objectives of this study are: (i) to examine the rates of R_e across an altitudinal transect ranging from mid- to high-alpine vegetation belts underlain by permafrost; (ii) to describe the patterns in R_e, (iii) to identify and explore factors that affect R_e and (iv) to consider possible implications of our results for future rates of R_e following climatic warming.

3.2. Study site

The study was conducted on the north-facing slope of Galdhøpiggen (2469 m above sea level (m a.s.l.) in NE Jotunheimen, Norway (61°N, 8°E) (Figure 3.1). The altitudinal transect covered 5.5 km and consisted of five sites located near the road (Galdhøpiggvegen) from Galdesanden to Juvvasshytta at 1550, 1750, 1800, 1850 and 1950 m a.s.l., i.e., with a 400 m altitudinal range between the highest and the lowest site. At each site, three sorted circles were investigated. All circles studied consisted of bare or sparsely vegetated centres grading to relatively more vegetated outer edges (Figure 3.2). Individual circles are composed of fine textured, silty sand centres bounded by gutters filled with coarse calibre clasts (cobbles to boulders). The diameters of the circle centres ranged between 1 and 4 m, with gutters up to 2 m wide (Figure 3.2).

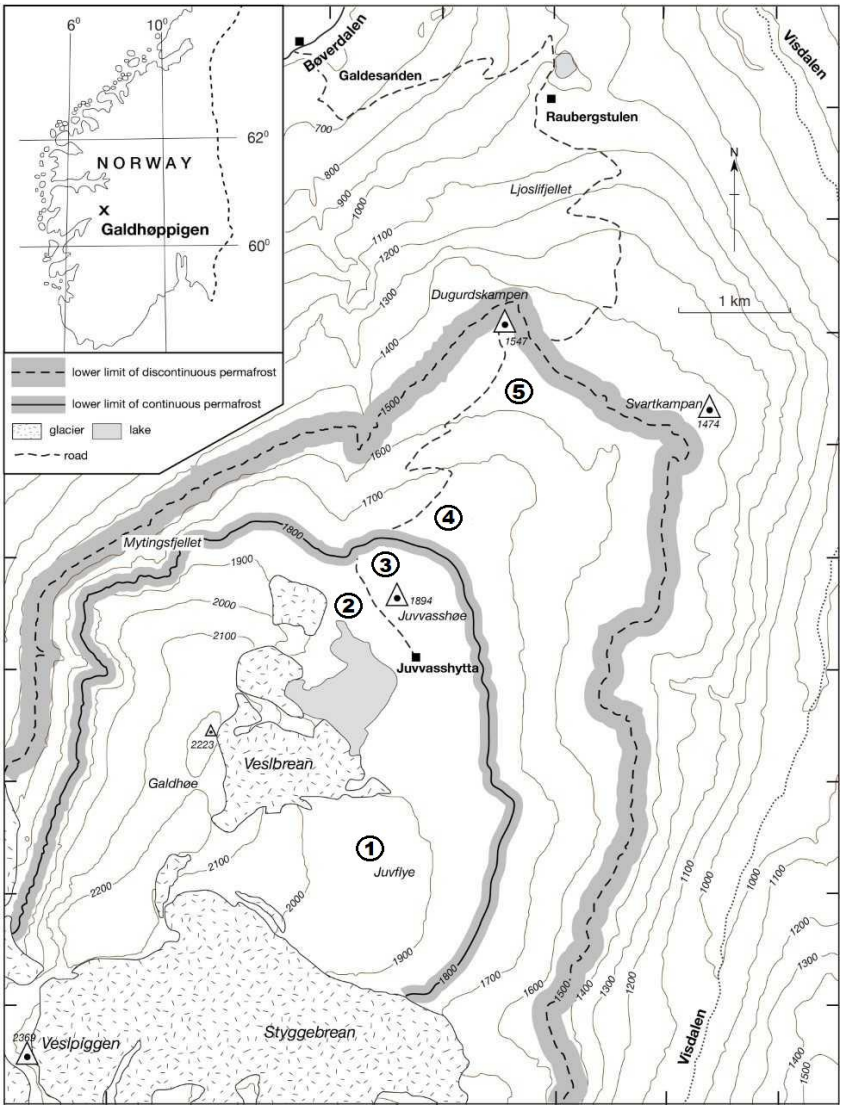

Figure 3.1. Altitudinal transect following the road from Galdesanden to Juvvasshytta on the north-facing slope of Galdhøpiggen in Jotunheimen. Site locations are indicated by a number (1-5).

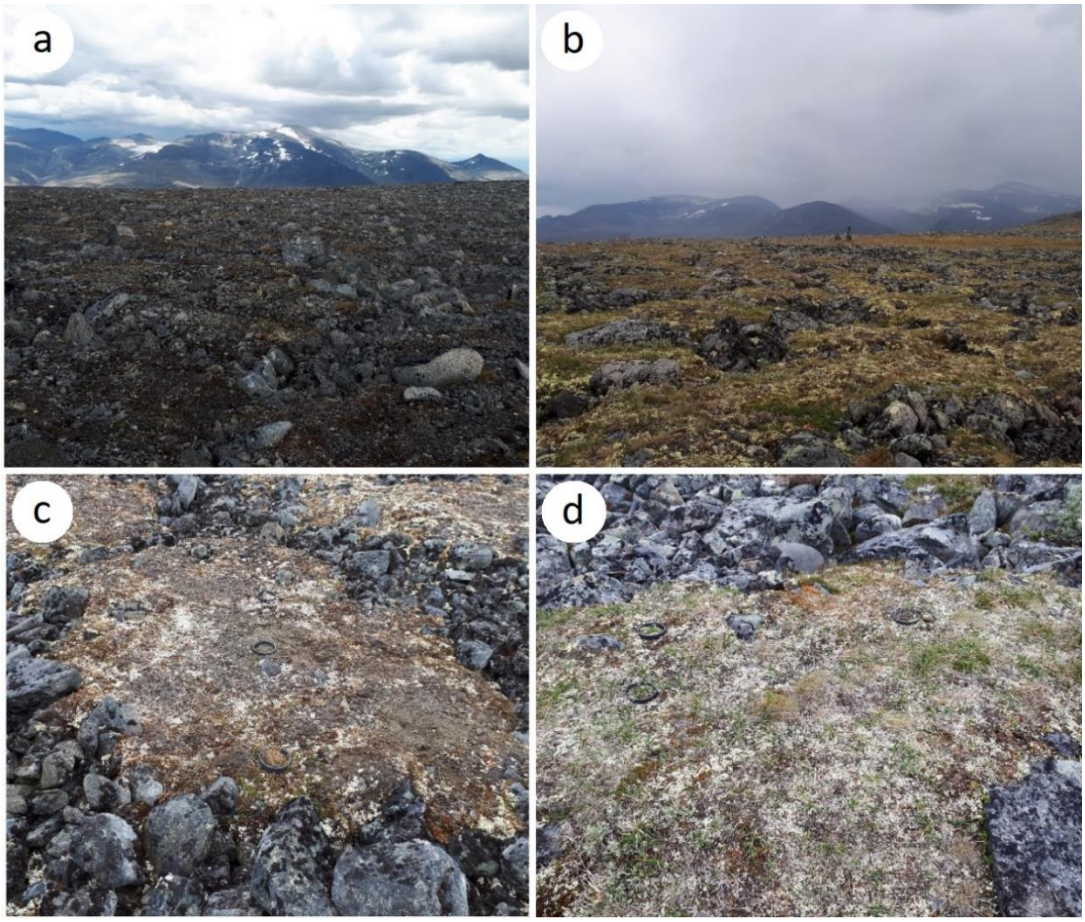

Figure 3.2. Sorted circles at 1950 m a.s.l. (site 1, a and c) and 1550 m a.s.l. (site 5, b and d).

In the mid-1990s, the lower limit of discontinuous permafrost on the north-facing slope of Galdhøpiggen was at ~1450 m a.s.l. (Ødegård et al., 1992, 1996; Farbrot et al., 2011; Hipp et al., 2012). At present this limit is assumed to be between ~1450 and 1500 m a.s.l. (see Figure 3.1). The thickness of the permafrost layer at Juvvasshøe (in the continuous permafrost zone at 1894 m a.s.l.; see Figure 3.1) is estimated to be 380 m (Isaksen et al., 2007). The active layer thickness varies between 1.6 m at Juvvasshøe (1851 m a.s.l., near site 2) and 8.6 m at 1559 m a.s.l. (near site 5), as recorded by Hipp et al. (2012). The altitudinal transect stretched from discontinuous to continuous permafrost zone, the latter is here assumed to occur between ~1750 and 1850 m a.s.l. (Figure 1). Of the five sites, the lowest two (sites 4 and 5) are in the discontinuous permafrost zone, site 3 is in the transitional zone to continuous permafrost and sites 1 and 2 are expected to be underlain by continuous permafrost (see Figure 3.1).

All five sites are situated above the tree line, which reaches up to ~1000 m a.s.l. (Matthews et al., 2018). The lowest site (site 5) lies in the mid-alpine vegetation belt (~1350-1600 m a.s.l.), which consists of grass and lichen heath communities, whilst the remaining sites are located in the high-alpine belt, which is mainly boulder-rich fjellfield. Further details of the alpine vegetation belts on the north-facing slope of Galdhøpiggen, including their altitudinal subdivisions and plant communities are outlined elsewhere (Matthews et al., 2018; NIJOS, 1991; Moen, 1999).

3.2.1. Climate

The mean annual air temperature (MAAT) at Juvvasshøe (1894 m a.s.l.) is - 4.5 °C (Farbrot et al., 2011) and the mean annual precipitation (MAP) of the area is between 800 mm and 1000 mm (Farbrot et al., 2011; Isaksen et al., 2007). As a result of strong winds, flat and exposed areas have little to no snow cover until March or April, and a maximum snow depth of 0.5 m in May (Ødegård, 1992). However, prevailing south-westerly winds result in snow accumulation on the north-facing slopes, providing insulation in winter (Isaksen et al., 2002).

Weather conditions during the field season (July 2018) were exceptionally warm and dry, with a mean air temperature ranging between 10-15 °C at the two lowest sites above 1500 m a.s.l., and 5-10 °C above 1700 m a.s.l. during the three weeks of field work (these values are 4-6 °C above the July average for 1971-2000 (NMI, 2019)). The precipitation in July 2018 was negligible.

Rapid changes in climatic conditions on Galdhøpiggen have been recorded. Between 1999 and 2009, there was an observed increase in mean ground temperatures, with a clear accelerated warming at 30-40 m depth (Isaksen et al., 2011). Greatest warming was detected at sites where ground temperatures remained slightly above 0°C, indicating sites with recent degradation of permafrost. These sites have experienced increases in snow depths due to increased winter precipitation and were insulated from cold temperatures during winter.

For several decades, the near-surface permafrost on Juvvasshøe has warmed by an average of 0.04–0.05 °C annually, which is mainly attributed to changes in air temperature (Isaksen et al., 2007). According to a heat flow model by Hipp et al. (2012), the lower limit of permafrost on Galdhøpiggen has moved up by

200 m to the altitude it is at today since 1860, and the active layer thickness has increased by 0.5-5 m at Juvvasshøe. A further 55-75% probability of permafrost degradation at 1900 m a.s.l. was predicted by 2100, and complete degradation of permafrost at 1561 m a.s.l. before 2050. The associated movement of the lower limit of discontinuous permafrost to above 1800 m a.s.l. (Figure 3.1) would lead to major transformations in the area, which would be unprecedented since the beginning of the Holocene (*cf* Lilleøren et al., 2012). Moreover, visible changes in vegetation patterns have already been observed. For example, based on information from aerial photography, there has been a considerable upslope advancement of *Betula pubescens* trees over the past 36 years (Figure 3.3).

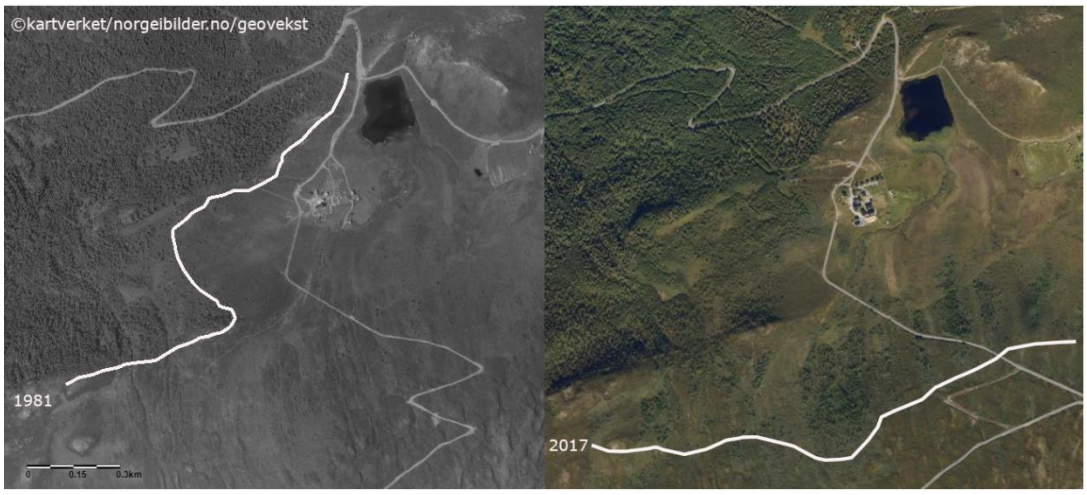

Figure 3.3. Aerial photos of Raubergstulen (covering the altitudes between 1000-1200 m a.s.l.) from 1981 (left) and from 2017 (right). The white lines illustrate the upslope advancement of trees and shrubs over the past 36 years. The peak of Galdhøpiggen is to the south-west. Reproduced with permission from Kartverket, 2019.

3.3. Methodology

Mountain slopes in alpine regions such as Galdhøpiggen are often used as 'natural laboratories', as they provide a setting where climatic and environmental conditions (e.g., soil microbial communities (Shen et al., 2015) and vegetation composition (Lomolino et al., 2001; Matthews et al., 2018) change over short distances. For example, an increase of 1000 m in altitude provides a comparable change in temperature as travelling 1000 km towards higher latitudes (Donhauser and Frey, 2018; Diaz et al., 2003).

This study similarly uses an altitudinal transect as a proxy for future climate warming (Yang et al., 2014; Sætersdal et al., 1998). We identified a number of variables that are likely to affect R_e in this alpine environment and estimated how their control over R_e changed across an altitudinal transect.

3.3.1. Vegetation

Vegetation cover plays an essential role in the carbon cycle, but only half of CO_2 flux studies have included descriptions of vegetation type (Virkkala et al., 2018), and data from cryptogam- and moss-covered landscapes are lacking. To estimate the degree of disturbance relative to vegetation cover on our sites, a relative measure combining both variables was adopted. On each individual circle, the degree of disturbance was estimated based on the visual assessment of vegetation cover. 'Bare/sparse' indicated the most disturbance and consisted of either bare ground or cryptogamic crust. 'Well-established' represented the most stable conditions, with mature vegetation types including herbaceous plants and shrubs. 'Transitional' was an example of intermediate, transitionary conditions between the two, often made up of cryptogams or graminoids. The percentage cover of each category was estimated on every circle to determine the effect of vegetation cover types over R_e. However, as the assessment was based on individual circles and as the ground cover varied across the altitudinal transect, the species present in each category differed between sites, causing minor overlap between categories. The effect of plant growth forms on R_e was investigated by further dividing vegetation cover into four functional groups (*a) crust, b) cryptogams, c) herbaceous plants, d) shrubs*) (Table 3.1).

Table 3.1. Overview of species divided into functional groups.

Crust	'Cryptogamic crust'
Cryptogams	Mosses: *Polytrichum* spp., *Racomitrium* spp. Lichens: *Cetraria* spp., *Cladonia* spp., *Alectoria* spp., *Stereocaulon* spp., *Thamnolia* spp., *Solorina* spp., *Cornicularia* spp., *Pettigera* spp.
Herbaceous plants	*Ranunculus glacialis, Hieracium alpinum, Festuca ovina, Carex bigelowii, Luzula arcuata, Poa alpina*
Shrubs	*Salix herbacea, Vaccinium vitis-idaea, Vaccinium uliginosum*

The cover fraction of each of the four groups was measured within individual collars (surface area = 314.16 cm²). Identifiable cryptogams, lichens and mosses (a), that exist as separate individuals or mats were distinguished from cryptogamic crust (b), in which the species are undifferentiated. Cryptogamic crusts in this area consist of mainly mosses and blue-green algae, and act as a good indicator of frost disturbance and as pioneer colonisers on glacier forelands (Matthews and Vater, 2015).

3.3.2. Carbon dioxide measurements

The closed chamber method for measuring R_e involves an infrared gas analyser that measures CO_2 emissions over a small area of ground, taking account of small-scale spatial variability in the heterogeneous tundra environments (McGuire et al., 2012). Here, these CO_2 emissions represent peak growing season ecosystem respiration (R_e), which is a combined value of autotrophic respiration (aboveground vegetation and roots) and heterotrophic respiration (soil microorganisms) (Hermle et al., 2010), expressed here in μmol C m^{-2} s^{-1}. R_e was measured repeatedly using a portable infrared gas analyser (LI-COR, LI-8100A) with an opaque 10 cm survey chamber. Three PVC collars (100 mm in diameter, 45 mm in height) were inserted 20 mm deep into the ground on each sorted circle for a minimum of 24 hours before the first measurement and were left in for the duration of the study period. Three land cover types were

identified on each circle: one collar was placed on the least vegetated part of the circle (*bare/sparse*), one on a fully vegetated area (*well-established*), and one within an area of intermediate vegetation cover (*transitional*) (Figure 3.4). Three consecutive measurements with the duration of two minutes were taken immediately after placing the survey chamber on a collar. There was a 30 second pause between measurements to purge the chamber. Repeated measurements were taken between 9.30 am and 5 pm on six separate days in July 2018 (n = 460 measurements). The aim was to conduct the measurements in similar atmospheric conditions over multiple days, which was achieved owing to the persistent dry and clear conditions throughout the study. The time of each measurement was noted and included in the analysis to determine whether R_e exhibits diurnal variation.

Soil moisture and temperature, both known to affect microbial soil respiration (Virkkala et al., 2018), were recorded simultaneously with two ECH2O Model EC-5 soil probes by inserting the probes into the top 30 mm of soil so that they were parallel with the soil surface. Probes were inserted adjacent to the collar for the duration of the chamber measurements. Air temperature, relative humidity and wind speed were recorded during each chamber measurement with a Kestrel 3000 Pocket Weather Meter at 1 m height above the ground surface. These data were used to calculate vapour pressure deficit (VPD).

Figure 3.4. Collars placed on three land cover types: bare/sparse (site 1, left), transitional (site 3, middle) and well-established (site 5, right).

3.3.3. Disturbance

The parameters selected to approximate the effects of cryogenic disturbance were based on a model that describes circular movement of soil within sorted circles (Ballantyne, 2018; Hallet, 2013). We hypothesise that the seasonal freeze-thaw cycles that drive circular movements in cell-like structures could create pathways for gas escape that extend deeper into the active layer, possibly reaching recently-thawed buried carbon in the deeper soil horizons that would thus facilitate and increase carbon release.

Clasts buried directly under the surface are expected to show evidence of preferred (vertical) long axis alignments if the surface was recently disturbed, for example by uplift or frost heave (Evans et al., 2007; Benn, 1994). The clast's long axis fabrics should reflect the strength of recent cryogenic processes taking place within the circle and the degree of alignment of this axis with the vertical is then a measure for the degree of disturbance by cryoturbation. We expect actual gas emission or soil respiration to be enhanced in areas of recent activity and close vertical clast alignments. The proxy variables used to record this level of disturbance are the percentage cover of bare ground on the sorted circle, orientation of the mean long axis of the clast fabrics, Isotropy and Elongation (Benn, 1994). Isotropy and Elongation indices (possible values ranging from 0 to 1) are commonly used in Eigenvalue or Bingham analysis of 3-dimensionally distributed (or orientation) data (Benn, 1994). A high Isotropy value (close to 1) indicates a uniform distribution of orientations whereas a value close to 0 indicates a clustering along a single direction or in a plane (a girdle distribution), i.e., some form of preferred orientation. A high Elongation value would identify single modes, i.e., a single preferred fabric signal or orientation of clasts. Measurements of long axis dip and orientation of 30 clasts were carried out on each circle on sites 1-4. On the lowest site, 15 clasts were measured on each circle due to a lack of availability.

3.3.4. Soil chemical properties

Soil chemical properties (pH, soil organic matter (SOM)) and nutrient content (phosphorus, carbon and nitrogen ratio (C:N)) were examined as they provide information on nutrient limitations that are common in tundra ecosystems and on carbon storage and respiratory losses from the soil (Benn, 1994). Soil samples were taken from each sorted circle; and were later dried, sieved and ground in the laboratory in preparation for analysis. Soil pH was measured by mixing 5 g of homogenised soil with 10 ml of deionised water and taking the reading with a pH probe. Soil organic matter (SOM) content was evaluated by loss on ignition at 550 °C. Soil carbon and nitrogen content and the C: N ratio were determined by using a mass spectrometer. An XRF spectrometer (Rigaku NexCG ED-XRF) was used for elemental analysis to determine the concentration of soil phosphorus (P).

3.3.5. Statistical analysis

Least angle regression (LARS) was employed to identify combinations of independent variables that explain most of the variance in CO_2 efflux from the soil. LARS is a technique to analyse multidimensional sets of explanatory variables. It ranks combinations of explanatory variables starting from none to potentially the full set. For each combination of variables, a criterion is calculated based on the sums of squares explained whilst at the same time adding a 'penalty' for incorporation of a higher number of variables. LARS has a similar objective as forward stepwise regression but employs a more efficient algorithm and has the advantage that selection of variables is less arbitrary. The LARS algorithm distributes equally the effect of correlated independent variables on the dependent variable (Efron et al., 2004). All statistical analyses were performed in R 3.6.1 (R Core Team 2019), and the R package 'lars' was used to conduct least angle regression (Efron et al., 2004).

3.4. Results

3.4.1. Least angle regression

Based on the LARS analysis (Figure 3.5) and the partial correlation coefficients (Table 3.2), a parsimonious set of seven predictor variables that explain the most variance in R_e were selected for further analysis. These variables are related to soil properties (soil moisture, soil temperature), vegetation cover (cover fraction of shrubs in a collar, cover fraction of herbaceous plants in a collar, cover fraction of crust in a collar and percentage of bare ground on the sorted circle) and weather (vapour pressure deficit). Figure 3.6 shows the results of a linear regression model predicting R_e for (a) the whole dataset and (b) for the top seven variables.

Table 3.2. Partial correlation coefficients between ecological/geomorphological predictor variables and R_e, and Cp values from the LARS analysis.

Predictor variable	Partial correlation coefficient	Cp
Soil moisture	0.19	195.1
Shrub cover (%)	0.58	169.8
Bare ground (%) on circle	-0.22	164.5
VPD	0.02	142.2
Crust (%)	-0.10	120.5
Soil temperature	0.21	70.4
Herbaceous cover (%)	0.18	47.5
Cryptogam cover (%)	0.16	34.0
Elongation	0.02	34.3
Isotropy	-0.12	32.1
Time of day	0.15	9.4
SOM	0.08	10.8
Elevation	-0.10	12.5
C:N ratio	0.06	13.6
pH	0.07	15.5
Average dip angle	-0.05	17.2
P	-0.08	18.0

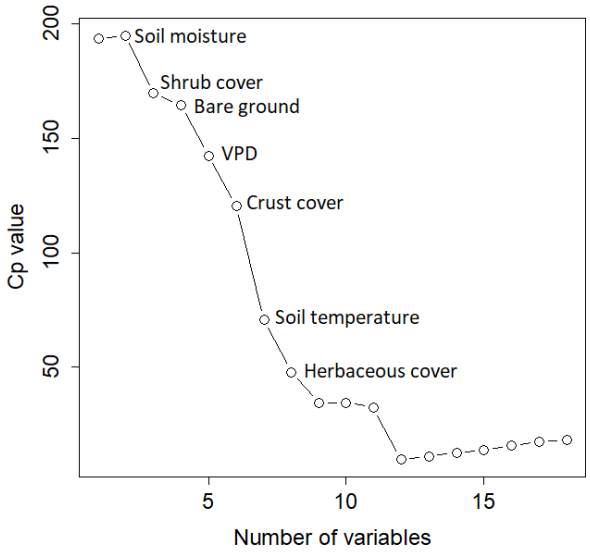

Figure 3.5. The Least Angle Regression model ranking the predictor variables according to their importance in explaining variance in R_e rates (overall model $R^2 = 0.593$).

Based on the comparison of the two predictive models (Figure 3.5), it is evident that the parsimonious set of seven predictor variables (Figure 3.6b) describes the observations almost equally well as the full set of explanatory variables. Therefore, the remainder of the discussion will focus on these seven variables.

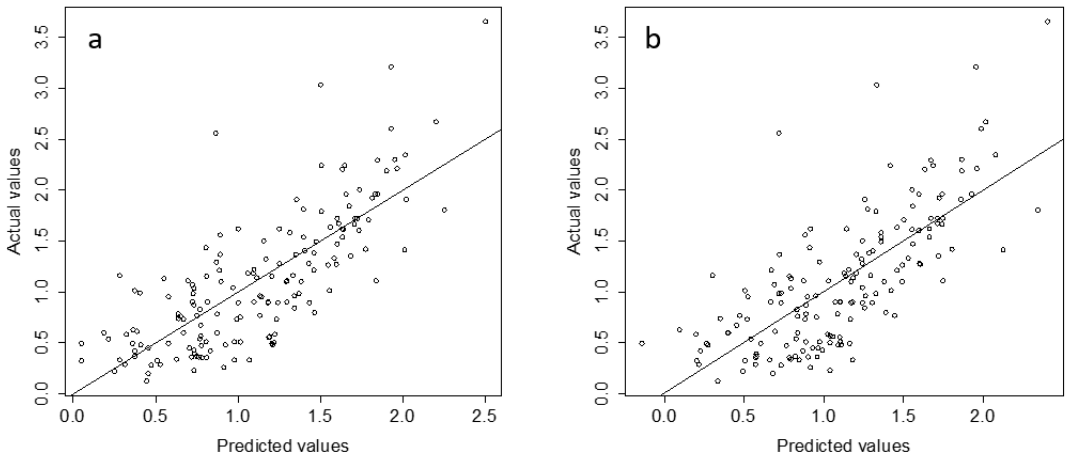

Figure 3.6. Observed values of R_e (µmol m^{-2} s^{-1}) plotted against predicted values for (a) the whole dataset (adjusted $R^2 = 0.59$) and (b) the top seven predictor variables (adjusted $R^2 = 0.52$).

3.4.2. Moisture and temperature

The study period during peak growing season was exceptionally warm and dry. Soil moisture content was low and ranged from 0.2% to 22.7% but showed no significant variation within individual sorted circles. Soil moisture increased (from an average of 6% at site 4 to 10% at site 1), but the highest value was found at the lowest site (14%) (Table 3.4). Moisture content did not show a statistically significant variation between the three land cover types. However, a noticeable pattern exists, as the bare and sparsely vegetated patches at higher altitudes (sites 1-3) tend to have on average a slightly higher moisture content (10%) compared to soils covered with well-established vegetation (7%). This pattern reverses at lower altitudes (sites 4-5), where the ground cover within circles is more uniform, and the average moisture content ranges from 9% under sparsely vegetated patches to 11% under fully vegetated surfaces. Soil moisture explained most of the variance in R_e and is positively correlated with it (r= 0.39, p =<0.001) (Figure 3.7a). This association was strongest on the transitional land cover type (r= 0.60, p =<0.001), followed by the well-established (r= 0.49, p =<0.001) and bare/sparse land cover types (r= 0.40, p =<0.005).

Table 3.3. Results of an ANOVA conducted with the top seven predictor variables that explained the most variance in R_e rates. Predictor variables related to vegetation cover are expressed in percentage cover fraction within collar.

Predictor	Df	Sum sq	Mean sq	F value	Pr(>F)
Soil moisture	1	10.94	10.937	51.362	2.99E-11
Shrub cover (%)	1	9.82	9.823	46.133	2.26E-10
Bare ground (%) on circle	1	8.82	8.822	41.429	1.47E-09
Crust cover (%)	1	3.26	3.260	15.310	0.000137
VPD	1	2.47	2.469	11.594	0.000844
Herbaceous cover (%)	1	1.81	1.810	8.499	0.004084
Soil temperature	1	0.77	0.770	3.615	0.059131
Residuals	154	32.79	0.213		

Table 3.4. Mean values and standard deviation of R_e, soil temperature and moisture, pH, C:N ratio and phosphorus content on individual sites.

Site and elevation (m a.s.l)	R_e (µmol $m^{-2}s^{-1}$)	Soil temperature (°C)	Soil moisture (%)	pH	C:N ratio (%)	P (ppm)
1 (1950)	1.31 ± 1.01	20.9 ± 9.0	10.6 ± 5.7	4.9 ± 0.3	10.9 ± 0.8	1580 ± 96
2 (1850)	0.60 ± 0.27	16.4 ± 2.2	8.2 ±4.4	4.6 ± 0.5	12.3 ± 1.1	1860 ± 60
3 (1800)	1.03 ± 0.68	23.4 ± 7.7	7.9 ± 4.0	4.7 ± 0.1	11.3 ± 0.6	1922 ± 157
4 (1750)	0.96 ± 0.82	19.5 ± 4.5	6.0 ± 5.3	4.4 ± 0.4	12.9 ± 1.3	2384 ± 270
5 (1550)	1.50 ± 0.51	24.6 ± 6.8	14.7 ± 4.5	4.3 ± 0.3	13.5 ± 1.1	2296 ± 405

Soil temperature in the top 30 mm ranged from 10 °C to 34 °C. It was highest in direct sunlight and decreased under cloudy conditions. Soil temperature showed little variation within individual sorted circles. R_e shows a slightly weaker positive relationship with soil temperature than with soil moisture that was similar across all three land cover types (r= 0.32, p = <0.001) (Figure 3.7b). The highest correlation between R_e and soil temperature was observed on well-established land cover types (r= 0.48, p =<0.001), followed by transitional (r= 0.34, p = 0.01) and bare/sparse types (r= 0.25, p = 0.06).

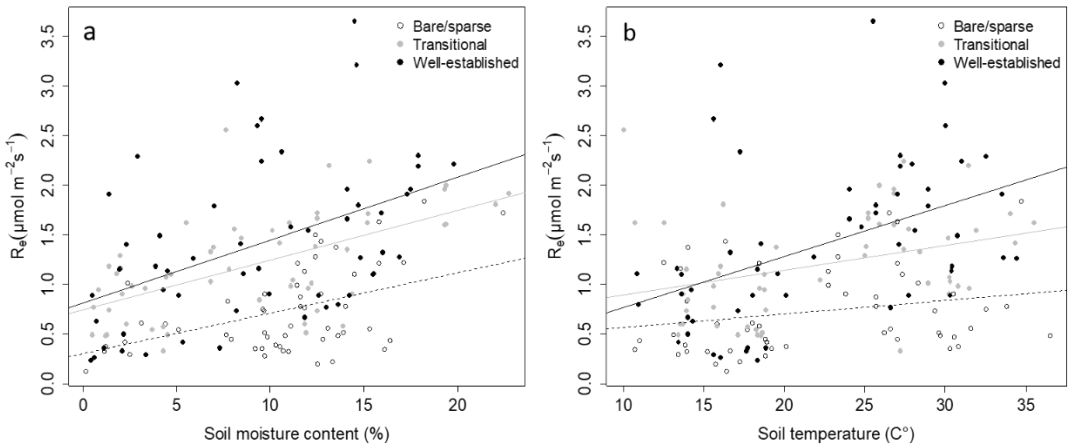

Figure 3.7. (a) soil moisture and (b) soil temperature correlated with R_e rates on bare/sparse (blank), transitional (grey) and well-established (black) vegetation covers.

3.4.3. Disturbance

Of the four proxy variables used to estimate the degree of disturbance, percentage bare ground on an individual circle explains most variance in R_e rates and has a significant negative relationship with R_e (r = -0.34, p =<0.001). The remaining three proxies (Elongation, Isotropy and average dip angle) are less significant (Figure 3.5 and Table 3.2) in explaining the variance in R_e.

Disturbance did not increase linearly with altitude, but a clear pattern between disturbance and R_e emerged. All four disturbance-related proxies indicate that site 2 (1850 m a.s.l.) experienced the highest rates of disturbance, whereas site 5 (1550 m a.s.l.) was most stable. Site 2 had the highest extent of bare ground, and lowest Isotropy indices (Figure 3.8a). Buried clasts were therefore more clustered, which indicates recent occurrence of cryoturbation such as frost heave. The opposite was found on site 5. R_e rates showed a close relationship with disturbance across elevations (Figure 3.8b).

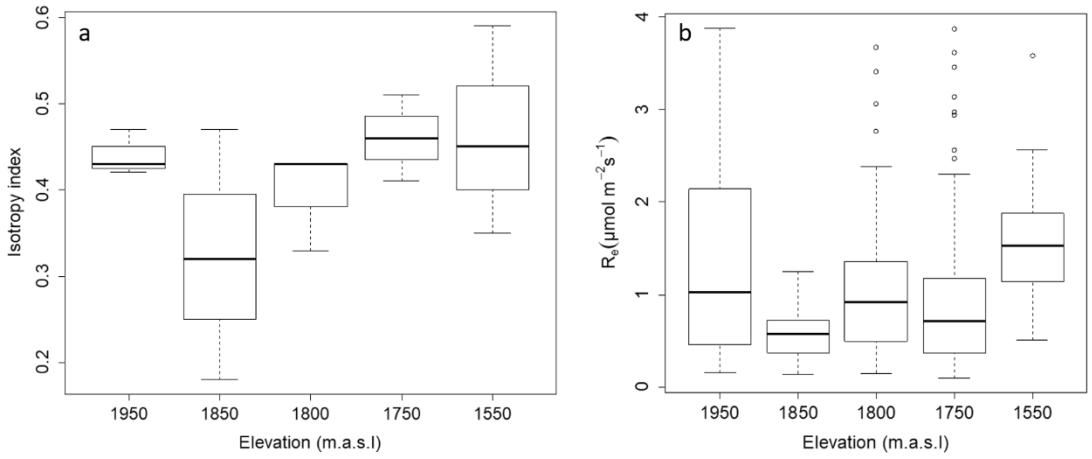

Figure 3.8. (a) Isotropy indices across all elevations. (b) R_e (µmol m^{-2} s^{-1}) rates across all elevations.

3.4.4. Vegetation

An association with vegetation cover was found as well. This association was highest and positive for stable vegetation cover consisting of shrubs (r= 0.58, p = <0.001), by contrast, it was weaker and negative for crust. Herbaceous plants and lichen cover were positively correlated with R_e. The distinct variation in R_e rates from surfaces covered by different plant species is shown in Figure 3.9b. The strong influence of shrub cover

on R_e rates is further illustrated by the large range of CO_2 efflux values at the highest elevation (Figure 3.8b). All collars placed on well-established vegetation cover on this site included a significant percentage of *Salix herbacea*, and the mean R_e for these collars reached 1.98 µmol m^{-2} s^{-1}, which is twice as high as the site mean.

R_e values ranged from 0.1 to 3.88 µmol m^{-2} s^{-1} (Table 3.4) and varied significantly between land-cover types (Chi squared = 89.91, p =< 0.001, df = 2). Highest efflux rates were recorded on well-established vegetation cover (mean: 1.45 ± 0.81 µmol m^{-2} s^{-1}, n = 159), whilst lowest emissions were from bare/sparse surfaces (mean: 0.77 ± 0.68 µmol m^{-2} s^{-1}, n = 151) (Figure 3.9a). This pattern is present on all sites. R_e rates did not vary significantly between individual circles on each site, and we found no clear evidence of a daily cycle.

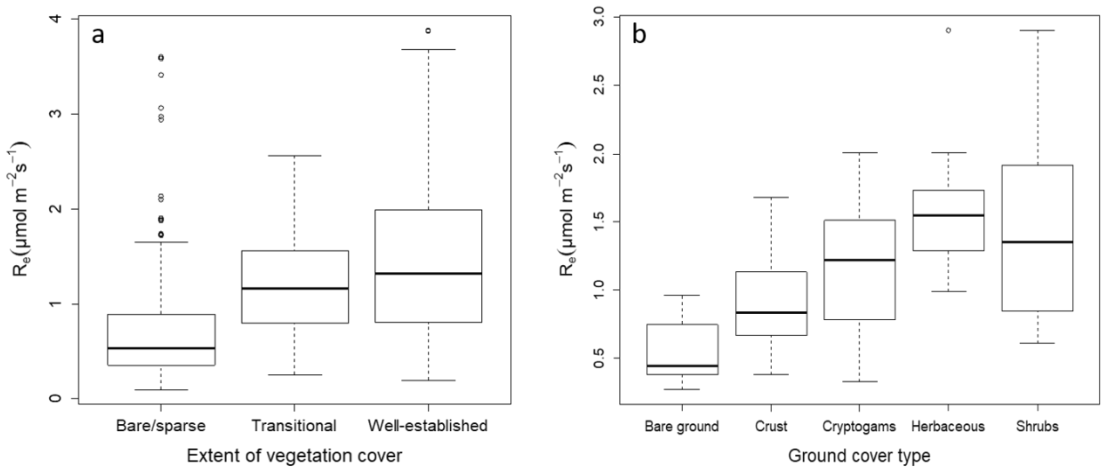

Figure 3.9. (a) R_e values (µmol $m^{-2}s^{-1}$) recorded on three categories of ground cover across all sites**.** (b) R_e rates (µmol $m^{-2}s^{-1}$) recorded from a subset of data (collars that contained 20% or higher cover of bare soil or different plant growth forms).

3.4.5. Soil chemistry

Soils are strongly acidic on all sites (pH 4.05 – 5.26), with greater pH values found on higher altitude sites (Table 3.4). Soil C:N ratio ranges from 10.52 to 14.74, and SOM ranges from 1.2 to 13.8%, with higher values recorded on lower sites. Soil phosphorus content decreases with elevation and shows a negative correlation with R_e on high-altitude sites. No significant correlation was found of R_e with either soil carbon, N and

P content, C:N ratio or soil pH (Table 3.4); these variables did not explain much of the variance in R_e in the LARS analysis either.

3.5. Discussion

The specific contribution of this study is to determine which, and to what extent environmental components affect growing season R_e rates in an alpine ecosystem. Our analysis across an elevational gradient indicates that R_e was controlled more strongly by soil microclimate and plant growth forms than by geomorphic indicators of cryoturbation in thawing permafrost or by atmospheric conditions.

3.5.1. Soil moisture and temperature

Soil moisture and temperature influence soil microbial communities, which are particularly important in cold alpine regions as the main drivers of carbon cycling (Donhauser and Frey, 2018). Both have a strong relationship with soil respiration (R_s) (Li et al., 2017; Saiz et al., 2007; Illeris et al., 2003). Whilst soil temperature has often been identified as the main controlling factor of R_s (Li et al., 2017; Saiz et al., 2007; Grand et al., 2016), this was not the case in our study. Whilst still among the top five most influential variables, soil temperature showed only a weak positive overall correlation with R_e rates (Table 3.3). Instead, soil moisture explained the most variance in R_e rates across the altitudinal transect.

Soil moisture did not exceed 23% throughout the extremely dry field season (Table 3.4). However, whilst excess soil moisture hinders microbial activity, a strong positive relationship with soil respiration has been noted when the soil water content is low, for example at times of drought (Saiz et al., 2007; Kim et al., 2014; Dagg and Lafleur, 2011; Johnson et al., 1996). Davidson et al. (1998) demonstrated that soil CO_2 efflux rates increased sharply in warm, dry conditions as the soil moisture increased from 0 to 0.12 m^3m^{-3}. This trend is followed by a steady decrease from 0.2 m^3m^{-3} onwards (Davidson et al., 1998). This in accordance with our study, as the two variables are positively correlated, and soil moisture content remained under 23% (0.23 $m^3\,m^{-3}$).

Whilst the soil moisture content did not vary significantly under different land cover types, a pattern could be detected. Bare patches at higher altitudes exhibited a slightly

higher soil moisture content compared to vegetated patches. This trend reversed at the lowest two altitudes, where the soil was moister under full vegetation. Both soil moisture and temperature have the strongest positive associations with R_e on sites with well-established vegetation; this influence diminishes with decreasing vegetation cover (Figure 3.7). This indicates that soil moisture and temperature conditions at the time of measurement were more favourable for root-and aboveground plant respiration or that microbial communities are more vigorous in these conditions.

Soil moisture and temperature can be highly variable in space and time in heterogeneous alpine environments (Li et al., 2017). On our sites, soil temperatures were relatively uniform across the sorted circles, but soil moisture showed some variability, in some cases on a sub-metre scale. Comparable results were reported by Aalto et al. (2013), who emphasized the strong effect of vegetation on soil moisture and temperature in Arctic and alpine environments. Therefore, the high heterogeneity of soil microclimate must be considered when assessing R_e on a landscape scale, as well as the interaction between abiotic and biotic components.

3.5.2. Bare ground and soil disturbance

Of the four variables used as proxies for disturbance, percentage bare ground explained the most variance in R_e rates. R_e decreases with increasing surface disturbance. This contradicts our hypothesis that disturbance stimulates carbon release by creating preferential pathways for gas escape (see Introduction). Instead our findings are in accordance with Becher et al. (2015), who studied non-sorted circles in Sweden and found that cryogenic processes resulting in surface disturbance were associated with lower soil respiration rates. It is possible that the chamber used to measure the CO_2 efflux predominantly recorded near-surface efflux, and the gas escaping from deeper layers made a negligible contribution. This negative influence of soil disturbance on R_e rates is likely a consequence of restrictions on the establishment of a stable vegetation cover.

The remaining three predictor variables associated with cryogenic disturbance (Elongation, Isotropy and average dip angle) were less significant in explaining the variance in R_e rates. This may be due to the relict status of the circles, especially at lower altitudes. Buried clasts in the most disturbed part of the circles did not generally

have a strong preferred orientation, suggesting that soil circulation was incomplete (Washburn, 1989; Kling, 1998) and frost disturbance was restricted to the surface.

Landforms experiencing frost heave exhibit substantial surface disturbance evident in the form of bare ground (Kade et al., 2005). This was observed on all our sites except the lowest, and the two highest sites (1950 m a.s.l. and 1850 m a.s.l.) had fresh sediment on the surface of the bare ground. Frost activity on patterned ground can vary in intensity over short spatial scales (Haugland, 2004), highlighting again the high heterogeneity of these landscapes. The percentage of bare ground on surface varied with altitude, and peaked at 1850 m a.s.l. However, the decline was not linear, as site 4 had defined patches of bare ground whilst none were detected on sites 3 and 5. This suggests that frost activity on this north-facing slope is dependent on site-specific conditions, such as surface (micro-)topography and exposure to wind and precipitation.

Whilst soil disturbance has the potential to hinder the development of plant roots and hinder the development of a stable vegetation cover (Kade et al., 2008), it has been found to facilitate the establishment of shrubs relative to other plants (Myers-Smith et al., 2011). Bare surfaces created by soil disturbance provide mineral-rich seedbeds ideal for shrub recruitment on patterned ground, which in turn stabilises the ground and provides a suitable environment for the establishment of continuous vegetation cover (Frost et al., 2013). Indeed, the decrease in cryogenic disturbances has been associated with temporal changes in vegetation dynamics, as vegetation colonises the bare ground (Becher et al. 2018).

3.5.3. Cover of shrubs, herbaceous plants and cryptogamic crust

Vegetation cover had a clear effect on R_e, with rates three times higher over shrub-covered surfaces compared to bare ground (Figure 3.8b, Figure 3.9). This could be explained by the variation in CO_2 sources: whilst CO_2 efflux from non-vegetated ground is mainly controlled by microbial decomposition of soil organic matter, vegetated ground has the additional CO_2 sources of root respiration and aboveground plant respiration. Out of the four vegetation types, shrub cover also explained the most variance in R_e rates (Table 3.2), followed by crust cover, herbaceous plants, and cryptogams.

R_e rates recorded from shrub-covered ground had the largest range and reached higher values compared to other plant growth forms (Figure 3.9b). Shrub-covered landscapes have indeed been found to exhibit higher rates of soil respiration compared to non-shrub tundra communities, presumably due to greater plant productivity (Ge et al., 2017) and higher litter input rates (Philips and Wurzburger, 2019). However, physical conditions may also play a role, as moist soil conditions over water tracks facilitate shrub growth, and higher respiration rates have been recorded over these areas compared to surrounding tundra (Curasi et al., 2016). Herbaceous plants (including graminoids) exhibited the greatest mean R_e values (Figure 3.9b). Highest rates of respiration have previously been recorded on graminoid-covered peatland sites (Dielman et al., 2017) due to their fast rate of litter decomposition that stimulates soil microbial activity (Hobbie, 1996).

There is a weak negative correlation between crust cover and R_e. The R_e values from crust-covered ground were lower than those from cryptogam-covered ground, but were comparable to the CO_2 efflux rates from biological soil crusts in Svalbard recorded by Chae et al. (2016). The results indicate that plant growth forms and functional groups exert differing degrees of control on R_e, which is in line with several other studies (e.g., Shaver et al., 2007; Williams et al., 2006; Loranty et al., 2018). This demonstrates that future changes in community composition will affect the CO_2 efflux from the ecosystem, especially in the case of shrub encroachment. Whilst the number of shrub species present on our study sites increased with decreasing altitude, *Salix herbacea* was present on all sites from mid- to high-alpine belts but was most abundant on the two highest sites. This indicates that surface disturbance can create a suitable environment for shrub recruitment, even at high altitudes. Moreover, the mean R_e from shrub-covered ground at the highest site was twice as high as the mean for the whole site, suggesting that shrub encroachment at higher altitudes on Galdhøpiggen is likely to result in greater CO_2 efflux from the ground.

Early-snowbed shrub species (*Vaccinium vitis-idaea* and *Vaccinium uliginosum*) were only present at the lowest altitude and have indeed been reported to prefer less cryogenically disturbed soils (Becher et al., 2018; Walker et al., 2011). This corresponds with the results of the vegetation survey conducted by Matthews et al. (2018) on the same north-facing slope. Their results show a gradual increase in the number of species with decreasing elevation, and an increase in the abundance and

number of most shrub species from mid-alpine to low-alpine belts, with the exception of *Salix herbacea*, which exhibited maximum abundance in the mid-alpine belt.

3.5.4. Future trends

Future changes in air temperatures and precipitation will have significant effects on ecosystem respiration. For example, increased soil moisture is predicted to affect soil and root respiration, especially in dry Arctic regions (Natali et al., 2015; Illeris et al., 2003). Concurrently, higher temperatures could create a more favourable environment for soil microbes in alpine regions, with the capacity to speed up carbon and nitrogen cycling (Donhauser and Frey, 2018), leading to net losses from these ecosystems (Rime et al., 2015).

Furthermore, warming temperatures facilitate the expansion of deciduous shrubs relative to other tundra vegetation, such as graminoids, bryophytes and lichens (Walker et al., 2006). Across the Arctic, *Salix* species have already extended their range along with shrubby species of *Betula* and *Alnus* (Tape et al., 2006). Similar patterns can be found on the north-facing slope of Galdhøpiggen, where *Betula pubescens* has advanced considerably upslope over the past 36 years (Figure 3.3).

Whilst the encroachment of shrubs can increase the uptake of carbon and the net primary productivity of the ecosystem, this effect is likely to be temporary, and can be offset by increases in ecosystem respiration during autumn and winter in the long term (Mekonnen et al., 2018). Shrub-covered ground has been observed to have lower SOC stocks, faster rates of respiration and high carbon turnover compared to heath and tussock tundra in permafrost (Wilmking et al. 2006) and non-permafrost environments (Parker et al., 2015). Moreover, Cahoon et al. (2012) revealed that shrub-covered sites were a net source of CO_2 in warm soil conditions (> 10 °C). Therefore, shrub encroachment in the Arctic, where soils store large amounts of carbon, could potentially lead to increased carbon loss from the ecosystem (Wilmking et al., 2006; Parker et al., 2015; Cahoon et al., 2012).

Lastly, surface disturbance in permafrost regions will also be affected by climatic changes. Future alterations in disturbance patterns could result in either increased shrub abundance as new seedbeds are created, or decreased abundance where degrading permafrost creates a waterlogged environment unsuitable for shrub growth

(Myers-Smith et al., 2011). Whilst there is evidence of cryoturbation leading to increased storage of SOC by mixing soil layers and redistributing carbon to deeper soil horizons (Bockheim, 2007; Kaiser et al., 2007), the future intensity of frost activity remains uncertain. Bockheim (2007) suggests that cryoturbation will increase as the warmer temperatures degrade permafrost. However, a model by Aalto et al. (2014) predicts an almost complete cessation of cryoturbation in northern Fennoscandia if current temperatures increase by 2°C. A number of other studies have also stated that warming will lead to a decline in cryogenic activities and the probable encroachment of previously cryoturbated surfaces by vegetation in the future (Kade et al., 2005; Becher et al., 2018; Väisänen et al., 2017) which was also observed in our study (Figures 3.2b and 3.2d).

In accordance with previous research (Becher et al., 2015; Väisänen et al., 2017), visual assessment of our study sites (Figure 3.2) indicates that vegetation is likely to colonise the sorted circles along the altitudinal transect as cryoturbation ceases. Global vegetation models based on satellite observations and climate data have already shown increased vegetation greenness, gross primary production, and respiration over the past decades as a response to increased atmospheric CO_2 levels and higher temperatures (Los, 2013; Zhu et al., 2016). If changing climatic conditions continue to make our study site favourable for shrub expansion, increased vegetation cover will accelerate carbon cycling and CO_2 emissions from the transformed landscape will increase. However, the relationship between frost disturbance and vegetation cover is not straightforward, especially in a highly heterogeneous alpine environment.

Mod et al. (2014) stress the importance of considering multiple environmental factors in order to improve our understanding of the ways in which abiotic conditions (i.e., cryogenic disturbance) affect biotic interactions in Arctic and alpine environments. For an accurate assessment of soil carbon fluxes, it is crucial to consider how soil respiration is influenced by spatial heterogeneity (Li et al., 2017) and how it will respond to future changes in the intensity of cryoturbation. Whilst the R_e measurements presented in our study were limited to the peak growing season, long-term measurements would improve the predictions. Lastly, there is a need for upscaling of the CO_2 fluxes on a landscape scale based on vegetation data (Virkkala et al., 2018).

3.6. Conclusions

Ecosystem respiration (R_e) was measured with an infrared gas analyser across an altitudinal transect under different permafrost conditions. Atmospheric, soil and vegetation parameters were measured simultaneously with the chamber measurements. R_e values ranged from 0.1 to 3.88 μmol m^{-2} s^{-1}. No distinct pattern was found with increasing altitude, and there was no significant correlation between soil chemistry and R_e. However, the highest rates of CO_2 were emitted from ground covered with well-established vegetation at all altitudes, whilst the lowest rates were recorded from bare ground. Following analysis (LARS), R_e was found to be controlled more strongly by soil microclimate and plant growth forms than by geomorphic indicators of cryoturbation in thawing permafrost or by atmospheric conditions. Of the four cryoturbation proxies, only surface disturbance exhibited a significant negative relationship with R_e. Conversely, vegetation cover had a positive effect on R_e, with shrub cover having the strongest influence on it. Heat flow models predict further permafrost degradation for our study site whilst satellite images provide evidence of increases in vegetation greenness and altitudinal upward shifts of plants across the northern hemisphere. In this context, our results indicate that the likely response of future warming in our study area will be decreased cryoturbation and enhanced upslope shrub encroachment. We predict that under this scenario, carbon cycling will intensify and CO_2 emissions from the transformed landscape may be expected to increase in the future.

Chapter 4

Tree line shifts, changing vegetation assemblages and permafrost dynamics on Galdhøpiggen (Jotunheimen, Norway) over the past ~4400 years

Fieldwork for this project was carried out on the Swansea University Jotunheimen Research Expedition in 2018. This paper constitutes Jotunheimen Research Expeditions Contribution No. **222** (see: http://jotunheimenresearch.wixsite.com/home).

Co-authors: Froyd CA, Hiemstra JF, Los SO

Published in: *The Holocene* (2022) 32(4): 308-320.

Abstract

An environmental reconstruction based on palynological evidence preserved in peat was carried out to examine late Holocene alpine tree line dynamics in the context of past climatic changes on Galdhøpiggen (Jotunheimen, southern Norway). We analysed a peat core taken from a mire at the present-day tree line (1000 m a.s.l.), c. 450 m downslope from the lower limit of sporadic permafrost. We adopted a combination of commonly used indicators of species' local presence to reconstruct past vegetation assemblages, such as the relative pollen abundance (%), pollen accumulation rate (PAR), and presence of indicator species. Additionally, fossil pollen from the peat sequence was compared to modern pollen from a surface moss polster in order to establish a modern analogue. The results were compared with studies covering the late-Holocene climatic changes in the area. The reconstruction demonstrates that a pine-dominated woodland reached above the present-day tree line at c. 4300 cal. yr BP, suggesting a warmer climate suitable for Scots pine (*Pinus sylvestris*) growth at this altitude. Scots pine retreated to lower altitudes between c. 3400-1700 cal. yr BP, accompanied by the descent of the low-alpine shrub-dominated belt, in response to cooling climatic conditions. The colder period covered c. 1700–170 cal. yr BP, and an open downy birch (*Betula pubescens*) woodland became widespread at 1000 m a.s.l., whilst pine remained sparse at this altitude. From c. 170 cal. yr BP onwards, warming allowed pine to re-establish its local presence alongside downy birch at 1000 m a.s.l.

4.1. Introduction

Over the past decades, northern mountainous areas have been experiencing the thawing of permafrost and alterations in vegetation patterns in response to increasing temperatures. Such changes have been recorded on Galdhøpiggen (Jotunheimen, Norway), the highest mountain in northern Europe and the subject of the current study. Previous studies carried out on Galdhøpiggen have recorded the decadal-scale warming of near-surface permafrost (Isaksen et al., 2007) and mean ground temperatures (Isaksen et al., 2011). Models indicate that the lower limit of permafrost has moved upslope by 200 m since 1860, to its present-day altitude of c.1450 m a.s.l. (Hipp et al., 2012). Concurrently, aerial photographs reveal upward altitudinal shifts in vegetation (notably *Betula pubescens*) on the north-facing slope over recent decades (Hallang et al., 2020). At higher elevations, shrub encroachment on Galdhøpiggen has been found to have a larger control over surface CO_2 emissions than geomorphological factors (Hallang et al., 2020).

To understand the response of northern alpine vegetation communities and tree lines to changing air temperatures, it is necessary to examine the patterns of such vegetation shifts over longer time periods. Past alpine tree line movements can assist in identifying warmer and colder periods and allow inferences about permafrost degradation and aggradation. In turn, examining the long-term vegetation- and permafrost dynamics could contribute to improving our understanding of the role of northern alpine regions in the future carbon cycle. Here, we analyse a palaeoecological sequence in order to gain insight into centennial- and millennial-scale movements of vegetation communities on the slope of Galdhøpiggen in response to past climatic changes.

Alpine regions are particularly suitable for studying vegetation dynamics, as they are sensitive to climatic variations and provide a setting where climatic and environmental conditions vary over short distances. Past palynological studies have used tree lines at their altitudinal limits as proxies to infer past climatic conditions in Norway (Aas, 1969; Barnett et al., 2001; Bjune, 2005; Caseldine, 1984; Eide et al., 2006). Here, we define the tree line as a general boundary area connecting the highest altitudinal patches of woodland on the north-facing slope of Galdhøpiggen (Aas, 1969; Körner,

1999). As the position of alpine tree lines is mainly controlled by temperature, they can be highly sensitive to even a small change in climate (Caseldine, 1984; Eide et al., 2006; Kullman, 2002). For example, tree lines in the Scandes have advanced by hundreds of metres in response to warming since 1950 (Kullmann, 2002). Therefore, a record of tree line trends over several thousand years can provide insight to past climatic changes.

The historic altitudinal movements of vegetation belts can be reconstructed from sedimentary deposits (peat- and lake deposits), whilst modern pollen trapped in moss polsters can be used to calibrate the palaeoecological record. However, an accurate estimation of the past vegetation composition based solely on palynological data is not as straightforward as simple quantification of pollen abundance, due to the differences in pollen production and dispersal methods between species. Here, we adopt a combination of commonly used indicators of local species' presence to reconstruct past vegetation assemblages on the slope of Galdhøpiggen. A peat core with an accompanying surface moss polster was taken from a mire near the present-day tree line at 1000 m a.s.l., 450 m downslope of the present-day lower limit of permafrost. Fossil- and modern pollen were extracted from the peat and moss polster and identified. The interpretation of data is enhanced by combining several approaches: (1) relative pollen abundance (%) is compared with thresholds from the literature; and (2) modern pollen abundance is compared with fossil assemblages. Pollen accumulation rates (PAR) and indicator species provide additional insight to past vegetation composition.

Galdhøpiggen has been the focus of several permafrost- and vegetation studies, which provide comprehensive background condition data over recent decades. Holocene climatic history and variability in the Jotunheimen region have also been extensively studied. Periods of glacial expansions and retreats since the beginning of the Holocene have been inferred from glaciolacustrine sediment cores (e.g., Matthews et al., 2000) and from minerogenic sediment layers in stream-bank mires (e.g., Matthews and Dresser, 2008). Holocene ground temperatures and permafrost extents on Galdhøpiggen have previously been modelled using temperature-monitored boreholes for model calibration (Hipp et al., 2012; Lilleøren et al., 2012). Combining the existing climate reconstructions with local palynological data will contribute to improving the

interpretation of changing environmental conditions on Galdhøpiggen over the past ~4400 years.

The specific objectives of this study are: (i) to reconstruct the late-Holocene vegetation assemblages on Galdhøpiggen and describe their patterns of distribution through time; and (ii) to analyse the reconstructed vegetation dynamics to infer the late-Holocene climatic conditions and permafrost limits on Galdhøpiggen.

4.2. Methodology

4.2.1. Study site

A 46 cm *Sphagnum* peat core was collected from a small mire (Figure 4.1) situated at 1000 m a.s.l. on the north-facing slope of Galdhøpiggen mountain in NE Jotunheimen, Norway (61°43'07.4"N, 8°23'58.7"E), approximately 250 m southeast of Raudbergstultjønne Lake. The mire is c. 460 m below the lower limit of discontinuous permafrost, which was most recently estimated at around 1450-1470 m a.s.l. (Farbrot et al., 2011; Isaksen et al., 2011).

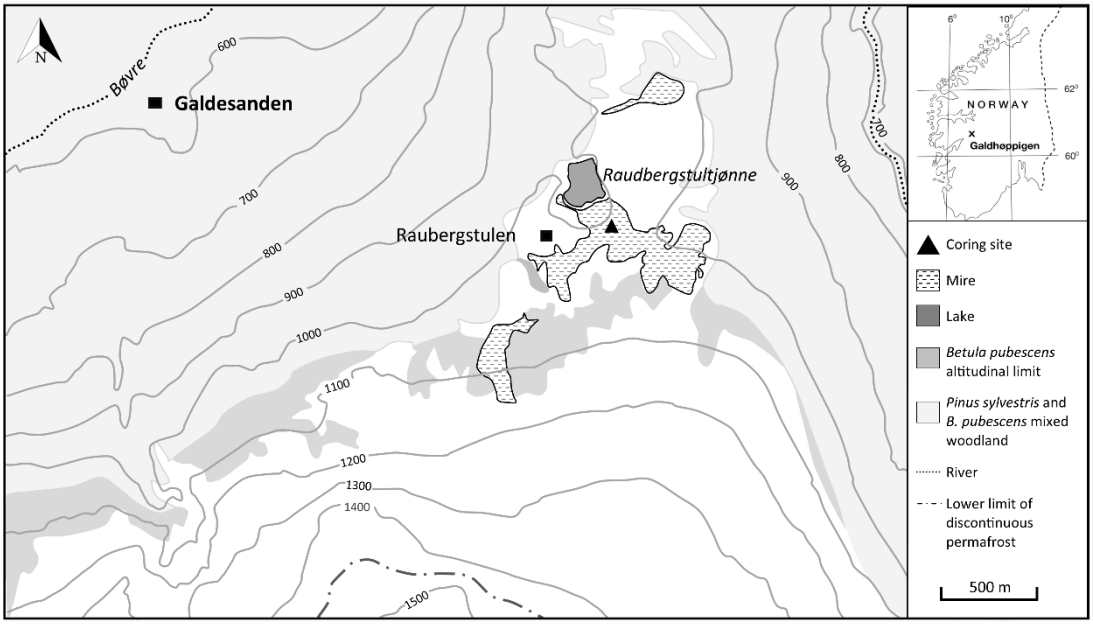

Figure 4.1. Coring site near Raubergstulen on the north-facing slope of Galdhøpiggen in Jotunheimen. Site location is indicated by a triangle, pine (*Pinus sylvestris*) and birch (*Betula pubescens*) upper altitudinal tree limits are shown in contrasting shades of grey.

The coring site lies approximately on the present-day tree line (Figure 4.1), near the upper boundary of the sub-alpine vegetation belt (Table 4.1). The upper altitudinal limit of the mixed pine-birch woodland at 1050 m a.s.l. (Figure 4.2) represents the 'timber line', or the limit of the continuous forest in the area. This is also the altitudinal limit of *Pinus sylvestris* (Scots pine), both here and in Jotunheimen (Bjune, 2005). The tree line extends up to almost 1200 m a.s.l., and consists of stands of *Betula pubescens* (downy birch).

Tree line positions have been related to the temperatures of the warmest month in the area (Körner, 1999) or a minimum of 100 days per year over 5°C (Ellenberg, 1963). Paus (2010) estimated that *Pinus sylvestris* requires minimum July mean temperatures of c. 11°C for growth in central Norway, whilst Nesje and Kvamme (1991) found that mean June-September temperatures of at least 7°C are required for *Betula pubescens*.

Based on data from the Fokstua meteorological station (60 km from site), the 2010-2019 mean July air temperature at c. 1000 m a.s.l. in the area is 11.4°C and the mean growing season (June-September) temperature is 9°C (NOAA, 2020). The mean number of days above 5°C per year was 121 during the past decade, a considerable increase from an annual mean of 110 days during 1950s, 1960s and 1970s (NOAA, 2020).

Figure 4.2. Present-day vegetation composition around the mire includes a sparse stand of *Pinus sylvestris* to the north (left of the lake) and the altitudinal upper limit of the *Betula pubescens* tree line to the south (right of the lake). The coring site is indicated by a star. Image reproduced from Google maps (2020).

The strategic location of the mire was selected to obtain a core with a surface moss polster that would contain a pollen assemblage representative of the vegetation at the present-day tree line. The surface vegetation on the mire is dominated by *Sphagnum* moss and sedges (e.g. *Eriophorum* spp.), with scattered shrubs including *Betula nana* (dwarf birch) and *Salix* (willow) species (*S. herbacea, S. glauca*). The mire is surrounded by a sparse stand of *Pinus sylvestris* c. 260 m to the north, mixed with individual junipers (*Juniperus communis*). Approximately 200 m to the south, scattered stands of *Betula pubescens* are mixed with *Salix* spp. and *Betula nana*. A birch-dominated mixed woodland is found 500 m to the east of the coring site, whilst the mixed woodland 600 m to the west is dominated by pine (Figure 4.2). The vegetation belts on Galdhøpiggen are described in Table 4.1.

Table 4.1. Vegetation assemblages across altitudinal vegetation belts on Galdhøpiggen, including (a) species characteristic of mature vegetation and (b) pioneer species found in each belt (based on Matthews et al. 2018).

Sub-alpine belt ~ 850–1025 m a.s.l.	**Low-alpine belt** ~1025-1350 m a.s.l.	**Mid-alpine belt** ~1375–1600 m a.s.l.	**High-alpine belt** ~1600-2200 m a.s.l.
Birch woodland mixed with meadowland and stands of pine	Dwarf-shrub heath above the tree line	Grass- and lichen heath with late-snowbed communities; shrubs at lower part of the belt	Discontinuous vegetation cover
(a) *Betula pubescens* *Pinus sylvestris* *Alnus incana* *Juniperus communis* *Empetrum nigrum* *Vaccinium myrtillus* *Vaccinium vitis-idaea* *Salix herbacea* *Salix glauca* *Betula nana* *Gymnocarpium dryopteris* (b) *Rumex acetosella* *Epilobium anagallidiflium* *Plantago lanceolata* *Trifolium repens* *Ranunculus acris*	(a) *Betula nana* *Salix glauca* *Salix lanata* *Juniperus communis* *Empetrum nigrum* *Vaccinium myrtillus* *Vaccinium vitis-idaea* *Vaccinium uliginosum* *Solidago virgaurea* *Hieracium* spp. (b) *Rumex acetosella* *Epilobium anagallidiflium* *Plantago lanceolata* *Trifolium repens* *Poa alpina* *Saxifraga spp.* *Festuca ovina*	(a) *Carex bigelowii* *Cetraria* spp. *Nardus sticta* *Salix herbacea* *Salix glauca* *Salix lanata* *Empetrum nigrum* *Vaccinium vitis-idaea* *Vaccinium uliginosum* (b) *Rumex acetosella* *Epilobium anagallidiflium* *Plantago lanceolata* *Trifolium repens* *Poa alpina* *Saxifraga spp.* *Festuca ovina*	(a) *Poa alpina* *Luzula arcuata* *Ranunculus glacialis* *Saxifraga* spp. *Cetraria nivalis* *Stereocaulon alpinum* *Racomitrium canescens*

4.2.2. Sample collection

A 50 cm Russian peat corer with a 5 cm chamber diameter was used to collect a 46 cm-long core (including a 5 cm moss polster) from the centre of the mire. Whilst the peat layer extended deeper, only the top 46 cm was extracted and analysed for the purposes of this study. The core was wrapped in plastic film and placed in a plastic tube for transportation. Prior to sub-sampling, the core was stored in dark conditions at 5°C. For laboratory analyses, the core was sub-sampled at one centimetre resolution to produce a total of 46 samples. A modified syringe was used to measure out a known volume (1 cm^3) of peat material per sample. Based on previous studies that estimated the pollen deposition time in moss polsters in Scandinavia (Lisitsyna and Hicks, 2014; Pardoe et al., 2010; Von Stedingk et al., 2008), the 5-cm *Sphagnum* moss polster covering the peat was assumed to represent c. four years of pollen accumulation. To examine the pollen composition throughout the moss, the polster was cut into segments at 1 cm resolution from the top down. To ensure that enough pollen was extracted from each segment, 2 cm^3 of material was measured out for analysis.

To determine the organic matter content and density of the peat, loss-on-ignition analysis was undertaken following the method outlined by Chambers et al. (2011). The core was sub-sampled at 2 cm intervals (covering depths between 16-44 cm due to the lack of sediment in the top 6-15 cm). Samples with known volume (1 cm^3) were dried overnight at 105 °C in weighed ceramic crucibles to determine the dry weight of each sample. The samples were then ignited at 550 °C for four hours to combust all organic matter, cooled to room temperature in a dessicator and weighed again.

4.2.3. Pollen extraction

Pollen extraction followed the standard method by Bennett and Willis (2001). Two *Lycopodium* spore tablets (Batch no. 3862) with known concentration of spores were used per sample as a marker to calculate the concentration of pollen (Stockmarr, 1971). The samples were first treated with hot HCl, humic acids were broken down with hot NaOH and sieving through a 180 µm sieve removed large particles from the peat material. Initial samples were tested with and without the use of hydrofluoric acid (HF). Due to the high organic matter content of the samples, the use of HF was determined to be unnecessary after the trial. All samples were subjected to three

minutes of acetolysis to remove polysaccharides. To increase the contrast of pollen grains, 0.2% aqueous safranin was added to stain the pollen. The samples were mounted on glass slides using silicone oil.

4.2.4. Radiocarbon dating and age calibrations

The humin fraction of three peat samples (taken at 10 cm, 24 cm and 46 cm depth) was dated using accelerator mass spectrometry (AMS) radiocarbon dating. The resulting ^{14}C dates for samples taken at depths of 24 cm and 46 cm were converted to calendar ages (cal. yr BP = calendar years before present [1950]) using the calibration software CALIB (8.2) (Stuiver et al., 2021) and the northern hemisphere terrestrial calibration curve IntCal20 (Reimer et al., 2020). The dates were determined using 2σ error (Stuiver and Reimer, 1993) meaning that there is a 95% probability that the reported median calibrated age falls within the estimated age range. The 'greater than modern' ($F^{14}C$) radiocarbon date at 10 cm depth was calibrated using the post-bomb northern hemisphere calibration dataset 'NHZ1' by Hua et al. (2013), and the online calibration resource CALIBomb (available from: calib.org/CALIBomb/).

4.2.5. Pollen counting

A Leica (DM 2000) light microscope was used at x400 and x1000 magnification to identify and count the pollen. A minimum of 500 TLP were counted at each depth; the sum includes all pollen taxa and spores (*Sphagnum* and Filicales). Moore (1994), Reille (1992) and a collection of reference slides held in the Department of Biosciences, Swansea University, were used to identify the pollen grains and the spores. Due to their different growth forms and ecological significance, pollen belonging to the genus *Betula* was identified to species level where possible as either *Betula nana*, *Betula pubescens* (Birks, 1968) or *Betula* hybrid (Karlsdóttir et al., 2008). The division was based on visual assessment of pollen combined with measurments of diameter (mean values: *B. nana* = 20.42 µm, *B. pubescens* = 24.20 µm) and pore depth (mean values: *B. nana* = 2.20 µm, *B. pubescens* = 2.81 µm) of individual grains. A number of *Betula* pollen grains that were damaged or deformed and therefore difficult to identify were counted as *Betula* undiff.

4.2.6. Pollen diagrams

Pollen relative abundance (%) and concentration (grains/cm^3) were calculated following Bennett and Willis (2001). All pollen diagrams were created using psimpoll (4.27) (Bennett, 2000). Statistically significant pollen assemblage zones based on the relative pollen abundance diagram were determined using binary splitting by sums-of-squares and constrained cluster analysis (CONISS); both methods resulted in the same output (Grimm, 1987). The influx diagram illustrating the pollen accumulation rates (grains cm^{-2} $year^{-1}$) for nine dominant taxa was created using input files with concentration values and calibrated ages for dated depths. PARs were not calculated for the modern moss polster because the exact age of the polster is not known.

4.2.7. Methods of analysis

Detection of Holocene tree line positions and dynamics based on pollen relative abundance is difficult (Aario, 1940; Birks and Bjune, 2010; Seppä and Hicks, 2006). Firstly, estimating the local presence of species through traditional pollen analysis is complicated because the relationships between pollen deposition and vegetation cover are rarely straightforward. Differences in the pollen type, production and dispersal methods of individual plant species, but also atmospheric conditions (e.g., wind speed and dominant direction) and topography will play a role in how and where pollen is deposited for long-term preservation (Jackson and Lyford, 1999). Secondly, *B. pubescens* and *P. sylvestris* have been found to produce less pollen near their altitudinal limits than at lower altitudes in Norway (Eide et al., 2006). Above the tree line, pollen production by local tundra species is similarly low, and pollen records are often dominated by long-distance derived tree pollen (up to 90%), masking the local tundra pollen component (Birks and Bjune, 2010; Pardoe, 2006; 2014).

Being aware of the complications regarding the use of pollen data to delineate past tree lines, and acknowledging the limitation posed by the absence of macrofossil analysis (Birks and Birks, 2000), we do not attempt to determine the exact position of the tree lines at any given time. Instead, we aim to describe the directions of past trends in vegetation cover, and draw general conclusions about the late Holocene environmental conditions on Galdhøpiggen in the context of previous publications. To achieve this,

we combine several proxies (relative pollen abundance, PAR, and indicator species) to interpret the pollen data. Relative pollen abundance has been used as an indicator of the presence of local taxa (e.g., Barnett et al., 2001; Huntley and Birks, 1983; Lisitsyna et al., 2011), and pollen percentage threshold values have been estimated for dominant European tree species to differentiate between local and regional pollen (compiled in Table 4.2). However, the use of relative pollen abundance alone to reconstruct past assemblages in open alpine tundra environments can be misleading, as it cannot distinguish between local and regional pollen (Birks and Bjune, 2010; Prentice and Webb, 1986). For example, Barnett et al. (2001) reported periods of local presence of birch and pine throughout the Holocene in Leirdalen, Norway (approximately 14 km from our site, at 920 m a.s.l.) based on relative pollen abundance (>10% and 55%, respectively). Conversely, similar relative abundance values of arboreal pollen (15-35% of birch, 20-60% of pine) were recorded in surface moss polsters collected from modern open pioneer communities on a nearby glacial foreland at Storbreen, far from tree cover (Pardoe, 2006).

Similarly, we have used the relative abundance of modern pollen in the surface moss polster (and in the top five centimetres of peat in our core) to establish a modern analogue and allow for comparison with fossil pollen assemblages in the peat. This tested approach allows a direct linkage of present-day pollen and vegetation, which can then be used to make inferences about palaeo-relationships (e.g., Caseldine, 1989; Caseldine and Pardoe, 1994; Jackson, 1991; Pardoe, 1996, 2006, 2014). Surface moss polsters are estimated to represent two to five years of pollen deposition and are considered a good analogue for determining plant community composition within palaeoecological records, but they cannot be used to calculate PAR if the exact age of the moss polster is unknown (Lisitsyna and Hicks, 2014; Pardoe, 2006). Moss polsters are useful for estimating local vegetation composition in tundra environments, where the relevant source area of pollen is relatively small (600-800 m) (Oswald et al., 2003).

To further characterise the Galdhøppigen palaeo-vegetation, we examined pollen accumulation rates throughout the core. PARs represent the net number of grains accumulated per unit area of sediment surface per unit time (Davis, 1969). PARs are not affected by the presence or absence of other (abundant) taxa in the pollen profile, allowing each taxon to be analysed individually over space and through time. Assessment of PARs have been used to determine species' local presence (Kuoppamaa

et al., 2009) and to quantify the presence of birch, pine and spruce at their latitudinal limit in northern Fennoscandia (Hicks, 2001). Using a network of pollen traps to estimate deposition rates over 18 years, Hicks (2001) found that the long-term average pollen deposition is an accurate indicator of the local presence, absence and abundance of arboreal species. The PAR threshold values for pine and birch presence from Hicks (2001) are also outlined in Table 4.2.

Table 4.2. Threshold values of *Betula pubescens*, *Pinus sylvestris* and *Picea abies* pollen accumulation rates (grains cm^{-2} yr^{-1}) and relative pollen abundance (%) from the literature indicating local and regional presence of arboreal species.

		Betula	*Pinus*	*Picea*
Hicks (2001) PAR (grains cm^{-2} yr^{-1})	Not present within 10 km	N/A	<300	<25
	Not present within 1 km	<500	300-500	25-50
	Sparse presence	500-1000	500-1500	50-100
	Open forest	1000-1500	1500-2000	100-300
	Dense forest	>1500	>2000	>300
Huntley and Birks (1983) % values	Local presence	10%	>25%	5%
	Local dominance	25%	>50%	N/A
	Dominant woodland	50%	N/A	N/A
Lisitsyna et al. (2011) % values	Regional presence	5%	10%	1-5%

Finally, we have identified several species in our pollen profile that may be indicative of certain environmental conditions. This approach has been evaluated in more detail by Birks et al. (2010) and introduced in more detail in the discussion.

4.3. Results

The peat sample is relatively uniform and consists of well-humified organic matter. The organic matter content is high (87-91%) throughout the tested 41 cm of peat material. The bulk density of the samples ranges from 0.14 to 0.23 g cm^{-3}, showing a gradual decline with increasing depth. The ash-free bulk density (organic matter density) shows a similar decline, from 0.12 to 0.2 g cm^{-3}. The pollen percentage values are presented in Figure 4.4 and influx values are outlined in Figure 4.5. The radiocarbon dates for three depths (10, 24 and 46 cm) and calibrated ages are listed in Table 4.3.

Table 4.3. Radiocarbon dates and age calibrations using the IntCal20 calibration curve (Reimer et al., 2020) and the post-bomb calibration dataset 'NHZ1' (Hua et al., 2013).

Depth (cm)	Laboratory ref. code	^{14}C Age (years BP)	$F^{14}C$	2σ Calibrated Age Ranges	Relative area under distribution	Median Calibrated Age
10	UBA-44553	-	1.0915 ±0.0021	1999-2001 AD	0.98	2000 ± 1 AD
24	UBA-42480	2872 ± 24	-	2921-3074 cal. yr BP	0.95	2997 ± 76 cal. yr BP
46	UBA-42479	3918 ± 32	-	4241-4424 cal. yr BP	1.00	4332 ± 91 cal. yr BP

An age-depth model (Figure 4.3) based on linear interpolation between the three dated levels of the core (10, 24 and 46 cm) and the surface was created using the 'clam' (2.2) package (Blaauw, 2010) in R (3.6.3) (R Core Team, 2021). The input file contained both ^{14}C ages and the calibrated $F^{14}C$ date. By default, 'clam' uses the IntCal13 calibration curve from Reimer et al. (2013) for ^{14}C ages. To include the $F^{14}C$ date, we selected the post-bomb calibration curve 'NHZ1' by Hua et al. (2013). The non-^{14}C dates (i.e., at 10 cm and at the surface) were assigned negative values to indicate their departure from 1950 AD to present. For example, the calibrated date at 10 cm is c. 2000 AD, therefore this depth was assigned the value '-50' in the input file. The surface

of the consolidated peat core is set at 6 cm, excluding the modern moss polster. Assuming that the 5 cm thick moss polster represents two to four years of accumulation (Lisitsyna and Hicks, 2014) and the core was collected in 2018, the age of the surface was set to 2014 (represented by '-64' in the input file).

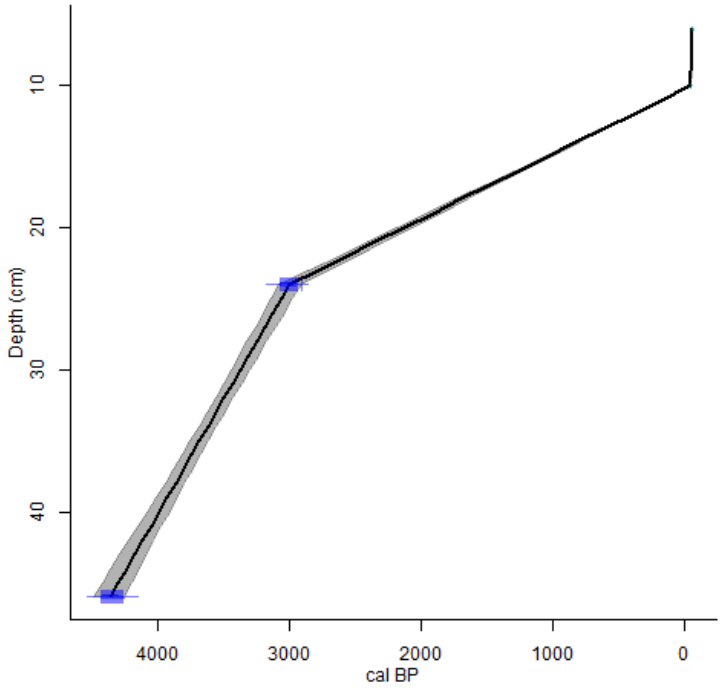

Figure 4.3. An age-depth model based on linear interpolation between dated levels (10, 24 and 46 cm) and the surface, using the calibration curves IntCal13 and post-bomb curve 'NHZ1'. The model was created using the 'clam' (2.2) package in R (3.6.3).

Accumulation rates vary throughout the core (see Supplementary Table 4.1). Between 46 and 24 cm, accumulation rates are relatively high, and 1 cm of peat covers 61 years. The rates drop between 24 and 10 cm, where 1cm covers 217 years. The remaining 4-cm section of peat at the top corresponds to only three years of accumulation per 1 cm. This apparently disproportionately high rate of accumulation can be explained by a combination of incomplete decomposition of the less compacted and less consolidated near-surface peat. Direct comparisons between the top and deeper parts of the core should be made with caution (*cf.* Young et al., 2019). In our study we therefore excluded the PARs of the section of the peat core between six and nine centimetres

from the influx diagram (see Figure 4.5). However, as the top four centimetres of peat date post-2000, the section provides an additional modern reference, and the relative abundance of pollen from this section can be used in comparison with deeper peat layers.

4.3.1. Zone 1 (4350 – 3430 cal. yr BP)

The relative abundance of arboreal pollen (86-92%) is high in the basal zone of the pollen profile (Figure 4.4). *Pinus sylvestris* pollen dominates the percentage diagram (45-64%), followed by *Betula pubescens* (20-35%). Both exhibit highest PARs at c. 3670 cal. yr BP (6500 and 3000 grains cm^{-2} $year^{-1}$, respectively). Other arboreal taxa, i.e., *Alnus, Quercus, Sorbus, Ulmus, Juniperus* and *Tilia*, are represented by small quantities of pollen (<3%). The proportions of shrub and herb pollen increase in the upper portion of the zone. The relative abundance of *Empetrum nigrum* pollen increases from 0.2% to 3%, with *Betula nana* and *Salix* pollen following a similar pattern. The highest relative pollen abundance of some herb genera throughout the 4400-year sequence (e.g., *Asteraceae, Filipendula, Rumex*) are recorded in this zone, whilst other genera (e.g., *Valeriana, Plantago*) appear exclusively in this time period. The relative abundance of Filicales spores decreases from 4% to 0.8% in Zone 1, and *Sphagnum* spore abundance increases from <0.5% to 1%.

4.3.2. Zone 2 (3430 – 1690 cal. yr BP)

A sharp decrease in PAR for all taxa is evident in the middle of Zone 2. Arboreal pollen relative proportions drop to the lowest values of the entire profile (77%), before recovering to 91% by 1690 cal. yr BP. *Pinus sylvestris* pollen exhibits a consistently lower PAR (300-2600 grains cm^{-2} $year^{-1}$), and its relative abundance decreases from 57% to 16% by c. 3000 cal. yr BP, recovering to 37% by c. 1690 cal. yr BP. The relative abundance of *Betula pubescens* pollen fluctuates between 20% and 52% throughout the zone, with PAR comparable to *P. sylvestris.* Relative pollen proportion of other arboreal taxa remains low. Shrub pollen abundance increases from 8% to 19% by mid-zone, followed by a decline to 6% by the end of the period. *Betula nana* pollen reaches the highest PAR (500 grains cm^{-2} $year^{-1}$) and relative abundance (14%) in the profile. *Salix, Empetrum nigrum* and *Vaccinium* pollen is recorded throughout the

period (≤4% each). Herb pollen and spores are present in small quantities in this zone (≤4% and ≤6% respectively). *Epilobium angustifolium* pollen occurs, whilst *Ulmus, Geranium* and Apiaceae pollen are not recorded in the profile after this time period. The relative abundance of Filicales and *Sphagnum* spores both fluctuate between 0.4% and 4%.

4.3.3. Zone 3 (1690 cal yr. BP –2014 AD)

PARs for all taxa remain low. Arboreal pollen continues to dominate the profile (84%-91%). *Pinus sylvestris* pollen exhibits lowest overall PAR (<500 grains cm^{-2} $year^{-1}$) and relative abundance (18-33%). *Betula pubescens* pollen shows higher values (30-52%) and PAR rates (500-1500 grains cm^{-2} $year^{-1}$) exceed those of *P. sylvestris*. *Picea abies* pollen appears in the profile from c. 800 cal. yr BP (≤1%). Shrub pollen relative abundance shows a slight increase, but remains between 6% and 11%. After an initial drop, *Betula nana* pollen exhibits a steady rise (3-9%) throughout this zone. *Empetrum nigrum* pollen proportion declines from 4% to 1% whilst *Salix* pollen abundance increases to 2%. Herb pollen drops below 1%, but regains values of 3%. The relative abundance of spores declines from 2% to 0.6%. *Sphagnum* spores exhibit the highest values (4%) whilst the proportion of Filicales spores remains consistently low (0.4-2%).

4.3.4. Zone 4: Modern moss polster (~2014-2018 AD)

The relative abundance of arboreal pollen is slightly higher (87-92%) in the modern moss polster compared to the underlying peat of Zone 3. *Pinus sylvestris* pollen abundance is also higher here (34-43%), and comparable to the abundance of *Betula pubescens* pollen (36-42%). *Picea abies* pollen is present throughout the moss at ≤1%. *Quercus* (0.5-2%) and *Alnus* (<0.4%) pollen retain low presence, *Tilia cordata* pollen is recorded again after an absence in Zone 3. Shrub pollen proportion is lower than in peat samples, and remains between 3-6%. Low relative abundances are recorded for *Betula nana* pollen (2-5%), *Empetrum nigrum* pollen (<1%) and *Salix* pollen (0.2-2%). Herb pollen abundance remains between 2-4%. Poaceae (1-2%) and Cyperaceae (≤2%) relative pollen proportions are higher than in underlying peat samples. *Aster, Filipendula, Rumex* and Ranunculaceae pollen are present, and Caryophyllaceae is

recorded again after being absent in Zone 3. Spores account for 0.5-3% of TLP. *Sphagnum* spores exhibit a lower relative abundance in the moss polster (0-1%), whereas the proportion of Filicales spores is slightly higher than in Zone 3 (up to 2%).

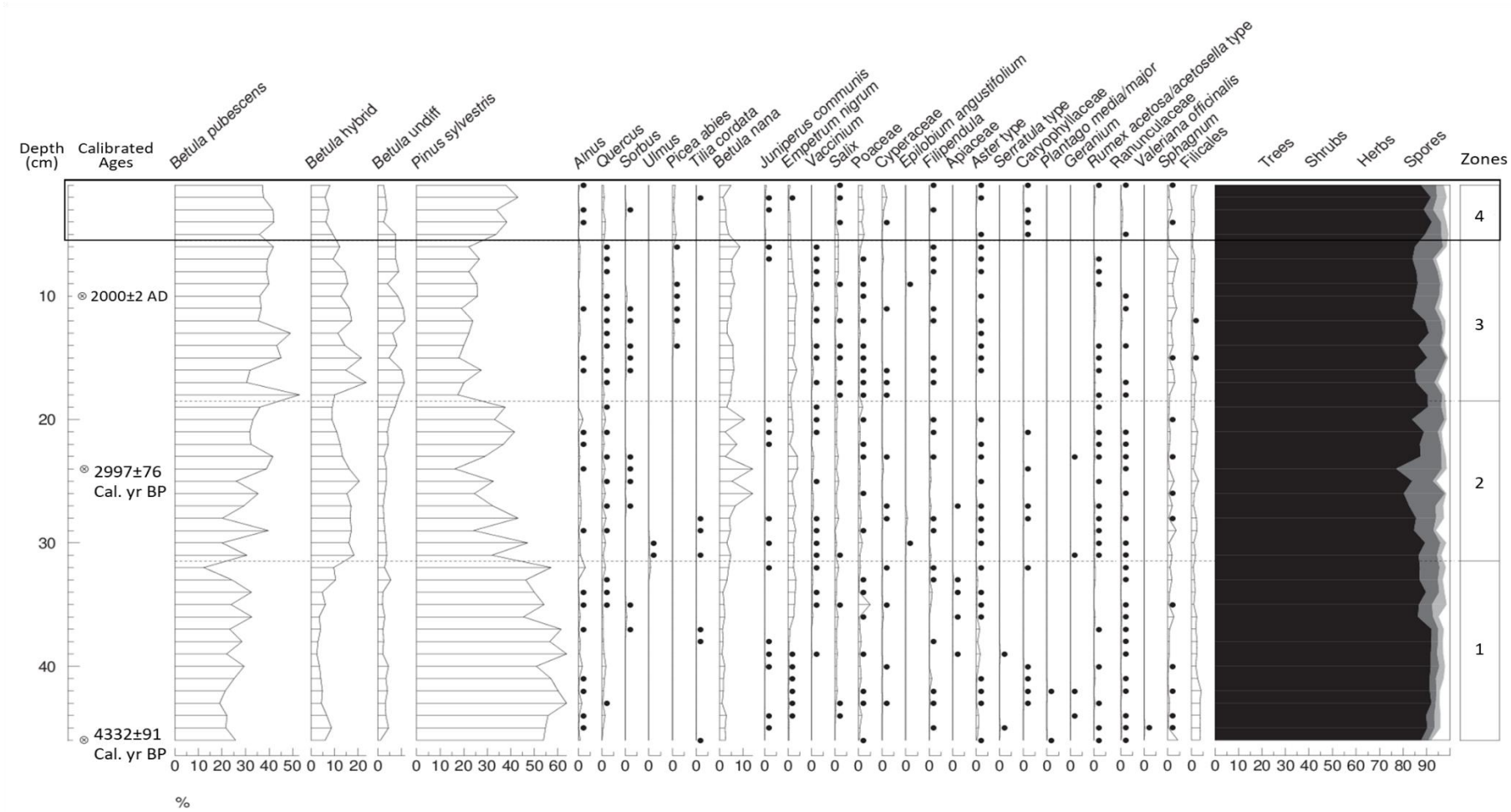

Figure 4.4. Pollen diagram summarising the relative abundance (%) of taxa throughout the peat core. Distinct zones in the pollen profile are separated by lines. The modern moss polster (top 5 cm) is indicated with a border. The ages (cal. yr BP) indicate departure from 2018 AD. Dots indicate the presence of pollen at ≤0.5%.

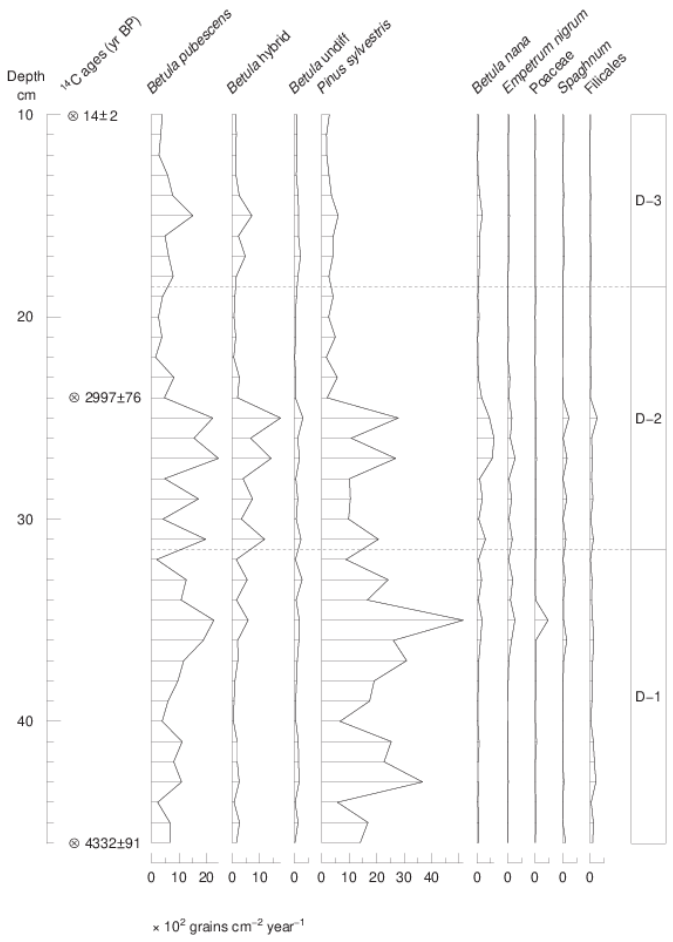

Figure 4.5. Pollen influx of select dominant taxa, illustrating the pollen accumulation rates between 46 and 10 cm of the peat core. The ages (cal. yr BP) indicate departure from 2018 AD.

4.4. Discussion

Comparison of present-day vegetation composition with pollen from moss polster and modern peat (2000-2018 AD) The relative abundance of *Betula pubescens* pollen in the modern (post-2000 AD) peat- and moss samples indicates the local dominance of the species (Table 4.2). *B. pubescens* is undoubtedly a dominant presence in the landscape today, and forms a belt between the mixed forest and the tundra, c. 200 m upslope from the coring site (Figure 4.1). There is a slight increase in *B. pubescens* pollen abundance between 2000-2014, which could be indicative of the increased abundance or maturation of the species in the area. The rapid warming over the past decades has increased the mean summer temperatures at the tree line by 2°C, and lengthened the growing season by 11 days compared to 1950s-1970s (NOAA, 2020; see Study site). Birch is highly sensitive to temperature fluctuations, because the

species grows quickly, reaches maturity early and has a short life span (Aas, 1969). The upslope advancement of *B. pubescens* in response to warming over the past decades has previously been recorded from aerial photographs in the area (Hallang et al., 2020). Whilst the climatic conditions today are favourable for tree growth at even higher altitudes above the tree line, the rapidity of the change has likely resulted in a lag in migratory response, as current species' compositions are often determined by the climate of previous decades (Klanderud and Birks, 2003). Additionally, the response is dependent on the availability of suitable substrate and habitat at higher altitudes for seedling recruitment.

The modern pollen abundance of *Pinus sylvestris* also accurately reflects local presence. *P. sylvestris* is less abundant around the mire compared to *B. pubescens*; the closest pine stand north of the mire is sparse, and the nearest dense woodland is c. 500 m downslope (Figure 4.1). There is also evidence of long-distance transported modern tree pollen of *Alnus, Quercus* and *Tilia cordata*, which likely originates from further down the valley, as they are not currently found near the sampling site. Whilst the presence of tree species is accurately estimated from the modern samples based on the threshold values in Table 4.2, the non-arboreal component of the surface moss sample contains some discrepancies. Despite the comparable presence of both *Betula nana* and *Salix* spp. on the surface of the mire around the coring site, *Salix* is under-represented in the moss sample with a mean of 0.5% in the moss (compared to 1.2% in the modern peat) whilst *B. nana* accounts for 3% and 6%, respectively. A similar under-representation of Salix pollen in 4 cm thick moss samples compared to adjacent pollen traps was observed in Lisitsyna and Hicks (2014).

The low presence of *Salix* pollen is unexpected, especially since for mire samples, the non-arboreal component of a pollen profile is often dominated by species from within a few metres of the sampling location, as mosses have the capacity to catch poorly distributed local pollen (Bunting, 2003). A strong correlation has previously been found in Jotunheimen (1150-1500 m a.s.l.) between the abundance of *Salix* in the dwarf-shrub vegetation assemblage and the frequency of *Salix* pollen in the pollen spectra (Caseldine, 1989). However, *Salix* pollen is present throughout the 4000-year peat sequence in comparably small quantities (≤1.6%). Due to the close proximity of the tree line, it is possible that the arboreal component dominates the pollen profile so

heavily that it masks non-arboreal species in the profile, suggesting that even the smallest signal of *Salix* pollen could indicate local presence of the species.

Additionally, the previously reported encroachment of shrubs affecting the higher elevations of Galdhøpiggen (≥1550 m a.s.l.) in response to warming in the recent decades (Hallang et al., 2020) is not evident from the modern peat- and moss samples. The shrub cover near the coring site has likely not changed significantly in the past 14 years, and samples from the mire at 1000 m a.s.l. are not reflecting the changes at higher elevations.

Several species that are considered indicative of certain environmental conditions are present in this zone. Previous studies conducted in Jotunheimen demonstrate strong correlations between the abundance of indicator taxa in tundra vegetation and their representation in the pollen spectrum (Pardoe 2006, 2014). Local non-arboreal taxa that produce little amounts of pollen, such as *Empetrum* and *Salix*, were found to be accurate indicators of the composition of local alpine plant communities above the treeline. Kuoppamaa et al. (2009) listed a number of taxa that are linked to disturbance from land-use change in northern Fennoscandia; the following also appear in our pollen profile: *Epilobium, Filipendula, Plantago major, Ranunculus acris*-type and *Rumex acetosa/acetosella*. In Table 4.1, we have compiled a list of pioneer species and species characteristic of mature vegetation assemblages on Galdhøpiggen today.

The species dominating the pollen spectra in this zone are largely characteristic of the present-day sub-alpine vegetation belt (Table 4.1). Several open-ground and disturbance indicators, such as *Rumex acetosa/acetosella* type and *Filipendula* (Kuoppamaa et al., 2009) are also present. The most likely Ranunculaceae species in the area is *Ranunculus acris*, whilst the common Caryophyllaceae species is *Silene dioica*; both occur in the 'tall herb' communities in the sub-alpine belt, and extend into the low-alpine belt (John Matthews, 2021, personal communication). The pollen of both families is found in the moss polster. Poaceae pollen is represented in the moss polster in higher quantities than throughout most of the sequence; the common local Poaceae species is the alpine meadow-grass (*Poa alpina*), another light-demanding pioneer species. The vegetation near the mire was recently disturbed in 2004, when the road leading up the slope was asphalted, creating roadside verges suitable for colonisation by pioneers (Matthews et al., 2018). However, no major disturbance

events in the surrounding landscape, such as clearing of the woodland or wildfires, have occurred in the period 2000-2018, and no disturbance indicator is represented by unusually high amounts of pollen in this zone.

4.4.2. Mid-Holocene pine-dominated mixed woodland (c. 4300-3400 cal. yr BP)

The altitude of the present-day tree line on Galdhøpiggen was covered by a local pine-birch woodland between c. 4300-3400 cal. yr BP. The relative abundance of pine pollen for most of the period exceeds the contemporary values by 50%, and indicates local dominance. PARs are up to 10 times higher than estimated for 2000 AD and indicate a dense pine forest (Table 4.2). This suggests relatively warm summer temperatures (likely exceeding contemporary values) at this altitude suitable for abundant pine growth, and the advancement of the pine tree line. Aas and Faarlund (1988) suggest that that pine tree lines were 200 m higher (at 1200 m a.s.l.) in Jotunheimen between (5000-2500 cal. yr BP), and c. 150 m higher than today towards the end of this period.

Further, past climatic reconstructions of the area have indicated a decrease in glacial extent between c. 4000-3000 cal. yr BP (Matthews and Dresser, 2008), and models suggest increased mean annual ground- and surface temperatures at higher altitudes on Galdhøpiggen (up to 1458 m a.s.l.) that remain above 0°C during this period (Lilleøren et al., 2012; Winkler et al., 2021). Higher temperatures, supported by the high relative abundance and PAR of pine pollen, certainly would have influenced the extent of regional permafrost. Combining the evidence from our pollen study with wider literature, we assume that the lower limit of permafrost reached above 1500 m a.s.l. (Figure 4.7).

Whilst *B. pubescens* also appears locally present at 1000 m a.s.l., the relative abundance of its pollen remains below the present-day values (2000-2014 AD) throughout (Figure 4.6). PAR, however, exceeds the modern (2000 AD) value during most of this period (Table 4.2). The lower relative abundance values could be due to the substantial dominance of pine pollen in the profile, as PARs suggest a more abundant birch presence. Moreover, a study combining pollen data with macrofossil evidence suggests that a subalpine birch zone has prevailed above the pine tree line

during the period 9000-2500 cal. yr BP, and despite the advanced pine tree lines, pine did not represent the upper forest limit at any point during this time (Aas and Faarlund, 1988). It is difficult to determine whether downy birch reached above the pine tree line on Galdhøpiggen during this period without incorporating macrofossil evidence, but birch was most likely a component of the pine-dominated mixed woodland at 1000 m a.s.l.

A woodland presence is further supported by the highest relative abundance of shade preferring Filicales spores (Kuoppamaa et al., 2009). The only common Filicales species at this altitude today is *Gymnocarpium dryopteris,* a fern that prefers shady north-facing slopes and forms a continuous carpet under birch trees (Matthews et al., 2018). The pollen of *Geranium*, which is commonly found in the understorey today, is also present. Other trees were absent from the woodland at this altitude, with *Alnus* pollen being regional, and *Quercus* and *Tilia cordata* pollen derived via long-distance transport (Lisitsyna et al., 2011).

However, several disturbance- and open ground indicating species are also present throughout this period. *Plantago media/major* occurs exclusively during this period, whilst Asteraceae, *Filipendula* and *Rumex acetosa/acetosella* type exhibit their highest relative abundances in the pollen profile, and Poaceae peaks in this zone. Several light-demanding Asteraceae species grow in the sub-alpine and low alpine belts today, including *Hieracium* spp., *Achillea millefolium*, *Solidago virgaurea* and *Gnaphalium norvegicum*. It is also notable that from around 3700 cal. yr BP, there is an increase in light-demanding shrub pollen (*Betula nana, Empetrum nigrum, Vaccinium* spp. and *Salix* spp.) (Robbins and Matthews, 2014). Whilst the shrub pollen might have originated from the surface mire vegetation, the high relative abundance of light-demanding herb pollen suggests that the mixed woodland may not have been as dense as indicated by pine PARs. Overall, the species present during this period are comparable to the mature vegetation assemblages of the present-day sub-alpine belt on Galdhøpiggen (Table 4.1).

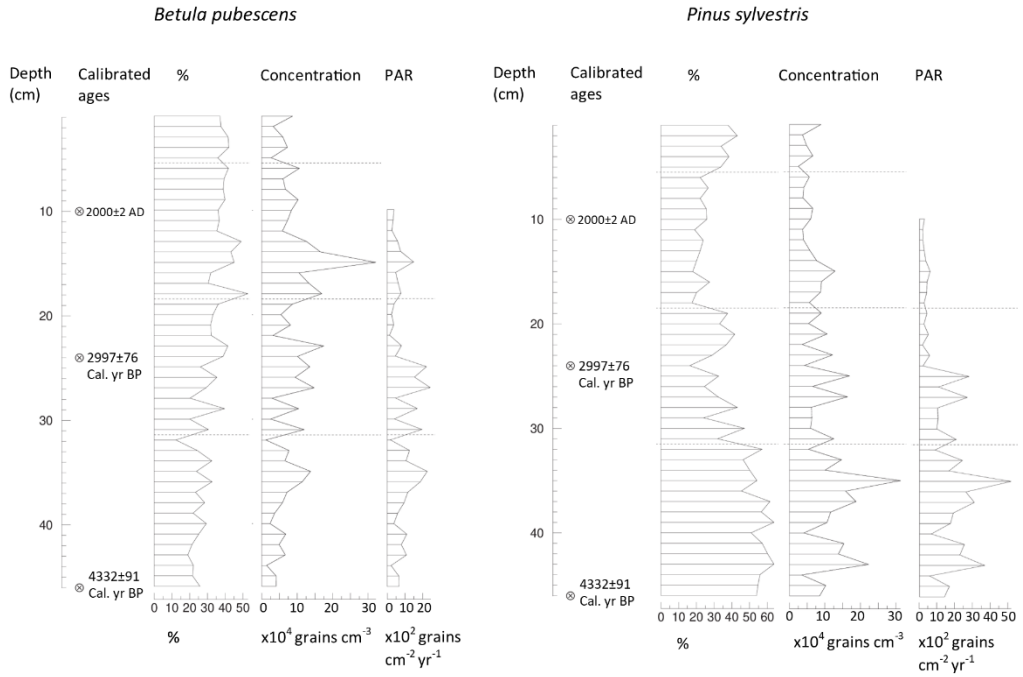

Figure 4.6. Relative abundance (%), concentration and pollen accumulation rates (PAR) of downy birch (*Betula pubescens*) and Scots pine (*Pinus sylvestris*).

4.4.3. Pine retreat and descent of the low-alpine belt (c. 3400 – 1700 cal. yr BP)

The progressive decline in relative abundance and PAR of pine pollen between c. 4330-3000 cal. yr BP coincides with the gradual decline in modelled temperatures in southern Norway. Modelled July temperatures were 1°C higher in 4500 cal. yr BP compared to present day (1961-1990 mean) values; by c. 3000 cal. yr BP, the temperatures had declined and resembled present-day values (Lilleøren et al., 2012). The heat flow model by Lilleøren et al. (2012) is based on studies examining pollen, macrofossils and chironomids from lake sediments, as well as the deposition rate of speleothems in Scandinavia, and the model is calibrated using modern borehole temperatures, including those recorded on Galdhøpiggen. Climatic cooling during this period is also suggested by the concurrent increase in downy birch pollen at the expense of pine. Relative pollen abundance indicates local dominance and PARs are indicative of open birch woodland for most of this period, suggesting that the conditions became cooler (and possibly wetter), which benefits birch rather than pine.

By c. 3000 cal. yr BP, pine pollen reaches its lowest relative abundance in the entire profile, coinciding with the decline of total arboreal pollen to its lowest level. Relative abundance and PAR suggest that pine was not present within one kilometre of the coring site at the time, whilst downy birch retains local dominance. Simultaneously, shrubs collectively reach their highest relative abundance in the entire sequence, suggesting that the landscape at 1000 m a.s.l. was becoming more open.

The synchronous increase in light-demanding species that characterise present-day low- and mid-alpine vegetation belts, such as *Betula nana, Empetrum*, *Vaccinium* spp., and *Salix* spp. Could indicate a possible descent of the low-alpine vegetation belt in response to colder temperatures. The timing of the pine retreat and shrub encroachment corresponds to a cold period of glacial expansion (Smørstabbtindan IV, 17 km from our site) between 3200-2550 cal. yr BP (Matthews and Dresser, 2008); and a drop in modelled ground temperatures on Galdhøpiggen by 0.2°C in the low alpine belt, and by 0.5°C in the mid-alpine belt between 4000 and 3000 cal. yr BP (Lilleøren et al., 2012). Moreover, Bjune (2005) reported a decline in arboreal pollen and the opening of the landscape at 1309 m a.s.l. due to cooler conditions in E Jotunheimen between 4950-2700 cal. yr BP.

All shrubs in our profile exhibit relative pollen abundance values that exceed the modern-day values, illustrating a scenario where the sampling site was covered by denser stands of dwarf shrubs at the expense of trees. Furthermore, *Epilobium angustifolium*, a light-preferring species often occurring on sites following disturbance such as windthrow of trees or vegetation dieback due to drought (Myerscough, 1980), appears in the profile at c. 3300 cal. yr BP in small quantities (0.7%). Other disturbance indicators, such as *Rumex acetosa/acetosella* type, Ranunculaceae, Caryophyllaceae (likely *Silene dioica*) and Asteraceae are also present. Simultaneously, the proportion of shade preferring Filicales spores remains low.

The pollen diagram (Figure 4.4) indicates signs of climatic warming between 2800-1900 cal. yr BP, as the relative abundance of arboreal pollen begins to recover whilst the proportion of shrub pollen declines. The relative abundances of pine- and downy birch pollen indicate local presence of pine and birch dominance. However, the PARs of pine and downy birch remain low between 2500-1700 cal. yr BP, indicating a merely sparse local presence. This could be due to the increase in cooler and more

humid periods from 2500 cal. yr BP to present, resulting in depressed tree lines and low pollen production (Aas and Faarlund, 1988). Matthews and Dresser (2008) identified numerous cold periods of glacial expansion in the area from c. 3000 cal. yr BP to present day, including between 2350-1700 cal. yr BP. Modelled July temperatures for southern Norway also decline further, remaining approximately 0.1-0.3°C lower than the 1961-1990 mean from 2000 cal. yr BP until c. 1900 AD (Lilleøren et al., 2012). Such conditions reflect a period suitable for permafrost aggradation and the possible depression of the limit of sporadic permafrost to altitudes lower than today (Figure 4.7). According to Lilleøren et al. (2012), however, the lower limit of permafrost on Galdhøpiggen never reached below 1200 m a.s.l. during the Holocene, suggesting that our coring site (1000 m a.s.l.) was free of permafrost throughout this period.

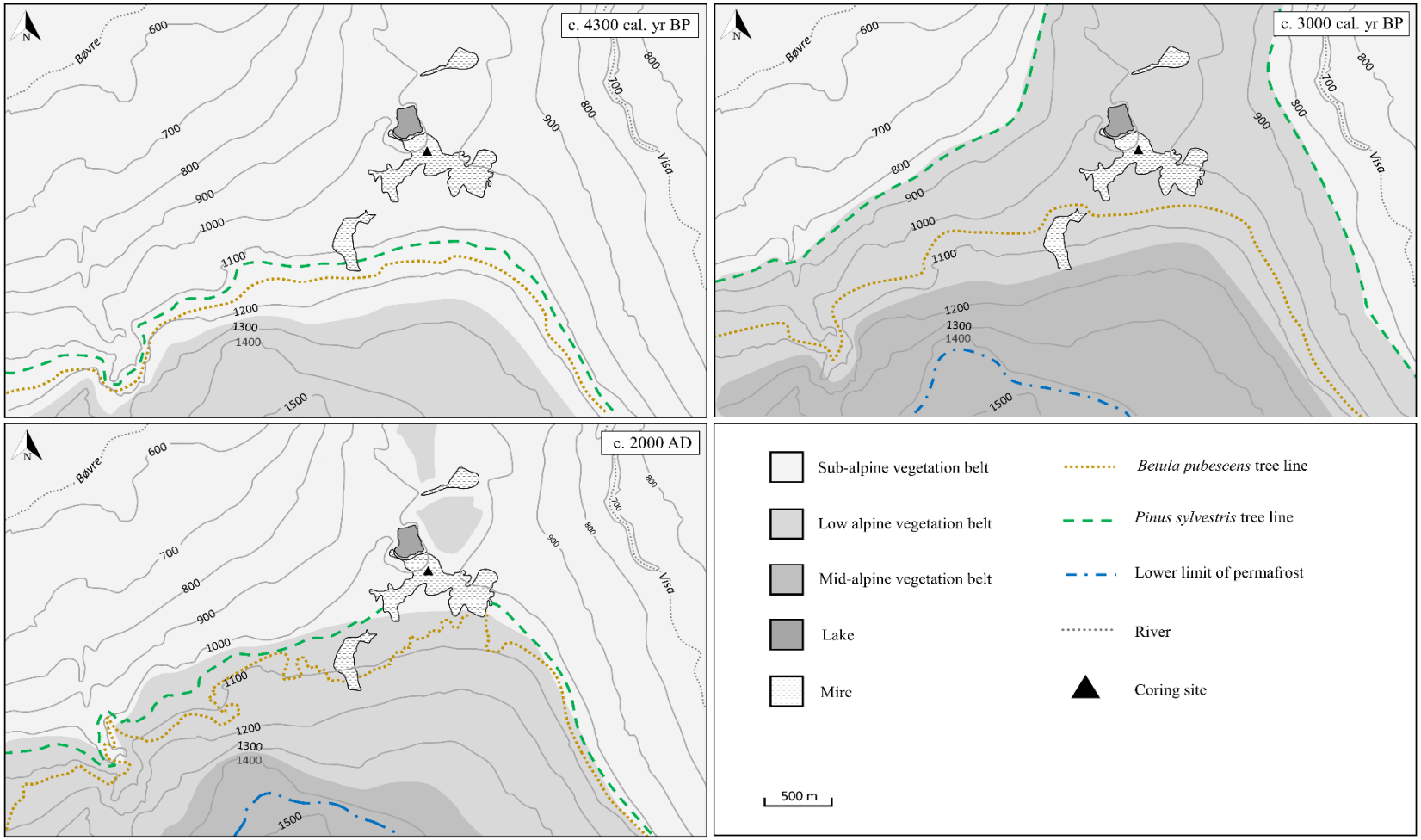

Figure 4.7. Schematic diagrams illustrating possible vegetation cover and permafrost limits at c. 4300 and 3000 cal. yr BP, and 2000 AD. Predictions are based on the relative abundance of pollen at these points in time. Note that the permafrost limit is higher than 600 m between 4350-3430 cal yr BP.

4.4.4. Pine decline and the establishment of birch-dominated open woodland (c. 1700 cal. yr BP- 2000 AD)

The topmost zone of the pollen profile covers c. 1700 years, and represents very low peat- and pollen accumulation rates. The relative pollen abundances of the main arboreal species indicate that from 1700 cal. yr BP to 2000 AD, downy birch was locally dominant, whilst pine fluctuated close to the threshold of local presence, remaining regionally present throughout most of this period (Table 4.2). Relative pollen abundances describe the local arboreal composition in 2000 AD accurately, demonstrating that pine was locally present (26%) and downy birch dominated (36%). PARs, however, are low for both species, fluctuating around the threshold value for sparse presence, and suggest that neither was present within 1-km radius from c. 600 cal. yr BP to 2000 AD. This is clearly an underestimation, as downy birch was locally established in the 1980s, and pine was growing c. 200 m from the coring site by 2000 AD (Hallang et al., 2020). Therefore, the relative abundance of downy birch and pine pollen can be considered as the more accurate indicator of local presence during this period.

The discrepancy between PARs and evidence from the area could indicate that the PARs in the top half of the core are not reliable, and their accuracy might be improved by incorporating more radiocarbon dates. Alternatively, the underestimation of arboreal PARs in the recent millennia could be caused by retreated tree lines and lower pollen production due to continuing cooler temperatures. Based on the consistently low relative abundance of pine pollen, the pine tree line was likely lower than today between c. 1700-170 cal. yr BP, whilst the climatic conditions remained more suitable for downy birch growth at 1000 m a.s.l. This scenario is in accordance with two longer periods of glacial expansion between 1400-750 and 500-0 cal. yr BP (Matthews and Dresser, 2008). The latest cold period also covers the Little Ice Age (LIA), a cold period between c. 1300-1850 AD (Grove, 2004). LIA peaked around 1750 AD to the end of the 19th century in southern Norway (Lilleøren et al., 2012). Lowest simulated ground temperatures occurred c. 250 years BP, and the lower limit of shallow permafrost is estimated to have reached as low as 1250 m a.s.l. (Lilleøren et al., 2012). Unfortunately, due to the coarse resolution of our pollen profile caused by low peat

accumulation rates, the effects of the LIA are not detectable. However, our results indicate that 1700-170 cal. yr BP was likely a cold period with a low altitudinal pine tree line and a possibly depressed permafrost limit.

Non-arboreal pollen also signals a more open landscape from 1690 cal. yr BP. The pollen of shrub species indicative of dwarf shrub tundra retains high values from 1690 cal. yr BP to 2000 AD. Light-demanding *Betula nana* is the dominant shrub in the landscape, and *Salix, Empetrum* and *Vaccinium* are present throughout. Disturbance-indicating herbaceous species and pioneers, such as Asteraceae, *Filipendula,* Ranunculaceae, Poaceae and *Rumex acetosa/acetosella* type are represented throughout by small quantities of pollen, and *Epilobium angustifolium* is briefly found again at c. 2003 AD. However, none of the disturbance indicator species show significant peaks in the pollen profile at any time. Therefore, in this case, it is difficult to confidently identify significant periods of increased disturbance based on the indicator species alone.

From c. 100 cal. yr BP, climatic conditions became warmer. Hipp et al. (2012) estimated that the lower limit of permafrost on Galdhøpiggen has moved up by 200 m since 1860. In south-east Norway, birch tree lines advanced by 40 m between 1918 and 1969 (Aas, 1969), and an increase in tundra species richness at altitudes between 1600–1800 m a.s.l. on Galdhøpiggen has been recorded between 1930 and 1998 (Klanderud and Birks, 2003). By 2000 AD, pine had established its altitudinal limit at 1000 m a.s.l. alongside downy birch. It is also notable that *Picea abies* pollen appears in the profile at around 800 cal. yr BP, several hundred years later than estimated in other pollen studies in the area (e.g., Barnett et al., 2001), but remains "regional" up to the present day (Table 4.2). The closest spruce stands are currently c. 2 km from the site, growing at an altitude 200 m lower than the tree line.

4.5. Conclusions

The late-Holocene vegetation dynamics on the slope of Galdhøpiggen were reconstructed by employing a combination of indicators of species′ local presence. From c. 4350 cal. yr BP until present, the area around 1000 m a.s.l. has been dominated by two arboreal species, *Betula pubescens* and *Pinus sylvestris*. Between c. 4300 and 3400 cal. yr BP, the area was covered by a pine-dominated mixed woodland,

suggesting that the climatic conditions were warmer than today. The lower limit of permafrost was likely above 1500 m a.s.l. From c. 3400-3000 cal. yr BP, pine began retreating to lower elevations, accompanied by the descent of the low-alpine shrub-dominated vegetation belt in response to climatic cooling. This was a period of colder temperatures and permafrost aggradation. The colder period continued through 1700 – 170 cal. yr BP, as pine retained a sparse presence, and an open downy birch woodland dominated the landscape at this altitude. The lower limit of permafrost likely reached lower altitudes than today. From c. 170 cal. yr BP onwards, the conditions became warmer, and pine had re-established its local presence at 1000 m a.s.l. by 2000 AD. Downy birch remained locally present throughout this period, and the lower limit of permafrost moved upslope to its present-day altitude of 1450 m a.s.l.

The complementing techniques used to determine the local presence of species here (relative pollen abundance, PAR, and indicator species) can sometimes produce conflicting results, especially when the profile is heavily dominated by arboreal pollen. Therefore, the combined use of several methods still requires an appreciation of the strengths and weaknesses of the individual methods.

Chapter 5

Permafrost, thermal conditions, and vegetation patterns since the mid-20th century: a remote sensing approach applied to Jotunheimen, Norway

Co-authors: Los SO, Hiemstra JF

This paper is under review for publication at the journal
Progress in Physical Geography.

Abstract

Northern high alpine regions are currently experiencing rapid warming, which often results in the degradation of sub-surface permafrost and the upslope advancement of vegetation. The present study combines remotely sensed MODIS Land Surface Temperatures (LSTs) and the Normalised Difference Vegetation Index (NDVI) with observed air temperatures to model the thermal and vegetational dynamics in NE Jotunheimen (Norway) for the period 1957-2019. An altitudinal transect on the north-facing slope of Galdhøpiggen was used for ground truthing. Model predictions indicate a substantial warming trend since the late 1950s, accompanied by increased NDVI. The spatial and temporal patterns of observed change were not uniform. Winter surface temperatures increased most rapidly, by 2.4-2.8°C at mid- and low altitudes (600-1500 m a.s.l.). The highest increases in NDVI (by ~0.1) were detected during the growing season (April-September) and over the mid-range altitudes (1050-1500 m a.s.l.), i.e., above the tree line on Galdhøpiggen. We attribute this to increased shrubification at these altitudes. Our results confirm that the surface temperatures near the previously estimated lower altitudinal limit of permafrost (~1450 m a.s.l.) have continued to increase during the past decade, likely facilitating further permafrost degradation. Finally, we demonstrate that mapping remotely sensed mean growing season LSTs below 0°C can be used to identify areas suitable for continuous sub-surface permafrost, and mean June-September LSTs above 7°C can detect areas suitable for tree (*Betula pubescens*) growth in NE Jotunheimen.

5.1. Introduction

Alpine tundra biomes are highly vulnerable to climatic changes, as increasing air temperatures drive the degradation of sub-surface permafrost and lead to associated shifts in aboveground vegetation patterns. The sensitivity of high mountain areas is rightly receiving attention because their warming rate is currently thought to outpace the global warming rate, in some cases by as much as 50% (Hock et al., 2019). Recent increases in ground temperature in mountain permafrost regions across the globe have been established at nearly 0.2 °C per decade (Biskaborn et al., 2019), whilst the rate at which tree lines shift upslope could be in the order of metres per year (Cazzolla Gatti et al., 2019). This response is observed in both trees and shrubs, as the conditions for growth become more favourable at higher altitudes (Dial et al., 2007; Hallinger et al., 2010; Myers-Smith et al., 2011). Such substantial changes in vegetation patterns across alpine tundra ecosystems can have wider ecological consequences. Increased vegetation cover at higher altitudes is likely to result in reduced surface albedo, which in turn intensifies surface heating of alpine areas through increased absorption of solar radiation (Chapin et al., 2005; Pearson et al., 2013). Furthermore, increased vegetation cover is expected to alter local and regional carbon cycles, potentially creating a positive feedback to climate warming (Cahoon et al., 2012; Frost et al., 2019; Post et al., 2009).

Significant increases in air-, ground- and ground surface temperatures have also been recorded over the past decades in the mountainous Jotunheimen region in southern Norway (Etzelmüller et al., 2020; Farbrot et al., 2011). *In-situ* geophysical and thermal monitoring methods have been used extensively to document and reconstruct the present and past states of mountain permafrost in parts of Jotunheimen (e.g., Hauck et al., 2004; Isaksen et al., 2007, 2011; Ødegård et al., 1996), and models have been used to suggest that the extent of permafrost will continue to decrease (Hipp et al., 2012). In addition, detailed field-based vegetation surveys have been conducted across bioclimatic gradients to study patterns of succession (Matthews et al., 2018; Robbins and Matthews, 2010, 2014), and evidence has been found to indicate shrubification and the upslope advancement of the tree line on the slope of Galdhøpiggen, the highest peak in Jotunheimen, over the past four decades (Hallang et al., 2020).

Galdhøpiggen and the surrounding area of Jotunheimen offer an excellent opportunity to further investigate the distribution and the thermal state of mountain permafrost and vegetation patterns, and to better understand how alpine tundra biomes respond to climatic changes (Etzelmüller et al., 2020; Myers-Smith et al., 2020). In this study, we build on aforementioned local field studies (e.g., Hallang et al., 2020; Hipp et al., 2012; Matthews et al., 2018) and employ remote sensing techniques with the main objective to temporally and spatially up-scale such observations and measurements and acquire easily accessible and useful data on a regional scale. Whilst detailed, *in-situ* methods for recording and monitoring alpine ground (surface) temperatures and vegetation dynamics remain indispensable, they are obviously labour-intensive, logistically complicated due to reduced access to remote sites, and expensive over longer temporal and spatial scales (Hachem et al., 2009), which led us to the use of satellite imagery.

Satellite remote sensing provides an inexpensive, easily accessed alternative to map and monitor vegetational trends and surface temperatures over large spatial and temporal scales. Here, we use the satellite-derived Land Surface Temperatures (LST) and the Normalised Difference Vegetation Index (NDVI) values as indicators of ground thermal conditions and 'greenness' (i.e., vegetation cover) across ascending altitudes in Jotunheimen. Observed LSTs over the past two decades are first combined with observed air temperatures from a regional meteorological station to model the satellite data back to the 1950s. A relationship is then formed between LSTs and observed NDVI, which allows us to model the NDVI back 62 years as well.

This approach is able to capture and identify seasonal, inter-annual and decadal changes in thermal and vegetational trends over a wider spatial scale, and contributes to the existing field-based research conducted in the region. Using a well-studied altitudinal transect on Galdhøpiggen for reference, we aim to identify the altitudes and vegetation belts that have been most vulnerable to surface warming or experienced the greatest change in vegetation cover in the study area.

This paper thus aims (i) to describe the thermal and vegetational dynamics in NE Jotunheimen over the past six decades by using satellite-derived data, (ii) to investigate spatial differences in the rate of change across altitudes to identify areas most susceptible to change and (iii) to test the applicability of growing season LSTs to map areas suitable for permafrost presence and tree growth in a mountainous region.

5.2. Study site

The study area (Figure 5.1) covers approximately 3780 km^2 of the mountainous NE Jotunheimen, Norway between the latitudes of 61°25'N and 61°99'N and longitudes of 7°91'E and 8°70'E. The area encompasses several valleys (as low-lying as 60 m a.s.l.) and massifs, including the two highest peaks in northern Europe, Galdhøpiggen (2469 m a.s.l) and Glittertind (2465 m a.s.l.).

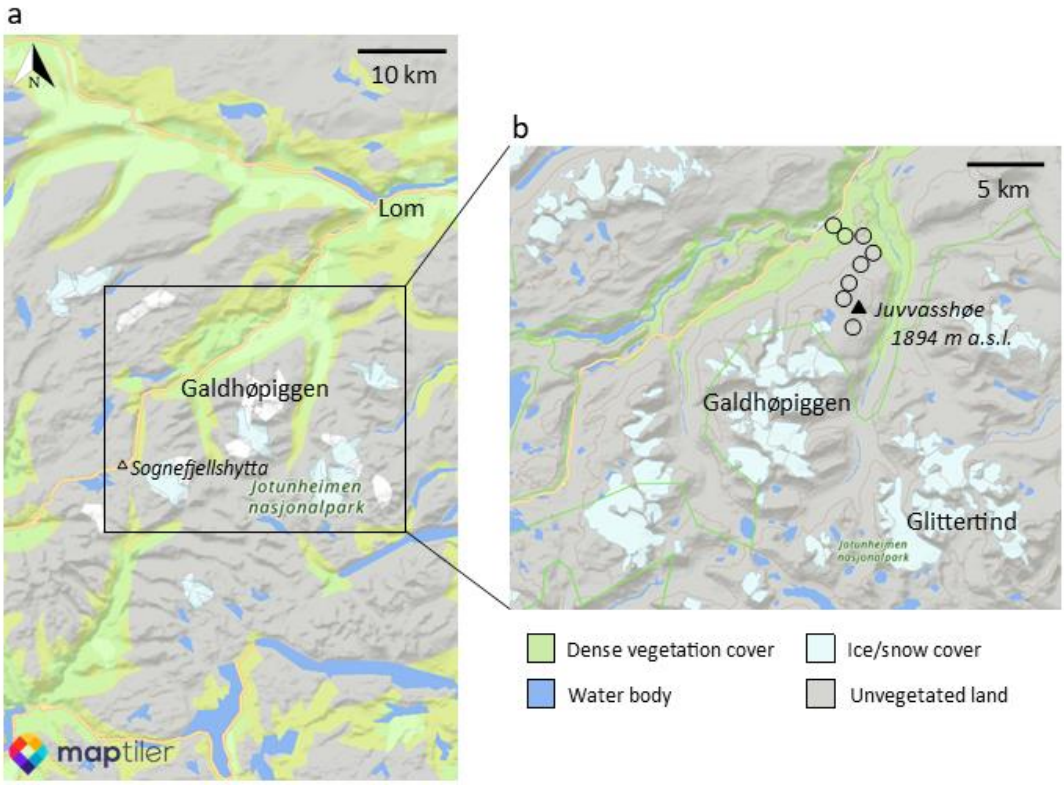

Figure 5.1. (a) A map of the full extent of the study area in Jotunheimen, Norway, (b) close-up of Galdhøpiggen. Circles represent a north to south altitudinal transect from 600 m a.s.l. to 1950 m a.s.l. Maps reproduced and modified with permission from MapTiler (2021).

Due to the large variation in elevations across the study area, climatic conditions vary considerably. The mean annual air temperatures (MAAT) for the normal period of 1961-1990 range from 0-4 °C in the valleys in the north (c. 400 m a.s.l.) to below -6 °C at higher elevations (≥1600 m a.s.l.) (Norwegian Meteorological Institute, 2021).

Southern Norway is influenced by mild air flows from the Atlantic Ocean, which ensures that temperatures below -30°C, even at higher elevations, are rare (Farbrot et al., 2011). The annual precipitation for the same period ranges from 500-700 mm in the valleys to 1500-2000 mm at high elevations such as Galdhøpiggen.

The vegetation at lower altitudes in the study area is dominated by a mixed woodland consisting of Scots pine (*Pinus sylvestris*), downy birch (*Betula pubescens*) and spruce (*Picea abies*), and the valleys are dominated by agricultural land and fields. The present-day tree line across the area is at c. 1050 m a.s.l. and higher altitudes can be divided into low-, mid- and high alpine vegetation belts (Matthews et al., 2018). Common species in the low-alpine belt include dwarf shrubs willow (*Salix* spp.), dwarf birch (*Betula nana*) and bilberry (*Vaccinium myrtillus*). The mid-alpine belt is dominated by grasses (*Carex bigelowii*) and occasional shrubs (*Empetrum nigrum*), whilst the high-alpine belt is sparsely vegetated, with isolated patches of grasses (e.g., *Poa alpina*) and forbs (e.g., *Ranunculus glacialis*).

5.3. Methodology

5.3.1. Data acquisition

Land Surface Temperature (LST) data for the study area were derived from the Moderate Resolution Imaging Spectrometer (MODIS) aboard NASA's Aqua satellite (MYD21A1D and MYD21A1N products, version 6.0; Hulley et al., 2016). The dataset comprises 8-day composites of night-time and day-time spatial measurements of land surface temperatures at 1 km resolution, covering the period January 2003 - December 2019.

MODIS Normalised Difference Vegetation Index (NDVI) data were obtained for the same area for the period January 2001 – December 2017. The data consist of 16-day composites of spatial estimates of NDVI values at 250 m resolution (MYD13A3 product, version 6.0; Didan et al., 2015). NDVI is the normalised difference ratio between the red reflectance (MODIS band 1) and near infrared (NIR) reflectance (MODIS band 2) and is calculated for every pixel as follows:

$$NDVI = \frac{(NIR - red)}{(NIR + red)}$$

Meteorological records for three nearby stations, Brata-Slettom (61°90' N 7°90' E, 664 m a.s.l.), Fokstua (62°11'N 9°28'E, 952 m a.s.l.) and Sognefjellshytta (61°60'N 7°99'E, 1413 m a.s.l.), were accessed through the Global Historical Climate Network (NOAA, 2020).

Fokstua meteorological station provided the most consistent record of daily resolution air temperature data from 1957 to present. To match the meteorological and the LST data, 8-day average maximum (T_{max}), minimum (T_{min}) and daily mean (T_{day}) air temperatures were calculated for the period 1957-2019. Any missing values in the Fokstua dataset were approximated by using the data from either Sognefjellhytta or Brata-Slettom stations and applying a temperature lapse rate of 0.42°C/100 m (Isaksen et al., 2002). The same temperature lapse rate was also used to estimate air temperatures at various altitudes on Galdhøpiggen, based on the meteorological data from Fokstua station.

To investigate seasonal trends, each year was divided into two seasons. The 'growing season' is defined here as the period between 1 April and 30 September, and 'winter' covers the period between 1 October and 31 March. Growing season LST (LST_{gs}) and NDVI ($NDVI_{gs}$) refer to the mean April-September temperature- and NDVI values at the pixel level.

All processing of MODIS data, satellite image analysis and statistical analysis were performed in R 4.0.3 (R Core Team 2020). Packages 'raster' and 'fields' were used in the image analysis (Hijmans et al., 2012; Nychka et al., 2017). The code used for analysis is outlined in Appendix iii.

5.3.2. Prediction of missing values in satellite data

Cloud cover in the satellite imagery resulted in a total of 23% of day-time LST data and 8% of night-time LST data being missing. Missing pixel values from used imagery were estimated using the R package 'gapfill', which follows the protocol described in Gerber et al. (2018). Gapfill uses both spatial coherence and temporal seasonal regularity to 'predict' missing values in spatio-temporal satellite datasets.

The method operates by selecting subsets of data surrounding the missing points, ranking the images within subsets using a scoring algorithm and predicting the missing values through quantile regression (see Gerber et al., 2018).

The accuracy of the 'gapfill' method was tested in an experiment in which we used a mask to remove a number of randomly distributed pixels with observed values from the original day-time and night-time datasets to generate two artificial datasets. Specifically, we removed 138 pixel values from every sixth image. The prediction process was repeated, and the Root Mean Squared Error (RMSE) was returned for both sets of data to approximate the prediction accuracy. We found RMSE values of 2.62 and 2.42 for day-time data and night-time data, respectively.

5.3.3. Estimation of LSTs from air temperature records

Pixel-level linear regression was performed between the gap-filled satellite-derived mean daily LST data and the measured mean daily air temperature data (T_{day}) from the three meteorological stations for the period 2003-2019. Daily mean LSTs were calculated by averaging the day-time and night-time observation values for each pixel. Separate pixel-level regressions were employed for day-time satellite images and T_{max}, as well as night-time images and T_{min}. Correlation coefficients were plotted for individual pixels in the entire study area (Figure 5.2). It is evident that the highest correlations were found in low- and mid-altitude areas, whereas the lowest correlations can be detected over lakes and mountain peaks.

Employing the mean daily (T_{day}) air temperature records from Fokstua meteorological station that extend back to 1957, another pixel-level regression was developed to predict the surface temperature as a function of meteorological data. The output comprised a total of 2898 1-km resolution maps of mean daily LSTs covering the period 1957-2019. The analysis was replicated with T_{max} and T_{min} to obtain day-time and night-time LST datasets.

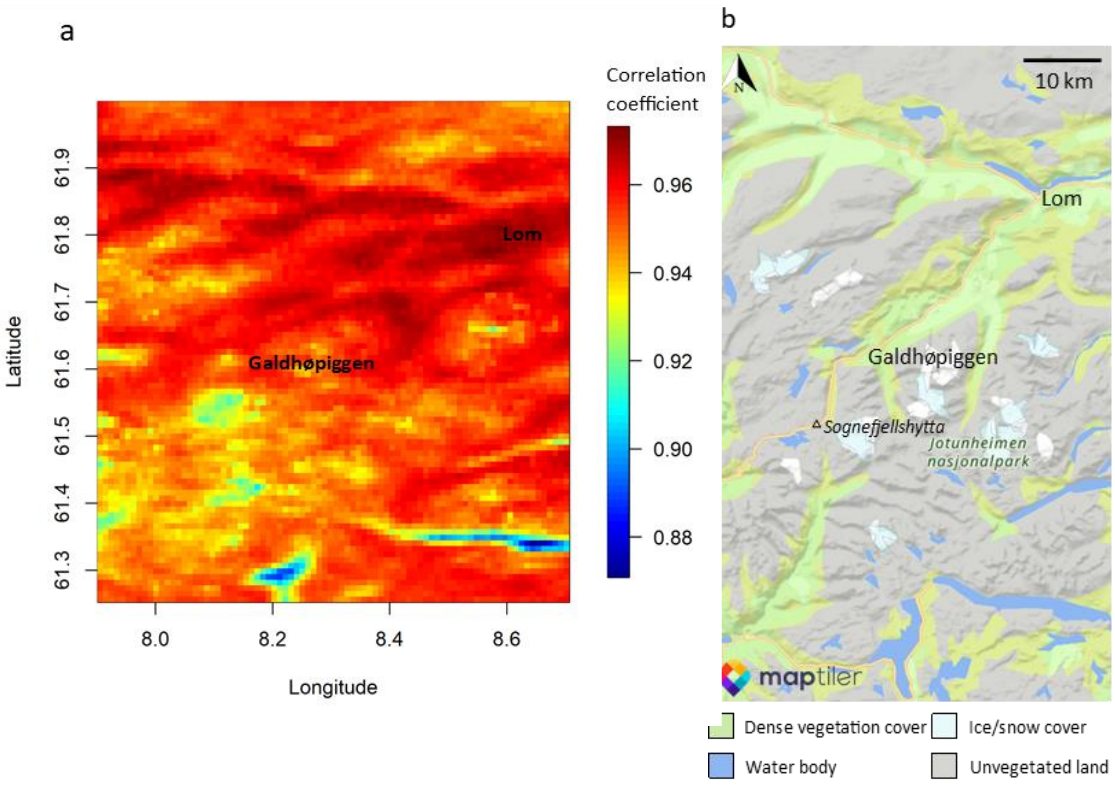

Figure 5.2. (a) Correlation coefficients (indicated by colour) between mean daily land surface temperature values and fitted values plotted for each pixel of the study area. The highest correlation is found in the valleys (>0.96), lowest over large water bodies (<0.88). (b) A map of the study area for reference.

5.3.4. Estimation of NDVI from LSTs

The correlation between mean annual LSTs and mean annual NDVI for the period 2003-2017 was low (only 5.3% of all pixels showing a statistically significant correlation) but the correlation between mean LST_{gs} and $NDVI_{gs}$ was considerably higher (38% of all pixels showing a significant correlation), which led us to using the growing season data for further analysis. This also ensured that the analysis is focused on the relationship between NDVI and vegetation instead of exploiting the relationship between NDVI and snow cover. Moreover, the NDVI in northern middle- and high latitudes is more strongly related to temperature rather than precipitation (Ji and Fan, 2019; Los et al., 2001; Tucker et al., 2001), which is why our main focus here is on the NDVI-temperature relationship.

Instead of fitting a single linear regression to describe the relationship, we used segmented regression to estimate pixel-level NDVI from growing season land surface temperatures for the period 1957-2019. This takes into account the non-linear behaviour of the NDVI – temperature relationship in the higher and lower temperature ranges (Figure 5.3). However, it needs to be kept in mind that this model ignores the influence of human land management, e.g., the deforested plots of land used for farming in the valleys.

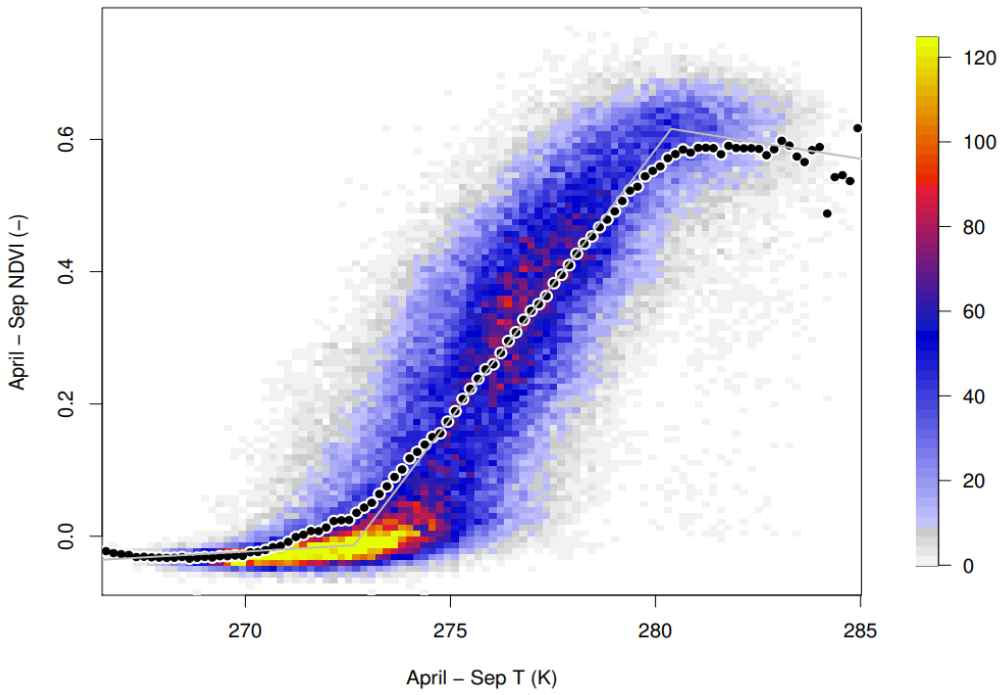

Figure 5.3. Density plot of the relationship between growing season (April-September) NDVI and land surface temperature (K) for the period 2004-2017 (n= 2,235,324). Colours indicate the number of occurrences of the NDVI - T relationship in an interval; dots show median values. Segmented regression (indicated by grey lines) was used to fit three lines to the curved relationship.

5.3.5. Altitudinal transect – ground truthing

To create a point of reference linking the satellite data to field conditions, we plotted an altitudinal transect consisting of 8 locations corresponding to individual pixels on the north-facing slope of Galdhøpiggen (see Figure 5.1). From north to south, the transect covers the mixed pine-birch woodland at 600 and 800 m a.s.l., the present-day tree line (1050 m a.s.l.), the present-day lower limit of permafrost (1450 m a.s.l.), the grass-heath dominated mid-alpine vegetation belt (1550 m a.s.l.) and the high-alpine belt with discontinuous vegetation cover at 1750, 1850 and 1950 m a.s.l. The

vegetation composition and permafrost distribution in this particular area, and particularly along this transect, are well known and outlined in numerous publications (e.g., Farbrot et al., 2011; Hallang et al., 2020; Hipp et al., 2012; Matthews et al., 2018). Therefore, the transect allows us to explore the spatial trends in satellite-derived LST and NDVI across altitudes whilst being familiar with the conditions on the ground.

Due to the large number of pixels covering the study area (n=7476), the significance values of the trends presented in results correspond to a pixel at 1050 m a.s.l. on the Galdhøpiggen transect. However, all trends were plotted for a minimum of 30 pixels across the study area to ensure that the pixel at 1050 m a.s.l. is representative of the trend.

5.4. Results

During the observation period 2003-2019, we found no statistically significant trend in the observed daily average (p=0.8), day-time (p=0.8) or night-time (p=0.7) LSTs in our study area. No statistically significant trends were identified in any of the observed air temperature measures, T_{max}, T_{min} and T_{day}, over this period either. The overall fit for the linear model that was used to predict LSTs from observed air temperatures for the period 1957-2019 was R^2= 0.86.

5.4.1. Warming trends 1957-2019

Whereas no significant increases in air temperatures were found for the area between 2003 and 2019, observed T_{max}, T_{min} and T_{day} all show a significant warming trend if we extend the period back to 1957 ($p < 0.001$, again corresponding to a pixel at 1050 m a.s.l.), and if we directly compare the periods 1957-1976 and 2000-2019. These two periods were selected because twenty years provides a sufficiently long time frame to calculate meaningful averages that can be compared, yet the periods are still far enough apart to allow us to contrast the conditions at the start of period of observation (the 1960s and 1970s) and the most recent two decades.
The largest increase in observed air temperatures recorded at Fokstua station (952 m a.s.l.) was found for minimum daily air temperatures T_{min} at 1.8 °C, but maximum air

temperatures T_{max} also increased by 1.2 °C and T_{day} by 1.4 °C within the same time frame (see Supplementary Table 5.3).

LSTs also increased across all locations in the study area (Figure 5.4). The increase was statistically significant for day-time and night-time temperatures (Figure 5.5), but also daily mean temperatures.

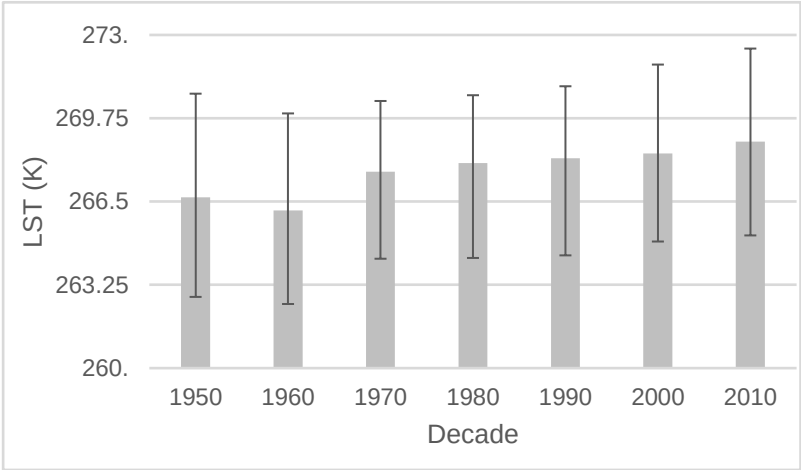

Figure 5.4 The mean land surface temperature (LST) over the entire NE Jotunheimen study area per decade. The mean of all pixels (n=7476) per image was calculated, resulting in 460 LST values per decade. These values were then averaged to produce the decadal mean. The error bars represent the mean day-time temperatures (maximum values) and mean night-time temperatures (minimum values).

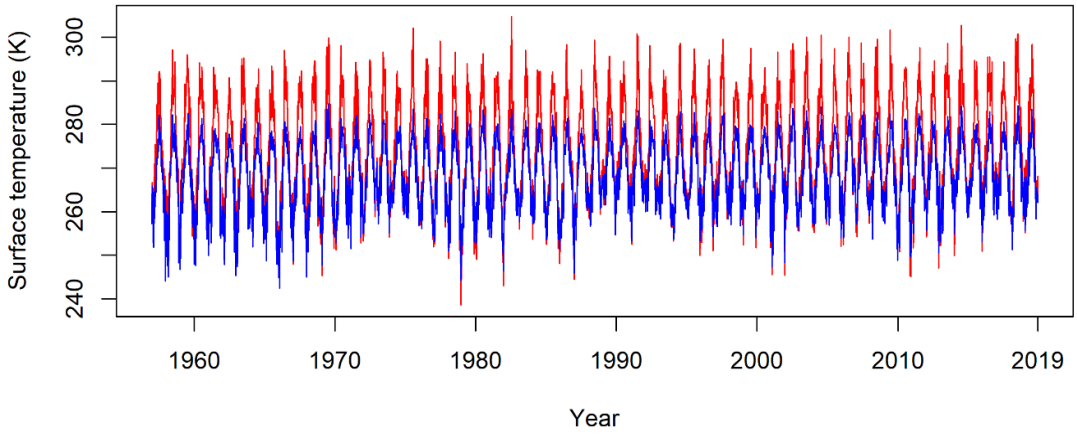

Figure 5.5. Day-time (red) and night-time (blue) 8-day resolution land surface temperatures corresponding to a pixel at 1050 m a.s.l. on Galdhøpiggen for the period 1957-2019.

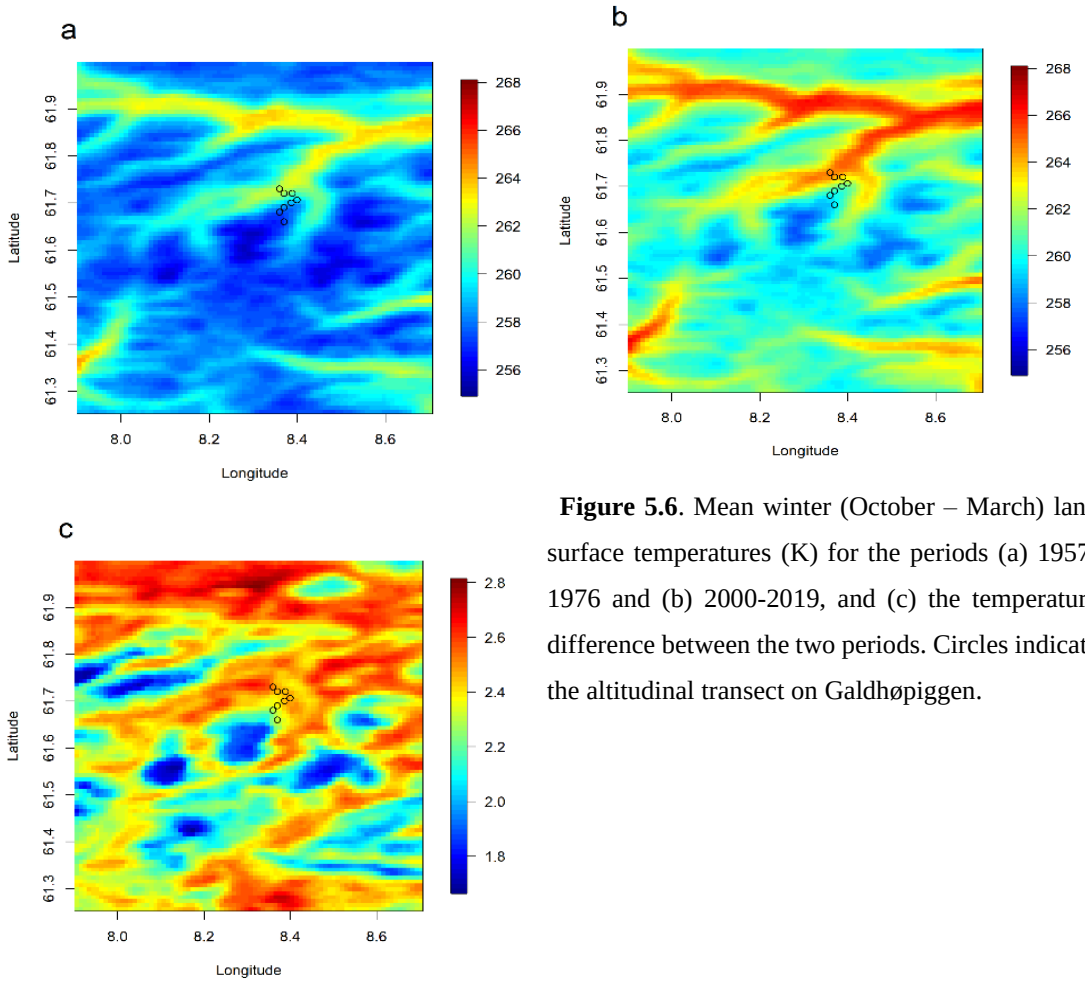

Figure 5.6. Mean winter (October – March) land surface temperatures (K) for the periods (a) 1957-1976 and (b) 2000-2019, and (c) the temperature difference between the two periods. Circles indicate the altitudinal transect on Galdhøpiggen.

The largest increase in decadal mean LSTs occurred in 1970s, with a steady increase over the two following decades. From 1990, the increase in decadal warming decelerates (Figure 5.4). Between the periods 1957-1976 and 2000-2019, mean daily LSTs increased by 1.2-2°C. The temperature increase was largest in the winter, as daily mean LSTs warmed by 1.8 °C at highest altitudes (>1900 m a.s.l.) and by 2.4-2.8 °C at mid- and low altitudes; the spatial pattern of temperature increase showed an almost inverse relationship with altitude (Figure 5.6).

Across the Galdhøpiggen transect, the highest annual mean LST increases (by ~1.8 °C) and LST_{gs} increases (by ~1.2 °C) were recorded at 600 m a.s.l. and 1550 m a.s.l. (Figure 5.7). Over the whole area, LST_{gs} increased by approximately 0.8 °C at the highest, snow-covered peaks, and by 1.4 °C in the valleys (Figure 5.8a).

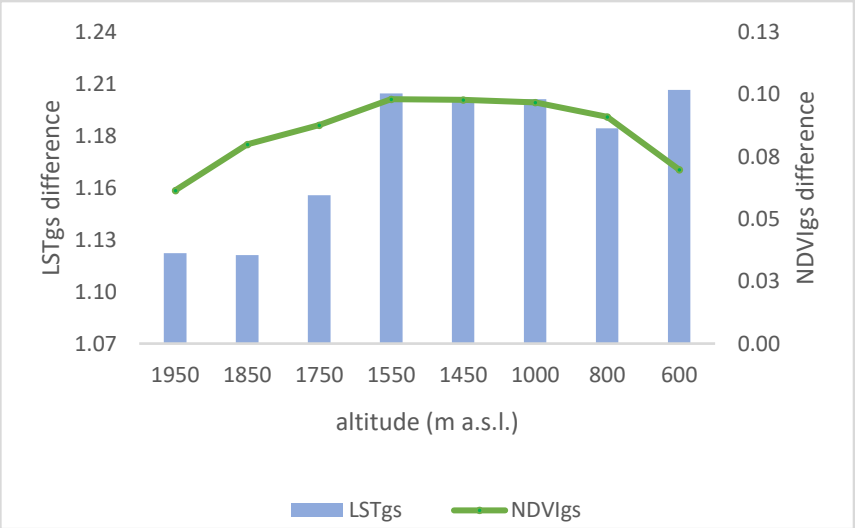

Figure 5.7. The differences between mean LST_{gs} and mean $NDVI_{gs}$ between the periods 1957-1976 and 2000-2019 at descending altitudes across the Galdhøpiggen altitudinal transect. The values were calculated by deducting the 1957-1976 mean from the 2009-2019 mean to estimate the change in both LST_{gs} and $NDVI_{gs}$.

Satellite-derived LSTs were consistently lower than observed air temperatures, and the mean difference between LST and air temperature varies across altitudes and seasons. For example, at 1450 m a.s.l. on Galdhøpiggen, the mean difference between MAAT and LSTs was 2.5 °C for the period 1957-2019. However, the mean difference is reduced to just 0.2 °C during the growing season (see Supplementary Figure 5.7). Spatially, the temperature difference during the growing season is smallest at altitudes around 1450-1550 m a.s.l. (0.2-0.8 °C) but increases towards the higher altitudes (up to 2 °C at 1950 m a.s.l.) as well as lower altitudes (1.2 °C at 1050 m a.s.l.).

Annual mean LST and LST_{gs} both increase with decreasing elevation (LST_{gs} values shown in Figure 5.7), and the range of temperatures follows the same pattern. The mean LST_{gs} over a wooded area at 600 m a.s.l. on the Galdhøpiggen transect was 6.4 ± 1.06 °C, whereas at the predominantly bare landscape at 1950 m a.s.l., the mean temperature was -0.1 ± 0.98 °C.

5.4.2. Trends in growing season NDVI

$NDVI_{gs}$ values predicted by the model showed a statistically significant increasing trend between the periods 1957-1976 and 2000-2019. Across most of the vegetated study area, $NDVI_{gs}$ increased by 0.06-0.1; the spatial patterns of $NDVI_{gs}$ increase are illustrated in Figure 5.8b. On the Galdhøpiggen transect, the increase was most significant at altitudes between 1050 – 1550 m a.s.l. (Figure 5.7; NDVI = 0.1, $p <$ .001), which are directly above the tree line and are dominated by dwarf shrub- and grass heaths. The observed $NDVI_{gs}$ (2001-2017) was found to have a much lower year-to-year variability than the modelled $NDVI_{gs}$ (2057-2019), suggesting that the model overestimates NDVI sensitivity.

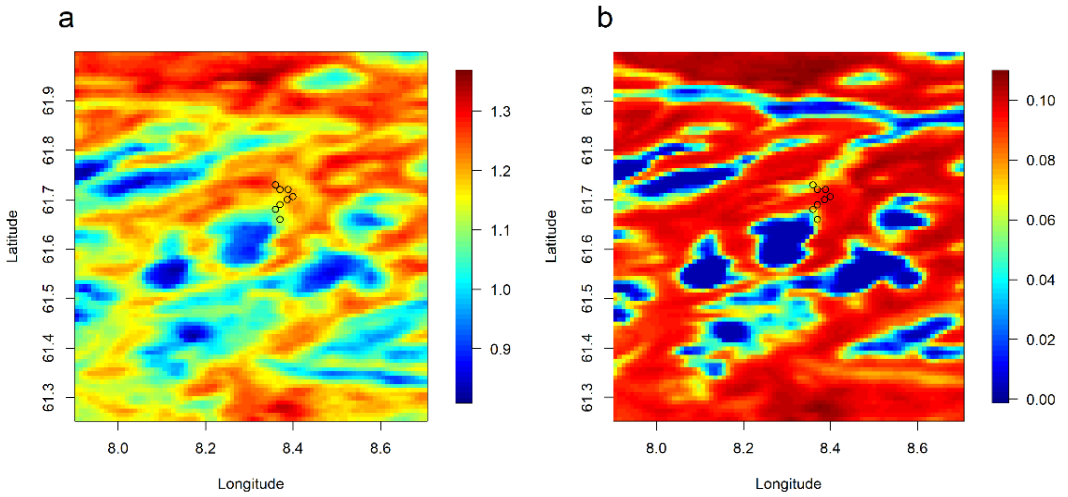

Figure 5.8. (a) Difference in mean growing season land surface temperatures (°C) and (b) difference in mean growing season NDVI values between the periods 1957-1976 and 2000-2019. Circles indicate the altitudinal transect on Galdhøpiggen.

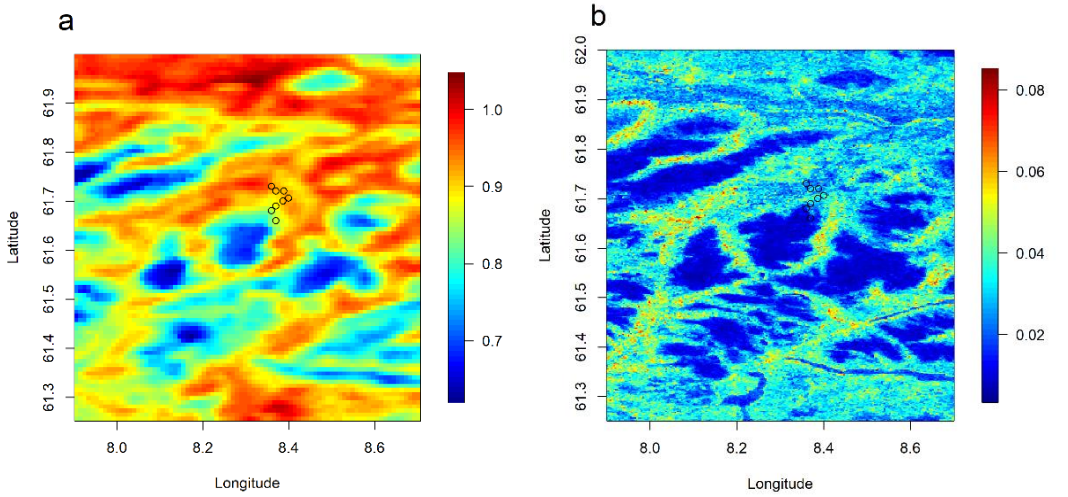

Figure 5.9. (a) Standard deviation of observed LST_{gs} at 1-km resolution and (b) Standard deviation of observed $NDVI_{gs}$ at 250m resolution over the period 2001-2017. Circles indicate the altitudinal transect on Galdhøpiggen.

Similar to the LST trend, $NDVI_{gs}$ is highest at lowest elevations (see Figure 5.13). Mean predicted $NDVI_{gs}$ during the period 1957-2019 was 0.04 at 1950 m a.s.l., increasing up to 0.5 at 600 m a.s.l. on the Galdhøpiggen transect (values correspond to individual pixels at these altitudes). However, whilst the standard deviation of LST_{gs} also increases linearly with decreasing altitude, the standard deviation of $NDVI_{gs}$

values peaks at altitudes between 1050 – 1550 m a.s.l., as demonstrated by the altitudinal transect in Figure 5.9b.

During the observation period (2003-2017), there was no statistically significant trend in overall observed NDVI ($p=0.9$) or $NDVI_{gs}$ ($p=0.4$) across altitudes.

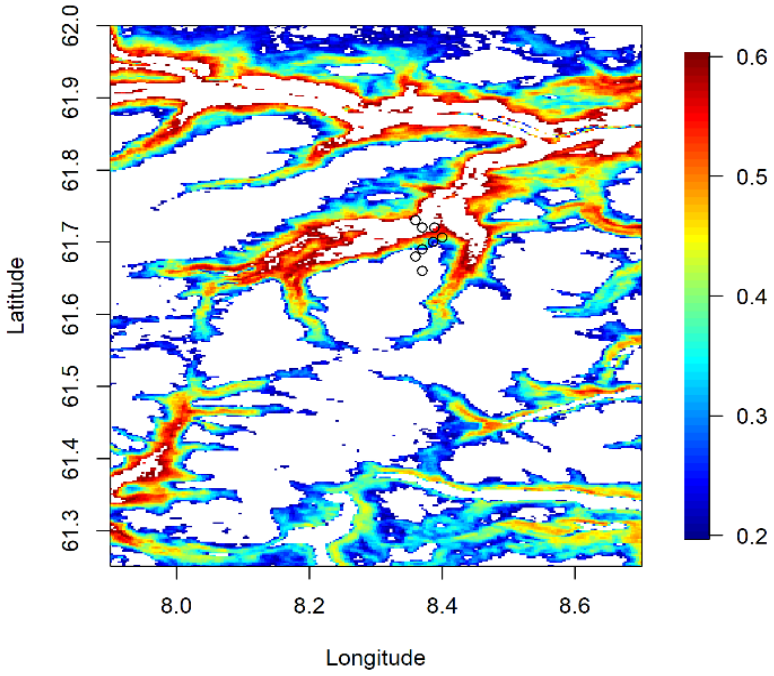

Figure 5.10. Observed mean growing season NDVI between 0.2-0.6 for the period 2001-2017 at 250 m resolution. NDVI values between 0.2 and 0.4 correspond to areas with sparse vegetation and NDVI of 0.4-0.6 indicates moderate vegetation cover (see Discussion). Areas with NDVI <0.2 and >0.6 are covered in white.

5.5. Discussion

5.5.1. Long-term warming trend

Analysis of observed MODIS LST and air temperature data revealed a slight positive trend in air- and surface temperatures over 17 years (2003-2019), but the trend is not statistically significant at any altitude. Correspondingly, the observed mean annual NDVI and mean $NDVI_{gs}$ also show an insignificant trend across altitudes over the period 2001-2017 (this trend is positive at altitudes 1050-1550 m a.s.l., but negative at altitudes above and below this range). However, as NDVI generally responds

positively to increasing temperatures (particularly growing season temperatures) in tundra environments (Blok et al., 2011; Cui and Shi, 2010; Raynolds et al., 2008; Walker et al., 2003), we should not expect a strong increase in NDVI during the period given insignificant increases in temperature.

Over the long term (1957-2019), however, modelled LSTs and NDVI reveal significant increases in both temperature and 'greenness' in Jotunheimen. The observed mean daily air temperatures and modelled mean LSTs over the period 2000-2019 were 1.4 °C and 1.2-2 °C higher than during the period 1957-1976. Simultaneously, the mean number of days per year with air temperature above 0 °C at 1050 m a.s.l. increased by ~12 days between the two periods (see Supplementary Figure 5.6).

The air temperature- and ground surface warming trend over the past decades is in line with other studies from the area (e.g., Etzelmüller et al., 2020), some of which specifically investigate permafrost degradation in response to warming air temperatures (Hipp et al., 2012; Isaksen et al., 2011, 2007). On Galdhøpiggen, Hipp et al. (2012) predict a rise of the lower limit of permafrost from the present-day limit at 1450 m a.s.l. to 1800 m a.s.l. by 2100, and the degradation of all permafrost at c. 1560 m a.s.l. before 2050. This prediction is based on a model that follows the moderate A1B emissions scenario (IPCC, 2007), which assumes a future increase in renewable energy sources and a decrease in CO_2 emissions. Based on the data from Juvvasshøe borehole (at 1894 m a.s.l., near the southernmost point of our altitudinal transect), Isaksen et al. (2002) report a ground surface warming of 0.5-1 °C over the past decades, and had at the time already predicted a similarly rapid rise of the permafrost limit, leading to major changes in periglacial processes. Our results confirm the trends highlighted in the earlier studies and, importantly, demonstrate that mean annual LSTs were 0.14 °C higher in 2010-2019 compared to 2000-2009, illustrating that the warming trend is continuing and contributing to permafrost degradation at its lower limits on Galdhøpiggen. Additionally, our results show considerable seasonal and diurnal differences in air- and LST warming trends. In the long term, T_{min} and winter (i.e., non-growing season) LSTs in Jotunheimen warmed at a higher rate than T_{max} and $LST_{gs.}$

Our findings for high-altitude environments draw parallels to high-latitude regions, where climatic warming is similarly predicted to be greater in the winter, and wintertime warming events will become more frequent (Bjerke et al., 2011; Callaghan et al., 2010; Kreyling et al., 2019; Stocker et al., 2013). In fact, a pronounced multi-decadal winter air temperature warming in Norway has been reported before (Førland et al., 2000; Isaksen et al., 2002). There is evidence that winter warming accelerates the thermal degradation of permafrost (Zhang et al., 2019), however, the impacts of more rapid winter warming compared to growing season warming largely remain unknown.

5.5.2. The use of MAAT, LST and LST_{gs} to infer sub-surface temperature conditions

Isaksen et al. (2002) reported that permafrost in southern Norway is rarely found on sites with a MAAT above -2°C. Furthermore, it has been proposed that the lower altitudinal limit of permafrost, as estimated from ground temperatures, correlates with a MAAT of -2.5 °C on Galdhøpiggen, and with -3.5 °C on neighbouring Glittertind (Ødegård et al., 1996). This provides a useful framework for review ofour data in the context of permafrost dynamics.

Using Galdhøpiggen as a reference, we examined the trends in observed air temperatures at the altitude of the estimated lower limit of permafrost. However, locating the exact position of the lower limit of altitudinal permafrost remains a challenge due to it typically occurring in patches below ground. Numerous studies have attempted to determine the position of the lower limit of discontinuous permafrost on Galdhøpiggen through direct, field-based approaches, such as ground temperature measurements from boreholes (Etzelmüller et al., 2020; Hipp et al., 2012; Lilleøren et al., 2012), and indirect approaches, such as measuring the bottom temperature of snow (Hauck et al., 2004; Isaksen et al., 2002) or using electrical resistivity tomography (Isaksen et al., 2002, 2011). The proposed lower limits range from 1410 to 1500 m a.s.l. (Hauck et al., 2004; Ødegård et al., 1996). Taking into account that the most recent measurements are a decade old, we here assign 1450 m a.s.l. as the lower limit of permafrost, as it also represents the mid-point of the suggested range.

The MAAT at 1450 m a.s.l. was calculated based on the observed air temperature data from Fokstua meteorological station by using the temperature lapse rate of 0.42°C/100 m. Our results reveal that the MAAT at this altitude has in fact largely remained above -2 °C since at least 1990, apart from a few, what could be considered anomalous years (Figure 5.11a). Taking the -2 °C threshold (*cf.* Isaksen et al., 2002), this would suggest that over the past decades conditions would have been too warm to sustain ground ice at this altitude. Whilst the calculated MAAT for the period 1957-1976 was indeed -2.5 °C, and theoretically sufficiently low to have supported permafrost (*cf.* Isaksen et al., 2002; Ødegård et al., 1996), the recent warming has resulted in a MAAT of -1.1 °C for 2000-2019. Furthermore, the MAAT at 1050 m a.s.l. is nearly a degree higher today compared to the estimation of -0.2 °C by Ødegård et al. (1996) over two decades ago. With ongoing warming, the MAAT of -2.5 °C is likely restricted to higher elevations on Galdhøpiggen today. However, it has to be noted that our temperature estimate was calculated based on data from a meteorological station c. 60 km from Galdhøpiggen. Air temperature calculations based on rise in elevation assume that temperature increase has been uniform across all altitudes. Whilst air temperature records provide insight of temporal patterns, this method fails to account for spatial differences in the microclimate of the slope, likely over- or underestimating the air temperature at 1450 m a.s.l.

MODIS LSTs, on the other hand, provide a complete spatial coverage and a high accuracy in permafrost tundra landscapes (Wan et al., 2004; Westermann et al., 2011) with a slight cold bias (i.e., underestimation of temperature) of -1.1 °C reported by Muster et al. (2015). In an attempt to improve the reliability of our inferences, we replaced MAAT with mean annual surface temperatures to determine whether they could be used to identify areas with thermal conditions suitable for permafrost. Although there is currently no universal remote-sensing method to accurately assess the presence of sub-surface permafrost or its thermal state (Obu et al., 2019), it is known that permafrost is controlled by both ground- and surface temperatures (Muster et al., 2015), and LSTs have therefore increasingly been used in permafrost modelling (Langer et al., 2010; Westermann et al., 2011, 2012).

However, mapping the observed mean annual LSTs above -2 °C from the period 2009-2019 revealed that surface temperatures at our reference point at 1450 m a.s.l. on Galdhøpiggen were significantly lower than air temperatures (Figure 5.11b), with a

mean of -4.2 °C. The large discrepancy of 3.1 °C between the mean annual air temperatures and LSTs at this altitude could be due to the LSTs being underestimated in the winter, as the surface of the snow cover can be colder than the ground surface underneath it. Moreover, the estimated air- and land surface temperatures match closely during the growing season, but exhibit a 2.5 °C difference in mean annual estimates (see Supplementary Figure 5.7). A strong wintertime cold bias in LST measurements over areas of the Arctic has been reported before (Langer et al., 2010; Westermann et al., 2011, 2012), as clear-sky conditions in the winter allow long-wave radiation emitted by the land surface to escape into the atmosphere, thus cooling the surface.

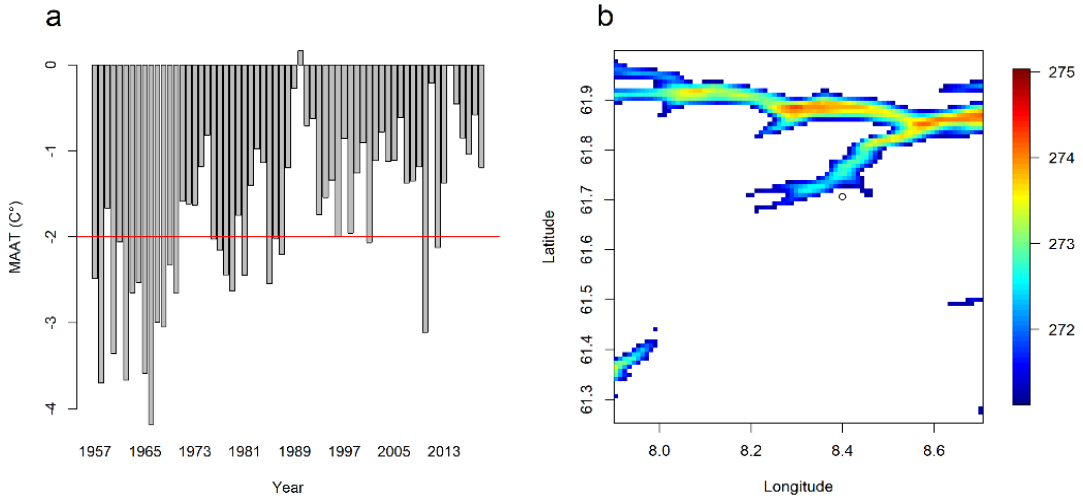

Figure 5.11. (a) MAAT (°C) at 1450 m a.s.l. calculated from observed temperatures from Fokstua meteorological station. (b) Mean annual LSTs (K) above -2 °C (271.15 K) for the period 2000-2019. The circle indicates the altitude of the estimated present-day lower limit of permafrost (1450 m a.s.l.).

Figure 5.11b illustrates the land surface area with mean annual temperature above -2°C, which is entirely constrained with the valleys. The remaining area of the map should, according to Isaksen et al. (2002), therefore be indicative of conditions suitable for permafrost presence (≤-2°C). This area extends to lower altitudes below the Galdhøpiggen reference point at 1450 m a.s.l. and covers the majority of the region. Whilst mountain permafrost is indeed widespread in the area, comparing Figure 5.11b to previously published permafrost maps and measured borehole temperatures (e.g.,

Farbrot et al., 2011; Lilleøren et al., 2012) suggests that annual mean LSTs overestimate the area suitable for permafrost presence in this region.

To eliminate this winter cold bias, we explored the applicability of growing season surface temperatures to delineating permafrost distribution. Permafrost forms where the ground is subject to a negative energy budget, i.e., mean annual LST below 0 °C (Ballantyne, 2018). Therefore, we identify the areas where mean LSTs remain below 0 °C all year round, including during the growing season (Figure 5.12). The mapped below-freezing surface corresponds to the highest peaks of the area that are largely covered with permanent snow and glaciers. On a large scale, the regions with LST_{gs} below 0 °C identified on Figure 5.12b are comparable in shape and extent with previously modelled and mapped permafrost distribution in Jotunheimen (Gisnås et al., 2011 *in* Lilleøren et al., 2012; Gisnås et al., 2017), albeit at a lower resolution. However, on closer inspection, both figures underestimate the lower limit of permafrost on Galdhøpiggen by about 300-400 m. Nevertheless, at higher altitudes of the slope, the surface with below-freezing LST_{gs} borders the reference point at 1850 m a.s.l. in Figure 5.12a, which corresponds to the continuous permafrost zone above 1800 m a.s.l. (Hipp et al., 2012). Therefore, the LST_{gs} below 0 °C could be indicative of the continuous permafrost zone rather than the entire extent of mountain permafrost in the area.

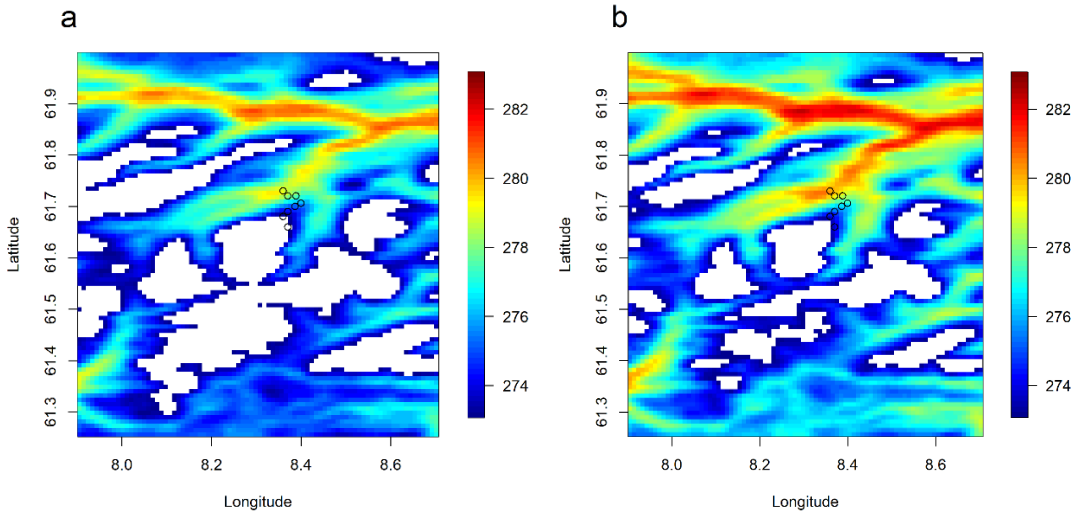

Figure 5.12. Mean growing season (April-September) LSTs (K) above 0 °C for (a) 1957-1976 and (b) 2000-2019. The white areas indicate LSTs below 0 °C.

5.5.3. Spatial variation in LST and NDVI, with highest increases over shrub- and graminoid heaths

The comparison of Figures 5.12a and 5.12b highlights the substantial LST_{gs} increase across NE Jotunheimen since 1957, and the visible decrease in the extent of land surface with LST_{gs} below 0°C. However, the changes have not been uniform across altitudes. At higher altitudes above c. 1700 m a.s.l., both growing season air- and surface temperatures showed lower increases over time as well as lower year-to-year variability (Figure 5.9). Although LSTs are known to decrease with altitude (Peng et al., 2020), this effect is likely to be enhanced by the higher albedo of the permanent snow cover or bare ground on the highest peaks in the Jotunheimen area (e.g., Galdhøpiggen, Glittertind). A higher proportion of shortwave radiation is reflected back to the atmosphere due to the high albedo of snow and ice (0.80) and the surrounding lichen-dominated alpine heaths (0.26) compared with the lower albedo of vegetation, for example shrubs (0.12) (Robock, 1980; Aartsma et al., 2020). Throughout the study area, higher altitudes are sparsely vegetated (Figure 5.10), and mountains like Galdhøpiggen are covered with extensive areas of block field and patterned ground (Isaksen et al., 2001; Winkler et al., 2016). The albedo of barren rock surfaces is found to be 7% higher than that of bare soil in Arctic permafrost landscapes, and bare rocks have been shown to remain about 5 °C cooler than the regional mean (Muster et al., 2015). Despite the patterned ground being partially covered by cryptogamic crust, herbaceous plants, and even prostrate shrubs at high altitudes (Hallang et al., 2020; Matthews et al., 2018), the vegetation cover is too sparse to be detected by low spatial resolution satellites. It is evident from Figure 5.10 that the highest altitudes where the NDVI indicates sparse vegetation along the Galdhøpiggen transect, remain below c. 1800 m a.s.l. ($NDVI \geq 0.2$). It may therefore be expected that the land surface at high altitudes will warm less during the growing season than more vegetated surfaces with a lower albedo (at lower altitudes), resulting in a lower range of recorded temperatures.

We found little change in the modelled $NDVI_{gs}$ values over the past six decades at higher altitudes (>1700 m a.s.l.). This is easily explained by the scarcity of green vegetation, but we also recorded little change at the lowest altitudes in the valleys (600-

800 m a.s.l.) (Figure 5.7). It is important to note here that the modelled NDVI is derived from the spatial variation of LSTs with NDVI, and an assumption is made that this corresponds to long-term temporal variation. Looking at old aerial photographs (Kartverket (2021), available at: www.norgeibilder.no), it is clear that a mature woodland was already established in the valleys in the late 1950s, which explains why any increase in NDVI (i.e., indicating the densification of the woodland) would be less pronounced here than over areas above the tree line (1050-1550 m a.s.l.), where vegetation is becoming more abundantly established on previously sparsely vegetated surfaces. Thus, the surface albedo at highest and lowest altitudes in NE Jotunheimen has remained stable over this period.

The highest increases in modelled $NDVI_{gs}$ occur in the low alpine dwarf shrub-heath and the grass- and lichen dominated mid-alpine vegetation belts (Matthews et al., 2018), which are thought to reflect increased shrubification at the expense of non-vascular plants: deciduous shrubs have larger canopy leaf areas and shrub communities tend to have higher NDVI than other tundra species (Boelman et al., 2011; Street et al., 2007; Walker et al., 2003). Moreover, NDVI increases are likely to occur near boundaries between graminoid and shrub communities and shrub and forest communities, as such transition zones are often vulnerable to climatic changes and can respond rapidly to warming (Epstein et al., 2004; Raynolds et al., 2008). Based on the classification in Raynolds et al. (2008), our $NDVI_{gs}$ values directly above the tree line (1050 m a.s.l.), provide evidence for a shift from dwarf shrub tundra ($NDVI_{gs}$ = 0.36) in 1957-1976 to low shrub tundra ($NDVI_{gs}$=0.45) in 2000-2019.

Although the increase in LST_{gs} with decreasing altitude on the Galdhøpiggen transect is arguably more linear compared to the increase in $NDVI_{gs}$ (Figure 5.7), we also detect a large increase in LST_{gs} (by 1.2°C) over low- and mid-alpine heaths (1050-1500 m a.s.l.). This can also be explained by the decrease in surface albedo driven by increased shrubification at these altitudes. The lower albedo of shrub-covered ground compared to graminoid- or lichen tundra (Juszak et al., 2014), leads to surface heating through the absorption of a larger proportion of incoming solar radiation. The high values of both $NDVI_{gs}$ and LST_{gs} at the low- and mid-alpine heaths above the tree line are therefore most likely caused by increased vegetation cover since 1957.

Moreover, increasing ground- and near-surface temperatures further facilitate the encroachment of shrubs in mountainous regions (Anthelme et al., 2007; Dullinger et al., 2003; Hallinger et al., 2010), creating a positive feedback loop. Additionally, increased shrub cover can alter local and regional carbon- and nutrient cycles (Cahoon et al., 2012; Chapin et al., 2005; Frost et al., 2019; Pearson et al., 2013; Post et al., 2009). In Jotunheimen, shrub encroachment at higher altitudes (on Galdhøpiggen) is predicted to result in increased CO_2 efflux from the ground (Hallang et al., 2020).

5.5.4. The applicability of growing season NDVI for monitoring alpine tree dynamics

Satellite-derived NDVI has previously been successfully used in detecting the increased cover and stature of shrubs in the Arctic tundra (Silapaswan et al., 2001), high-latitude tree line composition (Olthof and Pouliot, 2010) and alpine tree line dynamics (Brown, 2013; Franke et al., 2019; Zhang et al., 2009). Following this lead, we use the mean $NDVI_{gs}$ as an indicator of the tree line in our study area.

To complement Figure 5.8b, which spatially outlines increases in modelled NDVI in the area over 60 years, we added a higher pixel resolution (250 m) map of observed NDVI over the past two decades, which provides a more accurate estimate of the boundaries between vegetation belts (Figure 5.13). Mapping the NDVI values of 0.6 and above indicates the highest possible density of green leaves, i.e., tree cover (Aldoski et al., 2013; Groß et al., 2017). Figure 5.13 highlights the areas with mean $NDVI_{gs}$ of ≥ 0.6, and the altitudinal limit of tree-indicating NDVI on Galdhøpiggen corresponds very closely to the upper limit of the dense, pine-birch woodland (*cf.* Figure 5.1).

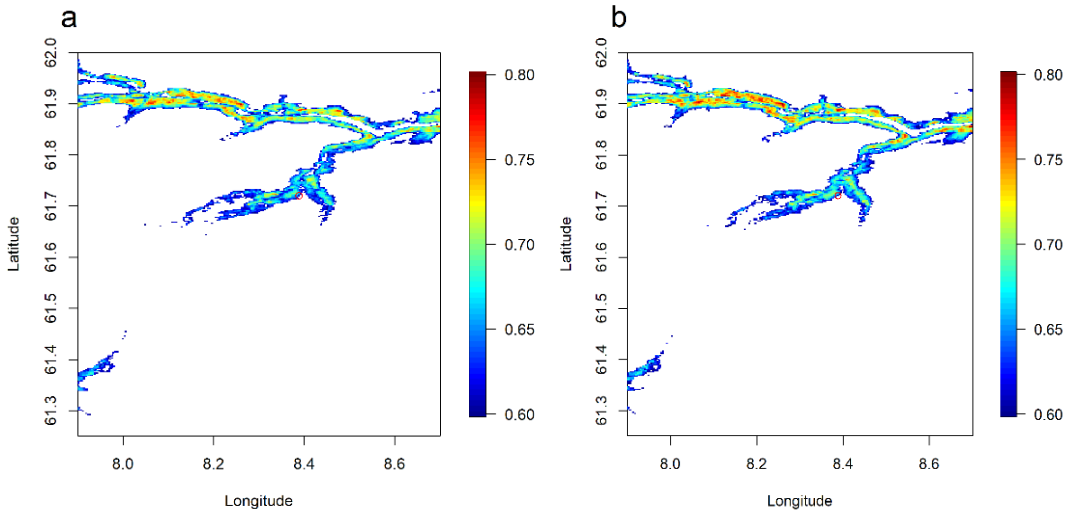

Figure 5.13. Observed mean growing season NDVI above 0.6 for periods (a) 2001-2009 and (b) 2010-2017. Only the areas with $NDVI_{gs} \geq 0.6$ (i.e., tree cover) are shown. The red circle indicates the present-day tree line on Galdhøpiggen at 1050 m a.s.l.

Evidence from aerial photographs (Kartverket, 2021) indicates that sparse stands of *Betula pubescens* reach altitudes of 1150 m a.s.l. on this particular site (Hallang et al., 2020); however, the NDVI of these stands appears to remain below 0.6. Nevertheless, the mean modelled $NDVI_{gs}$ at 1050 m a.s.l. has experienced one of the highest increases along the transect, from a mean of 0.35 in 1957-1976 to a mean of 0.45 in 2000-2019. The mean $NDVI_{gs}$ at this site has even reached the value of 0.6 on four occasions within the last two decades. Correspondingly, the LST maps suggest that the growing season conditions have improved at this altitude over the past 6 decades, becoming more favourable for the growth and expansion of *Betula pubescens* (Figure 5.14). Therefore, whilst Figure 5.13 demonstrates no significant expansion of the extent of land with NDVI of ≥0.6 during the past two decades, this could be due to a lag in response, or the inability of the decadal mean NDVI values to pick up on smaller year-to-year changes. This reasoning is substantiated by a study by Zhang et al. (2009) that found no shift in alpine tree lines on a site in NE China over two decades (1977-1999) using satellite-derived NDVI. However, by combining remote sensing with field surveys and using a ratio of NDVI between the birch tree line forest and the adjacent old-growth coniferous forest, they also found an increase in the NDVI ratio of tree line forest against the reference forest, indicating that the birch-dominated tree line forest had grown denser.

Although the observed NDVI of 0.6 does correspond closely to the dense mixed woodland in our study area, this value alone fails to identify the upslope advancement of smaller patches of trees, which is detectable on the ground and from aerial photographs (Hallang et al., 2020). The challenge of estimating the positions of tree lines is further complicated by the various definitions of the concept of 'tree line' (e.g., Aas, 1969; Kullman, 1990), and the inevitability that trees take time to reach maturity and form denser stands on previously treeless surfaces. Therefore, whilst the upper range of NDVI is a good indicator of mature, dense woodland in this mountainous area, we suggest combining NDVI with other methods like aerial photographs or field surveys to investigate the advancement of alpine tree lines in response to warming.

5.5.5. The potential of satellite-derived LSTs for estimating the altitudinal limit of the tree line

Having established the position of the dense woodland in our study area by using observed NDVI, we tested the applicability of satellite-derived surface temperatures that indicate suitable growing conditions as a possible proxy indicator of tree lines using the Galdhøpiggen transect as reference.

Similar to the approach taken when investigating the dynamics of the lower permafrost limit (see above), we here make attempt to use accepted temperature tolerances for tree species to make inferences about tree-line dynamics in the Jotunheimen area. Two examples of mapping the tree lines using LSTs are illustrated in Figure 5.14. From previous vegetational studies conducted in central Norway, it has been established that the *Pinus sylvestris* tree line correlates well with a July mean air temperature of 11°C (Paus, 2010). The mean July LST at the present-day tree line on the Galdhøpiggen transect was 11.3°C over the period 2000-2019. The temperature requirements mapped on Figure 13b therefore match perfectly with the tree line on Galdhøpiggen. However, the 1957-1976 mean July LST (Figure 13a) underestimates the pine tree lines in the area more significantly, as a comparison of the map with aerial images (Kartverket, 2021) shows that pine trees were fully established in the valley and at 1050 m a.s.l. in 1981.

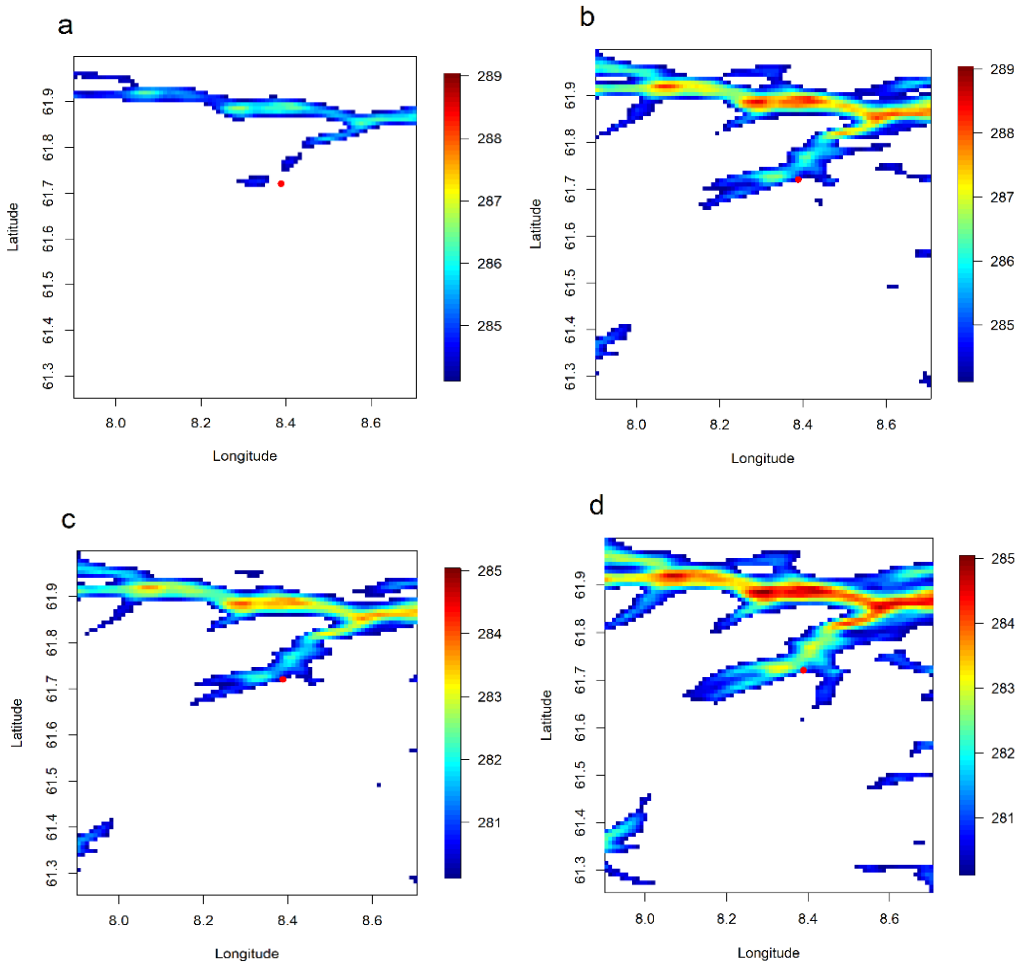

Figure 5.14. Mean July LSTs (K) above 11 °C (284.15 K) for (a) 1957-1976 and (b) 2000-2019, and mean June-September LSTs (K) above 7 °C (280.15 K) for (c) 1957-1976 and (d) 2000-2019. The circle represents the altitude of the present-day tree line (1050 m a.s.l.).

Birch (*Betula pubescens*) requires minimum summer (June-September) mean air temperatures of 7°C to grow (Nesje and Kvamme, 1991). On Galdhøpiggen, the mapped area of temperatures equal to and above 7°C for the period 2000-2019 covers the present-day birch tree line, which extends up to 1150 m a.s.l. in sparse stands (Figure 14d). In fact, the mean June-September temperature at 1150 m a.s.l. was 8.27°C, suggesting that the minimum summer temperatures required by birch currently extend above their present-day range, and Figure 14d is providing a slight overestimation of the altitude of the birch tree line. Conversely, the 1957-1976 summer LST averages slightly underestimate the tree line position, particularly on the east-facing slope of Galdhøpiggen (Figure 5.14c). Although the temperature values used here as a baseline refer to minimum growing season air temperature requirements, it is suggested that growing season LSTs can also be used successfully to locate the areas

suitable for birch and pine growth. In this case, however, the 1957-1976 mean LSTs provide a less reliable estimate of the full area suitable for tree growth, likely due to the low temperatures prevailing in the area in the 1960s (Figure 5.5). Nevertheless, there is potential in using satellite-derived mean LST_{gs} to identify areas suitable for the growth of specific tree species; particularly when the mean is calculated over a larger period.

5.6. Conclusions

Our results demonstrate substantial increases in air- and land surface temperatures in NE Jotunheimen from 1957 to 2019, particularly in winter temperatures (up to 2.4-2.6°C). NDVI also showed an increasing trend (by 0.06-0.1) during the same period. However, these changes have not been spatially uniform across altitudes.

We detect the highest increases in modelled $NDVI_{gs}$ and LST_{gs} over low- and mid-alpine heaths (1050-1500 m a.s.l.) by ~0.1 and 1.2°C, respectively. This can be attributed to increased shrubification, as deciduous shrubs are 'greener' than the surrounding tundra and capture more incoming solar radiation to heat the surface. The mid-altitude warming evident from our results confirm that the thermal conditions in the past decade have continued to be suitable for permafrost degradation on Galdhøpiggen (previously reported by Isaksen et al., 2011; Hipp et al., 2012), especially at its lower limits.

We found that MODIS growing season LSTs are a potentially useful tool for identifying the spatial distribution of areas with suitable conditions for continuous sub-surface alpine permafrost. Moreover, growing season LSTs also have potential to be used for mapping areas suitable for tree (*P. sylvestris* and *B. pubescens*) growth in alpine regions, as demonstrated in our study. MODIS LSTs thus provide an inexpensive, accessible tool with a potential to identify above-surface and below-surface conditions during the growing season based solely on surface thermal properties. However, the 1-km pixel resolution used here can be too coarse to precisely delineate the lower limit of permafrost or record the dynamics of tree lines in alpine regions where climatic and environmental conditions change over short distances. For greater accuracy, we suggest combining satellite data with other forms of ground verification in alpine settings.

Chapter 6

Synthesis and conclusions

The present thesis has examined, using an interdisciplinary approach, the response of the alpine Jotunheimen region to climatic changes over different time scales, with a specific focus on the response of permafrost and vegetation. The key methods – field measurements, palynological analysis and remote sensing – allowed the examination of aspects of the landscape at differing temporal (millennial, centennial and decadal) and spatial (local and regional) scales. As a result, each method provided insights into the processes affecting this area, and the interaction between these processes.

Chapter 3 investigated the ways in which ecosystem (soil and vegetation) and geomorphological (specifically cryogenic disturbance) factors may control or affect ecosystem respiration during the peak growing season. Identification of the seven variables that exhibit the highest influence over surface CO_2 efflux (i.e., ecosystem respiration, R_e) helped to better understand the response of carbon release in an alpine permafrost landscape under different scenarios of change. Such scenarios include, for example, changes in temperature, precipitation, vegetation cover or frost disturbance. Field-based measurements revealed that soil microclimate and plant growth forms controlled ecosystem respiration more strongly than cryoturbation or atmospheric conditions. During the dry peak growing season, increases in soil moisture led to higher R_e across all altitudes, whilst surface disturbance had a negative effect on R_e. Vegetation, particularly shrub cover, had a positive effect on R_e, and the findings suggest that increasing shrub cover at altitudes above 1500 m a.s.l. leads to elevated surface CO_2 efflux.

To understand the response of alpine vegetation assemblages to climatic changes in this area, Chapter 4 extended the temporal scale and examined how alpine vegetation belts and tree lines have shifted over millennial and centennial scales, specifically on Galdhøpiggen. This was achieved through reconstructing the past environment based on fossil pollen preserved in a peat core collected from a mire at the present-day tree line. The dominant tree species – *Pinus sylvestris* and *Betula pubescens* - were identified, and the limits of their respective ranges were reconstructed based on the relative abundance and accumulation rates of fossil pollen throughout the core. Using knowledge of the minimum growing season temperature requirements for each species, the past (during c. 4500 years) fluctuations of their altitudinal limits proved to be useful indicators of warmer and colder periods. Further, combining this information

with past studies on glacial fluctuations in the area, it was also possible to make inferences about past movements of the lower limit of permafrost.

Throughout the c. 4400-year sequence, the tree lines and the lower limit of permafrost were found to have fluctuated in altitude by hundreds of metres (Figure 6.1). Due to the pollen spectrum being dominated by arboreal species throughout the late Holocene, it proved difficult to identify the shifts in the shrub-dominated low- and mid-alpine vegetation belts higher upslope. However, the evidence in the pollen spectrum did indicate a period around 3000-2000 cal. yr BP where there was a significant depression of the low-alpine belt. The palynological evidence combined with past climate studies (e.g., Lilleøren et al., 2012; Matthews and Dresser, 2008) therefore reveals that arboreal and non-arboreal vegetation on Galdhøpiggen responded to Late Holocene climatic changes with significant altitudinal range shifts (100s of metres).

Since the early 1980s, changes in the extent and patterns of vegetation cover can be detected from air and from space. In Chapter 5, modelled vegetational trends as well as land surface temperatures in NE Jotunheimen were examined over the period of 1957-2019 with the aim to investigate spatial differences in the rate of change across altitudes and thus identify areas most susceptible to change. The results demonstrated substantial increases in air- and land surface temperatures (particularly winter temperatures), and an increasing trend in NDVI during the study period. The highest increases in growing season NDVI and LST were recorded over low- and mid-alpine heaths at altitudes between 1050-1500 m a.s.l., which was attributed to increased shrubification over these areas. The surface temperature increase of 1.2 °C at the altitude of the present-day lower limit of permafrost over the past six decades suggests that the ground thermal conditions near the lower limit of present-day permafrost have likely led to continued permafrost degradation on Galdhøpiggen, thus contributing to its shift up the slope.

In the present, final chapter, the results of the three different analyses are synthesised. Sub-Section 6.1 summarises the transformations on Galdhøpiggen from long to short temporal scales. Sub-Section 6.2 identifies the advantages and limitations related to the application of the used methods in this study, outlines the ways in which the encountered limitations were overcome, and reviews how the different methods complemented each other. The final sub-Section (6.3) outlines the likely future directions of each of the identified trends.

6.1. Thermal and vegetational changes on Galdhøpiggen from c. 4350 cal. yr BP to present

The *B. pubescens* and *P. sylvestris* tree lines and the lower limit of permafrost on the north-facing slope of Galdhøpiggen have fluctuated in altitude in response to climatic changes over the past 4350 years (Figure 6.1). The palynological record indicates that during the period between 4300-3400 cal. yr BP, warm and mild conditions suitable for the establishment of a dense pine-dominated woodland prevailed at the altitude of the present-day tree line (1000 m a.s.l.). With temperatures higher than today, permafrost was likely confined to higher elevations above the present-day lower limit (1450-1470 m a.s.l.). It could be speculated that the lower limit at the time was between 1500 and 1600 m a.s.l. (Figure 6.1), as permafrost was present above 1600 m a.s.l. even during the warm Holocene climatic optimum according to modelling reported by Lilleøren et al. (2012).

The warm period is followed by cooler conditions between 3400 and 1690 cal. yr BP, as the pollen record shows the simultaneous altitudinal depression of the pine tree line and the low-alpine shrub belt, whilst downy birch abundance at 1000 m a.s.l. increases. In response to the climatic deterioration, permafrost aggradation likely occurred, and it is estimated that the lower limit of permafrost reached c. 100 m lower than it is today. The pine tree line continued to retreat downslope during 1690-170 cal. yr BP, with downy birch becoming dominant at 1000 m a.s.l. Permafrost aggradation may also have continued, but it is unlikely that its lower limit reached below 1200 m a.s.l. (Lilleøren et al., 2012).

From 170 cal. yr BP onwards, vegetation belts advanced upslope and pine re-established at the present-day tree line at 1000 m a.s.l. in response to warming temperatures. Permafrost degrades rapidly at lower altitudes and reaches the present-day position of approximately 1450 m a.s.l. In fact, modelled borehole temperatures indicate that the permafrost limit advanced upslope by c. 200 m since 1860 (Hipp et al. 2012), illustrating the rapidity of the response to recent warming.

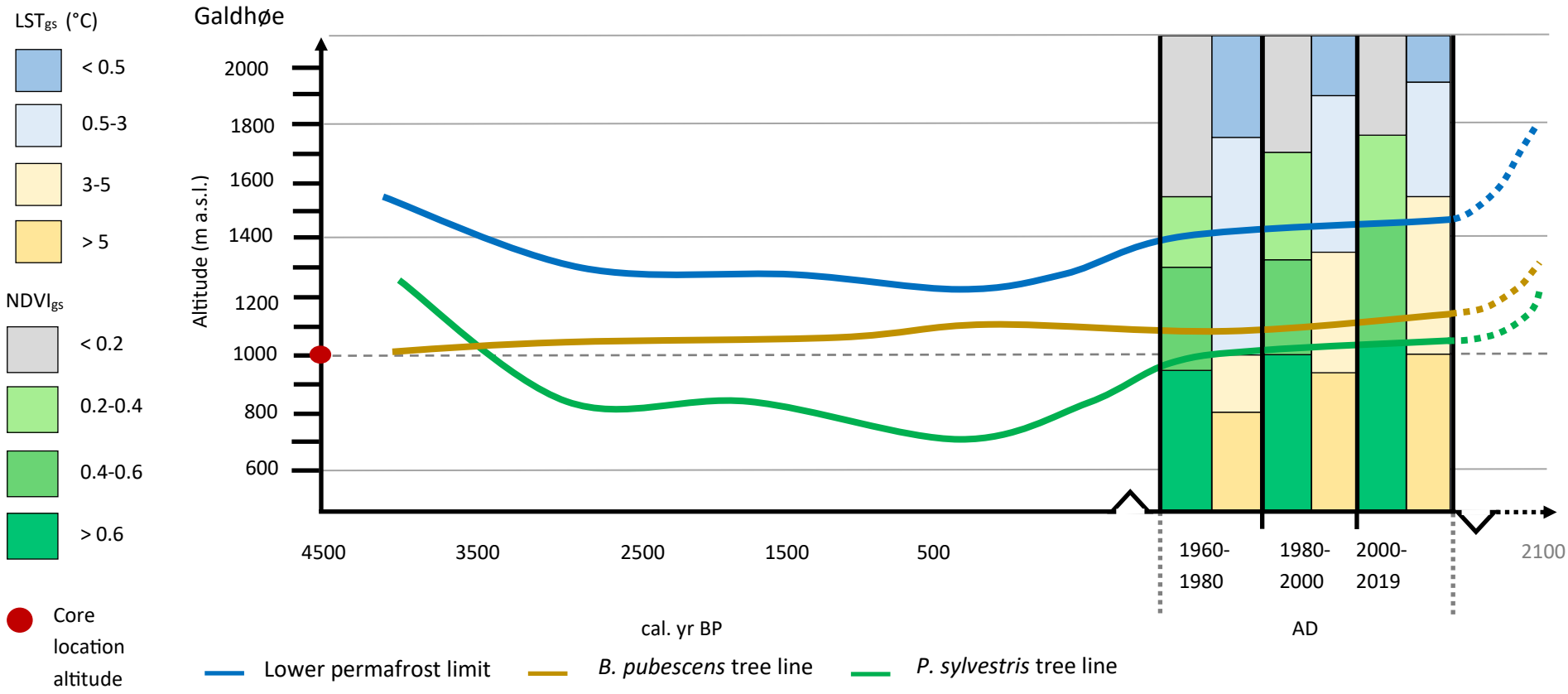

Figure 6.1. The reconstructed past and present dynamics of the birch- and pine tree lines and the lower limit of permafrost on Galdhøpiggen, and future projections (indicated by dotted lines). The approximate estimation of the past lower limit of permafrost is based on the environmental reconstruction presented in Chapter 4, staying within the limits of the permafrost extent modelled by Lilleøren et al. (2012) for the late Holocene. The future projection for the lower limit of permafrost is modelled by Hipp et al. (2012), following the A1B (IPCC, 2007) warming scenario. The period between 1960-2019 has been divided into 20-year periods, and the mean growing season land surface temperature and NDVI, based on the results presented in Chapter 5, are indicated for each altitude.

From 1957, the regional warming trend can be detected by combining remotely sensed satellite data with air temperatures recorded by a meteorological station in the area. The warming of air- and land surface temperatures from 1957 to 2019 is significant, with respective mean increases of 1.36 °C and 1.2-2 °C between the periods 1957-1976 and 2000-2019. The largest temperature increases have occurred in the winter (up to 2.4-2.6 °C). Whilst the rate of warming has slowed slightly during the past two decades, modelled land surface temperatures at the altitude of the present-day discontinuous permafrost limit suggest that the warming is creating conditions suitable for continued permafrost degradation. Although not detectable aboveground, the observed warming is expected to facilitate the upslope shift of the lower limit of permafrost. Vegetation responds to warming in a more visible way, and the largest increase in NDVI between the periods 1957-1976 and 2000-2019 was detected in the dwarf shrub- and grass dominated low- and mid-alpine vegetation belts that also cover the altitude of the lower limit of permafrost. The increase in NDVI suggests that the vegetation at these altitudes has increased either in stature, abundance, or both. Aerial photographs of the area (Kartverket, 2021), the earliest of which are from 1981, provide a valuable insight to complement satellite images in determining the position of downy birch – and pine tree lines and vegetation composition. For example, by comparing aerial images from 1981 and 2017, it is possible to identify areas directly above the forest line where trees were not present in 1981, and areas where they were present, but smaller in stature.

The increase in the abundance (and/or stature) of downy birch around 1000 m a.s.l. is evident from the modern pollen record, as the relative abundance of birch pollen increases slightly between 2000 and 2014. Shrub pollen abundance does not show significant changes during this period. As numerous species of shrubs have already established at 1000 m a.s.l. and cover the ground directly above the tree line, it may be concluded that shrub encroachment presently affects mid-alpine grass-dominated heaths between altitudes of ~1350-1600 m a.s.l at a greater magnitude (Chapter 5). Shrubs have also established at higher altitudes above 1800 m a.s.l., which was best detected in the field (Chapter 3). Vegetation surveys along an altitudinal transect on Galdhøpiggen in the summer of 2018 revealed that whilst the number of shrub species decreased with increasing altitude, dwarf species like *Salix herbacea* were present across the transect from the tree line to the predominantly barren, boulder-rich surface

at 1950 m a.s.l. Moreover, the abundance of *Salix herbacea* was high at altitudes between 1850 - 1950 m a.s.l., demonstrating that the species is already able to establish at these altitudes.

6.2. Evaluation of used methods for application in alpine tundra

Visiting a study site to make observations and take measurements is arguably the best way to get acquainted with an area (see Table 6.1). The field-based study in Jotunheimen (Chapter 3) involved several repeated visits to the sites of interest, whilst allowing observations of the surrounding landscape across all altitudes from the valley bottom up to 1950 m a.s.l. The open alpine tundra environment above the tree line on Galdhøpiggen is highly heterogenous in terms of topography, soil conditions and vegetation cover. Using a portable manual chamber to measure CO_2 efflux, a portable weather meter to record atmospheric conditions at 2 m above the surface, and probes to measure soil temperature and moisture in the top 30 mm of soil allowed me to focus directly on microhabitats that the landscape is comprised of, and to detect small differences between these habitats. Further, taking simultaneous real-time measurements of CO_2 efflux, soil moisture and soil temperature ensured that the measured variables are directly comparable. In clear, sunny conditions, soil temperature varied by up to 10 °C within just a few metres, both at high and low elevations, and reached highs of 30 °C at the peak of the day, despite the near-surface air temperature remaining around 20 °C. These results illustrate the very high surface microclimate heterogeneity in alpine tundra environments.

This does highlight a limitation: the small spatial coverage of the chamber requires repeated measurements across the landscape of interest, because the area covered by the chamber does not necessarily represent the CO_2 efflux from soil just a few metres away. To minimise this effect, the approach taken in Chapter 3 involved placing the chamber on different land cover types only a few metres apart. Nevertheless, a comprehensive estimation of CO_2 efflux from, for example, an entire sorted circle, would require numerous repeated measurements.

The small temporal scale can also restrict the application of the field methods (Table 6.1). The gas analyser and the temperature- and moisture probes only record the conditions in the space of a few minutes, providing a snapshot of the situation at a

given time; in this study, three consecutive two-minute measurement periods were used on each site. Moreover, unless the measurements are repeated during a 24-hour period and throughout the year, the portable chamber method fails to account for the diurnal and seasonal variability in CO_2 efflux. In Chapter 3, the method was adjusted to include repeated measurements on the same sites during different times of the day in an attempt to capture any variability in efflux; however, no significant patterns emerged.

To overcome the limitation posed by the small temporal scale, and to facilitate up- and down-scaling, the field methods were combined with palynological analysis and remote sensing. Combining pollen identification with radiocarbon dating of analysed samples makes it possible to estimate the age of different depths throughout the core, allowing to go back in time well beyond observational records.

To date, no previous palynological studies have been published based on a sample from Galdhøpiggen. Whilst a palynological study based on a peat core from Leirdalen (14 km from the coring site) was published by Barnett et al. (2001), the results presented in Chapter 4 likely provide a much finer temporal resolution, providing a time span of 61 years between samples in the bottom half of the core, and an interval as short as 3.5 years between samples at the top of the core.

Table 6.1. The individual advantages and limitations of three research methods used in this thesis in capturing the environmental conditions and trends over different periods of time, and the novel aspects of each approach.

Method	Advantages	Limitations	Novelty
Field-based measurements *Portable gas analyser, soil moisture- and temperature probes, clast fabrics analysis*	• Capacity to focus on microhabitats and detect differences between them • Captures the heterogeneity of tundra environments • Enables comparability of variables through simultaneous measuring of CO_2, temperature, and moisture	• Labour intensive, requires repeated measurements • Fails to account for diurnal and seasonal variability • Does not capture the regional or landscape-scale conditions	• The use of a gas analyser to measure surface CO_2 emissions on Galdhøpiggen • The use of clast fabrics as a proxy of soil disturbance • Testing of the hypothesis that soil disturbance might create 'preferential pathways' for CO_2 escape
Palynological analysis *Pollen extracted and identified from a 46 cm peat core;* *a combination of methods used in interpretation*	• Allows to go back in time beyond observational records • Provides insight into the past species assemblages in a given area	• Difficult to differentiate between local, regional and long-distance pollen as estimating the source of the pollen is problematic, especially in alpine areas • No universal method for accurately determining past local species presence and abundance • Cost limitation	• First high-resolution palynological study based on a core from Galdhøpiggen • Several methods combined to interpret the pollen profile
Satellite remote sensing *MODIS NDVI and surface temperature data*	• Provides information for large, otherwise inaccessible areas • Data accessible from online sources	• Fails to capture the small-scale variability in the landscape (minimum pixel resolution is 250 m); ground truthing often required • MODIS satellite observations only go back to 1999/2002; historic estimations rely on the accuracy of models	• First remote sensing study of the Jotunheimen area at 1-km and 250 m resolutions. • The use of growing season surface temperatures to delineate continuous permafrost and tree lines

Pollen analysis is an excellent tool in environmental reconstruction, but the accuracy of estimating the past local presence of individual species remains challenging (Table 6.1). The main problem is estimating the source area of the pollen, which complicates the interpretation of the pollen record (as discussed in detail in Section 2.3 and Chapter 4). To minimise overreliance on one interpretation method, several complementary methods were used simultaneously in Chapter 4. Combining the commonly used pollen relative abundance with pollen accumulation rates provides a better idea of the proportions of taxa present in the landscape at a given time. Additionally, a modern sample gives a reference point and enables comparison of present-day pollen proportions captured in peat and moss to past proportions, further facilitating the estimation of species' local presence. Finally, identifying species that are indicative of certain environmental conditions in the spectra provided yet another proxy to improve the reconstruction of the past vegetation assemblages on Galdhøpiggen.

Satellite remote sensing not only expanded the temporal scale of the field-based study, but also the spatial scale, covering NE Jotunheimen in addition to Galdhøpiggen (Table 6.1). Compared to the data collected using abovementioned field- and laboratory methods, satellite remote sensing data are more accessible, as they are available from online sources. The method also has the capacity to obtain information over large areas that can be otherwise inaccessible, such as high latitudes and alpine terrain. Whilst Jotunheimen is a relatively accessible mountainous region, field-based surface temperature measurements cannot compete with the spatial scale provided by satellite imagery.

The novel approach used in Chapter 5 tested the applicability of summer land surface temperatures for identifying areas suitable for the establishment and growth of *Betula pubescens* and *Pinus sylvestris*. This approach, however, requires prior knowledge of the minimum required growing season air temperatures of a specific species in a given area. The closest match was found between mean June-September LSTs and the *Betula pubescens* tree line on Galdhøpiggen. In the absence of air temperature records, there is therefore potential in mapping surface temperatures to determine the areas suitable for downy birch growth in an alpine region.

However, remote sensing often requires ground truthing for validation of the findings. This is especially important and valuable in the case of tree line- and vegetation dynamics. Whilst dense vegetation was easily identifiable by using NDVI, the small-

scale changes directly above the tree line and at sparsely vegetated high altitudes above 1800 m a.s.l. were more difficult to interpret. Remote sensing techniques employ the relationship between NDVI and the amount of solar radiation captured for photosynthesis and therefore provide a bulk measure of vegetation; the methods used are too crude to distinguish between spaces and this limits detection of spatial heterogeneity of alpine tundra- and permafrost landscapes (Westermann et al., 2011). Nevertheless, NDVI proved to be a valuable tool for mapping large-scale patterns and shifts in vegetation change on Galdhøpiggen (see Figure 6.1). From the field methods (Chapter 3) it was concluded that increased NDVI observed in the satellite data is linked to the increased abundance of shrubs over low- and mid-alpine heaths (~1050-1500 m a.s.l.).

Regarding satellite-derived land surface temperatures, validation is possible through field visits or comparison with other published work that reports directly measured LST data over the same period. As discussed in Chapter 5, satellite-derived LSTs may be underestimated in the winter, when snow cover results in high surface albedo. To overcome this problem, annual mean LSTs were replaced by growing season LSTs to successfully map the occurrence of continuous permafrost.

6.3. Future implications

6.3.1. Continued increase in air- and surface temperatures

Whilst climatic conditions in the alpine Jotunheimen region demonstrate a cooling trend from 4000 cal. yr BP to c. 170 cal. yr BP, the trend from 170 cal. yr BP to the present day indicates warming. Evidence of climatic warming is found in the palynological records (Chapter 4) as well as within the recorded air temperatures and modelled land surface temperatures from 1957 to 2019 (Chapter 5), with the most significant increase in winter land surface temperatures (by as much as 2.8 °C at mid- and low altitudes below 1600 m a.s.l.). Even though the results presented in Chapter 5 indicate that the local warming trend in air- and surface temperatures has slowed in the area since 2000, temperatures are predicted to continue to increase in Jotunheimen (Hipp et al., 2012) and across the northern hemisphere (Biskaborn et al., 2019).

6.3.2. Continued degradation of permafrost

In response to increasing temperatures, sub-surface permafrost on Galdhøpiggen is warming and degrading (Etzelmüller et al., 2020). Whilst the methods used in this thesis do not directly measure the temperature or extent of permafrost, extensive research has been previously conducted in the area to monitor and map the state of permafrost on Galdhøpiggen (see sub-Section 1.4.1).

At higher altitudes (Juvvasshøe, 1894 m a.s.l.), borehole monitoring reveals that near-surface permafrost has warmed by an average of 0.04–0.05 °C every year for several decades (Isaksen et al., 2007) and the thickness of the active layer has increased 5% per decade since 1999 (Etzelmüller et al., 2020). At lower altitudes on Galdhøpiggen, the lower limit of permafrost is shifting upslope. Models indicate that the limit has already moved up by 200 m since 1860 (Hipp et al., 2012), and the latest estimates position the present-day lower limit at c. 1450-1470 m a.s.l. (Farbrot et al., 2011; Isaksen et al., 2011). Past movements of the lower permafrost limit in the area can also be indirectly inferred from palynological records (Chapter 4).

Future scenarios based on models predict a 55-75% probability of permafrost degradation at 1900 m a.s.l. by 2100, and complete degradation of permafrost at 1561 m a.s.l. before 2050 (Hipp et al., 2012). This would mean the upslope movement of the lower permafrost limit to above 1800 m a.s.l., which is unprecedented since the early Holocene (Lilleøren et al., 2012), and could lead to drastic changes over areas presently underlain by permafrost.

The remote sensing approach presented in Chapter 5 can not be used to directly measure sub-surface temperatures. However, due to the close relationship between ground- and ground surface temperatures on Galdhøpiggen (Isaksen et al., 2003), land surface temperatures can be used to map areas suitable for continuous permafrost occurrence. In this case, areas were identified where mean growing season (April-September) LSTs remain below 0 °C, providing suitable conditions for permafrost formation and preservation. The modelled LST data revealed a significant decrease in the extent of land with LST_{gs} below 0 °C between 1957-1976 and 2000-2019, providing further evidence that the climatic conditions in Jotunheimen are becoming less suitable to support the widespread occurrence of permafrost. This mapping method can be a useful and accessible tool for monitoring temporal changes in the extent of land with below-freezing mean surface temperatures during the growing season, contributing to permafrost monitoring in the area.

6.3.3. Decrease in cryoturbation at higher altitudes

Warming air-, surface- and sub-surface temperatures and thawing permafrost will affect freezing and thawing processes in the soil, and thus surface disturbance. On Galdhøpiggen, the largest changes would be expected above c. 1800 m a.s.l., where frost disturbance in the centres of sorted circles is currently highest. Previous studies focused on Fennoscandia have predicted a significant decrease in cryogenic activities in the soil in response to future warming (Aalto et al., 2014; Kade et al., 2005; Becher et al., 2018). On sorted circles, vegetation is predicted to encroach the previously disturbed surfaces as frost disturbance diminishes (Becher et al., 2015; Väisänen et al., 2017), which was also observed in the study reported in Chapter 3, as sorted circles at lowest altitudes are fully covered by vegetation. Following the scenario of decreased cryoturbation and surface disturbance, the extent and abundance of vegetation cover are likely to increase in the high-alpine belt.

6.3.4. Tree line advancement and shrub encroachment

The upslope advancement of northern alpine tree lines and increased vegetation greenness in the northern hemisphere in response to warming over the recent decades have been reported in the literature (Los, 2013; Zhu et al., 2016). This thesis explored the past and present tree line dynamics. Palynological records suggest that the altitudinal limits of the two main tree species on Galdhøpiggen, *Betula pubescens* and *Pinus sylvestris,* have fluctuated by hundreds of metres since c. 4350 cal. yr BP (Chapter 4). Modern pollen evidence from the peat core and moss polster taken at 1000 m a.s.l. reveals a small increase in the abundance of *B. pubescens* pollen over the past 14 years. Additional evidence from historic aerial photographs and field visits (Chapter 3) combined with modelled NDVI (Chapter 5) show an upslope advancement of stands of *Betula pubescens* by c. 60-80 m on the north-facing slope of Galdhøpiggen since 1981. Moreover, NDVI shows an increase at the present-day tree line at 1050 m a.s.l. since 1957, which can be in part attributed to the maturation of the *Betula pubescens* and *Pinus sylvestris* stands, which also becomes evident when comparing aerial photographs from 1981 and 2017.

In Arctic and alpine tundra environments, warming often leads to the encroachment of shrubs (*Salix, B. nana, Alnus*) at the expense of graminoids, forbs, bryophytes and lichens (Walker et al., 2006; Tape et al., 2006). Evidence of shrubs reaching altitudes above 1900 m a.s.l. and the increase in shrub abundance and/or stature at 1400-1600 m a.s.l. on Galdhøpiggen was presented in Chapters 3 and 5.

In Chapter 3, the ergodic principle is adopted, which assumes that the vegetation change across the altitudinal transect from higher to lower altitudes reflects temporal changes (i.e., the vegetation composition and/or abundance at lower altitudes represents the possible future vegetation cover at higher altitudes as warming continues). This approach was used to examine how surface CO_2 emissions could change with future warming. However, vegetation change is not always straightforward. Studies of vegetation succession in Jotunheimen (Matthews et al., 2018; Matthews and Whittaker 1987; Whittaker 1989, 1991) emphasise the importance of physical environmental processes (e.g., disturbance) in vegetation establishment, and suggest a geo-ecological interpretation is best to explain patterns of vegetational change, especially in alpine regions.

Vegetation succession across an altitudinal transect on Galdhøpiggen was examined by Matthews et al. (2018). The study found that relay succession (where the pioneer species are replaced by a new set of species) occurred in the sub-alpine vegetation belt, whilst evidence for autosuccession (where pioneer- and climax communities are identical) was found at the highest altitudes above 2000 m a.s.l. In the low- and mid-alpine vegetation belts, relay succession dominates, and most of the pioneer species (e.g., *Festuca ovina*, *Poa alpina*, *Luzula spicata*) will be completely replaced by mature heath species (e.g., *Salix* spp., *Betula nana*, *Empetrum hermaphroditum*, *Vaccinium* spp.). Indeed, the modelled changes in NDVI over the past six decades presented in Chapter 5 indicate that the highest rates of NDVI increase have occurred in the low- and mid-alpine belts, which is attributed to the increase in shrubby vegetation.

At higher altitudes (>1800 m a.s.l.), vegetation cover is sparser and of small stature, and not detectable from satellite imagery. The harsher climatic conditions, higher rates of cryogenic soil disturbance and the patterned landscape formed by past cryoturbation in the high-alpine belt (Chapter 3) all affect the patterns of vegetation establishment. Whilst no assumption is made that the future vegetation cover in the high-alpine belt

will be identical in extent and stature to that found in the low-alpine belt today, there is evidence that certain shrubby species characteristic of mature heath communities are already able to establish at elevations above 1800 m a.s.l. The small-scale vegetation survey on the field (Chapter 3) recorded *Salix herbacea* at every altitude at sites ranging from 1550-1950 m a.s.l. Moreover, Matthews et al. (2018) found no decline in the abundance of *Salix herbacea* with increasing altitude; instead, the abundance of *Salix herbacea* increased with the increase in the area affected by late snowbeds.

Although *Salix herbacea* is not a pioneer species, it was unexpectedly abundant on the two highest sites that exhibited the highest rates of disturbance along the transect, suggesting that the species can successfully establish in microsites created by surface disturbance (Chapter 3). Combining the evidence from the field study with remotely sensed NDVI data and previous vegetation surveys therefore indicates that shrubification has been affecting the low- and mid-alpine belts over the recent decades, and shrubs (namely *Salix herbacea*) are likely to increase in abundance at higher altitudes in response to warming, given that the soil conditions are suitable.

6.3.5. Increased CO_2 emissions in response to warming

Increased temperatures can affect ecosystem respiration in additional ways. Higher alpine soil temperatures can stimulate the activity of soil microbes, increasing the speed of carbon cycling and its release from the soil (Donhauser and Frey, 2018). Further, results presented in Chapter 3 show elevated rates of R_e over shrub-covered areas on Galdhøpiggen, which was attributed by the regression technique to a combination of possible factors, including greater plant productivity and litter input rates, and the additional output from root respiration. Whilst higher shrub biomass can increase the uptake of carbon during the growing season, the effect is most likely to be temporary, as the uptake can be offset by increased ecosystem respiration during autumn and winter (Mekonnen et al., 2018).

Chapter 3 concludes that vegetation is likely to encroach bare, frost-disturbed surfaces at progressively higher altitudes as freeze-thaw processes slow down or cease. It is yet unclear whether this permafrost region as a whole will act as a source or a sink of carbon in response to future warming. However, the trend identified in Chapter 3

suggests that increasing shrub cover and abundance at altitudes above 1500 m a.s.l. leads to intensified carbon cycling and elevated carbon release from the ecosystem. Whilst increased shrub abundance leads to a higher uptake of carbon from the atmosphere during the growing season, this effect can be offset in the long term due to increased ecosystem respiration in autumn and winter (Mekonnen et al., 2018). Additionally, shrub tundra often has a lower SOC content and higher rates of respiration compared to other types of vegetated tundra (Wilmking et al. 2006), and warm soil conditions during the growing season turn shrub-covered landscapes into a net source of CO_2 (Cahoon et al., 2006). Therefore, following the scenario of warming-driven increased shrub encroachment to higher altitudes on Galdhøpiggen, CO_2 emissions from the land surface are expected to increase. However, the magnitude of the net land surface CO_2 source or sink remains uncertain, as estimates of carbon uptake by vegetation and year-round measurements of respiration would be required to make such conclusions.

Increased winter warming can be another driver of soil respiration. Kreyling et al. (2019) reported an increase in the aboveground plant biomass in a cool-temperate grassland following winter warming, whilst plant biomass was not affected by summer warming. Moreover, winter warming led to higher increases in soil respiration compared to summer warming (Kreyling et al., 2019). In Chapter 5, the modelled land surface temperatures reveal that winter warming in Jotunheimen has been more significant than summer warming. The phenomenon of winter warming has been previously reported in Scandinavia (Førland et al., 2000; Isaksen et al., 2002), but it presently remains undetermined whether winter warming will also increase aboveground biomass and enhance soil respiration in the alpine ecosystems of Jotunheimen.

As temperature is identified as the main driver of greening in the northern hemisphere (see Chapter 5), the focus of this thesis has been on the influence of increasing temperatures rather than the influence of changes in precipitation patterns on the ecosystem. Therefore, precipitation was only considered indirectly in Chapter 3, where soil moisture was found to positively affect R_e during peak growing season.

However, precipitation will have an important role in controlling the future CO_2 emissions from tundra environments; especially in dry Arctic regions, where increased soil moisture increases soil- and root respiration (Natali et al., 2015; Illeris et al., 2003).

A similar effect was described in Chapter 3, where even a small increase in soil moisture during the dry peak growing season enhanced R_e. Therefore, the future growing season surface emissions of CO_2 in Jotunheimen depend on not only the degree of warming, but also on any changes in precipitation patterns, as soil moisture extremes (excessively dry or waterlogged conditions) both inhibit soil- and root respiration.

Considering the results presented in Chapters 3-5, and the trends and model estimations presented in similar studies, the most likely future scenario in response to warming in Jotunheimen will be decreased cryoturbation combined with increased shrub encroachment and ecosystem respiration rates, a combination likely leading to increased CO_2 emissions from the ground in Jotunheimen and similar alpine permafrost regions.

References

Aalto J, Le Roux PC and Luoto M (2013) Vegetation mediates soil temperature and moisture in Arctic-Alpine environments. *Arctic, Antarctic, and Alpine Research* 45(4): 429–439.

Aalto J, Venäläinen A, Heikkinen RK, et al. (2014) Potential for extreme loss in high-latitude Earth surface processes due to climate change. *Geophysical Research Letters* 41(11): 3914–3924.

Aartsma P, Asplund J, Odland A, et al. (2020) Surface albedo of alpine lichen heaths and shrub vegetation. *Arctic, Antarctic and Alpine Research* 52(1): 312-322.

Aas, B (1969) Climatically Raised Birch Lines in Southeastern Norway 1918-1968. *Norsk Geografisk Tidsskrift* 23(3): 119–130.

Aas B and Faarlund T (1988) Postglacial forest limits in central south Norwegian mountains. Radiocarbon datings of subfossil pine and birch specimens. *Norsk Geografisk Tidsskrift* 42(1): 25-61.

Aario L (1940) Waldgrenzen und subrenzenten Pollenspektren in Petsamo, Lappland. *Annales Academiae Scientiarum Fennicae* 54(8): 1-20.

Al-doski J, Mansor S and Shafri HZM (2013) NDVI differencing and post-classification to detect vegetation changes in Halabja City, Iraq. *IOSR Journal of Applied Geology and Geophysics* 1(2): 1–10.

Anthelme F, Villaret JC and Brun JJ (2007) Shrub encroachment in the Alps gives rise to the convergence of sub-alpine communities on a regional scale. *Journal of Vegetation Science* 18(3): 355–362.

Auble DL and Meyers TP (1992) An open path, fast response infrared absorption gas analyzer for H_2O and CO_2. *Boundary-Layer Meteorology* 59: 243-256.

Ballantyne CK (2018) *Periglacial Geomorphology*. Chichester: Wiley-Blackwell.

Barnekow L (1999) Holocene tree-line dynamics and inferred climatic changes in the Abisko area, northern Sweden, based on macrofossil and pollen records. *The Holocene* 9(3): 253-265.

Barnett C, Dumayne-Peaty L and Matthews JA (2001) Holocene climatic change and tree-line response in Leirdalen, central Jotunheimen, south central Norway. *Review of Palaeobotany and Palynology* 117(1-3): 119–137.

Barrett K, Rocha A, Van De Weg MJ et al. (2012) Vegetation Shifts Observed in Arctic Tundra 17 Years after Fire. *Remote Sensing Letters* 3(8): 729–736.

Barry RG (2008) Geographical controls of mountain meteorological elements. In: Barry RG (eds) *Mountain Weather and Climate.* Cambridge: Cambridge University Press, pp.24–124.

Beamish A, Raynolds MK, Epstein H et al. (2020) Recent trends and remaining challenges for optical remote sensing of Arctic tundra vegetation: A review and outlook. *Remote Sensing of Environment* 246: 111872.

Becher M, Olofsson J and Klaminder J (2015) Cryogenic disturbance and its impact on carbon fluxes in a subarctic heathland. *Environmental Research Letters* 10(11): 114006.

Becher M, Olofsson J, Berglund L, et al. (2018) Decreased cryogenic disturbance: one of the potential mechanisms behind the vegetation change in the Arctic. *Polar Biology* 41(1): 101-110.

Beck PSA, Atzberger C, Høgda KA, et al. (2006) Improved monitoring of vegetation dynamics at very high latitudes: A new method using MODIS NDVI. *Remote Sensing of Environment* 100(3): 321–334.

Behre K (1981) The interpretation of anthropogenic indicators in pollen diagrams. *Pollen et spores* 23: 225-245.

Belshe EF, Schuur EAG and Bolker BM (2013) Tundra ecosystems observed to be CO_2 sources due to differential amplification of the carbon cycle. *Ecology Letters* 16(10): 1307–1315.

Benn DI (1994) Fabric Shape and the Interpretation of Sedimentary Fabric Data. *Journal of Sedimentary Research* 64(4A): 910-915.

Bennett K and Willis KJ (2001) Pollen. In: Smol JP, Birks HJB and Last WM (eds) *Tracking Environmental Change Using Lake Sediments.* Volume 3: Terrestrial, Algal and Siliceous Indicators. Dordrecht: Kluwer Academic Publishers, pp.5-31.

Bennett KD (2000) *Psimpoll* and *pscomb:* computer programs for data plotting and analysis. Available from: https://chrono.qub.ac.uk/psimpoll/psimpoll.html (accessed 10 May 2020).

Bhatt US, Walker DA, Raynolds MK, et al. (2013) Recent declines in warming and vegetation greening trends over Pan-Arctic tundra. *Remote Sensing* 5: 4229–4254.

Birks HH and Birks HJB (2000) Future uses of pollen analysis must include plant macrofossils. *Journal of Biogeography* 27(1): 31-35.

Birks HH and Bjune AE (2010) Can we detect a west Norwegian tree line from modern samples of plant remains and pollen? Results from the DOORMAT project. *Vegetation History and Archaeobotany* 19: 325-340.

Birks HH, Vorren K-D and Birks HJB (1996) Holocene treelines, dendrochronology and palaeoclimate. *Paläoklimaforschung* 20: 1-18.

Birks HJB (1968) The identification of *Betula nana* pollen. *New Phytologist* 67(2): 309-314.

Birks HJB and Birks HH (1980) *Quaternary Palaeoecology*. London: Arnold.

Birks HJB, Heiri O, Seppä H et al. (2010) Strengths and Weaknesses of Quantitative Climate Reconstructions Based on Late-Quaternary Biological Proxies. *The Open Ecology Journal* 3: 68-110.

Biskaborn BK, Smith SL, Noetzli J, et al. (2019) Permafrost is warming at a global scale. *Nature Communications* 10: 264.

Bjerke JW, Bokhorst S, Zielke M, et al. (2011) Contrasting sensitivity to extreme winter warming events of dominant sub-Arctic heathland bryophyte and lichen species. *Journal of Ecology* 99(6): 1481-1488.

Bjerke JW, Karlsen SR, Høgda KA, et al. (2014) Record-low primary productivity and high plant damage in the Nordic Arctic Region in 2012 caused by multiple weather events and pest outbreaks. *Environmental Research Letters* 9: 084006.

Bjune AE (2005) Holocene vegetation history and tree-line changes on a north-south transect crossing major climate gradients in southern Norway - evidence from pollen and plant macrofossils in lake sediments. *Review of Palaeobotany and Palynology* 133(3-4): 249–275.

Blaauw M (2010) Methods and code for 'classical' age-modelling of radiocarbon sequences. *Quaternary Geochronology* 5(5): 512-518.

Blaauw M and Christen JA (2005) Radiocarbon peat chronologies and environmental change. *Journal of the Royal Statistical Society* 54(4): 805-816.

Blok D, Heijmans MMPD, Schaepman-Strub G, et al. (2010) Shrub expansion may reduce summer permafrost thaw in Siberian tundra. *Global Change Biology* 161: 296–305.

Blok D, Schaepman-Strub G and Bartholomeus H (2011) The response of arctic vegetation to the summer climate: relation between shrub cover, NDVI, surface albedo and temperature. *Environmental Research Letters* 6(3): 035502.

Bockheim J (2007) Importance of Cryoturbation in Redistributing Organic Carbon in Permafrost-Affected Soils. *Soil Science Society of America Journal* 71(1): 1335-1342.

Boelman NT, Gough L, McLaren JR, et al. (2011) Does NDVI reflect variation in the structural attributes associated with increasing shrub dominance in arctic tundra? *Environmental Research Letters* 6(3): 035501.

Bokhorst S, Bjerke JW, Bowles FW, et al. (2008) Impacts of extreme winter warming in the sub-arctic: growing season responses of dwarf shrub heathland. *Global Change Biology* 14: 2603–2612.

Brown DG (2013) Comparisons of vegetation-topography relationships at the alpine tree ecotone. *Physical Geography* 15(2): 125-145.

Bunting MJ (2003) Pollen-vegetation relationships in non-arboreal moorland taxa. *Review of Palaeobotany and Palynology* 125(3-4): 285-298.

Cahoon SMP, Sullivan PF, Shaver GR, et al. (2012) Interactions among shrub cover and the soil microclimate may determine future Arctic carbon budgets. *Ecology Letters* 15(12): 1415–1422.

Callaghan TV, Bergholm F, Christensen TR, et al. (2010) A new climate era in the sub-Arctic: Accelerating climate changes and multiple impacts. *Geophysical Research Letters* 37(14): L14705.

Cannone N, Sgorbati S and Guglielmin M (2007) Unexpected impacts of climate change on alpine vegetation. *Frontiers in Ecology and the Environment* 5: 360–364.

Caseldine CJ (1984) Pollen analysis of a buried arctic-alpine Brown Soil from Vestre Memurubreen, Jotunheimen, Norway: evidence for postglacial high-altitude vegetation change. *Arctic and Alpine Research* 16(4): 423-430.

Caseldine CJ (1989) Pollen assemblage-plant community relationships on the Storbreen glacier foreland, Jotunheimen Mountains, southern Norway. *New Phytologist* 111: 105–118.

Caseldine CJ and Pardoe HS (1994) Surface pollen studies from alpine/sub-alpine southern Norway: applications to Holocene data. *Review of Palaeobotany and Palynology* 82(1-2): 1-15.

Cazzolla Gatti R, Callaghan T, Velichevskaya, A et al. (2019) Accelerating upward treeline shift in the Altai Mountains under last-century climate change. *Scientific Reports* 9: 7678.

Celis G, Mauritz M, Bracho R, et al. (2017) Tundra is a consistent source of CO_2 at a site with progressive permafrost thaw during 6 years of chamber and eddy covariance measurements. *Journal of Geophysical Research: Biogeosciences* 122(6): 1471–1485.

Chae N, Kang H, Kim Y, et al. (2016) CO_2 efflux from the biological soil crusts of the High Arctic in a later stage of primary succession after deglaciation, Ny-Ålesund, Svalbard, Norway. *Applied Soil Ecology* 98: 92-102.

Chambers FM, Beilman DW and Yu Z (2011) Methods for determining peat humification and for quantifying peat bulk density, organic matter and carbon content for palaeostudies of climate and peatland carbon dynamics. *Mires and Peat* 7(7): 1-10.

Chapin FS III (1983) Direct and indirect effects of temperature on arctic plants. *Polar Biology* 2: 47–52.

Chapin FS III, Sturm M, Serreze MC, et al. (2005) Role of land-surface changes in Arctic summer warming. *Science* 310(5748): 657–660.

Cho MH, Yang AR, Baek EH, et al. (2018) Vegetation-cloud feedbacks to future vegetation changes in the Arctic regions. *Climate Dynamics* 50: 3745–3755.

Choubin B, Soleimani F, Pirnia A, et al. (2019) Chapter 17 - Effects of drought on vegetative cover changes: Investigating spatiotemporal patterns. In: Melesse AM, Abtew W and Senay G (eds) *Extreme Hydrology and Climate Variability.* Elsevier, pp. 213-222.

Clifford N, Holloway S, Rice S, et al. (2009) *Key Concepts in Geography*. 2nd ed. London: SAGE Publications Ltd.

Comiso JC (2003) Warming trends in the Arctic from clear sky satellite observations. *Journal of Climate* 16: 3498–3510.

Comiso JC (2006) Arctic warming signals from satellite observations. *Weather* 61: 70–76.

Coops NC, Wulder MA and Iwanicka D (2009) Large area monitoring with a MODIS-based Disturbance Index (DI) sensitive to annual and seasonal variations. *Remote Sensing of Environment* 113: 1250–1261.

Cray AC and Pollard WH (2015) Vegetation Recovery Patterns Following Permafrost Disturbance in a Low Arctic Setting: Case Study of Herschel Island, Yukon, Canada. *Arctic, Antarctic, and Alpine Research* 47(1): 99-113.

Cui L and Shi J (2010) Temporal and spatial response of vegetation NDVI to temperature and precipitation in eastern China. *Journal of Geographical Sciences* 20(2): 163-176.

Curasi SR, Loranty MM and Natali SM (2016) Water track distribution and effects on carbon dioxide flux in an eastern Siberian upland tundra landscape. *Environmental Research Letters* 11(4): 045002.

Dagg J and Lafleur P (2011) Vegetation Community, Foliar Nitrogen, and Temperature Effects on Tundra CO_2 Exchange across a Soil Moisture Gradient. *Arctic, Antarctic, and Alpine Research* 43(2): 189-197.

Davidson EA, Belk E and Boone RD (1998) Soil water content and temperature as independent or confounded factors controlling soil respiration in a temperate mixed hardwood forest. *Global Change Biology* 4(2): 217-227.

Davis MB (1967) Pollen accumulation rates at Rogers Lake, Conneticut, during late- and postglacial time. *Review of Palaeobotany and Palynology* 2: 219-230.

Davis MB (1969) Climatic Changes in Southern Connecticut Recorded by Pollen Deposition at Rogers Lake. *Ecology* 50(3): 409-422.

Davis MB and Sugita S (1997) Reinterpreting the fossil pollen record of Holocene tree migration. In: Huntley B, Cramer W, Morgan AV et al. (eds) *Past and Future Rapid*

Environmental Changes. NATO ASI Series (Series I: Global Environmental Change). Berlin: Springer, pp.181-193.

Dial R J, Berg E E, Timm K, et al. (2007) Changes in the alpine forest-tundra ecotone commensurate with recent warming in southcentral Alaska: evidence from orthophotos and field plots. *Journal of Geophysical Research* 112: G04015.

Diaz S, Symstad, AJ, Chapin FS III, et al. (2003) Functional diversity revealed by removal experiments. *Trends in Ecology & Evolution* 18(3): 140–146.

Dieleman CM, Branfireun BA and Lindo Z (2017) Northern peatland carbon dynamics driven by plant growth form - the role of graminoids. *Plant Soil Journal* 415(1-2): 25-35.

Didan K, Barretto Munoz A, Solano R, et al. (2015) MODIS Vegetation Index User's Guide (MOD13 Series). University of Arizona, US, June.

Doetterl S, Stevens A, Six J, et al. (2015) Soil carbon storage controlled by interactions between geochemistry and climate. *Nature Geoscience* 8: 780-783.

Donhauser J and Frey B (2018) Alpine soil microbial ecology in a changing world. *FEMS Microbiology Ecology* 94(9): fiy099.

Dullinger S, Dirnböck T and Grabherr G (2003) Patterns of shrub invasion into high mountain grasslands of the Northern Calcareous Alps, Austria. *Arctic, Antarctic, and Alpine Research* 35(4): 434–41.

Efron B, Hastie T, Johnstone I, et al. (2004) Least angle regression. *Annals of Statistics* 32(2): 407-499.

Eide W, Birks HH, Bigelow NH et al. (2006) Holocene forest development along the Setesdal valley, southern Norway, reconstructed from macrofossil and pollen evidence. *Vegetation History and Archaeobotany* 15: 65-85.

Ellenberg H (1963) *Vegetation Mitteleuropas mit den Alpen in kausaler, dynamischer und historischer Sicht.* Stuttgart: Eugen Ulmer.

Epstein HE, Beringer J, Gould WA, et al. (2004) The Nature of Spatial Transitions in the Arctic. *Journal of Biogeography* 31(12): 1917-1933.

Etzelmüller B, Berthling I and Sollid JL (1998) The distribution of permafrost in Southern Norway; a GIS approach. *Collection Nordicana* 57: 251– 257.

Etzelmüller B, Guglielmin M, Hauck C, et al. (2020) Twenty years of European mountain permafrost dynamics—the PACE legacy. *Environmental Research Letters* 15(10): 104070.

Euskirchen E, McGuire A and Chapin FS (2007) Energy feedbacks of northern high-latitude ecosystems to the climate system due to reduced snow cover during 20th century warming. *Global Change Biology* 13: 2425–2438.

Euskirchen ES, Bret-Harte MS, Shaver GR, et al. (2017) Long-Term Release of Carbon Dioxide from Arctic Tundra Ecosystems in Alaska. *Ecosystems* 20(5): 960-974.

Evans DJA, Hiemstra JF and O'Cofaigh C (2007) An assessment of clast macrofabrics in glacigenic sediments based on A/B plane data. *Geografiska Annaler Series A Physical Geography* 89(2): 103-120.

Farbrot H, Hipp TF, Etzelmüller B, et al. (2011) Air and ground temperature variations observed along elevation and continentality gradients in Southern Norway. *Permafrost and Periglacial Processes* 22(4): 343-360.

Forbes BC, Fauria MM and Zetterberg P (2010) Russian Arctic warming and 'greening' are closely tracked by tundra shrub willows. *Global Change Biology* 16: 1542–1554.

Førland E, Roald LA, Tveito OE, et al. (2000) Past and future variations in climate and runoff in Norway. Report no. 19/00, Norwegian Meteorological Institute, Norway, 8 September.

Fox AM, Huntley B, Lloyd CR et al. (2008) Net ecosystem exchange over heterogeneous Arctic tundra: Scaling between chamber and eddy covariance measurements. *Global Biogeochemical Cycles* 22(2): GB2027.

Fox AM, Huntley B, Lloyd CR, et al. (2008) Net ecosystem exchange over heterogeneous Arctic tundra: Scaling between chamber and eddy covariance measurements. *Global Biogeochemical Cycles* 22(2): GB2027.

Francis JA and Hunter E (2006) New insight into the disappearing Arctic sea ice. *Eos Transactions American Geophysical Union* 87: 509– 511.

Franke AK, Feilhauer H, Bräuning A, et al. (2019) Remotely sensed estimation of vegetation shifts in the polar and alpine tree-line ecotone in Finnish Lapland during the last three decades. *Forest Ecology and Management* 454: 117668.

Frost GV, Bhatt US, Epstein HE et al. (2019) Tundra Greenness. In: Richter-Menge J, Druckenmiller ML and Jeffries M (eds) *Arctic Report Card 2019.* Available at: http://www.arctic.noaa.gov./Report-Card (accessed 10 May 2020).

Frost GV, Epstein HE, Walker DA, et al. (2013) Patterned ground facilitates shrub expansion in Low Arctic tundra. *Environmental Research Letters* 8: 015035.

Ge L, Lafleur PM and Humphreys ER (2017) Respiration from Soil and Ground Cover Vegetation Under Tundra Shrubs. *Arctic, Antarctic, and Alpine Research* 49(4): 537-550.

Gerber F, de Jong R, Schaepman E, et al. (2018) Predicting missing values in spatio-temporal remote sensing data. *IEEE Transactions on Geoscience and Remote Sensing* 56(5): 2841 - 2853.

Giesecke T and Bennett KD (2004) The Holocene spread of *Picea abies* (L.) Karst. in Fennoscandia and adjacent areas. *Journal of Biogeography* 31: 1523-1548.

Gisnås K, Etzelmüller B, Lussana C, et al. (2017) Permafrost Map for Norway, Sweden and Finland. *Permafrost and Periglacial Processes* 28(2): 359–378.

Goward SN, Cruickshanks GD and Hope AS (1985) Observed relation between thermal emission and reflected spectral radiance of a complex vegetated landscape. *Remote Sensing of Environment* 18: 137−146.

Grace J, Berninger F and Nagy L (2002) Impacts of climate change on the tree line. *Annals of Botany* 90(4): 537–544.

Grand S, Rubin A, Verrecchia EP, et al. (2016) Variation in Soil Respiration across Soil and Vegetation Types in an Alpine Valley. *PLoS ONE* 11(9): e0163968.

Graversen RG, Mauritsen T, Tjernstrom M, et al. (2008) Vertical structure of recent Arctic warming. *Nature* 451: 53–56.

Grimm EC (1987) CONISS: a FORTRAN 77 program for stratigraphically constrained cluster analysis by the method of incremental sum of squares. *Computers & Geosciences* 13(1): 13-35.

Groß E, Mård J, Kalantari Z, et al. (2018) Links between Nordic and Arctic hydroclimate and vegetation changes: contribution to possible landscape-scale nature-based solutions. *Land Degradation and Development* 29(10): 3663-3673.

Grosse G, Goetz S, McGuire AD, et al. (2016) Changing permafrost in a warming world and feedbacks to the Earth system. *Environmental Research Letters* 11(4): 040201.

Grove JM (2004) *Little Ice Ages: Ancient and Modern.* London: Routledge.

Gruber S (2012) Derivation and analysis of a high-resolution estimate of global permafrost zonation. *The Cryosphere* 6: 221–233.

Grytnes J, Kapfer J, Jurasinski G, et al. (2014) Identifying the driving factors behind observed elevational range shifts on European mountains. *Global Ecology and Biogeography* 23: 876–884.

Haberli W (2013) Mountain permafrost - research frontiers and a special long-term challenge. *Cold Regions Science and Technology* (96): 71-76.

Hachem S, Allard M and Duguay CR (2009) Using the MODIS Land Surface Temperature Product for Mapping Permafrost: An Application to Northern Quebec and Labrador, Canada. *Permafrost and Periglacial Processes* 20: 407-416.

Hachem S, Duguay CR and Allard M (2012) Comparison of MODIS-derived land surface temperatures with ground surface and air temperature measurements in continuous permafrost terrain. *The Cryosphere* 6: 51-69.

Haeberli W, Noetzli J, Arenson L, et al. (2010) Mountain permafrost: development and challenges of a young research field. *Journal of Glaciology* 56(200): 1043-1058.

Hallang H, Hiemsta JF, Los SO, et al. (2020) Carbon dioxide emissions from periglacial patterned ground under changing permafrost conditions and shrub encroachment in an alpine landscape, Jotunheimen, Norway. *Permafrost and Periglacial Processes* 31(4): 524-537.

Hallet B (2013) Stone circles: Form and soil kinematics. *Philosophical Transactions of the Royal Society A: Mathematical, Physical and Engineering Sciences* 371: 20120357.

Hallinger M, Manthey M and Wilmking M (2010) Establishing a missing link: warm summers and winter snow cover promote shrub expansion into alpine tundra in Scandinavia. *New Phytologist* 186(4): 890–899.

Hansen J and Nazarenko L (2004) Soot Climate Forcing via Snow and Ice Albedo. *Proceedings of the National Academy of Sciences of the United States of America* 101: 423–428.

Hauck C, Isaksen K, Mühl DV, et al. (2004) Geophysical Surveys Designed to Delineate the Altitudinal Limit of Mountain Permafrost: an Example from Jotunheimen, Norway. *Permafrost and Periglacial Processes* 15(3): 191-205.

Haugland J (2006) Short-term Periglacial Processes, Vegetation Succession, and Soil Development within Sorted Patterned Ground: Jotunheimen, Norway. *Arctic, Antarctic and Alpine Research* 38(1): 82-89.

Haugland JE (2004) Formation of patterned ground and fine-scale soil development within two late Holocene glacial chronosequences: Jotunheimen, Norway. *Geomorphology* 61(3-4): 287-301.

Hermle S, Lavigne MB, Bernier PY, et al. (2010) Component respiration, ecosystem respiration and net primary production of a mature black spruce forest in northern Quebec. *Tree Physiology* 30(4): 527–540.

Hicks Pries CE, Schuur EAG and Grummer KG (2012) Holocene Carbon Stocks and Carbon Accumulation Rates Altered in Soils Undergoing Permafrost Thaw. *Ecosystems* 15: 162-173.

Hicks S (2001) The use of annual arboreal pollen deposition values for delimiting tree-lines in the landscape and exploring models of pollen dispersal. *Review of Palaeobotany and Palynology* 117(1-3): 1-29.

Hicks S (2006) When no pollen does not mean no trees. *Vegetation History and Archaeobotany* 15: 253-261.

Hijmans RJ and van Etten J (2012) Raster: Geographic analysis and modeling with raster data. R package version 2.0-12. Available at: http://CRAN.R-project.org/package=raster (accessed 12 October 2020).

Hinzman LD, Deal CJ, McGuire AD, et al. (2013) Trajectory of the Arctic as an integrated system. *Ecological Applications* 23: 1837-1868.

Hipp T, Etzelmüller B, Farbrot H, et al. (2012) Modelling borehole temperatures in Southern Norway - insights into permafrost dynamics during the 20th and 21st century. *The Cryosphere* 6(3): 553-571.

Hobbie SE (1996) Temperature and plant species control over litter decomposition in Alaskan tundra. *Ecological Monographs* 66(4): 503-522.

Hock R, Rasul G, Adler C, et al. (2019) High Mountain Areas. In: Pörtner HO, Roberts DC, Masson-Delmotte V, et al. (eds) *IPCC Special Report on the Ocean and Cryosphere in a Changing Climate.* In press.

Holtmeier F and Broll G (2005) Sensitivity and response of northern hemisphere altitudinal and polar treelines to environmental change at landscape and local scales. *Global Ecology and Biogeography* 14: 395–410.

Hope A and Stow D (1995) Shortwave reflectance properties of Arctic tundra. In: Reynolds J and Tenhuenen J (eds) *Landscape function and disturbance in Arctic tundra. Ecological Studies.* Heidelberg: Springer, pp. 155–164.

Hope A, Engstrom R and Stow D (2005) Relationship between AVHRR surface temperature and NDVI in Arctic tundra ecosystems. *International Journal of Remote Sensing* 26(8): 1771-1776.

Hua Q, Barbetti M and Rakowski A (2013) Atmospheric Radiocarbon for the Period 1950–2010. *Radiocarbon* 55(4): 2059-2072.

Hugelius G, Strauss J, Zubrzycki S, et al. (2014) Estimated stocks of circumpolar permafrost carbon with quanti-fied uncertainty ranges and identified data gaps. *Biogeosciences* 11(23): 6573–6593.

Hulley G, Freepartner R, Malakar N, et al. (2016) Moderate Resolution Imaging Spectroradiometer (MODIS) Land Surface Temperature and Emissivity Product (MxD21) User Guide. National Aeronautics and Space Administration, California, December.

Huntley B and Birks HJB (1983) *An atlas of past and present pollen maps for Europe: 0–13000 years ago.* Cambridge: Cambridge University Press.

Illeris L, Michelsen A and Jonasson S (2003) Soil plus root respiration and microbial biomass following water, nitrogen, and phosphorus application at a high arctic semi-desert. *Biogeogeochemistry* 65: 15–29.

IPCC (2007) Summary for Policymakers. In: Solomon S, Qin D, Manning M et al. (eds) Climate *Change 2007: The Physical Science Basis. Contribution of Working Group I to the Fourth Assessment Report of the Intergovernmental Panel on Climate Change*. Cambridge: Cambridge University Press.

Isaksen K, Hauck C, Gudevang E, et al. (2002) Mountain permafrost distribution in Dovrefjell and Jotunheimen, southern Norway, based on BTS and DC resistivity tomography data. *Norsk Geografisk Tidsskrift* 56(2): 122-136.

Isaksen K, Heggem ESF, Bakkehøi S, et al. (2003) Mountain permafrost and energy balance on Juvvasshøe, southern Norway. In: *Proceedings Volume 1, Eighth International Conference on Permafrost* (ed M Philips, SM Springmann and LU Arenson), Zurich, Switzerland, 21-25 July 2003, pp.467-472. Lisse: Swets Zeitlinger.

Isaksen K, Ødegård RS, Etzelmüller B, et al. (2011) Degrading mountain permafrost in Southern Norway: Spatial and temporal variability of mean ground temperatures, 1999-2009. *Permafrost and Periglacial Processes* 22(4): 361-377.

Isaksen K, Sollid JL, Holmlund P, et al. (2007) Recent warming of mountain permafrost in Svalbard and Scandinavia. *Journal of Geophysical Research* 112: F02S04.

Jackson ST (1991) Pollen representation of vegetational patterns along an elevational gradient. *Journal of Vegetation Science* 2(5): 613-624.

Jackson ST and Lyford ME (1999) Pollen Dispersal Models in Quaternary Plant Ecology: Assumptions, Parameters, and Prescriptions. *The Botanical Review* 65(1): 39-75.

Ji L and Fan K (2019) Climate Prediction of Satellite-Based Spring Eurasian Vegetation Index (NDVI) using Coupled Singular Value Decomposition (SVD) Patterns. *Remote Sensing* 11: 2123.

Jia GJ, Epstein HE and Walker DA (2002) Spatial characteristics of AVHRR-NDVI along latitudinal transects in northern Alaska. *Journal of Vegetation Science* 13: 315–326.

Jin M and Dickinson RE (2010) Land surface skin temperature climatology: Benefitting from the strengths of satellite observations. *Environmental Research Letters* 5: 044004.

Johansson M, Callaghan TV, Bosiö J, et al. (2013) Rapid responses of permafrost and vegetation to experimentally increased snow cover in sub-arctic Sweden. *Environmental Research Letters* 8: 035025.

Johnson LC, Shaver GR, Giblin AE, et al. (1996) Effects of drainage and temperature on carbon balance of tussock tundra microcosms. *Oecologia* 108(4): 737–748.

Juszak I, Erb AM, Maximov TC, et al. (2014) Arctic shrub effects on NDVI, summer albedo and soil shading. *Remote Sensing of Environment* 153: 79-89.

Jönsson P and Eklundh P (2004) TIMESAT—A program for analyzing time-series of satellite sensor data. *Computers & Geosciences* 30(8): 833–845.

Kade A and Walker D (2008) Experimental Alteration of Vegetation on Nonsorted Circles: Effects on Cryogenic Activity and Implications for Climate Change in The Arctic. *Arctic, Antarctic, and Alpine Research* 40(1): 96-103.

Kade A, Walker DA and Raynolds MK (2005) Plant communities and soils in cryoturbated tundra along a bioclimate gradient in the Low Arctic, Alaska. *Phytocoenologia* 35(4): 761-820.

Kaiser C, Meyer H, Biasi C et al. (2007) Conservation of soil organic matter through cryoturbation in arctic soils in Siberia. *Journal of Geophysical Research* 112(2): G02017.

Karlsdóttir L, Hallsdóttir M, Thórsson AT et al. (2008) Characteristics of pollen from natural triploid Betula hybrids. *Grana* 47(1): 52–59.

Kartverket (2021) Norge i Bilder. Available at: www.norgeibilder.no (accessed 4 January 2021).

Keenan TF and Riley WJ (2018) Greening of the land surface in the world's cold regions consistent with recent warming. *Nature Climate Change* 8: 825-828.

Kessler MA, Murray AB and Werner BT (2011) A Model for Sorted Circles as Self-Organized Patterns. *Journal of Geophysical Research* 106(B7): 13287-13306.

Kim Y, Nishina N, Park SJ, et al. (2014) Constraint of soil moisture on CO_2 efflux from tundra lichen, moss,and tussock in Council, Alaska, using a hierarchical Bayesian model. *Biogeosciences* 11(19): 5567-5579.

Klaminder J, Giesler R and Makoto K (2013) Physical mixing between humus and mineral matter found in cryoturbated soils increases short-term heterotrophic respiration rates. *Soil Biology and Biochemistry* 57: 922-924.

Klanderud K and Birks H (2003) Recent increases in species richness and shifts in altitudinal distributions of Norwegian mountain plants. *The Holocene* 13(1): 1-6.

Kling J (1998) Observations of sorted circle development, Sweden. *Permafrost and Periglacial Processes* 8(4): 447-453.

Körner C (1999) *Alpine Plant Life: Functional Plant Ecology of High Mountain Ecosystems*. Berlin: Springer.

Kreyling J, Grant K, Hammerl V, et al. (2019) Winter warming is ecologically more relevant than summer warming in a cool-temperate grassland. *Scientific Reports* 9: 14632.

Kullman L (1990) Dynamics of altitudinal tree-limits in Sweden: a review. *Norsk Geografisk Tidsskrift* 44(2): 103-116.

Kullman L (2001) 20th century climate warming and tree-limit rise in the southern Scandes of Sweden. *Ambio* 30: 72–80.

Kullman L (2002) Rapid recent range-margin rise of tree and shrub species in the Swedish Scandes. *Journal of Ecology* 90(1): 68-77.

Kullman L and Öberg L (2009) Post-Little Ice Age tree line rise and climate warming in the Swedish Scandes: a landscape ecological perspective. *Journal of Ecology* 97(3): 415-429.

Kumar M and Monteith JL (1982) Remote sensing of plant growth. In: H. Smith (eds) *Plants and daylight spectrum*. London: Academic Press, pp.133-144.

Kumpula T, Pajunen A and Kaarlejärvi E (2011) Land use and land cover change in arctic Russia: ecological and social implications of industrial development. *Global Environmental Change* 215: 50–62.

Kuoppamaa M, Goslar T and Hicks S (2009) Pollen accumulation rates as a tool for detecting land-use changes in a sparsely settled boreal forest. *Vegetation History and Archaeobotany* 18: 205-217.

Lagouarde J-P, Irvine M and Dupont S (2015) Atmospheric turbulence induced errors on measurements of surface temperature from space. *Remote Sensing of Environment* 168: 40–53.

Langer M, Westermann S and Boike J (2010) Spatial and temporal variations of summer surface temperatures of wet polygonal tundra in Siberia - implications for MODIS LST based permafrost monitoring. *Remote Sensing of Environment* 114: 2059–2069.

Lara MJ, Nitze I, Grosse G, et al. (2018) Reduced arctic tundra productivity linked with landform and climate change interactions. *Scientific Reports* 8: 2345.

Larsen K, Ibrom A, Jonasson S, et al. (2007) Significance of cold-season respiration and photosynthesis in a subarctic heath ecosystem in Northern Sweden. *Global Change Biology* 13: 1498–1508.

Li G, Mu J, Liu Y, et al. (2017) Effect of microtopography on soil respiration in an alpine meadow of the Qinghai-Tibetan plateau. *Plant Soil Journal* 421(1-2): 147-155.

Libby WF (1972) Dating by radiocarbon. *Accounts of Chemical Research* 5(9): 289-295.

LI-COR Biosciences (2015) Using the LI-8100A Automated Soil CO_2 Flux System and LI-8150 Multiplexer. Available at: https://www.licor.com/env/support/LI-8100A/home.html (accessed 14 April 2018).

Lilleøren KS, Etzelmüller B and Schuler TV, et al. (2012) The relative age of permafrost – estimation of Holocene permafrost limits in Norway. *Global and Planetary Change* 92-93: 209-223.

Lindsey R and Herring D (2020) MODIS Moderate Resolution Imaging Spectroradiometer. Available at: https://modis.gsfc.nasa.gov/about/media/modis_brochure.pdf (accessed 15 May 2021).

Lisitsyna OV and Hicks S (2014) Estimation of pollen deposition time-span in moss polsters with the aid of annual pollen accumulation values from pollen traps. *Grana* 53(3): 232-248.

Lisitsyna OV, Giesecke T and Hicks S (2011) Exploring pollen percentage threshold values as an indication for the regional presence of major European trees. *Review of Palaeobotany* 166(3-4): 311-324.

Liu Z, Wu C, Liu Y, et al. (2017) Spring green-up date derived from GIMMS3g and SPOT-VGT NDVI of winter wheat cropland in the North China Plain. *ISPRS Journal of Photogrammetry and Remote Sensing* 130: 81-91.

Lomolino MV (2001) Elevation gradients of species-density, historical and prospective views. *Global Ecology and Biogeography* 10(1): 3–13.

Loranty MM, Berner LT, Taber ED, et al. (2018) Understory vegetation mediates permafrost active layer dynamics and carbon dioxide fluxes in open-canopy larch forests of northeastern Siberia. *PloS one* 13(3): e0194014.

Loranty MM, Goetz SJ and Beck PSA (2011) Tundra vegetation effects on pan-arctic albedo. *Environmental Research Letters* 6: 024014.

Los SO (2013) Analysis of trends in fused AVHRR and MODIS NDVI data for 1982-2006: Indication for a CO_2 fertilization effect in global vegetation. *Global Biogeochemical Cycles* 27: 318-330.

Los SO, Collatz GJ, Bounoua L, et al. (2001) Global Interannual Variations in Sea Surface Temperature and Land Surface Vegetation, Air Temperature, and Precipitation. *Journal of Climate* 14(7): 1535–1549.

Lund M, Raundrup K, Westergaard-Nielsen A, et al. (2017) Larval outbreaks in West Greenland: instant and subsequent effects on tundra ecosystem productivity and CO_2 exchange. *Ambio* 46: 26–38.

Lundin E, Klaminder J, Giesler R, et al. (2016) Is the subarctic landscape still a carbon sink? Evidence from a detailed catchment balance. *Geophysical Research Letters* 43(5)*:*1988-1995.

Luo G and Dai L (2013) Detection of alpine tree line change with high spatial resolution remotely sensed data. *Journal of Applied Remote Sensing* 7(1): 073520.

Macias-Fauria M, Forbes BC, Zetterberg P, et al. (2012) Eurasian Arctic greening reveals teleconnections and the potential for structurally novel ecosystems. *Nature Climate Change* 2: 613–618.

MapTiler (2021) Open-source maps made for self-hosting. Available at: http://openmaptiles.org/ (accessed 20 May 2021).

Marchenko S, Hachem S, Romanovsky V, et al. (2009) Permafrost and active layer modeling in the Northern Eurasia using MODIS Land Surface Temperature as an input data. *Geophysical Research Abstracts* 11: EGU2009-11077.

Marsh P, Bartlett P, MacKay M, et al. (2010) Snowmelt energetics at a shrub tundra site in the western Canadian Arctic. *Hydrological Processes* 24: 3603–3620.

Martin AC, Jeffers ES, Petrokofsky G, et al. (2017) Shrub growth and expansion in the Arctic tundra: an assessment of controlling factors using an evidence-based approach. *Environmental Research Letters* 12: 085007.

Marushchak ME, Kiepe I, Biasi C, et al. (2013) Carbon dioxide balance of subarctic tundra from plot to regional scales. *Biogeosciences* 10(1): 437-452.

Mathisen IE, Mikheeva A, Tutubalina OV, et al. (2014) Fifty years of tree line change in the Khibiny Mountains, Russia: advantages of combined remote sensing and dendroecological approaches. *Applied Vegetation Science* 17(1): 6–16.

Matthews JA (1992) *The ecology of recently deglaciated terrain: a geoecological approach to glacier forelands and primary succession*. Cambridge: Cambridge University Press.

Matthews JA (1999) Disturbance regimes and ecological response on recently deglaciated substrates. In: Walker LR (eds) *Ecosystems of Disturbed Ground*. 1 ed. Amsterdam: Elsevier Science, pp.1–16.

Matthews JA and Dresser PQ (2008) Holocene glacier variation chronology of the Smørstabbtindan massif, Jotunheimen, southern Norway, and the recognition of century- to millennial-scale European Neoglacial Events. *The Holocene* 18(1): 181-201.

Matthews JA and Vater AE (2015) Pioneer zone geo-ecological change: observations from a chronosequence on the Storbreen glacier foreland, Jotunheimen, southern Norway. *Catena* 135: 219-230.

Matthews JA and Whittaker RJ (1987) Vegetation Succession on the Storbreen Glacier Foreland, Jotunheimen, Norway: A Review. *Arctic and Alpine Research* 19(4): 385-395.

Matthews JA, Dahl SO, Nesje A et al. (2000) Holocene glacier variations in central Jotunheimen, southern Norway based on distal glaciolacustrine sediment cores. *Quaternary Science Reviews* 19(16): 1625-1647.

Matthews JA, Hill JL, Winkler S, et al. (2018) Autosuccession in alpine vegetation: Testing the concept on an altitudinal bioclimatic gradient, Jotunheimen, southern Norway. *Catena* 170: 169-182.

Matthews JA, Shakesby RA, Berrisford MS, et al. (1998) Periglacial patterned ground on the Styggedalsbreen glacier foreland, Jotunheimen, southern Norway: micro-topographic, paraglacial and geoecological controls. *Permafrost and Periglacial Processes* 9: 147–166.

May JL, Hollister RD, Betway KR, et al. (2020) NDVI Changes Show Warming Increases the Length of the Green Season at Tundra Communities in Northern Alaska: A Fine-Scale Analysis. Frontiers in Plant Science 11: 1174.

McGuire AD, Anderson LG, Christensen TR, et al. (2009) Sensitivity of the carbon cycle in the Arctic to climate change. *Ecological Monographs* 79(4): 523–555.

McGuire AD, Christensen TR, Hayes D, et al. (2012) An assessment of the carbon balance of Arctic tundra: comparisons among observations, process models, and atmospheric inversions. *Biogeosciences* 9(8): 3185–3204.

Mekonnen ZA, Riley WJ and Grant RF (2018) 21st century tundra shrubification could enhance net carbon uptake of North America Arctic tundra under an RCP 8.5 climate trajectory. *Environmental Research Letters* 13(5): 054029.

Mellon FA (2003) Mass spectrometry: Principles and Instrumentation. In: Caballero B (eds) *Encyclopaedia of Food Sciences and Nutrition* (Second Edition). Academic Press, pp.3739-3749.

Meredith M, Sommerkorn M and Cassotta S (2019) Polar Regions. In: Pörtner H-O, Roberts DC, Masson-Delmotte V, et al. (eds*) IPCC Special Report on the Ocean and Cryosphere in a Changing Climate*. In press, pp.203-320.

Mildrexler D, Zhao M, Heinsch FA, et al. (2007) A New Satellite-based methodology for continental-scale disturbance detection. *Ecological Applications* 17(1): 235-250.

Mod HK, Le Roux PC and Luoto M (2014) Outcomes of biotic interactions are dependent on multiple environmental variables. *Journal of Vegetation Science* 25(4): 1024-1032.

Moe D and Odland A (1992) The influence of the temperature climate on the vertical distribution of *Alnus incana* (Betulaceae) through the Holocene in Norway. *Acta Botanica Fennica* 144: 35–49.

Moen A (1999) *National Atlas of Norway: Vegetation*. Hønefoss: Norwegian Mapping Authority.

Moore PD, Collinson ME and Webb JA (1994) *Pollen Analysis, Second edition*. Oxford: Blackwell Scientific Publications.

Moreno Á, García-Haro FJ, Martínez B, et al. (2014) Noise reduction and gap filling of fAPAR time series using an adapted local regression filter. *Remote Sensing* 6(9): 8238–8260.

Muster S, Langer M, Abnizova A, et al. (2015) Spatio-temporal sensitivity of MODIS land surface temperature anomalies indicates high potential for large-scale land cover change detection in Arctic permafrost landscapes. *Remote Sensing of Environment* 168: 1-12.

Myerscough, PJ (1980) Epilobium Angustifolium L. *Journal of Ecology* 68(3): 1047-1074.

Myers-Smith IH, Forbes B, Wilmking M, et al. (2011) Shrub expansion in tundra ecosystems: dynamics, impacts and research priorities. *Environmental Research Letters* 6(4):045509.

Myers-Smith IH, Kerby JT, Phoenix GK, et al. (2020) Complexity revealed in the greening of the Arctic. *Nature Climate Change* 10: 106-117.

NASA (2021) MODIS Moderate Resolution Imaging Spectroradiometer. Available at: modis.gsfc.nasa.gov/ (accessed 19 April 2021).

Natali S, Schuur E and Rubin R (2012) Increased plant productivity in Alaskan tundra as a result of experimental warming of soil and permafrost. *Journal of Ecology* 100: 488–449.

Natali SM, Schuur EAG, Mauritz M, et al. (2015) Permafrost thaw and soil moisture driving CO_2 and CH_4 release from upland tundra. *Journal of Geophysical Research: Biogeosciences* 120(3): 525-537.

Natali SM, Schuur EAG, Trucco C, et al. (2011) Effects of experimental warming of air, soil and permafrost on carbon balance in Alaskan tundra. *Global Change Biology* 17(3): 1394-1407.

Nauta AL, Monique MPD Heijmans MMPD, et al. (2014) Permafrost collapse after shrub removal shifts tundra ecosystem to a methane source. *Nature Climate Change* 5: 67-70.

Nemani RR and Running SW (1996) Global vegetation cover changes from coarse resolution satellite data. *Journal of Geophysical Research* 101(D3): 7157-7162.

Nesje A and Kvamme M (1991) Holocene glacier and climate variations in western Norway: Evidence for early Holocene glacier demise and multiple Neoglacial events. *Geology* 19(6): 610-612.

Neteler M (2010) Estimating daily land surface temperatures in mountainous environments by reconstructed MODIS LST data. *Remote Sensing* 2(1): 333–351.

Newton EJ, Pond BA and Brown GS (2014) Remote sensing reveals long-term effects of caribou on tundra vegetation. *Polar Biology* 37: 715–725.

NIJOS (1991) Vegetasjonskart: Galdhøpiggen 1518II (1:50,000). Norsk Institutt for Jord- og Skogkartlegging (NIJOS): Ås.

Nitze I, Grosse G, Jones BM, et al. (2018) Remote sensing quantifies widespread abundance of permafrost region disturbances across the Arctic and Subarctic, Lake dataset. *Nature Communications* 9(1): 5423.

NOAA (2020) Global Historical Climate Network. Available at: ncdc.noaa.gov/cdo-web/datasets#GHCND (accessed 1 October 2020).

Norwegian Meteorological Institute (2020) Klima. Available at: http://senorge.no (accessed 3 February 2020).

Norwegian Meteorological Institute (2021) Klima. Available at: http://senorge.no (accessed 10 January 2021).

Nychka D, Furrer R, Paige J and Sain S (2017) Fields: Tools for spatial data. R package version 12.3. Available at: https://github.com/NCAR/Fields (accessed 12 October 2020).

Obu J, Westermann S, Bartsch A, et al. (2019) Northern Hemisphere permafrost map based on TTOP modelling for 2000–2016 at 1 km^2 scale. *Earth-Science Reviews* 193: 299–316.

Ødegård RA, Hoelzle M, Johansen KV, et al. (1996) Permafrost mapping and prospecting in southern Norway. *Norsk Geografisk Tidsskrift* 50(1): 41-53.

Ødegård RS, Sollid JL and Liestøl O (1988) Periglacial forms related to terrain parameters in Jotunheimen, southern Norway. In: Permafrost: V International Conference on Permafrost. Tapir: Trondheim, pp.59-61.

Ødegård RS, Sollid JL and Liestol O (1992) Ground temperature measurements in mountain permafrost, Jotunheimen, southern Norway. *Permafrost and Periglacial Processes* 3(3): 231-234.

Olthof I and Pouliot D (2010) Treeline vegetation composition and change in Canada's western Subarctic from AVHRR and canopy reflectance modeling. *Remote Sensing of Environment* 114: 805-815.

Oswald WW, Brubaker LB, Hu FS, et al. (2003) Pollen-vegetation calibration for tundra communities in the Arctic Foothills, northern Alaska. *Journal of Ecology* 91(6): 1022-1033.

Overland JE, Hanna E, Hanssen-Bauer I, et al. (2019) Surface Air temperature. In: Richter-Menge J, Druckenmiller ML and Jeffries M (eds) *Arctic Report Card 2019.* Available at: http://www.arctic.noaa.gov./Report-Card (accessed 10 May 2020).

Pardoe HS (1996) Micro-scale patterns of modern pollen deposition within three alpine plant communities. *New Phytologist* 132(2): 327–341.

Pardoe HS (2006) Surface pollen deposition on glacier forelands in southern Norway I: Local patterns of representation and source area at Storbreen, Jotunheimen. *The Holocene* 16(8): 1149–1161.

Pardoe HS (2014) Surface pollen deposition on glacier forelands in southern Norway II: Local patterns of representation and source area at Storbreen, Jotunheimen. *The Holocene* 24(12): 1675 –1685.

Pardoe HS, Giesecke T, van der Knaap WO et al. (2010) Comparing pollen spectra from modified Tauber traps and moss samples: examples from a selection of woodlands across Europe. *Vegetation History and Archaeobotany* 19: 271–283.

Parker TC, Subke JA, Wookey PA (2015) Rapid carbon turnover beneath shrub and tree vegetation is associated with low soil carbon stocks at a subarctic treeline. *Global Change Biology* 21(5): 2070–2081.

Pattison RR, Jorgenson JC, Raynolds MK, et al. (2015) Trends in NDVI and tundra community composition in the Arctic of NE Alaska between 1984 and 2009. *Ecosystems* 18: 707–719.

Paus A (2010) Vegetation and environment of the Rødalen alpine area, Central Norway, with emphasis on the early Holocene. *Vegetation History and Archaeobotany* 19: 29–51.

Pearson R, Phillips S, Loranty M, et al. (2013) Shifts in Arctic vegetation and associated feedbacks under climate change. *Nature Climate Change* 3: 673-677.

Peeters L and Totland Ø (1999) Wind to insect pollination ratios and floral traits in five alpine *Salix* species. *Canadian Journal of Botany* 77(4): 556-563.

Peng X, Wu W, Zheng Y, et al. (2020) Correlation analysis of land surface temperature and topographic elements in Hangzhou, China. *Scientific Reports* 10: 10451.

Pettorelli N (2013) *The Normalised Difference Vegetation Index.* London: Oxford University Press.

Phillips CA and Wurzburger N (2019) Elevated rates of heterotrophic respiration in shrub-conditioned arctic tundra soils. *Pedobiologia* 72: 8–15.

Phillips M and Schweizer J (2007) Effect of mountain permafrost on snow-pack stability. *Cold Regions Science and Technology* 47: 43–49.

Phoenix GK and Bjerke JW (2016) Arctic browning: extreme events and trends reversing arctic greening. *Global Change Biology* 22: 2960–2962.

Pomeroy JW, Bewley DS, Essery RLH, et al. (2006) Shrub tundra snowmelt. *Hydrological Processes* 20: 923–41.

Post E, Forchhammer MC, Bret-Harte MS, et al. (2009) Ecological dynamics across the Arctic associated with recent climate change. *Science* 325(5946): 1355–1358.

Prentice IC and Webb III T (1986) Pollen percentages, tree abundances and the Fagerlind effect. *Journal of Quaternary Science* 1(1): 35-43.

Price JC (1990) Using Spatial Context in Satellite Data to Infer Regional Scale Evapotranspiration. *IEEE Transactions on Geoscience and Remote Sensing* 28(5): 940-948.

R Core Team (2019) R: A language and environment for statistical computing. The R Project for Statistical Computing. Available at: https://www.R-project.org/ (accessed 14 April 2019).

R Core Team (2021) R: A language and environment for statistical computing. The R Project for Statistical Computing. Available at: https://www.R-project.org/ (accessed 14 May 2021).

Raich JW and Tufekcioglu A (2000) Vegetation and soil respiration: Correlations and controls. *Biogeochemistry* 48: 71-90.

Raynolds MK, Comiso JC, Walker DA, et al. (2008) Relationship between satellite-derived land surface temperatures, arctic vegetation types, and NDVI. *Remote Sensing of Environment* 112(4): 1884–1894.

Raynolds MK, Walker DA, Epstein HE, et al. (2012) A new estimate of tundra-biome phytomass from trans-Arctic field data and AVHRR NDVI. *Remote Sensing Letters* 3(5): 403-411.

Reille, M. (1999) *Pollen et spores d'europe et d'afrique du nord*. Marseille: Laboratoire de Botanique historique et Palynologie.

Reimer PJ, Austin WEN, Bard E, et al. (2020) The IntCal20 Northern Hemisphere Radiocarbon Age Calibration Curve (0–55 cal k BP) *Radiocarbon* 62(4): 725–757.

Reimer PJ, Bard E, Bayliss A, et al. (2013) IntCal13 and Marine13 Radiocarbon Age Calibration Curves 0–50,000 Years cal BP. *Radiocarbon* 55(4): 1869–1887.

Rime T, Hartmann M and Brunner I (2015) Vertical distribution of the soil microbiota along a successional gradient in a glacier forefield. *Molecular Ecology* 24(5): 1091–108.

Robbins JA and Matthews JA (2010) Regional variation in successional trajectories and rates of vegetation change on glacier forelands in south-central Norway. *Arctic, Antarctic, and Alpine Research* 42(3): 351-361.

Robbins JA and Matthews JA (2014) Use of ecological indicator values to investigate successional change in boreal to high-alpine glacier foreland chronosequences, south Norway. *The Holocene* 24(11): 1453-1464.

Robock, A (1980) The seasonal cycle of snow cover, sea ice and surface albedo. *Monthly Weather Review* 108(3): 267–285.

Rocha, AV, Loranty MM, Higuera PE, et al. (2012) The footprint of Alaskan tundra fires during the past half-century: implications for surface properties and radiative forcing. *Environmental Research Letters* 7: 044039.

Romanovsky VE, Smith SL and Christiansen HH (2010) Permafrost thermal state in the Polar Northern Hemisphere during the international polar year 2007-2009: a synthesis. *Permafrost and Periglacial Processes* 21(2): 106–116.

Running SW, Justice CO, Salomonson V, et al. (1994) Terrestrial remote sensing science and algorithms planned for EOS/MODIS. *International Journal of Remote Sensing* 15(17): 358-3620.

Sætersdal M, Birks HJB and Peglar SM (1998) Predicting changes in Fennoscandian vascular-plant species richness as a result of future climatic change. *Journal of Biogeography* 25(1): 111-122.

Saiz G, Black K, Reidy B, et al. (2007) Assessment of soil CO_2 efflux and its components using a process-based model in a young temperate forest site. *Geoderma* 139(1-2): 79-89.

Sazonova T and Romanovsky V (2003) A model for regional-scale estimation of temporal and spatial variability of active layer thickness and mean annual ground temperatures. *Permafrost Periglacial Processes* 14: 125–139.

Schuur EAG, Bockheim J, Canadell JG, et al. (2008) Vulnerability of permafrost carbon to climate change: implications for the global carbon cycle. *BioScience* 58(8): 701–714.

Schuur EAG, McGuire AD, Schädel C, et al. (2015) Climate change and the permafrost carbon feedback. *Nature* 520: 171-179.

Schuur EAG, Vogel JG, Crummer KG, et al. (2009) The effect of permafrost thaw on old carbon release and net carbon exchange from tundra. *Nature* 459(7246): 556–559.

Seppä H (1996) Post-glacial dynamics of vegetation and tree-lines in the far north of Fennoscandia. *Fennia - International Journal of Geography* 174(1): 1-96.

Seppä H and Birks HJB (2001) July mean temperature and annual precipitation trends during the Holocene in the Fennoscandian tree-line area: pollen-based climate reconstructions. *The Holocene* 11(5): 527-539.

Serreze MC and Barry RG (2011) Processes and impacts of Arctic amplification: A research synthesis. *Global and Planetary Change* 77: 85-96.

Serreze MC, Walsh JE, Chapin III FS, et al. (2000) Observational evidence of recent change in the northern high-latitude environment. *Climatic Change* 46: 159-207.

Shaver, GR, Street LE, Rastetter EB, et al. Functional convergence in regulation of net CO_2 flux in heterogeneous tundra landscapes in Alaska and Sweden. *Journal of Ecology* 95(4): 802-817.

Shen ZX, Li YL and Fu G (2015) Response of soil respiration to short-term experimental warming and precipitation pulses over the growing season in an alpine meadow on the Northern Tibet. *Applied Soil Ecology* 90: 35–40.

Shindell D and Faluvegi G (2009) Climate response to regional radiative forcing during the twentieth century. *Nature Geoscience* 2: 294–300.

Silapaswan CS, Verbyla DL and McGuire AD (2001) Land cover change on the Seward Peninsula: The use of remote sensing to evaluate the potential influences of climate warming on historical vegetation dynamics. *Canadian Journal of Remote Sensing* 27(5): 542–554.

Stocker TF, Qin D, Plattner GK, et al. (2013) *Climate Change 2013: The Physical Science Basis.* Working Group I Contribution to the Fifth Assessment Report of the Intergovernmental Panel on Climate Change. UK: Cambridge University Press. pp.1-1535.

Stockmarr J (1971) Tablets with spores used in absolute pollen analysis. *Pollen Spores* 13: 615-621.

Stow DA, Hope A, McGuire D, et al. (2004) Remote sensing of vegetation and land-cover change in Arctic Tundra Ecosystems. *Remote Sensing of Environment* 89: 281–308.

Street LE, Shaver GR, Williams M, et al. (2007) What is the relationship between changes in canopy leaf area and changes in photosynthetic CO_2 flux in arctic ecosystems? *Journal of Ecology* 95(1): 139–150.

Streletskiy DA, Biskaborn BK, Noetz J, et al. (2017) Permafrost thermal state. *Bulletin of the American Meteorological Society* 98(8): 19-21.

Stuiver M and Reimer PJ (1993) Extended 14C data base and revised CALIB 3.0 14C age calibration program. *Radiocarbon* 35(1): 215–230.

Stuiver M, Reimer PJ and Reimer RW (2021) CALIB 8.2. Available at: http://calib.org (accessed 10 May 2021).

Sturm M, McFadden JP, Liston GE, et al. (2001) Snow–shrub interactions in arctic tundra: a hypothesis with climatic implications. *Journal of Climate* 143: 36–44.

Sturm M, Racine C and Tape K (2001) Increasing shrub abundance in the Arctic. *Scientific Reports* 411: 546–547.

Tape K, Sturm M and Racine C (2006) The evidence for shrub expansion in northern Alaska and the Pan-Arctic. *Global Change Biology* 12(4): 686–702.

Tarnocai C, Canadell JG, Schuur EAG, et al. (2009) Soil organic carbon pools in the northern circumpolar permafrost region. *Global Biogeochemical Cycles* 23(2): GB2023.

Tempfli K, Kerle N, Huurneman GC, et al. (eds) (2009) *Principles of Remote Sensing*. Fourth edition. Enschede: ITC.

Thermo Fisher Scientific (2021) What is XRF (X-ray Fluorescence) and How Does it Work? Available at: https://www.thermofisher.com/blog/ask-a-scientist/what-is-xrf-x-ray-fluorescence-and-how-does-it-work/ (accessed 1 June 2021).

Tomlinson C, Chapman L, Thornes J, et al. (2011) Remote sensing land surface temperature for meteorology and climatology: a review. *Meteorological Applications* 18(3): 296-306.

Treharne R, Bjerke JW and Tømmervik H (2019) Arctic browning: Impacts of extreme climatic events on heathland ecosystem CO_2 fluxes. *Global Change Biology* 25: 489-503.

Tucker CJ and Sellers PJ (1986) Satellite remote sensing of primary production. *International Journal of Remote Sensing* 7(11): 1395–1416.

Tucker CJ, Slayback DA, Pinzon JE, et al. (2001) Higher northern latitude normalized difference vegetation index and growing season trends from 1982 to 1999. *International Journal of Biometeorology* 45: 184–190.

Turetsky MR, Abbott BW, Jones MC, et al. (2019) Permafrost collapse is accelerating carbon release. *Nature* 569(7754): 32-34.

Twiddle C (2012) Section 4.1.4: Pollen Analysis: Not Just a Qualitative Tool. In: Cook SJ, Clarke LE and Nield JM (eds) *Geomorphological Techniques* (Online Edition). London: British Society for Geomorphology, ISSN: 2047-0371.

Uxa T, Mida P and Křížek M (2017) Effect of Climate on Morphology and Development of Sorted Circles and Polygons. *Permafrost and Periglacial Processes* 28: 663-674.

Van der Knaap WO, van Leeuwen JFN, Svitavská-Svobodová H, et al. (2010) Annual pollen traps reveal the complexity of climatic control on pollen productivity in Europe and the Caucasus. *Vegetation History and Archaeobotany* 19: 285-307.

Verger A, Baret F, Weiss M, et al. (2013) The CACAO method for smoothing, gap filling, and characterizing seasonal anomalies in satellite time series. *IEEE Transactions on Geoscience and Remote Sensing* 51(4): 1963–1972.

Virkkala AM, Virtanen T, Lehtonen A et al. (2018) The current state of CO_2 flux chamber studies in the Arctic tundra: A review. *Progress in Physical Geography* 42(2): 162-184.

Von Stedingk H, Fyfe RM, Allard A (2008) Pollen productivity estimates from the forest–tundra ecotone in west-central Sweden: Implications for vegetation reconstruction at the lim- its of the boreal forest. *The Holocene* 18(2): 323–332.

Vonk J, Tank S, Bowden W et al. (2015) Reviews and syntheses: Effects of permafrost thaw on Arctic aquatic ecosystems. *Biogeosciences* 12(i): 7129-7167.

Vonlanthen CM, Walker DA, Raynolds MK et al. (2008) Patterned-ground plant communities along a bioclimate gradient in the High Arctic, Canada. *Phytocoenologia* 38: 23-63.

Väisänen M, Krab EJ and Dorrepaal E (2017) Carbon dynamics at frost-patterned tundra driven by long-term vegetation change rather than by short-term non-growing season warming. *Biogeochemistry* 136(1): 103-117.

Walker DA, Epstein H, Gould WA, et al. (2004) Frost-boil ecosystems: complex interactions between landforms, soils, vegetation and climate. *Permafrost and periglacial processes* 15: 171-188.

Walker DA, Epstein HE, Jia GJ, et al. (2003) Phytomass, LAI, and NDVI in northern Alaska: Relationships to summer warmth, soil pH, plant functional types, and extrapolation to the circumpolar Arctic. *Journal of Geophysical Research* 108(D2): 8169.

Walker DA, Kuss P, Epstein HE, et al. (2011) Vegetation of zonal patterned-ground ecosystems along the North America Arctic bioclimate gradient. *Applied Vegetation Science* 14(4): 440-463.

Walker MD, Wahren CH, Hollister RD, et al. (2006) Plant community responses to experimental warming across the tundra biome. *Proceedings of the National Academy of Sciences of the United States of America* 103(5): 1342–1346.

Walther GR, Beissner S and Burga CA (2005) Trends in upward shift of alpine plants. *Journal of Vegetation Science* 16: 541–548.

Wan Z, Zhang Y and Zhang YQ (2004) Quality assessment and validation of the global land surface temperature. *International Journal of Remote Sensing* 25(1): 261-274.

Wan Z, Zhang Y, Zhang Q et al. (2002) Validation of the land-surface temperature products retrieved from Terra Moderate Resolution Imaging Spectroradiometer data. *Remote Sensing of Environment* 83(1-2): 163-180.

Wang J, Rich PM and Price KP (2003) Temporal responses of NDVI to precipitation and temperature in the central Great Plains, USA. *International Journal of Remote Sensing* 24(11): 2345-2364.

Washburn AL (1989) Near-surface soil displacement in sorted circles, Resolute area, Cornwallis Island, Canadian High Arctic. *Canadian Journal of Earth Sciences* 26(5): 941–955.

Westermann S, Langer M and Boike J (2011) Spatial and temporal variations of summer surface temperatures of high-arctic tundra on Svalbard — Implications for MODIS LST based permafrost monitoring. *Remote Sensing of Environment* 115: 908–922.

Westermann S, Østby TI, Gisnås K, et al. (2015) A ground temperature map of the North Atlantic permafrost region based on remote sensing and reanalysis data. *The Cryosphere* 9: 1303–1319.

Whittaker RJ (1989) The vegetation of the Storbreen Gletschervorfeld, Jotunheimen, Norway. III. Vegetation-environment relationships. *Journal of Biogeography* 16: 413-433.

Whittaker RJ (1991) The vegetation of the Storbreen gletschervorfeld, Jotunheimen, Norway. IV. Short-term vegetation change. *Journal of Biogeography* 18: 41-52.

Wik M, Crill P, Varner R, et al. (2013) Multiyear measurements of ebullitive methane flux from three subarctic lakes. *Journal of Geophysical Research: Biogeosciences* 118: 1307–1321.

Wilcox EJ, Keim D, de Jong T (2019): Tundra shrub expansion may amplify permafrost thaw by advancing snowmelt timing. *Arctic Science* 5: 202–217.

Williams M, Street LE, Van Wijk MT et al. (2006) Identifying differences in carbon exchange among arctic ecosystem types. *Ecosystems* 9(2): 288-304.

Wilmking M, Harden J and Tape K (2006) Effect of tree line advance on carbon storage in NW Alaska. *Journal of Geophysical Research: Biogeosciences* 111(G2): G02023.

Wilson SD and Nilsson C (2009) Arctic alpine vegetation change over 20 years. *Global Change Biology* 15: 1676–1684.

Winkler S, Donner A, Tintrup gen. Suntrup A (2021) Periglacial Landforms in Jotunheimen, Central Southern Norway, and Their Altitudinal Distribution. In: Beylich AA (eds) Landscapes and Landforms of Norway. Switzerland: Springer Nature, pp.69-202.

Winkler S, Matthews JA, Mourne RW et al. (2016) Schmidt-hammer exposure ages from periglacial patterned ground (sorted circles) in Jotunheimen, Norway, and their interpretive problems. *Geografiska Annaler: Series A Physical Geography* 98(3): 265–285.

Yang Y, Gao Y, Wang S, et al. (2014) The microbial gene diversity along an elevation gradient of the Tibetan grassland. *The ISME Journal* 8(2): 430–440.

Ylänne H, Stark S, Tolvanen A, et al. (2015) Vegetation shift from deciduous to evergreen dwarf shrubs in response to selective herbivory offsets carbon losses: evidence from 19 years of warming and simulated herbivory in the subarctic tundra. *Global Change Biology* 21(10): 3696–3711.

Yoshikawa K and Hinzman LD (2003) Shrinking thermokarst ponds and groundwater dynamics in discontinuous permafrost near council, Alaska. *Permafrost and Periglacial Processes* 14(2): 151-160.

Young DM, Baird AJ, Charman DJ et al. (2019) Misinterpreting carbon accumulation rates in records from near-surface peat. *Scientific Reports* 9: 17939.

Zhang H, Piilo SR, Amesbury MJ, et al. (2018) The role of climate change in regulating Arctic permafrost peatland hydrological and vegetation change over the last millennium. *Quaternary Science Reviews* 182: 121-130.

Zhang T, Barry RG, Knowles K, et al. (1999) Statistics and characteristics of permafrost and ground-ice distribution in the Northern Hemisphere. *Polar Geography* 23: 132–154.

Zhang Y, Xu M, Adams J, et al. (2009) Can Landsat imagery detect tree line dynamics? *International Journal of Remote Sensing* 30(5): 1327-1340.

Zhang, X, Friedl MA, Schaaf CB, et al. (2004) Climate controls on vegetation phenological patterns in northern mid- and high latitudes inferred from MODIS data. *Global Change Biology* 10: 1133–1145.

Zhu Z, Piao S, Myneni R, et al. (2016) Greening of the Earth and its drivers. *Nature Climate Change* 6: 791-796.

Zhu Y, Kang EL, Bo Y et al. (2015) A robust fixed rank Kriging method for improving the spatial completeness and accuracy of satellite SST products. *IEEE Transactions on Geoscience and Remote Sensing* 53(9): 5021–5035.

Appendices

i) Supplementary material: Chapter 3

Supplementary Table 3.1. The extent (%) of different land cover types within individual collars, listed by site.

	Collar	Crust/lichen	Moss	Herbaceous	Shrub	Unvegetated
Site 1	**1.1.1**	0	0	0	0	100
	1.2.1	0	0	0	0	100
	1.3.1	5	0	0	0	95
	1.1.2	90	0	0	10	0
	1.2.2	90	10	0	0	0
	1.3.2	65	0	10	25	0
	1.1.3	10	0	50	40	0
	1.2.3	65	10	0	25	0
	1.3.3	50	0	0	50	0
Site 2	**2.1.1**	10	0	10	0	80
	2.2.1	95	0	5	0	0
	2.3.1	0	0	0	0	100
	2.1.2	60	0	10	30	0
	2.2.2	85	0	0	15	0
	2.3.2	50	0	0	50	0
	2.1.3	90	0	0	10	0
	2.2.3	85	0	0	15	0
	2.3.3	90	0	0	10	0
Site 3	**3.1.1**	95	5	0	0	0
	3.2.1	90	5	5	0	0
	3.3.1	80	10	5	0	5
	3.1.2	20	0	80	0	0
	3.2.2	25	0	50	15	10
	3.3.2	80	0	15	0	5
	3.1.3	30	0	70	0	0
	3.2.3	30	20	50	0	0
	3.3.3	15	0	85	0	0

Site 4	**4.1.1**	50	0	0	10	40
	4.2.1	40	0	0	10	50
	4.3.1	15	0	0	0	85
	4.1.2	65	0	0	35	0
	4.2.2	90	0	10	0	0
	4.3.2	70	0	0	20	10
	4.1.3	55	0	0	45	0
	4.2.3	10	0	85	5	0
	4.3.3	25	0	0	75	0
Site 5	**5.1.1**	80	5	5	10	0
	5.2.1	80	0	0	20	0
	5.3.1	95	5	0	0	0
	5.1.2	95	0	0	5	0
	5.2.2	80	5	5	10	0
	5.3.2	65	5	5	25	0
	5.1.3	40	5	40	15	0
	5.2.3	50	0	30	20	0
	5.3.3	90	0	0	10	0

ii) Supplementary material: Chapter 4

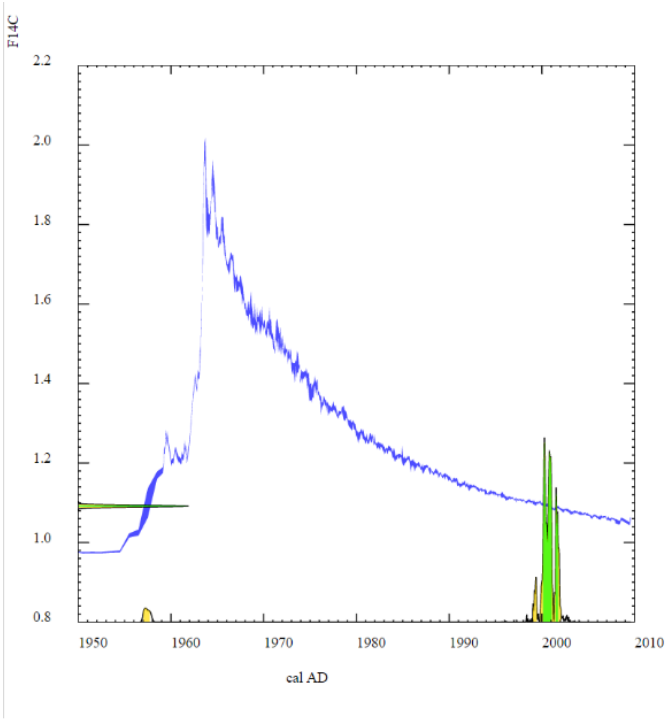

Supplementary Figure 4.1. The calibration output for the 'greater than modern' radiocarbon date ($F^{14}C$ = 1.0915±0.0021) using the post-bomb calibration dataset 'NHZ1' by Hua et al. (2013). The left-hand axis shows radiocarbon concentration (in fracion of modern, $F^{14}C$) and the bottom axis shows calendar years (cal AD). The dark blue lines indicate the radiocarbon measurements of the peat sample (±1 standard deviation). The green spike on the left-hand axis shows the radiocarbon concentration in the peat sample, whilst the green and yellow lines on the bottom axis indicate possible ages for that peat sample, with higher peaks indicating the more likely ages.

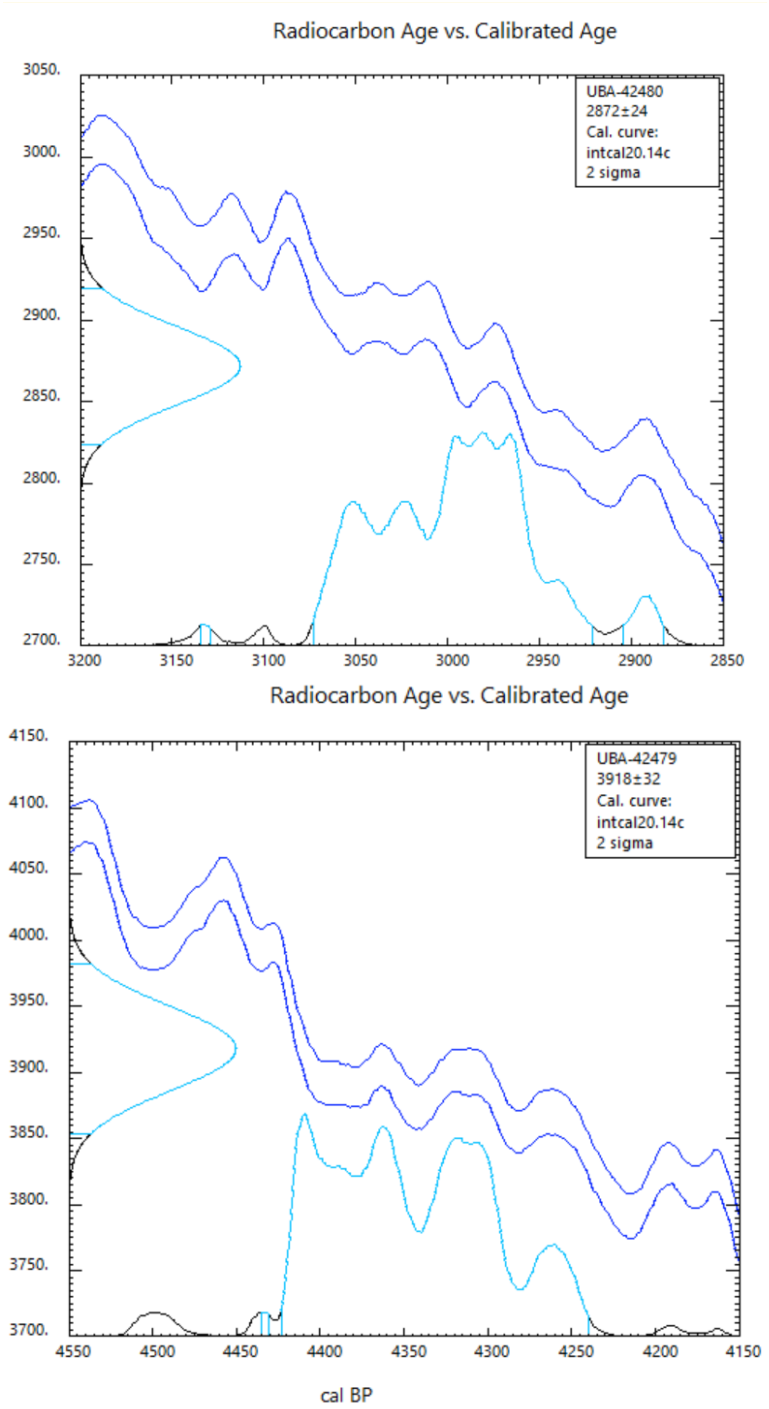

Supplementary Figure 4.2. The calibration output for the radiocarbon dates at 24 cm (upper image) and 46 cm (lower image) depth using the IntCal20 calibration curve (Reimer et al. 2020) and the software CALIB (8.2). The left-hand axis shows radiocarbon concentration (in years before present) and the bottom axis shows calendar years before present (cal BP). The dark blue lines indicate the radiocarbon measurements of the peat sample (±1 standard deviation). The light blue line on the left shows the radiocarbon concentration in the peat sample, whilst the light blue line on the bottom axis indicates possible ages for that peat sample, with higher peaks indicating the more likely ages.

Supplementary Table 4.1. Calendar age (cal. yr BP) estimates (at 95% confidence ranges) and sediment accumulation rates throughout a peat core taken from Galdhøpiggen (see Chapter 4). The estimates are based on the age-depth model created in R (3.6.3). Negative values indicate departure from 1950 AD towards present.

Depth (cm)	Min 95%	Max 95%	Best estimate	Sediment accumulation rate
6	-66	-62	-64	3.51
7	-62	-59	-60	3.51
8	-58	-56	-57	3.51
9	-55	-52	-53	3.51
10	-52	-48	-50	217.59
11	161	174	168	217.59
12	371	397	385	217.59
13	582	619	603	217.59
14	793	842	820	217.59
15	1004	1065	1038	217.59
16	1215	1288	1256	217.59
17	1426	1512	1473	217.59
18	1637	1735	1691	217.59
19	1847	1958	1908	217.59
20	2058	2181	2126	217.59
21	2269	2404	2344	217.59
22	2480	2627	2561	217.59
23	2691	2850	2779	217.59
24	2902	3073	2996	61.66
25	2967	3133	3058	61.66
26	3032	3192	3120	61.66
27	3097	3253	3181	61.66
28	3165	3318	3243	61.66
29	3231	3379	3305	61.66
30	3295	3440	3366	61.66
31	3357	3500	3428	61.66
32	3423	3558	3490	61.66
33	3486	3619	3551	61.66

34	3548	3680	3613	61.66
35	3610	3746	3675	61.66
36	3670	3808	3736	61.66
37	3730	3873	3798	61.66
38	3791	3941	3859	61.66
39	3849	4006	3921	61.66
40	3907	4075	3983	61.66
41	3966	4145	4044	61.66
42	4024	4214	4106	61.66
43	4081	4281	4168	61.66
44	4139	4349	4229	61.66
45	4195	4416	4291	61.66
46	4252	4478	4353	NA

iii) Supplementary material: Chapter 5

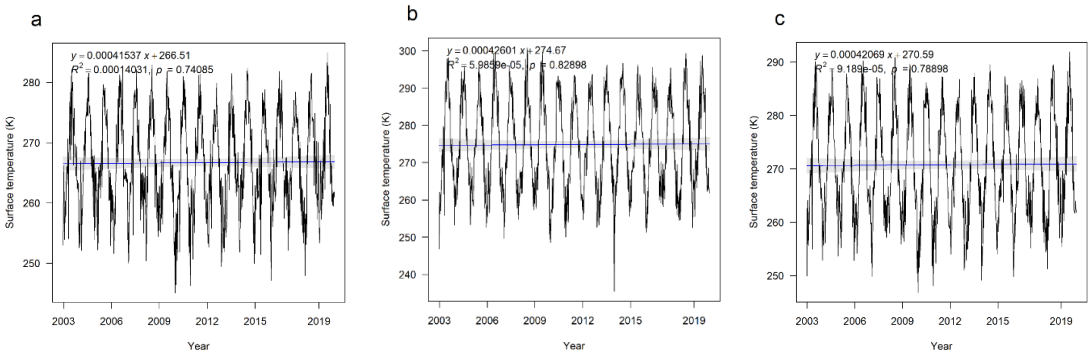

Supplementary Figure 5.1. 8-day mean MODIS land surface temperature measurements plotted for a single pixel at 1050 m a.s.l. over the period 1 Jan 2003- 31 Dec 2019. (a) Night-time LSTs, (b) day-time LSTs and (c) mean daily LSTs.

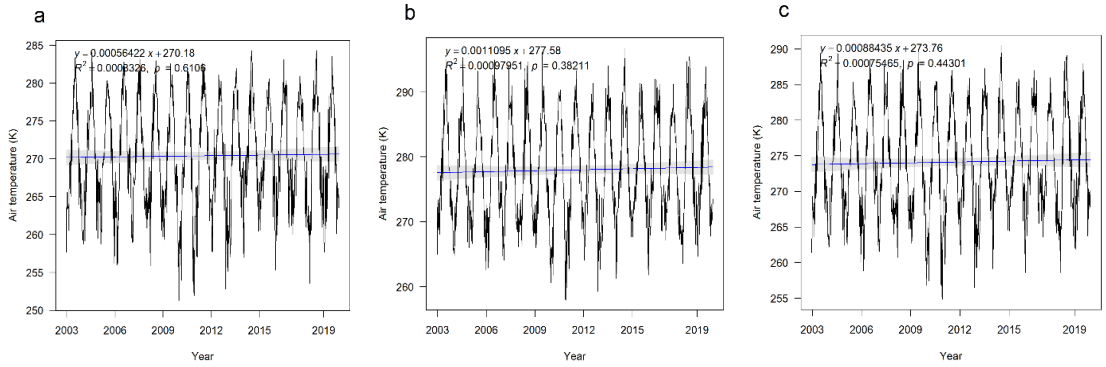

Supplementary Figure 5.2. 8-day mean air temperatures recorded at Fokstua meteorological station (952 m a.s.l.) over the period 1 Jan 2003 – 31 Dec 2019. (a) Daily minimum (T_{min}), (b) daily maximum (T_{max}) and (c) daily mean (T_{day}) air temperatures.

1950 m a.s.l

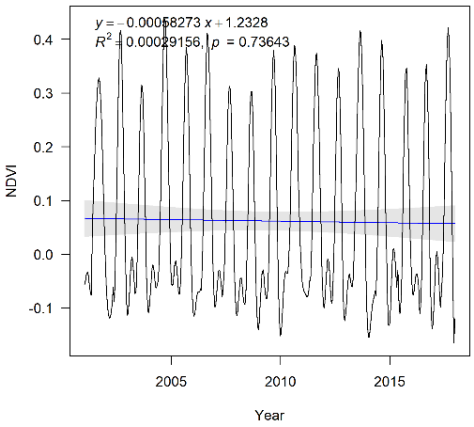

1850 m a.s.l.

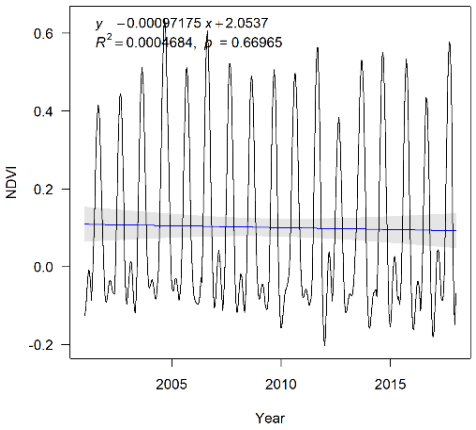

1750 m a.s.l.

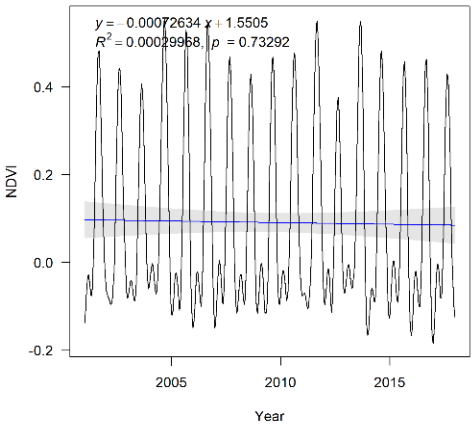

1550 m a.s.l.

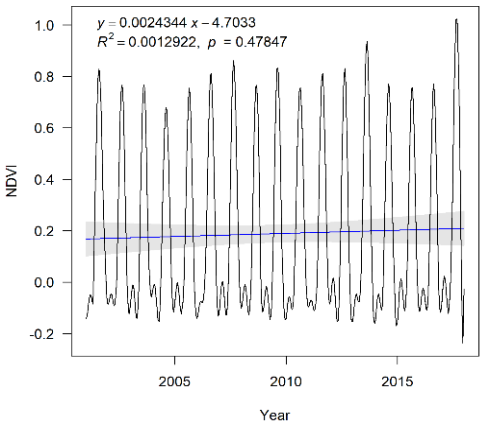

1450 m a.s.l.

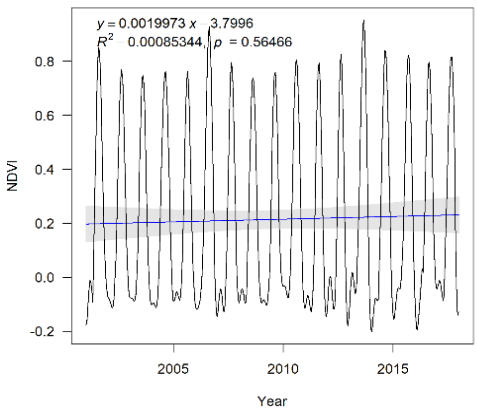

1050 m a.s.l.

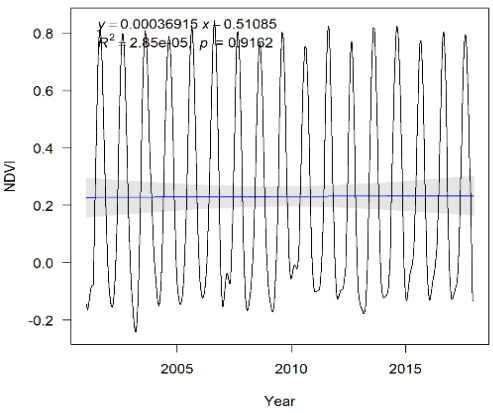

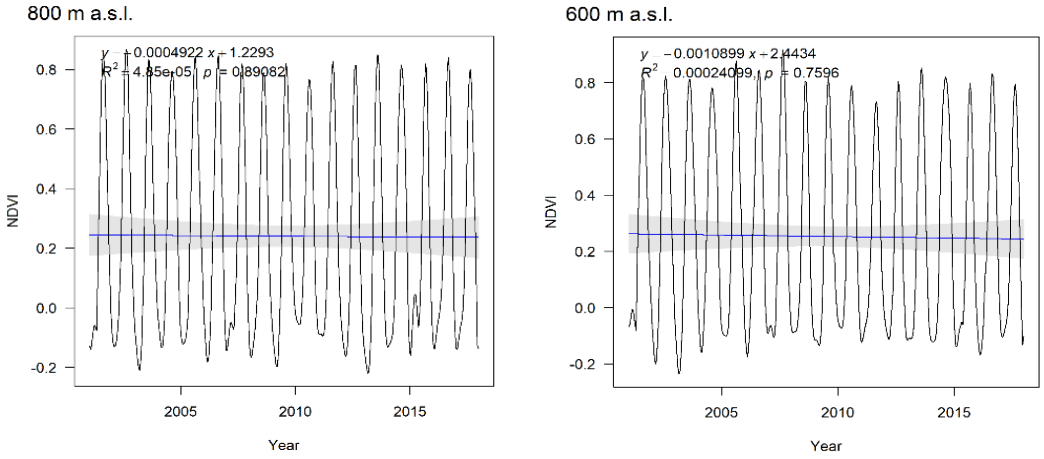

Supplementary Figure 5.3. 8-day average NDVI values plotted for individual pixels across the Galdhøpiggen transect for the period 1 Jan 2001-31 Dec 2017. Statistically insignificant positive trends over the 17-year period are recorded at 1050, 1450 and 1550 m a.s.l., negative trends at 600, 800, 1750, 1850 and 1950 m a.s.l.

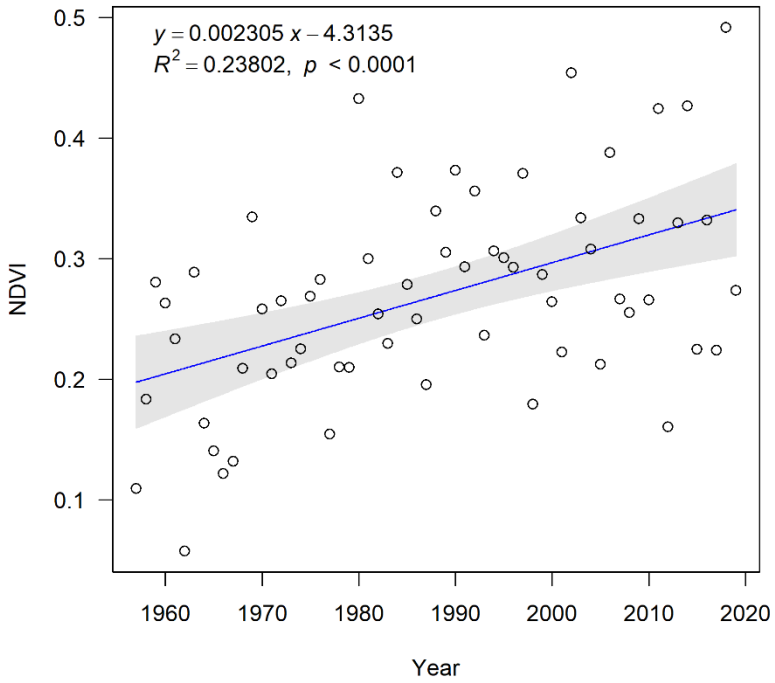

Supplementary Figure 5.4. Annual growing season NDVI plotted for a pixel at the lower limit of permafrost (1450 m a.s.l.) on the Galdhøpiggen transect over the period 1957-2019. Each dot represents the mean growing season NDVI for an individual year.

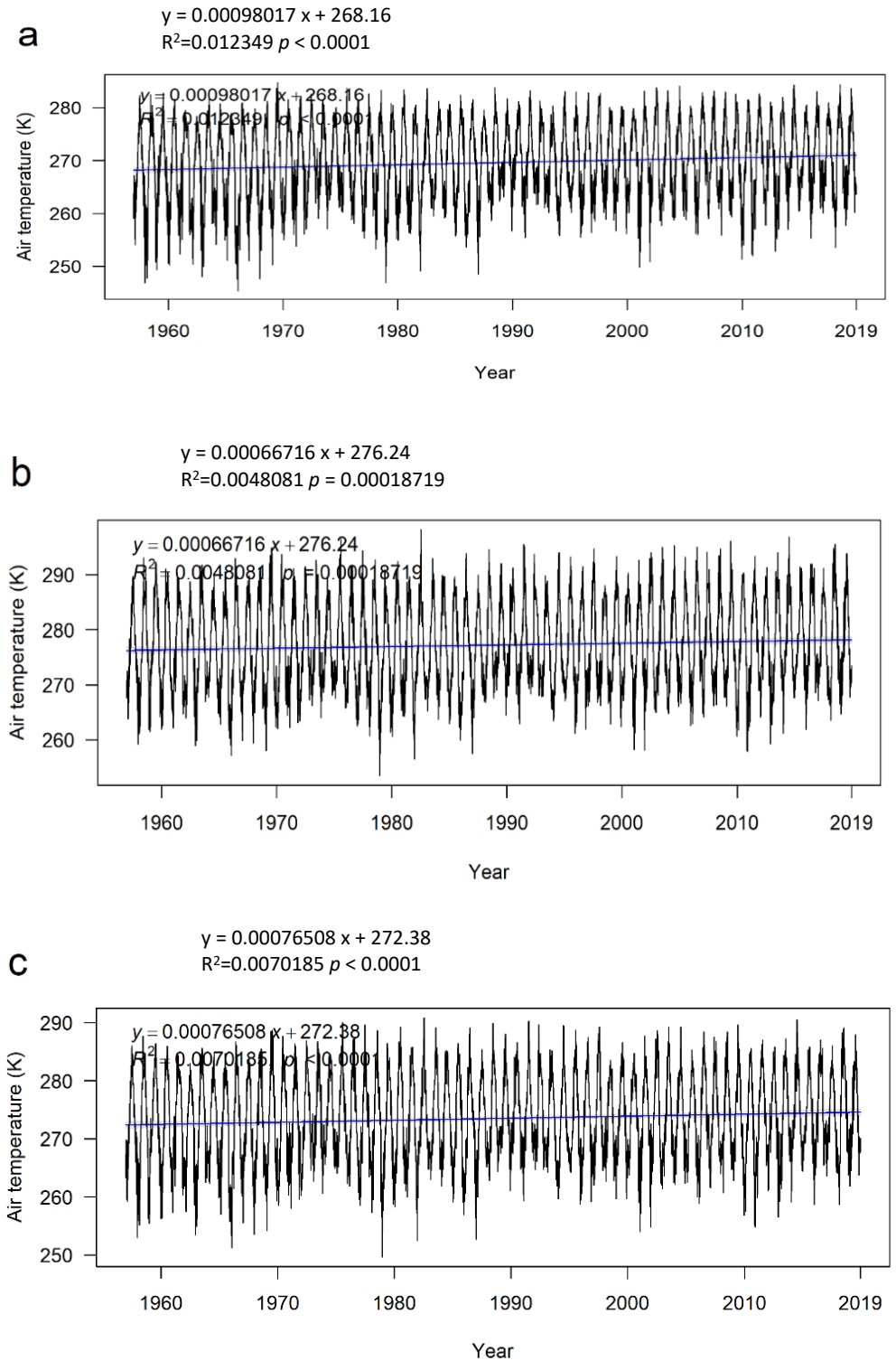

Supplementary Figure 5.5. 8-day mean air temperatures recorded at Fokstua meteorological station (952 m a.s.l.) over the period 1 Jan 1957 – 31 Dec 2019. (a) Daily minimum (T_{min}), (b) daily maximum (T_{max}) and (c) daily mean (T_{day}) air temperatures. The fitted lines represent annual means.

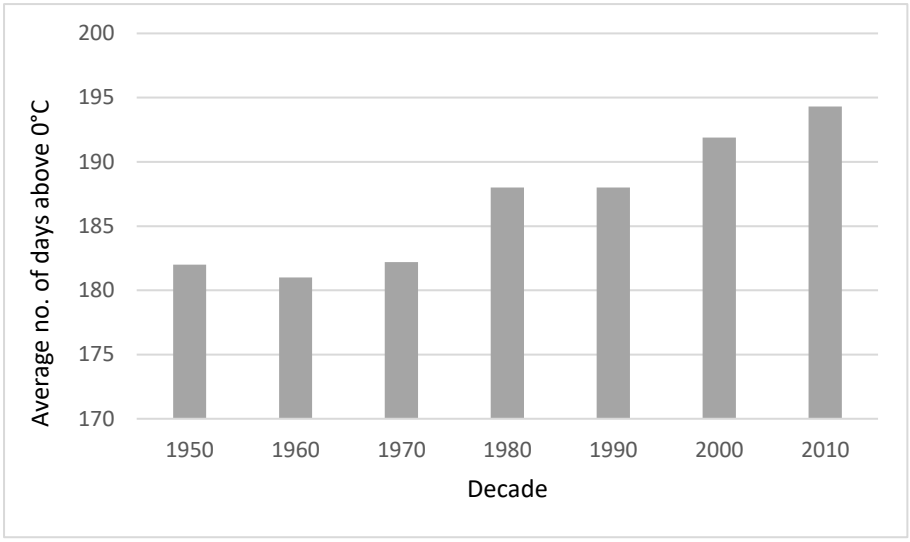

Supplementary Figure 5.6. Mean number of days with air temperatures above 0°C per decade (recorded at Fokstua meteorological station at 952 m a.s.l.)

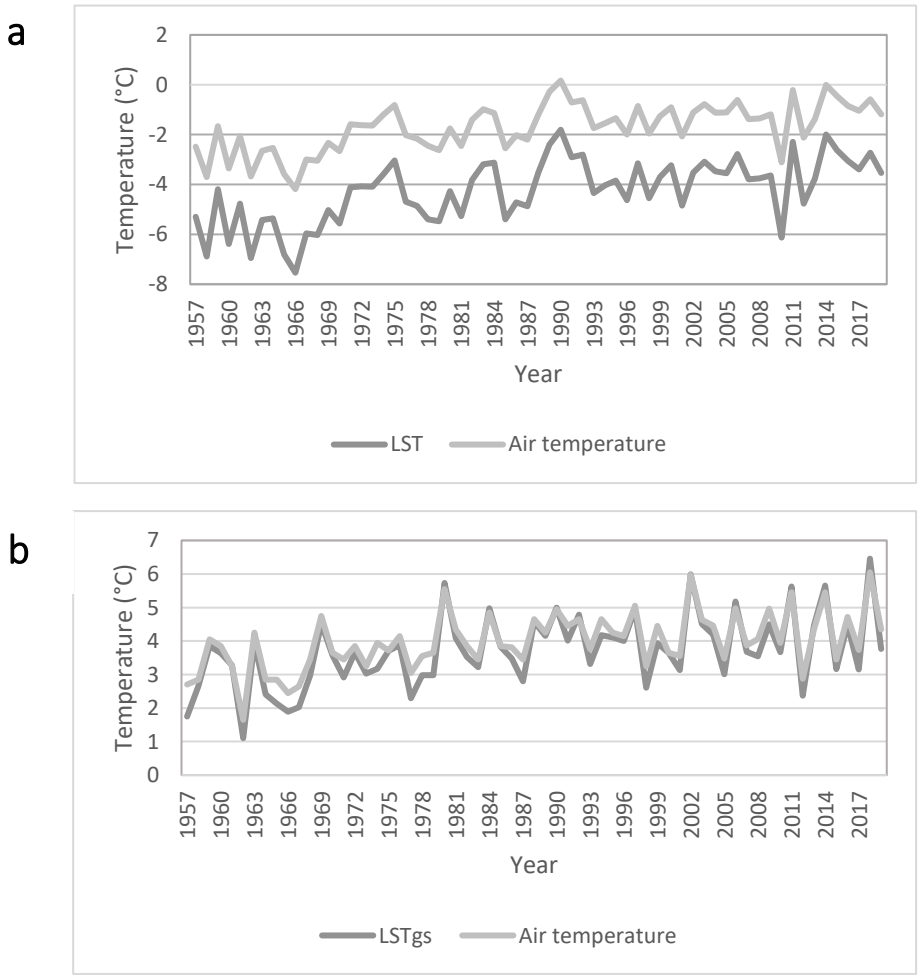

Supplementary Figure 5.7. (a) Mean annual land surface temperature (LST) and observed air temperature and (b) mean growing season land surface temperature (LSTgs) and observed air temperature plotted for a single pixel at the lower limit of permafrost (1450 m a.s.l.) on the Galdhøpiggen transect over the period 1957-2019. LSTs were MODIS-derived, and the observed air temperatures were recorded by Fokstua meteorological station.

Supplementary Table 5.1. Mean growing season NDVI for 1957-1976 and 2000-2019 and the NDVI difference between these periods. Each altitude corresponds to a single pixel on the Galdhøpiggen transect.

Altitude (m a.s.l.)	**1950**	**1850**	**1750**	**1550**	**1450**	**1050**	**800**	**600**
1957-1976 mean NDVI	0.003	0.043	0.063	0.158	0.212	0.355	0.406	0.491
2000-2019 mean NDVI	0.065	0.123	0.150	0.256	0.309	0.452	0.497	0.561
Difference	**0.062**	**0.080**	**0.088**	**0.098**	**0.098**	**0.097**	**0.091**	**0.070**

Supplementary Table 5.2. Mean growing season LST (°C) for 1957-1976 and 2000-2019 and the temperature difference between these periods. Each altitude corresponds to a single pixel on the Galdhøpiggen transect.

Altitude (m a.s.l.)	**1950**	**1850**	**1750**	**1550**	**1450**	**1050**	**800**	**600**
1957-1976 mean LST (°C)	-0.72	0.06	0.36	1.61	2.27	4.02	4.65	5.70
2000-2019 mean LST (°C)	0.40	1.18	1.51	2.82	3.47	5.23	5.84	6.91
Difference	**1.121**	**1.119**	**1.151**	**1.205**	**1.202**	**1.202**	**1.187**	**1.207**

Supplementary Table 5.3. Mean air temperatures (daily mean, daily maximum and daily minimum) for 1957-1976 and 2000-2019 recorded at Fokstua meteorological station (at 952 m a.s.l.), and the temperature difference between these periods.

	Daily mean (°C)	**Mean T_{max} (°C)**	**Mean T_{min} (°C)**
1957-1976 mean	-0.45	4.82	-4.55
2000-2019 mean	0.95	3.15	-2.76
Difference	**1.40**	**1.20**	**1.79**

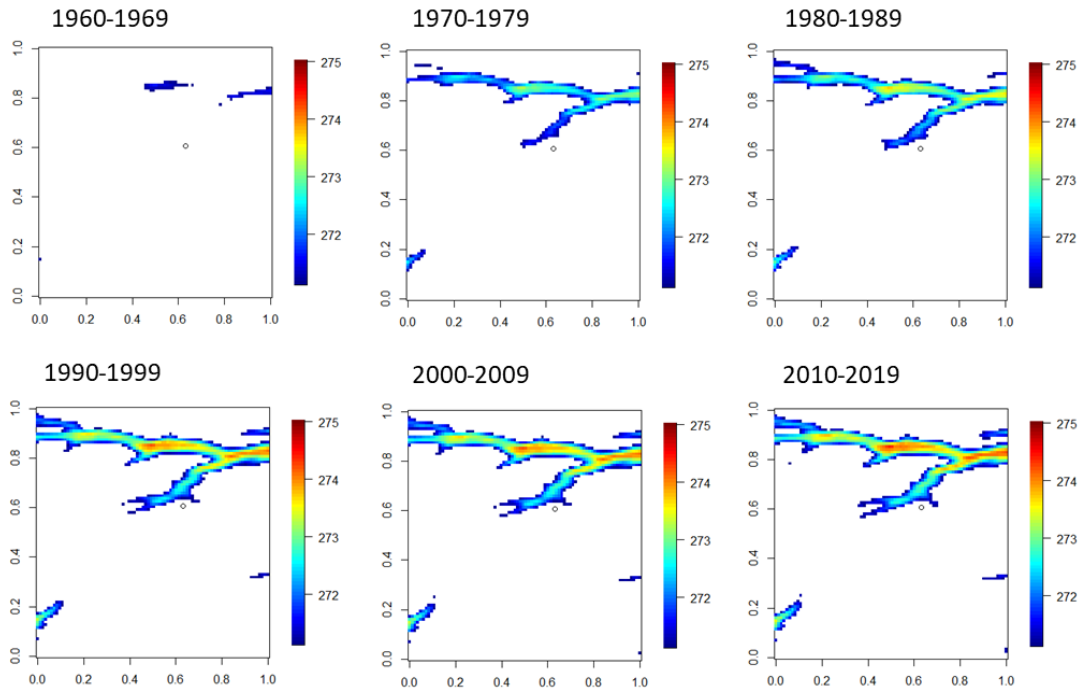

Supplementary Figure 5.8. Mean annual land surface temperatures (K) above -2°C (271.15 K) per decade (the range of years is indicated above each figure). The circle indicates the altitude of the present-day lower limit of permafrost on Galdhøpiggen (1450 m a.s.l.).

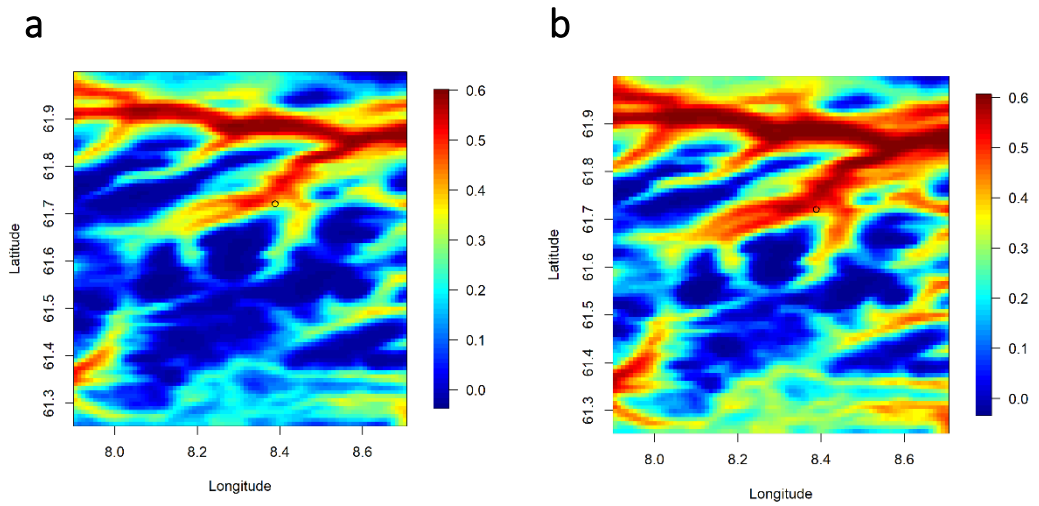

Supplementary Figure 5.9. Mean growing season (April-September) NDVI for (a) the period 1957-1976 and (b) the period 2000-2019. The circle indicates the present-day tree line on Galdhøpiggen at 1050 m a.s.l.

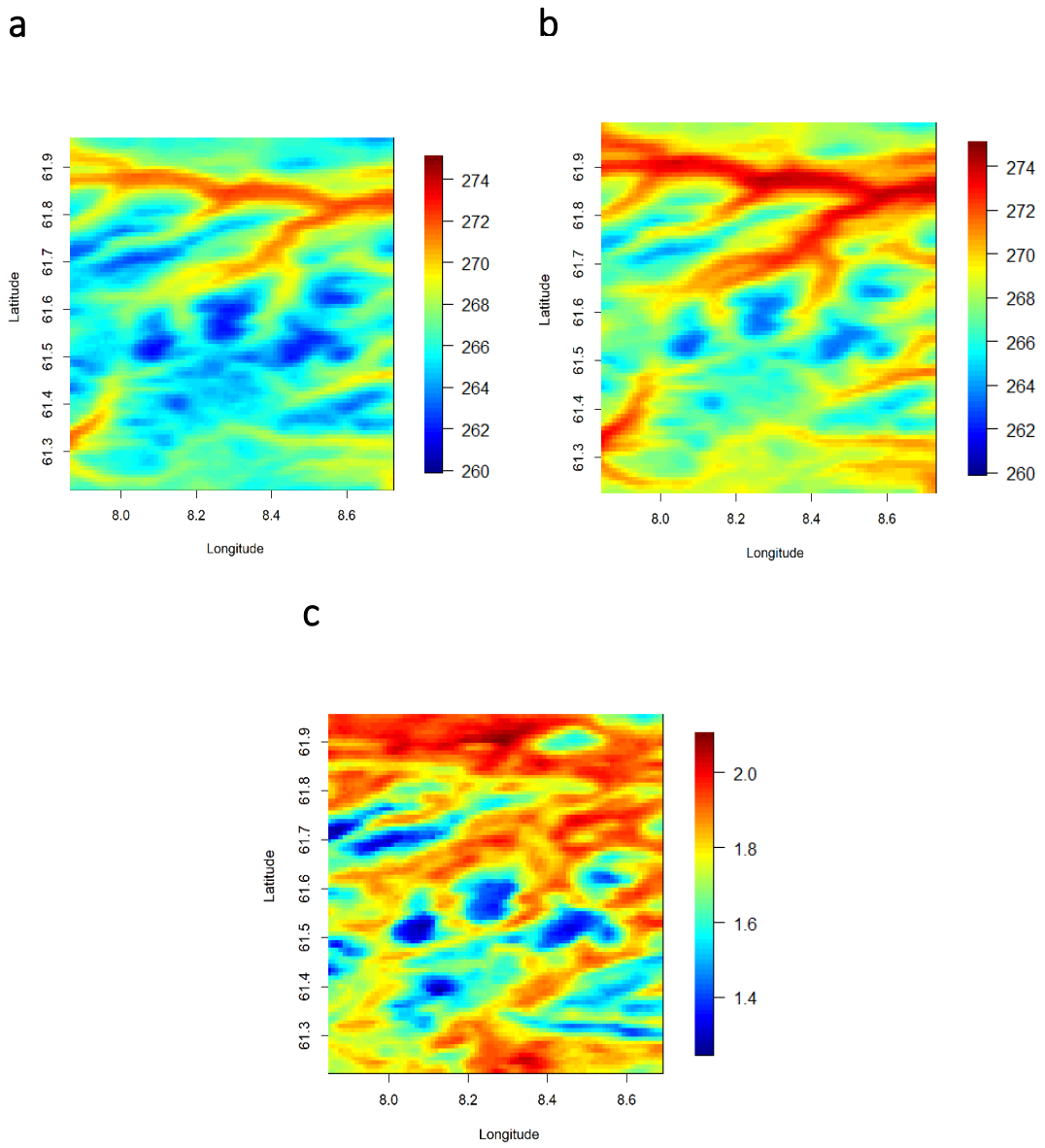

Supplementary Figure 5.10. Mean annual land surface temperatures for the periods (a) 1957-1976, (b) 2000-2019; and (c) the temperature difference between the two periods (°C).

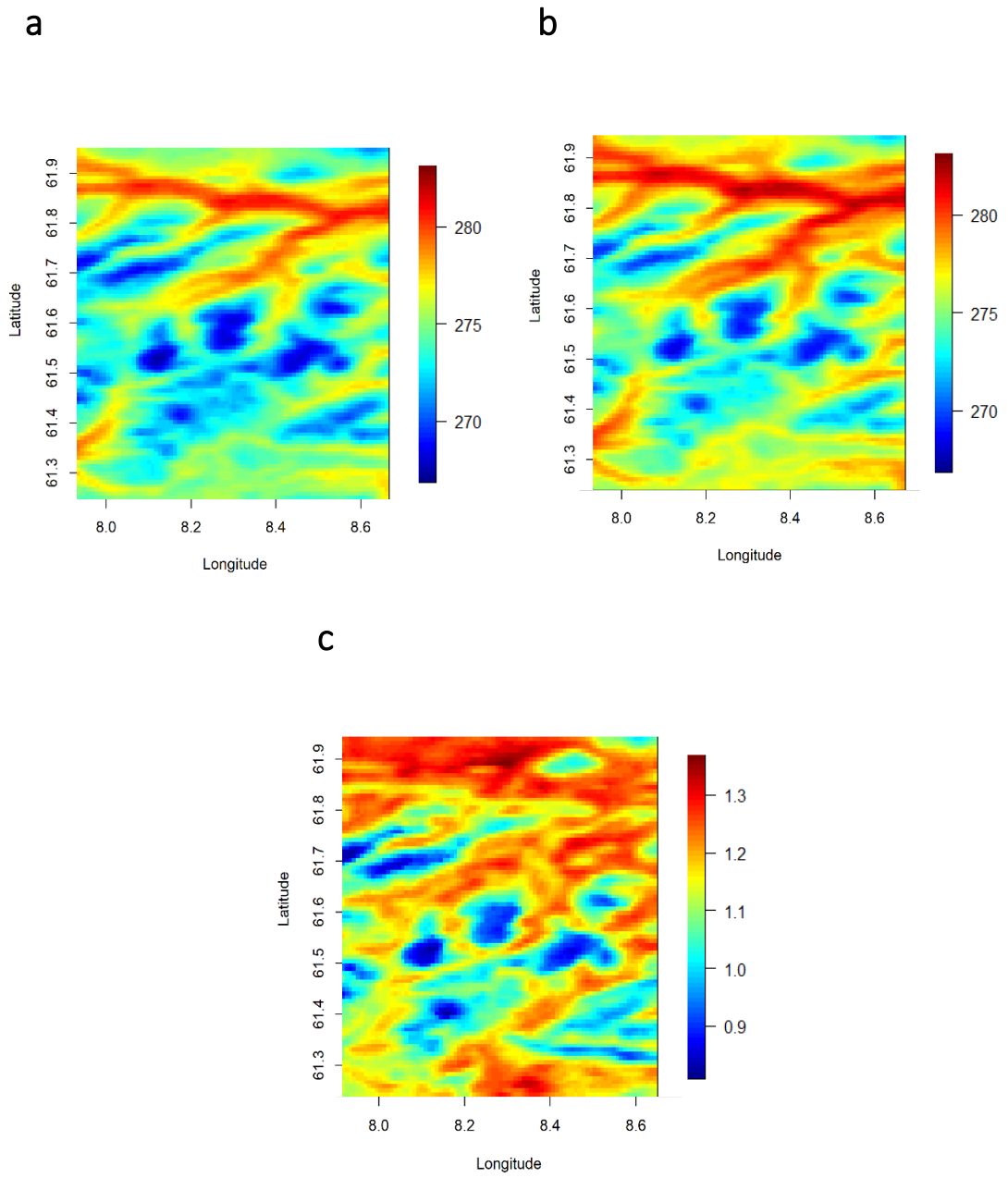

Supplementary Figure 5.11. Mean growing season (April-September) LSTs for the periods (a) 1957-1976, (b) 2000-2019; and (c) the temperature difference between the two periods (°C).

5.1. R code for analysis

5.1.1. Running ‘gapfill’

```
load("Tday03_19.R")
read.dayT<- function(){

# fnames <- scan('xxx.mod', what=character())

 year <- 2003
 iii <- day8 <- 1
 tmp <-
raster('cu1km_day/cu1km_dayT2003001.tif')
 print(tmp)
 dx <- dim(tmp)

 o.ar <- array(dim=c(dx[2], dx[1], 46,
length(2003:2019)))
 iy <- 1
 for (year in 2003:2019){
  iday <- 1
    for(day8 in seq(1,366,8)){
    if (day8 >= 100) {iname <-
paste('cu1km_day/cu1km_dayT',
as.character(year), as.character(day8), '.tif',
sep='')
    }
    else if (day8 >= 10) {
     iname <-
paste('cu1km_day/cu1km_dayT',
as.character(year), '0', as.character(day8),
'.tif', sep='')
    }
    else{
     iname <-
paste('cu1km_day/cu1km_dayT',
as.character(year), '00', as.character(day8),
'.tif', sep='')
    }
#   print(iname)
    tmp <- raster(iname)
    tmp <- matrix(tmp, ncol=dx[1],
nrow=dx[2])[,dx[1]:1]
    o.ar[,,iday, iy] <- tmp
    iday <- iday + 1
    if (iday > 46){
     iday <- 1
     iy <- iy + 1
    }
  }
 }
 o.ar
}
```

```
Lon1km <- seq(7.901125 + 0.002398649*2,
8.699875+3*0.002398649, 0.002398649*4)
Lat1km <- seq(61.25187 + 0.002098315*2,
61.99887 , 0.002098315*4)
Year <- 2003:2019
day <- seq(1,366, 08)
dimnames(Tday1km) <-
list(as.character(Lon1km),
as.character(Lat1km), as.character(day),
as.character(Year))

str(Tday1km)
mean(is.na(Tday1km))
Image(Tday1km)

out <- Gapfill(data = Tday1km)
```

5.1.2. Removing pixels to validate ‘gapfill’

 # dataset: daytime values. Pixels removed from three locations on every 6th image.

```
load("avg.day")
library(fields)
library(gapfill)

mask=!is.na(avg3d[,,1])==1

mask[35:40, 1:8]=0
mask[40:47, 42:49]=0
mask[65:72, 64:71]=0

image(mask)

test.data=Tday1km

for(i in seq (1,46,6))for(j in
1:17){tmp=test.data[,,i,j];tmp[mask==0]=NA;t
est.data[,,i,j]=tmp}

test.data[,,7,1][1:50]
image.plot(test.data[,,7,1])

out <- Gapfill(data = test.data)

test.fill<-out$fill

image.plot(test.fill[,,7,1])
image.plot(test.data[,,7,1])
image.plot(Tday1km[,,7,1])
```

```
Validate(test.data, test.fill, Tday1km, include
= rep(TRUE, length(test.data)))
```

#same steps were repeated with the nighttime data

5.1.3. Plotting the temperature trends across the altitudinal transect over 17 years

#dataset: daily averages

```
sum<- Tday.fill + Tnight.fill
avg.day<-sum/2

avg3d <- array(dim=c(dim(avg.day)[1:2],
dim(avg.day)[3]*dim(avg.day)[4]) )

for (i in 1:17) { i1 <- (i-1)*46+1; i2 <- i*46;
avg3d[,,i1:i2] <- avg.day[,,i]}

plot(avg3d[52,56,],type="l")  #coring site
lines(avg3d[51,54,],col="blue")
lines(avg3d[50,52,],col="yellow")
lines(avg3d[49,52,],col="green")
lines(avg3d[48,52,],col="red")
lines(avg3d[49,49,],col="purple")
```

5.1.4. Calculating 8-day temperature averages for weather station data (example: Fokstua, year 2003)

#8-day averages calculated for maximum, minimum and average daily temperatures

```
F.temp <- read.csv("fokstua_temp.csv",
header=TRUE)
attach(F.temp)

library(TTR)
y01<-subset(F.temp, year =="1")

mavg.8day <- SMA(y01$avg, n=8)
mavg.8day2 <- SMA(y01$min,n=8)
mavg.8day3 <- SMA(y01$max, n=8)

m <- mavg.8day
m2 <- mavg.8day2
m3 <- mavg.8day3

n<- m[seq(0, length(m), 8)]
n2<- m2[seq(0, length(m2), 8)]
n3<- m3[seq(0, length(m3), 8)]

matrix(n)
matrix(n2)
matrix(n3)
```

5.1.5. Regression

#Dataset: daily averages

```
load("avg.day")
stationsavg <- read.csv("stationsavg.csv",
header=TRUE)

library(raster)
library(fields)
library(gapfill)

avg3d <- array(dim=c(dim(avg.day)[1:2],
dim(avg.day)[3]*dim(avg.day)[4]) )

for (i in 1:17) { i1 <- (i-1)*46+1; i2 <- i*46;
avg3d[,,i1:i2] <- avg.day[,,i]}

avgday.fit<- avg3d*NA

for (i in 1:84) { for(j in 1:89) { lm1 <- lm(
avg3d[i,j,] ~ stationsavg$st1.b +
stationsavg$st2.f + stationsavg$st3.s);
avgday.fit[i,j,] <- lm1$coef[1] +
lm1$coef[2]*stationsavg$st1.b +
lm1$coef[3]*stationsavg$st2.f +
lm1$coef[4]*stationsavg$st3.s } }


plot(avg3d[52,56,],type="l")
lines(avgday.fit[52,56,],col="blue")
```

#same steps were repeated with daytime and nighhtime images/max-min station temperature data

5.1.6. Plotting correlation coefficients for individual pixels

```
r.obs.fit <-avg3d[,,1]*NA

d.x <- dim(avg3d)
for (i in 1:d.x[1]) for (j in 1:d.x[2]) { t1 <-
avg3d[i,j,]; t2 <- avgday.fit[i,j,]; r.obs.fit[i,j] <-
cor(t1,t2, use='complete.obs')}

r.obs.fit[52,49]
```

```
image.plot(r.obs.fit)
```

5.1.7. Modelling the LSTs for 1957-2019

```
fokstua <- read.csv("fokstua.csv",
header=TRUE)

new3d <- array(dim=c(dim(avg3d)[1:2],
dim(avg3d)[3]+2116) )


short.ts <- fokstua$f.avg[-c(1:2116)]
long.ts <- fokstua$f.avg


for (i in 1:84) {
  for(j in 1:89) {
     lm1 <- lm( avg3d[i,j,] ~ short.ts);
     new3d[i,j,] <- lm1$coef[1] +
lm1$coef[2]*long.ts
}}

plot(new3d[52,56,],type="l")
lines(new3d[73,76,],type="l", col="red")
```

#same steps were repeated with daytime and nighhtime images/max-min station temperature data